

**ABILITY OF SEVEN AQUATIC PLANT SPECIES TO
ABSORB AND TRANSFORM METAL IONS TO
NANOPARTICLES**



**A Thesis Submitted in Partial Fulfillment of the Requirements for the
Doctor of Philosophy in Environmental Biology
Suranaree University of Technology
Academic Year 2019**

ความสามารถของพืชน้ำเจ็ดชนิดในการดูดซึมและเปลี่ยนไอออนโลหะเป็น
อนุภาคนาโน

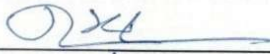


วิทยานิพนธ์นี้เป็นส่วนหนึ่งของการศึกษาตามหลักสูตรปริญญาวิทยาศาสตรดุษฎีบัณฑิต
สาขาวิชาชีววิทยาสิ่งแวดล้อม
มหาวิทยาลัยเทคโนโลยีสุรนารี
ปีการศึกษา 2562

ABILITY OF SEVEN AQUATIC PLANT SPECIES TO ABSORB AND TRANSFORM METAL IONS TO NANOPARTICLES

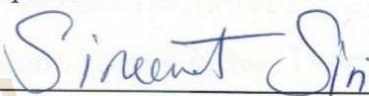
Suranaree University of Technology has approved this thesis submitted in partial fulfillment of the requirements for the Degree of Doctor of Philosophy.

Thesis Examining Committee




(Asst. Prof. Dr. Duangkamol Maensiri)

Chairperson




(Assoc. Prof. Dr. Sineenat Siri)

Member (Thesis Advisor)




(Assoc. Prof. Dr. Wattana Pattanagul)

Member




(Asst. Prof. Dr. Patcharin Chaisuwan)

Member




(Asst. Prof. Dr. Santi Watthana)

Member



(Assoc. Prof. Flt. Lt. Dr. Kontorn Chamniprasart)

Vice Rector for Academic Affairs
and Internationalization



(Assoc. Prof. Dr. Worawat Meevasana)

Dean of Institute of Science

จิราพร ชุมพล : ความสามารถของพืชน้ำเจ็ดชนิดในการดูดซึมและเปลี่ยนไอออน โลหะเป็นอนุภาคนาโน (ABILITY OF SEVEN AQUATIC PLANT SPECIES TO ABSORB AND TRANSFORM METAL IONS TO NANOPARTICLES) อาจารย์ที่ปรึกษา : รองศาสตราจารย์ ดร.สินีนานู ศิริ, 222 หน้า.

พืชน้ำหลายชนิดจัดเป็นพืชที่ฟื้นฟูสิ่งแวดล้อมปนเปื้อนโลหะหนัก เนื่องจากพืชสามารถดูดซับและสะสมไอออนโลหะหนักไว้ได้ อย่างไรก็ตามโอกาสที่ไอออนโลหะเหล่านี้ภายในเซลล์จะเปลี่ยนรูปเป็นอนุภาคนาโนยังไม่ทราบแน่ชัด ดังนั้นงานวิจัยนี้จึงต้องการศึกษาความสามารถของพืชน้ำเจ็ดชนิดในการดูดซับและเปลี่ยนไอออนของทองแดง เหล็ก ตะกั่ว นิกเกิล และเงิน เป็นอนุภาคนาโน ซึ่งพืชน้ำเหล่านี้มีการกระจายทั่วประเทศไทย คือ *Azolla pinnata* R.Br. (แห่นางดำ) *Salvinia molesta* D.S. Mitch. (จอกหูหนู) *Lemna minor* L. (แห่น้ำเต้า) *Lemna perpusilla* Torr. (แห่น้ำเต้า) *Spirodela polyrrhiza* (L.) Schleid (แห่น้ำเต้าใหญ่) *Wolffia globosa* (Roxb.) Hartog & Plas (ไข่น้ำ) และ *Eichhornia crassipes* (Mart.) Solms (ผักตบชวา) ทั้งนี้ความเป็นพิษของไอออนโลหะเหล่านั้นได้วิเคราะห์จากการเปลี่ยนแปลงทางสัณฐานวิทยาของใบ คือ การเหี่ยว และ/หรือ เปลี่ยนเป็นสีน้ำตาล โดยการศึกษาการเกิดอนุภาคนาโนโลหะในเซลล์ได้ใช้ความเข้มข้นของสารละลายโลหะที่ความเป็นพิษร้อยละ 10 ผลการวิเคราะห์ธาตุด้วยการเรืองแสงของรังสีเอกซ์พบชัดเจนว่าพืชมีการดูดซับไอออนของโลหะในระดับสูงเมื่อเปรียบเทียบกับพืชในชุดควบคุม และยังพบการลดลงของธาตุโพแทสเซียมและแคลเซียมอย่างมีนัยสำคัญ ซึ่งคาดว่า การเปลี่ยนแปลงสมดุลของธาตุเหล่านี้เป็นผลจากสภาวะเครียดของพืชต่อไอออนโลหะ ผลการศึกษาด้วยอินฟราเรดสเปกโทรสโกปีแบบ attenuated total reflectance พบการเปลี่ยนแปลงการสั่นของหมู่ฟังก์ชันของสารประกอบอินทรีย์ภายใต้สภาวะเครียดจากโลหะ ซึ่งชี้ว่าพืชมีการตอบสนองต่อสภาวะเครียดจากโลหะโดยมีการเพิ่มของสารชีวโมเลกุลที่มีฟอสฟอรัสเป็นองค์ประกอบ ไขมัน การแสดงออกของยีน และการสังเคราะห์โปรตีน จากภาพถ่ายกล้องจุลทรรศน์อิเล็กตรอนแบบส่องผ่านพบว่าการสร้างอนุภาคนาโนในระดับเซลล์ ซึ่งส่วนใหญ่กระจายอยู่ในบริเวณเยื่อหุ้มเซลล์ ทั้งนี้พบว่าการสร้างอนุภาคนาโนที่มีรูปร่างและขนาดที่แตกต่างกันขึ้นอยู่กับชนิดพืช และไอออนของโลหะบางชนิดเท่านั้นที่ถูกเปลี่ยนเป็นอนุภาคนาโนได้ โดยพืชที่ศึกษาทั้งหมดไม่สามารถชักนำการสร้างอนุภาคนาโนของนิกเกิลได้ ทั้งนี้แม้ว่าอนุภาคนาโนของโลหะส่วนใหญ่ที่ตรวจพบมีรูปร่างทรงกลม แต่พบว่าการสร้างอนุภาคนาโนตะกั่วรูปร่างแท่งในเซลล์รากของ *A. pinnata* R.Br. ได้ ผลการวิเคราะห์ด้วยเทคนิคการกระเจิงของอิเล็กตรอนแบบเลี้ยวเบนที่ และการเลี้ยวเบนของรังสีเอกซ์ยืนยันได้ว่าโครงสร้างของอนุภาคนาโนโลหะในเซลล์พืชเป็น อนุภาคนาโนของเงิน (Ag) ทองแดง (Cu) และ

CuO) เหล็ก (Fe FeO Fe₂O₃ และ Fe₃O₄) และตะกั่ว (Pb และ PbO) ผลการทดลองนี้ชี้ให้เห็นทิศทางของไอออนโลหะที่ถูกเปลี่ยนเป็นอนุภาคนาโนในเซลล์พืช ซึ่งอาจเป็นอีกทางเลือกในการผลิตอนุภาคนาโนโลหะจากไอออนของโลหะที่อยู่ในสิ่งแวดล้อมปนเปื้อน

THESIS ADVISOR : ASSOC. PROF. SINEENAT SIRI, Ph.D., 222 PP.

AQUATIC PLANT/BIOGENESIS/DETOXIFICATION METAL IONS/
NANOPARTICLES/PHYTOREMEDIATION PLANT

Several aquatic plant species are considered as metal-phytoremediation plants as they efficiently uptake and store metals. Nevertheless, the possibility of these cellular metal ions to transform into metal nanoparticles (NPs) has remained unclear. Thus, this research aimed to investigate the capability of seven aquatic plant species commonly distributed in Thailand, to absorb and transform copper (Cu), iron (Fe), lead (Pb), nickel (Ni), and silver (Ag) into NPs. *Azolla pinnata* R.Br., *Salvinia molesta* D.S., *Wolffia arrhiza* (L.) Selden, *Chara sp.*, *Hydrilla verticillata* (L.) Rostk & Schmidt, *Elodea canadensis* (Mart.) Johns, *Utricularia* sp. and *Eichhornia crassipes* (Mart.) Solms. The uptake of these metal ions was determined by the morphological changes in leaves including withering, chlorosis, and browning and the 10% toxicity concentration was also determined. The cellular formation of metal NPs. Energy dispersive X-ray fluorescence (EDXRF) analysis clearly showed the high uptake levels of these metal ions as compared with the control and the reduced levels of potassium and calcium elements suggested the effects of metal-stress on the balance of these cellular ions. The attenuated total reflectance-fourier transform

สาขาวิชาชีววิทยา

ปีการศึกษา 2562

ลายมือชื่อนักศึกษา

จิราพร วัฒน

ลายมือชื่ออาจารย์ที่ปรึกษา

Sinuat Jui

JIRAPORN CHUMPOL : ABILITY OF SEVEN AQUATIC PLANT SPECIES
TO ABSORB AND TRANSFORM METAL IONS TO NANOPARTICLES
THESIS ADVISOR : ASSOC. PROF. SINEENAT SIRI, Ph.D. 222 PP.


AQUATIC PLANT/BIOGENESIS/DETOXIFICATION/METAL IONS/
NANOPARTICLES/PHYTOREMEDIATION PLANT

Several aquatic plant species are considered as metal-phytoremediation plants as they efficiently uptake and store metal ions. Nevertheless, the possibility of these cellular metal ions to transform into metal nanoparticles (NPs) has remained unclear. Thus, this research aimed to investigate the capability of seven aquatic plant species, commonly distributed in Thailand, to absorb and transform copper (Cu), iron (Fe), lead (Pb), nickel (Ni), and silver (Ag) metal ions into NPs; *Azolla pinnata* R.Br., *Salvinia molesta* D.S. Mitch., *Lemna minor* L., *Lemna perpusilla* Torr., *Spirodela polyrrhiza* (L.) Schleid., *Wolffia globosa* (Roxb.) Hartog & Plas and *Eichhornia crassipes* (Mart.) Solms. The toxicity of these metal ions was determined by the morphological changes of leaves including witheredness and/or browning and the 10% toxicity concentration was used to study the cellular formation of metal NPs. Energy dispersive X-ray fluorescence (EDXRF) analysis clearly showed the high uptake levels of these metal ions as compared with the control and the reduced levels of potassium and calcium elements suggested the effects of metal-stress on the balances of these cellular ions. The attenuated total reflectance-Fourier transform infrared (ATR-FTIR) results revealed the changes of functional group vibrations of organic compounds under metal-stress conditions. These results suggested the induction of phosphorus-containing biomolecules, lipids, gene expression, and

protein synthesis in response to the metal-stress conditions. Transmission electron microscopy (TEM) images revealed the formation of cellular metal NPs that were dominantly located in the vicinity of plasma membrane. Interestingly, the formation of different shapes and sizes of metal NPs greatly depended on each plant species. Also, only some metal ions were efficiently transformed into NPs. All studied plants were unable to induce the formation of NiNPs. Although spherical NPs were detected in most studied plants, the rod-shaped PbNPs were efficiently formed by root cells of *A. pinnata* R.Br. Selected area electron diffraction (SAED) and energy-dispersive X-ray (EDX) analyses were used to confirm the identity of NPs inside the plant cells in this study. The results confirmed the structure of the cellular metal NPs, which identified to AgNPs (Ag), CuNPs (Cu and CuO), FeNPs (Fe, FeO, Fe₂O₃ and Fe₃O₄), and PbNPs (Pb and PbO). These results have shed light on the fate of metal ions to transform into metal NPs inside the cells, which may suggest the alternative route to produce metal NPs from wasted metal ions in the environment.

School of Biology

Academic Year 2019

Student's Signature 

Advisor's Signature 

ACKNOWLEDGEMENTS

The author wishes to acknowledge the funding support from the National Research Fund under Grant No. SUT1-104-59-24-06 and the Potential Graduate Student Program-Academic Scholarship, Suranaree University of Technology

I would like to express my deepest and sincere gratitude to my advisor, Associate Professor Dr. Sineenat Siri for her kindness in providing an opportunity to be her advisee. I am also appreciated for her valuable supervision, suggestions, encouragement, supporting, and guidance.

My appreciation is also expressed to all staffs in the School of Biology, Institute of Science, Suranaree University of Technology, Nakhon Ratchasima for providing helps and wonderful work environment. Also, I am much appreciated the friendship from all friends and SIRI lab's members that gave me helps and supports.

Finally, I would like to express my sincere gratitude and appreciation to my dear parents, Mr. Boonmak Chumpol and Mrs. Somchit Chumpol who always give me the support and provide me the opportunity to pursue the Ph.D. study. I deeply thank my sister, Ms. Jirapan Chumpol, who helps me taking care of our parents.

Jiraporn Chumpol

CONTENTS

	Page
ABSTRACT IN THAI	I
ABSTRACT IN ENGLISH	III
ACKNOWLEDGEMENT	V
CONTENTS	VI
LIST OF TABLES	XII
LIST OF FIGURES	XV
LIST OF ABBREVIATIONS	XXV
CHAPTER	
I INTRODUCTION	1
1.1 Background Problem	1
1.2 Significance of the Study	4
1.3 Research Objectives	4
1.4 Scope of the Study	6
II LITERATURE REVIEWS	7
2.1 Metal Nanoparticles	7
2.1.1 Copper nanoparticles	7
2.1.2 Iron nanoparticles	11
2.1.3 Lead nanoparticles	15
2.1.4 Nickel nanoparticles	17

CONTENTS (Continued)

	Page
2.1.5 Silver nanoparticles	19
2.2 Syntheses of Metal Nanoparticles	23
2.2.1 Chemical and physical syntheses of metal nanoparticles	23
2.2.2 Biosynthesis of metal NPs	24
2.2.2.1 Living microorganisms	25
2.2.2.2 Biomolecule extracts	28
2.3 Phytoremediation of Contaminated Heavy Metals in Water	35
2.3.2 <i>Azolla pinnata</i> R.Br.	36
2.3.2 <i>Salvinia molesta</i> D.S. Mitch.	37
2.3.3 <i>Lemna minor</i> L.	38
2.3.4 <i>Lemna perpusilla</i> Torr.	39
2.3.5 <i>Spirodela polyrrhiza</i> (L.) Schleid.	40
2.3.6 <i>Wolffia globosa</i> (Roxb.) Hartog & Plas	41
2.3.7 <i>Eichhornia crassipes</i> (Mart.) Solms	41
2.4 Review of Related Studies	44
III MATERIALS AND METHODS	
3.1 Materials	49
3.2 Experiments	49
3.2.1 Toxicity analysis	49
3.2.2 Cross-sections of metal-treated roots	50

CONTENTS (Continued)

	Page
3.2.3 Analysis of metal uptake by the plant samples	50
3.2.4 Analysis of chemical functional groups of biomolecules	51
3.2.5 Cellular accumulation of nanoparticles in plant cells	52
3.2.6 Characterization of metal nanoparticles	53
3.2.7 Statistical analysis	54
IV RESULTS AND DISCUSSION PART I	
Salviniaceae family: The ability of <i>Azolla pinnata</i> R.Br. and <i>Salvinia molesta</i> D.S. Mitch to absorb and transform metal ions to metal nanoparticles	54
4.1 Toxicity Test	54
4.2 The Elemental Mass Profile Analysis	61
4.3 Changed Profiles of Biomolecules in Response to Metal Treatments	66
4.4 Accumulation of Metal Nanoparticles	69
4.1.1 Accumulation of metal nanoparticles in <i>Azolla pinnta</i> R.Br.	69
4.1.2 Accumulation of metal nanoparticles in <i>Salvinia molesta</i> D.S. Mitch.	75
4.5 Characterization of Metal Nanoparticles in the Plant Cells	79
4.5.1 SAED-TEM analyses	79
4.5.2 EDX analyses	82

CONTENTS (Continued)

	Page
V RESULTS AND DISCUSSION PART II	
Araceae family: The ability of <i>Lemna minor</i> L., <i>Lemna perpusilla</i> Torr., <i>Spirodela polyrhiza</i> (L.) Schleid., and <i>Wolffia globosa</i> (Roxb.) Hartog & Plas. to absorb and transform metal ions to metal nanoparticles	88
5.1 Toxicity Study	88
5.1.1 Toxicity of the tested metal solutions to <i>Lemna minor</i> L. and <i>Lemna perpusilla</i> Torr.	89
5.1.2 Toxicity of the tested metal solutions to <i>Spirodela polyrhiza</i> (L.) Schleid.	92
5.1.3 Toxicity of the tested metal solutions to <i>Wolffia globosa</i> (Roxb.) Hartog & Plas	93
5.2 The elemental Mass Profiles	95
5.2.1 <i>Lemna minor</i> L. and <i>Lemna perpusilla</i> Torr.	95
5.2.2 <i>Spirodela polyrhiza</i> (L.) Schleid.	101
5.2.3 <i>Wolffia globosa</i> (Roxb.) Hartog & Plas	104
5.3 ATR-FTIR Profiles in Response to Metal Treatments	107
5.3.1 <i>Lemna minor</i> L. and <i>Lemna perpusilla</i> Torr.	107
5.3.2 <i>Lemna perpusilla</i> Torr.	124
5.3.3 <i>Spirodela polyrhiza</i> (L.) Schleid.	130
5.3.4 <i>Wolffia globosa</i> (Roxb.) Hartog & Plas	136

CONTENTS (Continued)

	Page
VI RESULTS AND DISCUSSION PART III	
Pontederiaceae family: The ability of <i>Eichhornia crassipes</i> (Mart.)	
Solms to absorb and transform metal ions to metal nanoparticles	145
6.1 Toxicity Test	145
6.2 The Elemental Mass Profiles	147
6.3 The ATR-FTIR Profiles of Water Hyacinth Roots	150
6.4 Accumulation of Metal Nanoparticles	154
6.5 Characterization of Metal Nanoparticles	155
VII RESULTS AND DISCUSSION PART III	
Comparison of seven plant species to uptake and transform metal ions	
into nanoparticles	162
7.1 Metal Uptake	163
7.2 Formation of Metal Nanoparticles	164
7.3 Proposed Mechanism of the Formation of Metal Nanoparticles	169
VII CONCLUSION	171
REFERENCES	175
APPENDICES	
APPENDIX A CHEMICALS AND MEDIA	203
APPENDIX B REAGENT PREPERATION	206
APPENDIX C SUPPLEMENTARY DATA	211

CONTENTS (Continued)

	Page
CURRICULUM VITAE	222



LIST OF TABLES

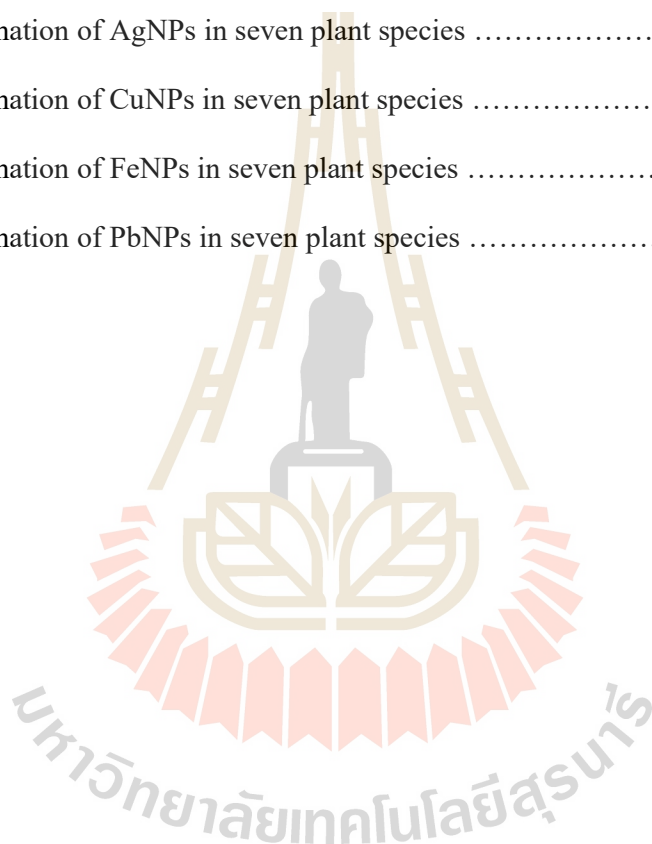
Table	Page
2.1	Publication scenario of synthesis of AgNPs under standard publishers (1980–2014)20
2.2	Intracellular synthesis of metal NPs by various microorganisms27
2.3	The extracellular synthesis metal NPs by various microbes29
2.4	Biosynthesis of metal NPs using the extraction of plant species33
2.5	Capacity of water hyacinth to adsorb heavy metals43
4.1	The quantitative levels of metal elements in <i>Azolla pinnata</i> R.Br. roots by EDXRF analysis64
4.2	The quantitative levels of metal elements in <i>Salvinia molesta</i> D.S. Mitch. roots by EDXRF analysis65
4.3	The summary of the ATR-FTIR spectral peaks of <i>Azolla pinnata</i> R.Br. roots treated with AgNO ₃ , Cu(NO ₃) ₂ , Fe(NO ₃) ₃ , Ni(NO ₃) ₂ and Pb(NO ₃) ₂68
4.4	The summary of the ATR-FTIR spectral peaks of the <i>Salvinia molesta</i> D. Mitch. roots in response to metal exposures68
4.5	Data summary of <i>Azolla pinnata</i> R.Br. and <i>Salvinia molesta</i> D.S. Mitch. in response to five metal ions and their capability to produce metal NPs87
5.1	Elemental mass quantification of the roots of <i>Lemna minor</i> L. in response to metal exposures by EDXRF analysis98

LIST OF TABLES (Continued)

Table	Page
5.2	Elemental mass quantification of the roots of <i>Lemna perpusilla</i> Torr. in response to metal exposures by EDXRF analysis100
5.3	Elemental mass quantification of the roots of <i>Spirodela polyrhiza</i> (L.) Schleid in response to metal exposures by EDXRF analysis103
5.4	Elemental mass quantification of the roots of <i>Wolffia globosa</i> (Roxb.) Hartog & Plas in response to metal exposures by EDXRF analysis106
5.5	The summary of the FTIR spectral peaks of two aquatic roots in response to metal exposures 111
5.6	The summary of ATR-FTIR spectral peaks of <i>Spirodela polyrhiza</i> (L.) Schleid. roots in response to metal exposures114
5.7	The summary of the ATR-FTIR spectral peaks of <i>Wolffia globosa</i> (Roxb.) Hartog & Plas in response to metal exposures117
5.8	Summary data of <i>Lemna minor</i> L., <i>Lemna perpusilla</i> Torr., <i>Spirodela polyrhiza</i> (L.) Schleid, and <i>Wolffia globosa</i> (Roxb.) Hartog & Plas in response to five metal ions and their capability to produce metal NPs142
6.1	Toxicity concentrations of five metal ions on water hyacinth145
6.2	Elemental mass of water hyacinth roots in response to metal exposures149
6.3	The summary of ATR-FTIR spectral peaks of the metal-treated roots of water hyacinth153

LIST OF TABLES (Continued)

Table	Page
6.4 Data summary of water hyacinth in response to five metal ions and its capability to produce	161
7.1 Formation of AgNPs in seven plant species	164
7.2 Formation of CuNPs in seven plant species	165
7.3 Formation of FeNPs in seven plant species	166
7.4 Formation of PbNPs in seven plant species	168



LIST OF FIGURES

Figure	Page
1.1 Seven common aquatic plants used in this study	3
2.1 The different colors of various forms of Cu	8
2.2 The relation of color and size of colloidal CuNPs solution	9
2.3 The FCC structure of CuNPs	9
2.4 Various morphologies of CuNPs	10
2.5 The proposed mechanisms of the antibacterial activity of CuNPs	11
2.6 Fe complexes in the continental crust	12
2.7 The crystal structure of various iron oxide NPs	13
2.8 Different morphology of FeNPs with diameter ranges of 100–500 nm	13
2.9 Biomedical applications of FeNPs	14
2.10 Various forms of lead oxide complexes	15
2.11 Different shapes of PbNPs	16
2.12 Different shapes of PbSNPs synthesized by controlling the reducing and stabilizing agents	17
2.13 Morphology and crystal structure of NiNPs	18
2.14 TEM image of the different shaped NiNPs	19
2.15 UV-Vis spectra of colloidal AgNPs with different sizes and shapes	22
2.16 The colors of colloidal AgNPs and their TEM images	23

LIST OF FIGURES (Continued)

Figure	Page
2.17	Scheme of top-down and bottom-up approaches to synthesize metal NPs.....23
2.18	Biological synthesis of metal NPs in biomedical and environmental field.....25
2.19	Mechanism of microbial-mediated synthesis of metal and metaloxide NPs26
2.20	Mechanism of extracellular synthesis of AgNPs by fungi28
2.21	Images of the waver ant larvae image at the 3 rd instar stage and their extracted proteins visualized on a 12.5% SDS-PAGE gel30
2.22	Images of TEM analysis of the synthesized AgNPs and their growth inhibition zones against <i>Escherichia coli</i> and <i>Staphylococcus aureus</i>31
2.23	Mechanism of plant extracts to mediate the synthesis of metal NPs32
2.24	Images of the growing <i>Azolla pinnata</i> R.Br. and <i>Anabaena azollae</i>36
2.25	The morphology of <i>Salvinia molesta</i> D.S. Mitch. 37
2.26	The morphology of <i>Lemna minor</i> L.39
2.27	The morphology of <i>Lemna perpusilla</i> Torr.40
2.28	The morphology of <i>Spirodela polyrrhiza</i> (L.) Schleid.40
2.29	The morphology of <i>Wolffia globosa</i> (Roxb.) Hartog & Plas.41
2.30	The morphology of <i>Eichhornia crassipes</i> (Mart.) Solms.42
2.31	Chemical structure of pectin44
2.32	The possible cross-linking between metals and pectin alginic acid45
2.33	TEM images of lead deposits in cell wall46

LIST OF FIGURES (Continued)

Figure	Page
2.34 The uptake of gold ions by <i>Arabidopsis</i>	47
2.35 TEM images of chloroplasts in cortex of untreated plants and electron dense of gold observing in the treated plants	47
2.36 TEM micrograph of cross ultrathin sections of the root cortical cells of <i>Brassica napus</i> L.	48
4.1 The toxicity effects of 5 metal ions on <i>Azolla pinnata</i> R.Br.	57
4.2 The toxicity effects of 5 metal ions on <i>Salvinia molesta</i> D.S. Mitch.	58
4.3 The EDXRF mapping images of <i>Azolla pinnata</i> R.Br. roots treated with AgNO_3 , $\text{Cu}(\text{NO}_3)_2$, $\text{Fe}(\text{NO}_3)_3$, $\text{Ni}(\text{NO}_3)_2$, and $\text{Pb}(\text{NO}_3)_2$ solutions	62
4.4 The EDXRF mapping images of <i>S. molesta</i> D.S. Mitch. roots treated AgNO_3 , $\text{Cu}(\text{NO}_3)_2$, $\text{Fe}(\text{NO}_3)_3$, $\text{Ni}(\text{NO}_3)_2$, and $\text{Pb}(\text{NO}_3)_2$ solutions	62
4.5 TEM images of cross-sections of cortical tissues of <i>Azolla pinnata</i> R.Br. roots	70
4.6 Size distribution of metal NPs detected in cortical tissues roots of <i>Azolla</i> <i>pinnata</i> R.Br. roots	71
4.7 TEM images of cross-sections of xylem tissues of <i>Azolla pinnata</i> R.Br.	73
4.8 Average sizes and size distribution of metal NPs in xylem tissues of <i>Azolla pinnata</i> R.Br. roots	74
4.9 TEM images of cross-sections of cortical tissues of <i>Salvinia molesta</i> D.S Mitch. roots	76

LIST OF FIGURES (Continued)

Figure	Page
4.10 Average sizes and size distribution of metal NPs in cortical tissues of <i>Salvinia molesta</i> D.S. Mitch. roots	77
4.11 TEM images of cross-sections of vascular tissues of <i>Salvinia molesta</i> D.S. Mitch. roots	78
4.12 Average diameters and size distribution of metal NPs in vascular tissues of <i>Salvinia molesta</i> D.S. Mitch. roots	79
4.13 SAED-TEM analyses of metal NPs in the Ag-, Cu-, Fe-, Ni-, and Pb-treated roots of <i>Azolla pinnata</i> R.Br.	81
4.14 SAED-TEM analyses of metal NPs in the Ag-, Cu-, Fe-, Ni-, and Pb-treated roots of <i>Salvinia molesta</i> D.S. Mitch.	82
4.15 EDX-TEM analyses of the Ag-, Cu-, Fe-, Ni-, and Pb-treated roots of <i>Azolla pinnata</i> R.Br as compared with the control root	84
4.16 EDX-TEM analyses of the Ag-, Cu-, Fe-, Ni-, and Pb-treated roots of <i>Salvinia molesta</i> D.S. Mitch. as compared with the control root	85
5.1 The morphological changes of <i>Lemna minor</i> L. and <i>Lemna perpusilla</i> Torr. in response to AgNO ₃ , Cu(NO ₃) ₂ , Fe(NO ₃) ₂ , Ni(NO ₃) ₂ , and Pb(NO ₃) ₂ treatments	91
5.2 TC10 values of AgNO ₃ , Cu(NO ₃) ₂ , Fe(NO ₃) ₃ , Ni(NO ₃) ₂ , and Pb(NO ₃) ₂ a determined in <i>Lemna minor</i> L. and <i>Lemna perpusilla</i> Torr.	92

LIST OF FIGURES (Continued)

Figure	Page
5.3	The morphological changes and TC10 values of <i>Spirodela polyrhiza</i> (L.) Schleid. plant in response to AgNO ₃ , Cu(NO ₃) ₂ , Fe(NO ₃) ₂ , Ni(NO ₃) ₂ , and Pb(NO ₃) ₂ treatments93
5.4	The morphological changes (A) and TC10 values (B) of <i>Wolffia globosa</i> (Roxb.) Hartog & Plas in response to AgNO ₃ , Cu(NO ₃) ₂ , Fe(NO ₃) ₂ , Ni(NO ₃) ₂ , and Pb(NO ₃) ₂ treatments94
5.5	EDXRF mapping analysis of <i>Lemna minor</i> L. exposed to AgNO ₃ , Cu(NO ₃) ₂ , Fe(NO ₃) ₂ , Ni(NO ₃) ₂ , and Pb(NO ₃) ₂ solutions97
5.6	EDXRF mapping analysis of <i>Lemna perpusilla</i> Torr. exposed to AgNO ₃ , Cu(NO ₃) ₂ , Fe(NO ₃) ₂ , Ni(NO ₃) ₂ , and Pb(NO ₃) ₂ solutions99
5.7	EDXRF mapping analysis of <i>Spirodela polyrhiza</i> (L.) Schleid. exposed to AgNO ₃ , Cu(NO ₃) ₂ , Fe(NO ₃) ₂ , Ni(NO ₃) ₂ , and Pb(NO ₃) ₂ solutions102
5.8	EDXRF mapping analysis of <i>Wolffia globosa</i> (Roxb.) Hartog & Plas exposed to AgNO ₃ , Cu(NO ₃) ₂ , Fe(NO ₃) ₂ , Ni(NO ₃) ₂ , and Pb(NO ₃) ₂ solutions105
5.9	ATR-FTIR spectra of the control and metal-treated of <i>Lemna minor</i> L. roots as determined in the wavelength range of 4000–400 cm ⁻¹109
5.10	ATR-FTIR spectra of the control and metal-treated of <i>Lemna perpusilla</i> Torr. roots as determined in the wavelength range of 4000–400 cm ⁻¹110

LIST OF FIGURES (Continued)

Figure	Page
5.11 ATR-FTIR spectra of the control and metal-treated of <i>Spirodela polyrhiza</i> (L.) Schleid. roots as determined in the wavelength range of 4000–400 cm ⁻¹	113
5.12 ATR-FTIR spectra of the control and metal-treated <i>Wolffia globosa</i> (Roxb.) Hartog & Plas as determined in the wavelength range of 4000–400 cm ⁻¹	116
5.13 TEM images of metal NPs in cortical cells of the Ag-, Cu-, Fe-, Ni-, and Pb-treated roots of <i>Lemna minor</i> L.	119
5.14 Size distribution histograms and average sizes of AgNPs, FeNPs, and PbNPs in cortical cells of <i>Lemna minor</i> L. roots	120
5.15 TEM images of metal NPs in vascular tissues of the Ag-, Cu-, Fe-, Ni-, and Pb-treated roots of <i>Lemna minor</i> L.	121
5.16 Size distribution histograms and average diameters of AgNPs, FeNPs, and PbNPs in vascular tissues of the Ag-, Fe-, and Pb-treated roots of <i>Lemna minor</i> L.	122
5.17 SAED-TEM analyses of the Ag-, Cu-, Fe-, Ni-, and Pb-treated roots as compared with the control	123
5.18 EDX-TEM analyses of the Ag-, Cu-, Fe-, Ni-, and Pb-treated roots as compared with the control	124

LIST OF FIGURES (Continued)

Figure	Page
5.19 TEM images of metal NPs in cortical tissue of the Ag-, Cu-, Fe-, Ni-, and Pb-treated roots of <i>Lemna perpusilla</i> Torr.	125
5.20 Size distribution histograms and average diameters of AgNPs and PbNPs. in cortical tissue of the Ag- and Pb-treated roots of <i>Lemna perpusilla</i> Torr.	126
5.21 TEM images of metal NPs in vascular tissues of the Ag-, Cu-, Fe-, Ni-, and Pb-treated roots of <i>Lemna perpusilla</i> Torr.	127
5.22 Size distribution histograms and average diameters of AgNPs and PbNPs in vascular tissues of the Ag- and Pb-treated roots of <i>Lemna perpusilla</i> Torr.	128
5.23 SAED-TEM analyses of the Ag-, Cu-, Fe-, Ni-, and Pb-treated roots of <i>Lemna perpusilla</i> Torr. as compared with the control.	129
5.24 EDX-TEM analyses of the Ag-, Cu-, Fe-, Ni-, and Pb-treated roots of <i>Lemna perpusilla</i> Torr. as compared with the control.	130
5.25 TEM images of metal NPs in cortical tissues of the Ag-, Cu-, Fe-, Ni-, and Pb-treated roots of <i>Spirodela polyrhyza</i> (L.) Schleid.	131
5.26 Size distribution histograms and average diameters of AgNPs and PbNPs in cortical tissues of the Ag- and Pb-treated roots of <i>Spirodela polyrhyza</i> (L.) Schleid.	132

LIST OF FIGURES (Continued)

Figure	Page
5.27	TEM images of metal NPs in vascular tissues of the Ag-, Cu-, Fe-, Ni-, and Pb-treated roots of <i>Spirodela polyrhiza</i> (L.) Schleid133
5.28	Size distribution histograms and average diameters of AgNPs and PbNPs in vascular tissues of the Ag- and Pb-treated roots of <i>Spirodela polyrhiza</i> (L.) Schleid.134
5.29	SAED-TEM analyses of the Ag-, Cu-, Fe-, Ni-, and Pb-treated roots of <i>Spirodela polyrhiza</i> (L.) Schleid. as compared with the control135
5.30	EDX-TEM analyses of the Ag-, Cu-, Fe-, Ni-, and Pb-treated roots of <i>Spirodela polyrhiza</i> (L.) Schleid as compared with the control136
5.31	TEM images of metal NPs in the Ag-, Cu-, Fe-, Ni-, and Pb-treated <i>Wolffia globosa</i> (Roxb.) Hartog & Plas.137
5.32	Size distribution histograms and average diameters of AgNPs, FeNPs, and PbNPs in the Ag-, Fe-, and Pb-treated <i>Wolffia globosa</i> (Roxb.) Hartog & Plas.137
5.33	SAED-TEM analyses of the Ag-, Cu-, Fe-, Ni-, and Pb-treated <i>Wolffia globosa</i> (Roxb.) Hartog & Plas as compared with the control139
5.34	EDX-TEM analyses of the Ag-, Cu-, Fe-, Ni-, and Pb-treated <i>Wolffia globosa</i> (Roxb.) Hartog & Plas as compared with the control140

LIST OF FIGURES (Continued)

Figure	Page
6.1 Cross-sections in cortex tissue of water hyacinth roots exposed to AgNO_3 , $\text{Cu}(\text{NO}_3)_2$, $\text{Fe}(\text{NO}_3)_3$, $\text{Ni}(\text{NO}_3)_2$, and $\text{Pb}(\text{NO}_3)_2$ solutions observed under a light microscope	146
6.2 Cross-sections in the vascular tissue of water hyacinth roots exposed to AgNO_3 , $\text{Cu}(\text{NO}_3)_2$, $\text{Fe}(\text{NO}_3)_3$, $\text{Ni}(\text{NO}_3)_2$, and $\text{Pb}(\text{NO}_3)_2$ solutions observed under a light microscope	147
6.3 EDXRF elemental mapping of the water hyacinth roots treated with AgNO_3 , $\text{Cu}(\text{NO}_3)_2$, $\text{Fe}(\text{NO}_3)_3$, $\text{Ni}(\text{NO}_3)_2$, and $\text{Pb}(\text{NO}_3)_2$ solutions	152
6.4 ATR-FTIR spectra of the control and metal-treated roots of water hyacinth in the wavelength range of $4000\text{--}400\text{ cm}^{-1}$	152
6.5 TEM images of cortical cells of the Ag-, Cu-, Fe-, Ni-, and Pb-treated roots	154
6.6 TEM images of xylem of the Ag-, Cu-, Fe-, Ni-, and Pb-treated roots of water hyacinth	155
6.7 HR-TEM analyses of the Ag-, Cu-, Fe-, Ni-, and Pb-treated roots as compared with the control root	156
6.8 SAED-TEM analyses of metal-treated roots of water hyacinth	157
6.9 EDX-TEM analyses of the Ag-, Cu-, Fe-, Ni-, and Pb-treated roots as compared with the control root	159

LIST OF FIGURES (Continued)

Figure	Page
7.1 The quantitative metal-uptake analysis of ^{47}Ag , ^{29}Cu , ^{26}Fe , ^{28}Ni , and ^{82}Pb in roots of seven aquatic plants treated with AgNO_3 , $\text{Cu}(\text{NO}_3)_2$, $\text{Fe}(\text{NO}_3)_3$, $\text{Ni}(\text{NO}_3)_2$, and $\text{Pb}(\text{NO}_3)_2$ solutions	163
7.2 The proposed mechanism of the formation of metal NPs in plant root cells	170

LIST OF BREVIATIONS

AgNPs	Silver Nanoparticles
ATR-FTIR	Attenuated Total Reflectance Fourier Transform Infrared
AuNPs	Gold Nanoparticles
BBC	Body-centered Cubic
COPT	Copper-transporter Protein
CuONPs	Copper Oxide Nanoparticles
CuNPs	Copper Nanoparticles
EDXRF	Energy Dispersive X-ray Fluorescence
EDX-TEM	Electron Diffraction X-Ray Transmission Electron Microscopy
FCC	Face-centered Cubic
FeNPs	Iron Nanoparticles
GSH	Glutathione
HR-TEM	High Resolution Transmission Electron Microscopy
IRT	Iron-regulated Transporter
JSPDS	Joint Committee on Powder Diffraction Standards
MA	Mugineic Acid
NiNPs	Nickel Nanoparticles
NRAMP	Natural Resistance Associated Macrophage Protein
NPs	Nanoparticles
PbNPs	Lead Nanoparticles

LIST OF BREVIATIONS (Continued)

PCs	Phytochelatins
ROS	Reactive Oxygen Species
SAED-TEM	Selected Area Electron Diffraction Transmission Electron Microscopy
SDS-PAGE	Sodium Dodecyl Sulfate Polyacrylamide Gel Electrophoresis
SEM	Scanning Electron Microscope
SPR	Surface Plasmon Resonance
TC	Toxicity Concentration
TEM	Transmission Electron Microscopy
ZIP	zinc-responsive Transporter/iron-responsive Transporter-like Protein

CHAPTER I

INTRODUCTION

1.1 Background Problem

Heavy metals have been excessively released into the environment due to rapid industrialization, thus leading to a major global concern on their effects to the environment and human health. Heavy metals such as copper (Cu), iron (Fe), lead (Pb), nickel (Ni), and silver (Ag) are often detected in industrial wastewater and sometimes in natural water reservoirs. Accumulation of these heavy metals in living organisms potentially lead to toxic and carcinogenic effects. Removal or reduction of contaminated heavy metals in the environment, therefore, is one of the approaches to improve the safety environment for living organisms. These approaches are such as chemical precipitation, ion-exchanging, membrane separation, reverse osmosis, electrodialysis, and solvent extraction (Wan and Hanafiah, 2008). Although these methods effectively remove heavy metals from the environment, they have some disadvantages such as high expense, time-consuming process, high energy operation, and long-term sludge disposal problem (Aziz et al., 2008). Thus, economical methods to diminish these heavy metals from the environment have received many research interests, including the uses of living plants to absorb the heavy metals and the uses of low-cost agricultural wastes and by-products (sugarcane bagasse, rice husk, sawdust, coconut husk, oil palm shell, and neem bark) as absorbent materials (Hegazi, 2013).

Phytoremediation offers an eco-friendly alternative method to remove contaminated heavy metals in the environment via the use of metal hyperaccumulator plants to absorb and accumulate heavy metals in their aboveground parts (Thakur et al., 2016). Glutathione (GSH) is a key component in such metal scavenging due to the high affinity of metals to its thiol (-SH) group and as a precursor of phytochelatin (PCs). Besides metal homeostasis, plants possess a well-equipped antioxidative defense system to manage the metal imposed oxidative challenge (Jozefczak et al., 2012). Several aquatic plants are known in accumulating metals from water environment; *Salvinia minima* Baker, *Lemna gibba* L., *Elodea canadensis* Michx., *Typha angustifolia* L., *Ceratophyllum demersum* L., *Vallisneria spiralis* L., and *Potamogeton crispus* L. (Rezania et al., 2016; Verma and Suthar, 2015). However, the study of absorption and transformation of metal ions to nanoparticles (NPs) in aquatic plant cells is still lacking. Thus, this research was interested to investigate a biological synthesis of metallic NPs by seven common aquatic plants in three families; Salviniaceae (*Azolla pinnata* R.Br. and *Salvinia molesta* D.S. Mitch.), Araceae (*Lemna minor* L., *Lemna perpusilla* Torr., *Spirodela polyrrhiza* (L.) Schleid, and *Wolffia globosa* (Roxb.) Hartog & Plas), and Pontederiaceae (*Eichhornia crassipes* (Mart.) Solms) (Figure 1.1). Salviniaceae is a family of vascular seedless plants (Pteridophytes), which is in the group of aquatics, heterosporous ferns with endosporic gametophytes. With these characteristics, they are more similar to seed plants than other ferns (Lumpkin, 1983). For Salviniaceae family, two plant species (*A. pinnata* R.Br. and *S. molesta* D.S. Mitch.) belonging to the family Salviniaceae were chosen for the study. Araceae is a family of monocotyledonous flowering plants. For Araceae, four plant species were used as the representative plants; *L. minor* L., *L.*

perpusilla Torr., *S. polyrrhiza* (L.) Schleid., and *W. globosa* (Roxb.) Hartog & Plas. The first three plant species, *L. minor* L., *L. perpusilla* Torr., and *S. polyrrhiza* (L.) Schleid, are duckweeds that are commonly used as the model system for ecotoxicology and bioremediation studies. The latter one, *W. globosa* (Roxb.) Hartog & Plas, is the smallest flowering plant and considered as the nutritious food plant (Tel-Or and Forni, 2011). Pontederiaceae is the family of monocotyledonous flowering plants, also known as spiderwort family. For Pontederiaceae, one species was used, *E. crassipes* (Mart.) Solms or water hyacinth, which is a free-floating perennial aquatic plant and considered as one of the problematic invasive plant species in Thailand (Hassan and Edwards, 1992).

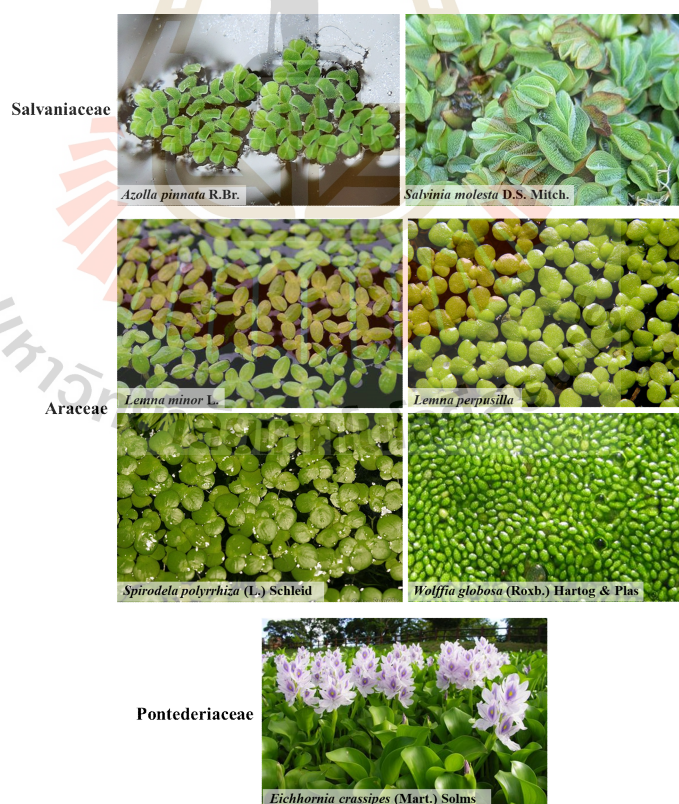


Figure 1.1 Seven common aquatic plants used in this study.

1.2 Significance of the Study

Alternative to chemical and physical methods, phytoremediation offers the eco-friendly approach to remove contaminated metal ions with low cost. This research use plants to absorb and accumulate metal ions in their parts. Although, it is known that several plant species could uptake and accumulate metal ions in compartments, their ability, perhaps similar to some bacteria, to transform these metal ions to NPs is still the lack of study. Thus, this work was interested to use seven species of aquatic plants commonly found in natural reservoirs as the models to study the uptake and transformation of Ag, Cu, Fe, Ni, and Pb to NPs: Salviniaceae (*A. pinnata* R.Br. and *S. molesta* D.S. Mitch.), Araceae (*L. minor* L., *L. perpusilla* Torr., *S. polyrrhiza* (L.) Schleid, and *W. globosa* (Roxb.) Hartog & Plas), and Pontederiaceae (*E. crassipes* (Mart.) Solms). If some of these plants can produce metal NPs from the uptake metal ions, they will offer the phytoremediation means for these contaminated metal ions in water as well as the valuable by-products, the metal NPs.

1.3 Research Objectives

The objectives of this study are as below:

1.3.1 To investigate the toxicity of Ag, Cu, Fe, Ni, and Pb ion solutions to seven aquatic plant species: *A. pinnata* R.Br., *S. molesta* D.S. Mitch., *L. minor* L., *L. perpusilla* Torr., *S. polyrrhiza* (L.) Schleid., *W. globosa* (Roxb.) Hartog & Plas, and *E. crassipes* (Mart.) Solms.

1.3.2 To study the ability of these plant species to uptake ions (copper (II) nitrate, iron (III) nitrate, lead (II) nitrate, nickel (II) nitrate, and silver nitrate) and the effects of the uptake ions on the levels of other ions in the plant roots.

1.3.3 To analyze the changes of functional groups of some biomolecules in the metal-treated plants.

1.3.4 To determine and characterize the formed metal NPs in roots of the metal-treated plants.



1.4 Scope of the Study

Contaminated heavy metals in water are environmentally concerned. This work aims to study the capability of seven aquatic plant species to remove and transform some metal ions to NPs: Salviniaceae (*A. pinnata* R.Br. and *S. molesta* D.S. Mitch.), Araceae (*L. minor* L., *L. perpusilla* Torr., *S. polyrrhiza* (L.) Schleid., and *W. globosa* (Roxb.) Hartog & Plas), and Pontederiaceae (*E. crassipes* (Mart.) Solms).



I. Toxicity of metal solution to each plant

II. Uptake and changes of ions in plant roots after exposing to metal solutions

III. Changes of chemical functional groups of biomolecules in plants after treating with metal solutions

IV. Determination of the formation and identity of metal NPs



Outcomes

New data on these plants to absorb and transform some metal ions to NPs

CHAPTER II

LITTERATURE REVIEWS

4.1 Toxicity Test

Metal nanoparticles (NPs) have unique size-effect properties such as thermal, optical, chemical, magnetic, and mechanical properties, which are different from their bulk materials. Due to these special properties, they are used for various applications, including catalysis (Zhou et al., 2018), biomedical agents (Jiang et al., 2018), electronics, optics, biosensors (Yonezawa, 2018), textile industry, and food packaging (Tamayo et al., 2019). In general, production of metal NPs is carried out by chemical and physical methods as via "top-down" and "bottom-up" approaches (Wang and Xia, 2004). Metal NPs such as silver nanoparticles (AgNPs), copper nanoparticles (CuNPs), iron nanoparticles (FeNPs), nickel nanoparticles (NiNPs), and lead nanoparticles (PbNPs), which are the interests of this work, have been continuously used and modified to enable their applications (Mody et al., 2010). The

2.1.1 Copper nanoparticles

Cu is the chemical element that has an atomic number of 29. In nature, Cu can be found less than 1% in the Earth's crust as the pure native Cu. The native Cu has a red-orange color with a very soft and flexible structure. In addition to the native form, Cu occurs as the compound by combining with various elements, such as

copper sulfide (CuS), azurite ($\text{Cu}_3(\text{CO}_3)_2(\text{OH})_2$), cuprite (Cu_2O), chalcopyrite (CuFeS_2), chalcocite (Cu_2S), and malachite ($\text{Cu}_2\text{CO}_3(\text{OH})_2$) (Amcoff and Holényi, 1996). The morphology and color of native and compound forms of Cu are presented in Figure 2.1. Unlike the bulk structure, CuNPs are the particles of Cu having sizes in a range of 1 – 100 nm. The color of colloidal CuNPs is also changed according to the particle sizes as seen in Figure 2.2, in which the colors of CuNPs of 13.54 – 190.14 nm are varied from light yellow to dark brown (Yadav et al., 2017).

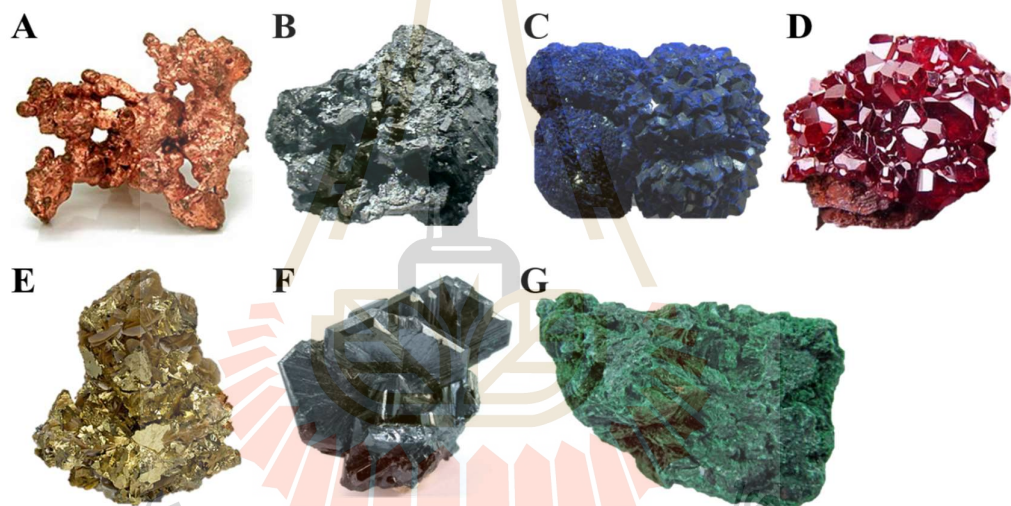


Figure 2.1 The different colors of various forms of Cu; (A) native Cu, (B) copper sulfide, (C) azurite, (D) cuprite, (E) chalcopyrite, (F) chalcocite, and (G) malachite (Amcoff and Holényi, 1996).

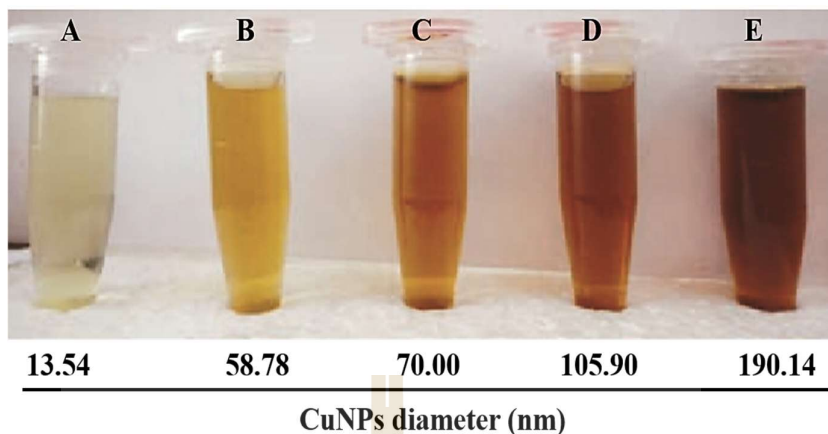


Figure 2.2 The relation of color and size of colloidal CuNPs solution; (A) light yellow, (B) yellow, (C) brown yellow, (D) brown, and (E) dark brown (Yadav et al., 2017).

The crystalline structure of CuNPs is often found in the face-centered cubic (FCC) form (Ojha et al., 2017). This FCC crystal structure has Cu atom at every corner of the cube and six atoms at each face of the cube as shown in Figure 2.3. Although the CuNPs are mostly produced in quasi-spherical and spherical shapes, the anisotropic shapes such as branched, truncated octahedral, and octahedral shapes are also reported (Ojha et al., 2017) as shown in Figure 2.4.

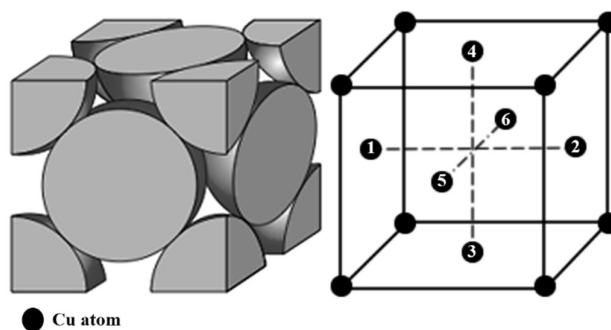


Figure 2.3 The FCC structure of CuNPs (Cutton, 2018).

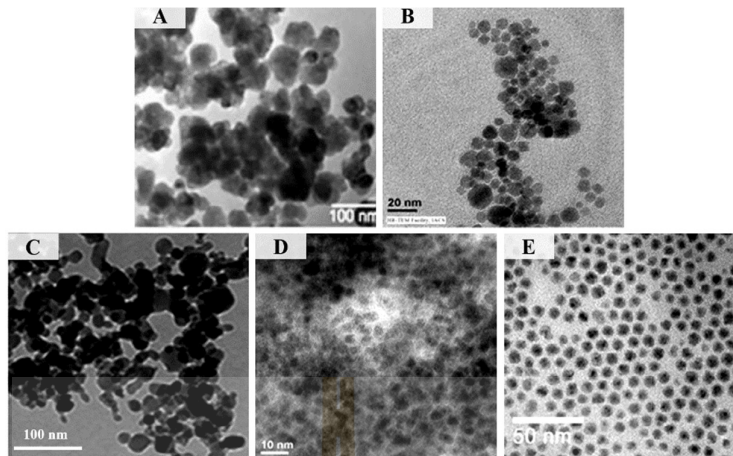


Figure 2.4 Various morphologies of CuNPs; (A) quasi-spherical shape, (B) spherical shapes, (C) branched shapes, (D) truncated octahedral shapes, and (E) octahedral shapes (Ojha et al., 2017).

CuNPs have unique properties suitable for many potential applications; high melting point (1,083 °C) (Schaper et al., 2004), magnetism property (such as ferromagnetism of 80 nm CuONPs) (Gao et al., 2010), specific absorption at 550 nm (Mohindroo et al., 2016), electrical and thermal conductivity (Huang et al., 1997), and antibacterial activity (Chatterjee et al., 2014; Mahmoodi et al., 2018). Therefore, CuNPs have been used in various applications such as catalysts, colorimetric sensors, antibacterial agent, photocatalyst, and electrocatalysts (Tamilvanan et al., 2014). CuNPs are commonly used as electrocatalysts because of their low cost, high melting point, and corrosion resistance. Hirunsit and colleagues reported the use of colloidal CuNPs as electrocatalysts in the electroreduction process to produce the hydrogen energy, methane, and methanol, which they offered several advantages including the short reaction time and the single step process (Hirunsit et al., 2015). Moreover, Wang and colleagues reported the use of CuNPs as the antibacterial agent. The antibacterial

activity of CuNPs was proposed as shown in Figure 2.5. Cu ions that generated by CuNPs may interact with the negative charge of the bacterial membrane via the electrostatic reaction, causing the cell damage and death. In addition, small CuNPs can penetrate into the bacterial cells and interact with thiol ($-SH$) and phosphate ($-PO_4^-$) groups of proteins and nucleic acid, leading to the inhibition of electron transport chain, disruption of enzymatic functions and modulation of the bacterial metabolic processes (Wang et al., 2017).

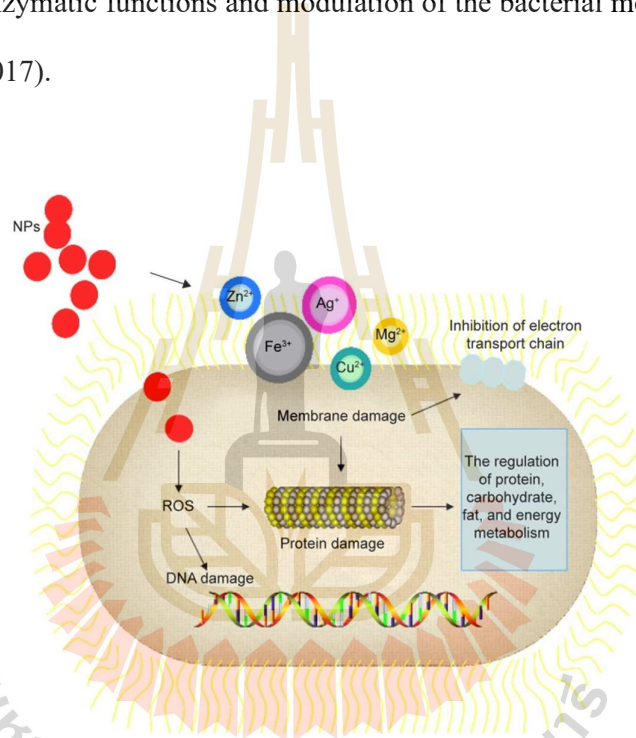


Figure 2.5 The proposed mechanisms of the antibacterial activity of CuNPs (Wang et al., 2017).

2.1.2 Iron nanoparticles

Fe is an abundant metal element with an atomic number of 26. This metal is found at approximately 5.0% in the continental crust (Huber, 2005). As seen in Figure 2.6, Frey and Reed reported some Fe complexes that were naturally found in the continental crust, including mononuclear Fe, dinuclear Fe ($2Fe-2S$), ternary iron-

nickel-sulfur (Fe–Ni–S) clusters, Fe protoporphyrin X, and many other complexes (Frey and Reed, 2012).

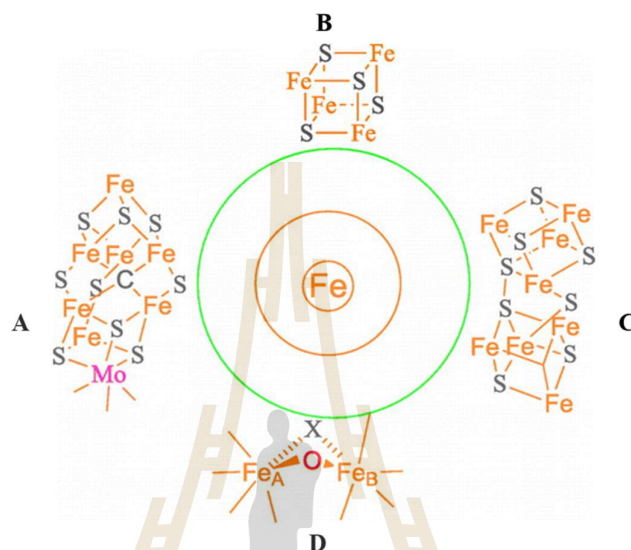


Figure 2.6 Fe complexes in the continental crust; (A) mononuclear Fe, (B and C) dinuclear irons, and (D) Fe protoporphyrin X (Frey and Reed, 2012).

FeNPs are particles of Fe in the diameter of 1–100 nm. In general, FeNPs are easily oxidized by oxygen atoms to form oxides of Fe such as ferrous oxide (FeO), hematite (Fe₂O₃), magnetite (Fe₃O₄), greigite (Fe₃S₄), goethite (FeO(OH)), and maghemite (γ-Fe₂O₃). Among the FeNPs, hematite and maghemite are mostly used in various fields of applications because of their magnetic properties and colloidal stability in aqueous solutions (Moacă et al., 2018). The crystal structure of various FeNPs is shown in Figure 2.7. The magnetite has an inverse spinel pattern with alternating and overlapping of tetrahedral-octahedral layers (Yew et al., 2018). The hematite crystal structure shows a Rietveld refinement pattern, which is based on the hexagonal close

packing of oxygen atoms with two-thirds of the octahedral site by iron atoms (Tadic et al., 2017). Unlike magnetite, the maghemite has a spinel pattern in its crystal structure. This pattern is formed by capping the tetrahedral site on the hexagonal layer (Albrecht et al., 2019). Based on the literature, the various morphology of FeNPs were reported, including spherical, microdisks, drum-like, spindles, and hexagonal as shown in Figure 2.8 (Xu et al., 2015).

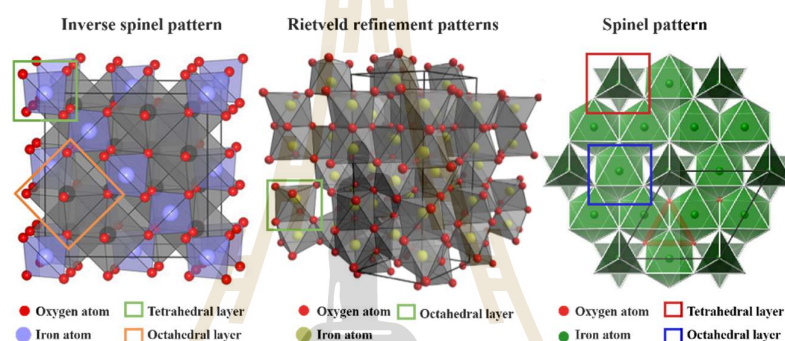


Figure 2.7 The crystal structure of various iron oxide NPs (Albrecht et al., 2019; Odkhuu et al., 2014; Tadic et al., 2017).

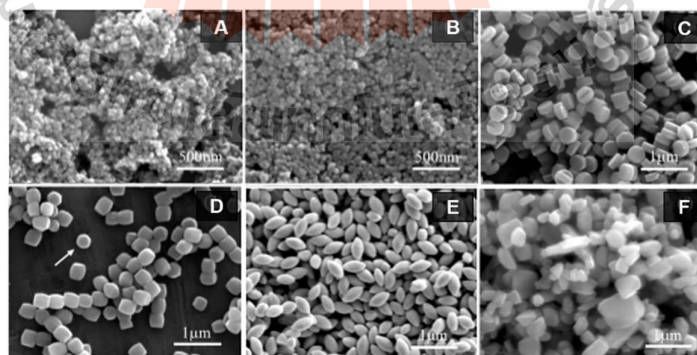


Figure 2.8 Different morphology of FeNPs with diameter ranges of 100–500 nm; (A and B) spherical, (C) microdisks, (D) drum-like, (E) spindles, and (E) hexagonal particles (Xu et al., 2015).

FeNPs with the diameter of 10 – 50 nm were used for many applications such as microelectronic devices, gas sensing, catalyst, nanocarrier for targeted drug delivery, and energy storage devices (Chifiriuc and Grumezescu, 2016; Cortalezzi et al., 2003; Lee, 2015; McKerracher et al., 2015; Paul and Sharma, 2010; Saif et al., 2016; Yadav and Raizaday, 2016). The magnetic FeNPs (such as gregrite, magnetite, and maghemite) attract increasing attention because they have excellent magnetic properties and can be potentially used in a large number of biological applications such as to isolate of genomic and plasmid DNA, control drug delivery, remove contaminated mercury from industrial effluent, support enzyme immobilization for bio-catalysis, and extract pharmaceutical chemicals. Also, FeNPs can be used in many biomedical applications as shown in Figure 2.9 (Fu and Ravindra, 2012).

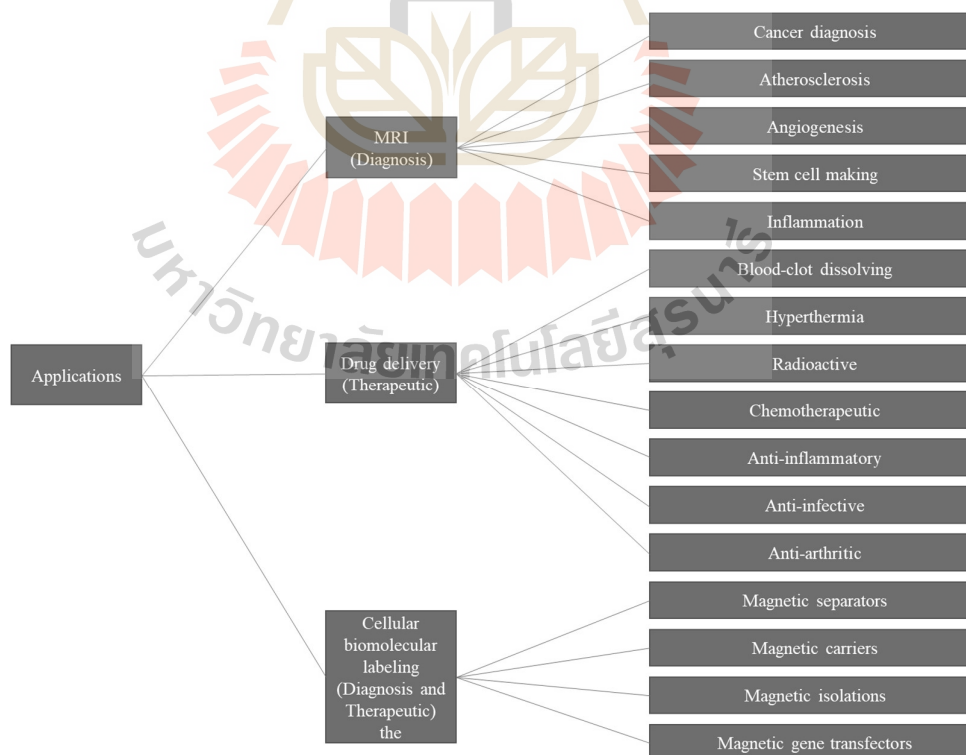


Figure 2.9 Biomedical applications of FeNPs (Fu and Ravindra, 2012).

2.1.3 Lead nanoparticles

Pb is a heavy metal element with the atomic number of 82, which is found approximately 0.001% in the Earth's crust. Various forms of Pb are naturally detected such as lead monoxide (PbO), lead tetroxide (Pb₃O₄), lead dioxide (PbO₂), and lead sulfide (PbS) (Moody, 2013) as seen in Figure 2.10. If lead exceeds the optimal level, it is toxic to human health. The contaminated lead in food, air, and water when enters the human body can cause damage to the nervous system and respiratory system.

PbNPs are particles of Pb in the dimension size of 1 – 100 nm. PbONPs are used in various applications such as storage, pigment, sensor, and electronic device. PbNPs can be synthesized in different shapes including nanoplate, nanorod (Kwon et al., 2011), nanocube (Abeywickrama et al., 2018), nanosphere (Yousefi et al., 2014), flower-like, and hexagonal nanostructure (Pratap and Nath, 2011) as seen in Figure 2.11.

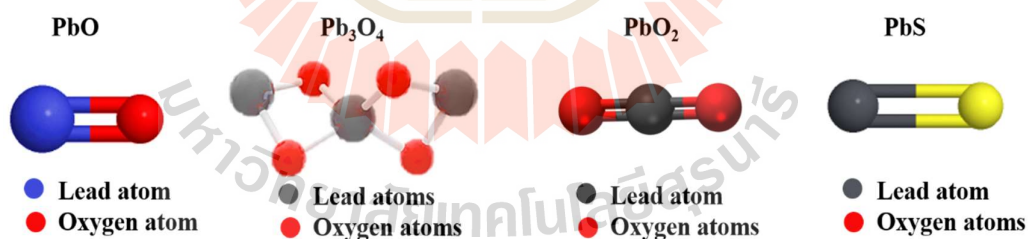


Figure 2.10 Various forms of lead oxide complexes (Volkman et al., 2019).

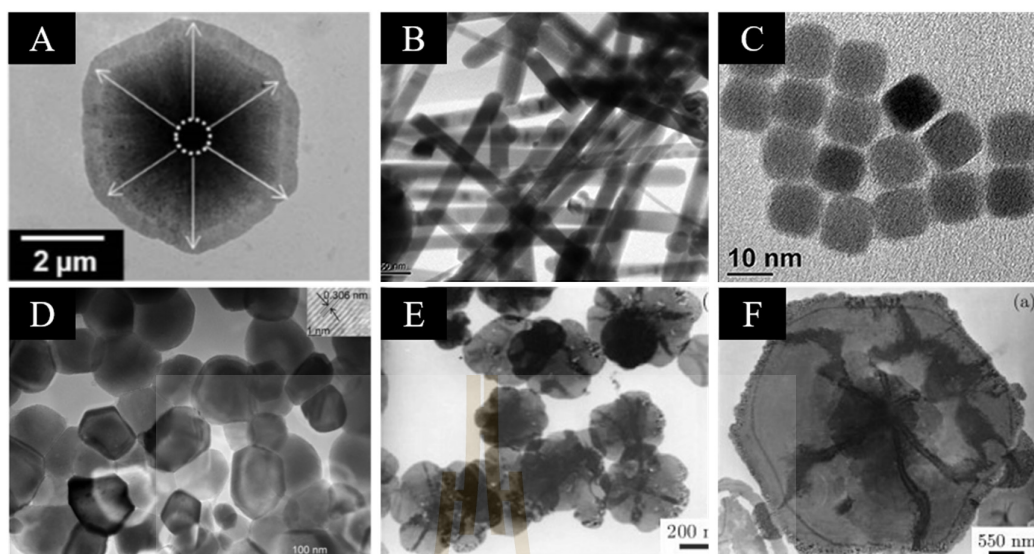


Figure 2.11 Different shapes of PbNPs; (A) nanoplate, (B) nanorod, (C) nanocube, (D) nanosphere, (E) flower-like, and (F) hexagonal nanostructure (Abeywickrama et al., 2018; Kwon et al., 2011; Pratap and Nath, 2011; Yousefi et al., 2014)

Among PbNPs, lead sulfide NPs (PbSNPs) are one of the important nanomaterials, which are widely used in semiconductor devices for optoelectronic applications. Gerdes and colleagues reported various shapes of the synthesized PbSNPs such as quasi-spherical, octahedral, star-structured, and irregular-structured shapes (Figure 2.12) by controlling the ratio of acetic acid and 1,2-dichloroethane, which were used as reducing and stabilizing agents, respectively. They hypothesized that the ratio of reducing and stabilizing agents was important for seed formation and growth process at (100) and (111) planes, resulting in the formation of different shapes of PbNPs (Gerdes et al., 2015).

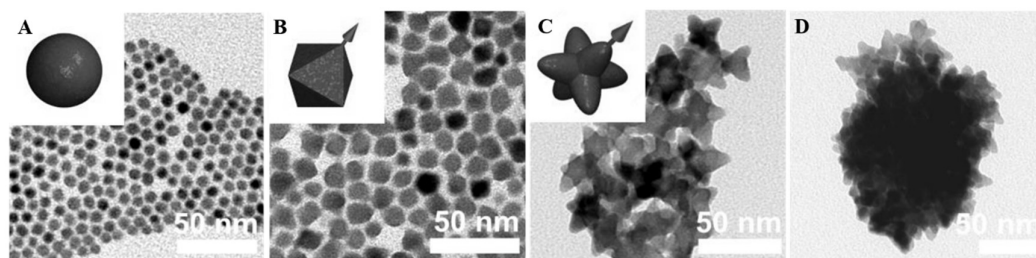


Figure 2.12 Different shapes of PbSNPs synthesized by controlling the reducing and stabilizing agents; (A) quasi-spherical, (B) octahedral, (C) star-structured, and (D) irregular-structured shapes (Gerdes et al., 2015).

2.1.4 Nickel nanoparticles

Ni is a metal element, which has the atomic number of 28. Ni occurs in the continental crust at approximately 0.01%. Major forms of Ni in nature include nickel sulfide (NiS), nickel oxide (NiO), and nickel silicate (NiO₃Si). Geological phenomena including weathering, volcanoes, and human activities such as industrial processes, agricultural activities, and combustion of fossil fuels can release Ni into an environment (Schaumlöffel, 2012). Ni element can be deposited to the surface of water and soil. Therefore, it can accumulate in microorganisms, plants, and animals living in that environment (Ahmad and Ashraf, 2011; Iyaka, 2011). The main effect of Ni on human involves unusual inhalation, ingestion, and dermal retention (Zambelli et al., 2016). Nevertheless, Ni can be used for many applications, especially NiO that has excellent electric and thermal properties and potentially used in a variety of applications (El-Kemary et al., 2013). As compared with the bulk of Ni, NiNPs have superior properties in surface energy, magnetism, and surface area to volume ratio (Magaye and Zhao, 2012). Most synthesized NiNPs were in a spherical shape with a body-centered cubic lattice (BBC). The BBC has an atom centered in the body of the cube, unlike the FCC

crystal structure that has atoms at each corner of the cube and six atoms at each face of the cube (Tian et al., 2005) as seen in Figure 2.13.

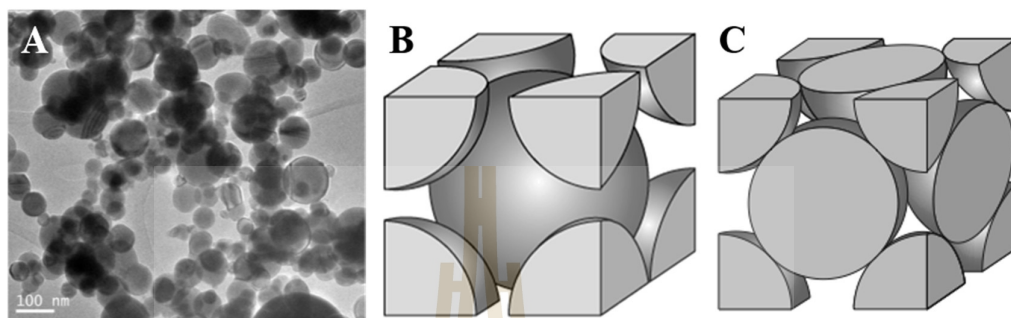


Figure 2.13 Morphology and crystal structure of NiNPs; (A) spherical shape, (B) BCC crystal structure, and (C) FCC crystal structure (Redwing, 2019).

In addition to a spherical shape, Kim and colleagues synthesized the different shapes of NiNPs including cube-shaped, elongated hourglass-shaped, hexagonal-shaped, octagonal-shaped, large sea urchin-like, and hourglass-shaped NiNPs (Figure 2.14). These different shaped NiNPs were synthesized by controlling the ratio of the reducing and stabilizing agents (hexadecylamine and trioctylphosphine, respectively) under the hydrogen pressure (Kim et al., 2014).

NiNPs are more commonly used as an anode device of solid-oxide fuel cells or conductive electrolytic layer of proton exchange membrane fuel cells in renewable energy applications. Gao and colleagues reported that NiNPs demonstrated the high effectiveness of NiNPs to improve the electrocatalytic activity over nonmetallic carbon materials (Gao et al., 2001).

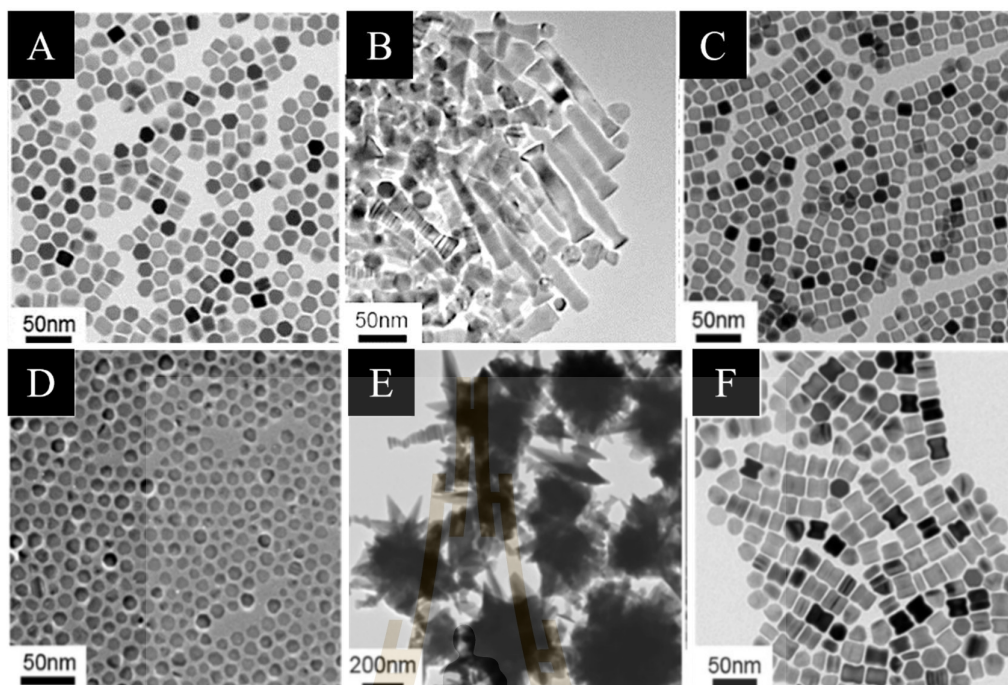


Figure 2.14 TEM image of the different shaped NiNPs; (A) cube-shaped, (B) elongated hourglass-shaped, (C) hexagonal-shaped, (D) octagonal-shaped, (E) large sea urchin-like, and (F) hourglass-shaped (Kim et al., 2014).

2.1.5 Silver nanoparticles

Silver is one of the chemical metals with the atomic number of 47. The silver element occurs in the earth crust approximately $7.9 \times 10^{-6}\%$. Naturally, it is often found to complex with gold. With their nanometer size, AgNPs exhibit excellent physical, chemical, and biological properties, thus they are incorporated into many commercial products. The global market of AgNPs is predicted to reach 2.45 billion USD by 2022 according to a new study by Grand View Research, which is on account of rising demands from various industries such as electronic devices, appliances, textiles, and antimicrobial agents (Tran and Le, 2013). The development of synthesis approaches of AgNPs is also received tremendous interests as indicated by the number of articles

published by the standard publishers from 1980 to September 2014 as seen in Table 2.1 (Keat et al., 2015).

Table 2.1 Publication scenario of synthesis of AgNPs under standard publishers (1980 – 2014).

Scenario number	Name of the publishers	Total number of journal articles
1	American Chemical Society	3,323
2	WILEY	3,026
3	Royal Society of Chemistry	2,140
4	Elsevier Science	8,790
5	Springer	2,668
6	Taylor & Francis	299

Reference: (Keat et al., 2015).

Several methods are employed to synthesize AgNPs, including physical, chemical, and biological methods. For physical methods, an evaporation-condensation is mostly used to synthesize AgNPs. The advantage of this processes is to provide a mass production but it has several drawbacks including a requirement of high space for production, consumption of high temperature and energy, and long reaction time (Abou El-Nour et al., 2010). Other physical methods for producing AgNPs are included microwave irradiation, ultrasonic irradiation, photoinduction, photocatalytic reduction, irradiation reduction (Firdhouse and Lalitha, 2015). In addition, different sizes and

shapes of AgNPs can be synthesized via the control of salt precursor, reducing agent, stabilizing agent, and the wavenumber of light (Abou El-Nour et al., 2010). For chemical methods, a chemical reduction is a mostly used approach to synthesize stable AgNPs with high mass production. The chemical reaction is based on the use of chemical reagents to reduce silver ion (Ag^+) to zero-valence silver (Ag^0), which initiate a formation of Ag nuclei. Later, the growth of seed nuclei leads to a formation of AgNPs that are stabilized by capping agents (Agnihotri et al., 2014). However, this process has several drawbacks including a generation of toxic chemical byproducts, a requirement of high energy and temperature, and time-consuming (Bhattarai et al., 2018). From the above limitation, biological methods are, thus, proposed as the alternative methods for the production of AgNPs, which are simple, rapid, stable, biocompatible, eco-friendly, and cost-effective. In biological methods, plant extracts, proteins, amino acids, organic acids, vitamins, flavonoids, alkaloids, polyphenol compounds, and polysaccharides were reported to function as reducing and stabilizing agents to mediate a formation of AgNPs (Duan et al., 2015). In addition to the use of phytochemicals and biomolecules to facilitate the production of AgNPs, some microorganisms were found to be able to synthesize AgNPs. These microorganisms generally have the ability to accumulate and detoxify heavy metal via the actions of their cellular and secreted enzymes, resulting in the extra- and intracellular syntheses of AgNPs (Singh, 2016).

AgNPs have the unique optical property with their characteristic surface plasmon resonance (SPR) is about 400 nm. They can interact with light causing the conduction of electrons on the metal surface to undergo a collective oscillation. The unique SPR peak can be used to speculate sizes, shapes, and amounts of AgNPs (Figure

2.15). In addition, the colors of colloidal AgNPs are varied, depending on their sizes and shapes as some examples are seen in Figure 2.16 (Helmlinger et al., 2016).

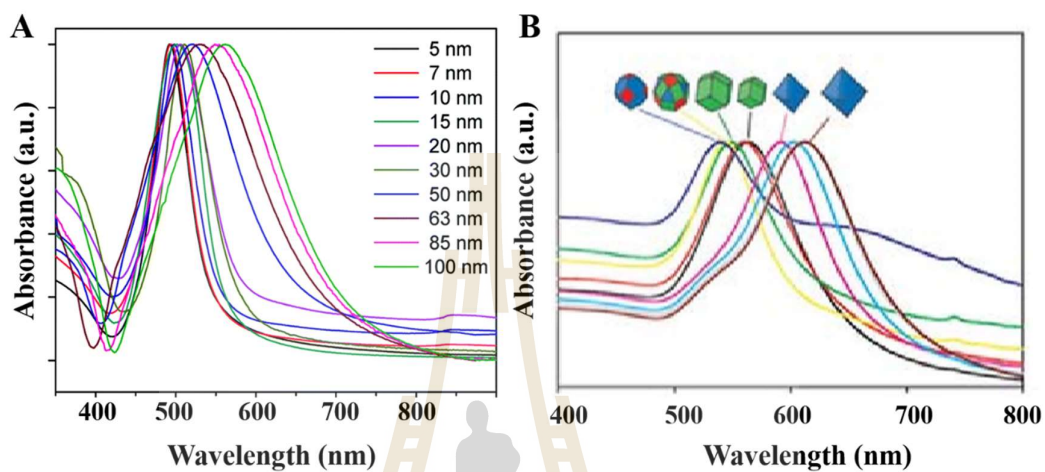


Figure 2.15 UV-Vis spectra of colloidal AgNPs with (A) different sizes and (B) shapes (Mukherji et al., 2019).



Figure 2.16 The colors of colloidal AgNPs (upper) and their TEM images (lower) (Helmlinger et al., 2016).

2.2 Syntheses of Metal Nanoparticles

2.2.1 Chemical and physical syntheses of metal nanoparticles

Metal NPs are commonly synthesized via two strategies: "top-down" and "bottom-up" as seen in Figure 2.17 (Fendler and Tian, 2007). A "top-down" synthesis method implies that the nanostructures are synthesized by etching out crystal planes (removing crystal planes), which are already present on the substrate. Thus, a "top-down" approach can be viewed as an approach that the building blocks are removed from the substrate to form the nanostructure. In a "bottom-up" approach, the nanostructures are synthesized onto the substrate by stacking atoms onto each other, which gives rise to crystal planes and the crystal planes further stack onto each other, resulting in the synthesis of the nanostructures. Therefore, a "bottom-up" approach can be viewed as a synthesis approach that the building blocks are added onto the substrate to form the nanostructures (Wang and Xia, 2004).

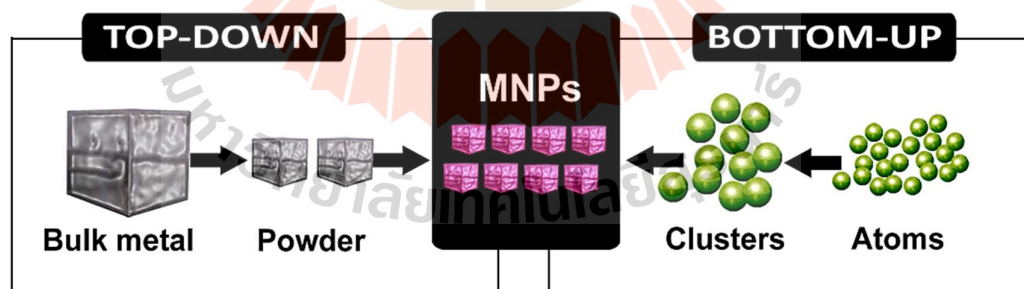


Figure 2.17 Scheme of "top-down" and "bottom-up" approaches to synthesize metal NPs (Wang and Xia, 2004).

The traditional and most widely used methods for synthesis of metal NPs are the wet-chemical procedures. A typical procedure involves growing NPs in a liquid

medium containing various reactants, in particular reducing agents (e.g. sodium borohydride, potassium bitartrate, methoxy polyethylene glycol, and hydrazine). To prevent the agglomeration of metal NPs, a stabilizing agent, such as sodium dodecyl benzyl sulfate, and polyvinyl pyrrolidone, is also added to the reaction mixture. Generally, the chemical methods are low-cost for high volume production; however, they have some drawbacks such as contamination from precursor chemicals, use of toxic solvents, and generation of hazardous by-products.

2.2.2 Biosynthesis of metal nanoparticles

Biological synthesis offers a cost-effective, eco-friendly, and simple method for the production of metal NPs. In addition, the obtained metal NPs are suitable for biomedical and environmental applications. Among metal NPs, AgNPs are mostly used in the medical field due to their antimicrobial effects, while zinc and titanium dioxide NPs (ZnNPs and TiO₂NPs) are frequently used in cosmetics. AgNPs and ZnNPs are also used in food packaging, wound dressings, catheters for drug delivery and so on, due to their broad range of antimicrobial effects. The second application area of biological NPs is the development of sensors for various biomolecules related to environment and agriculture. Furthermore, NPs are also used in gene delivery, cell labeling, and medicine. Some applications of metal NPs are still in extensive development, such as photoimaging, photothermal therapy, and magnetically responsive drug delivery. The biological methods to synthesize metal NPs can be divided into 2 main approaches; the synthesis by living microorganisms (yeasts, bacteria, and fungi) and the synthesis mediated by biomolecules extracted from microbes, plants, and animals (Figure 2.18).

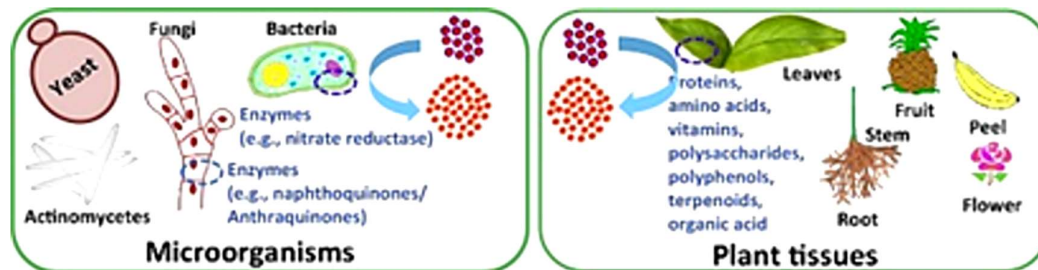


Figure 2.18 Biological synthesis of metal NPs in biomedical and environmental fields

(Domènech et al., 2012).

2.2.2.1 Living microorganisms

Living microorganisms can function as bio-factories to produce metal NPs, which offer immense potential advantages in eco-friendly and cost-effective process, no toxic or harsh chemicals produced, and no requirement of high energy input. Up to our knowledge, some bacteria, yeast, and fungi were reported to synthesize metal NPs from the uptake of metal ions. Detailed information is described as follows.

Naturally, microorganisms have the capability to accumulate and detoxify heavy metals via the use of various reductase enzymes that are able to reduce metal salts and subsequently form metal NPs with narrow size distribution and less polydispersity. Over the past few years, microorganisms, including bacteria (such as actinomycetes), fungi, and yeasts, have been studied for their extra- and intracellularly syntheses of metal NPs (Singh, 2016). The mechanism of microbial-mediated synthesis of metal and metal oxide NPs is not clear; however, it is hypothesized via the following three phases (Figure 2.19). First, the metal cation is trapped by bacterial or fungal cell wall due to electrostatic interactions between the negatively charged cell wall and the positively charged metal cation. Second, bacterial and fungal cells release reductase

enzymes to reduce the metal cations into the zero-valent metal atom. Third, these atoms aggregate and form metal NPs. The formed NPs are capped by biomolecules produced by bacteria or fungi, which prevent further aggregation of metal NPs. The formed NPs can diffuse out from the cell wall or remain inside the cells depending on each bacterial and fungal species. Lists of microorganisms capable of producing metal NPs are in Table 2.2.

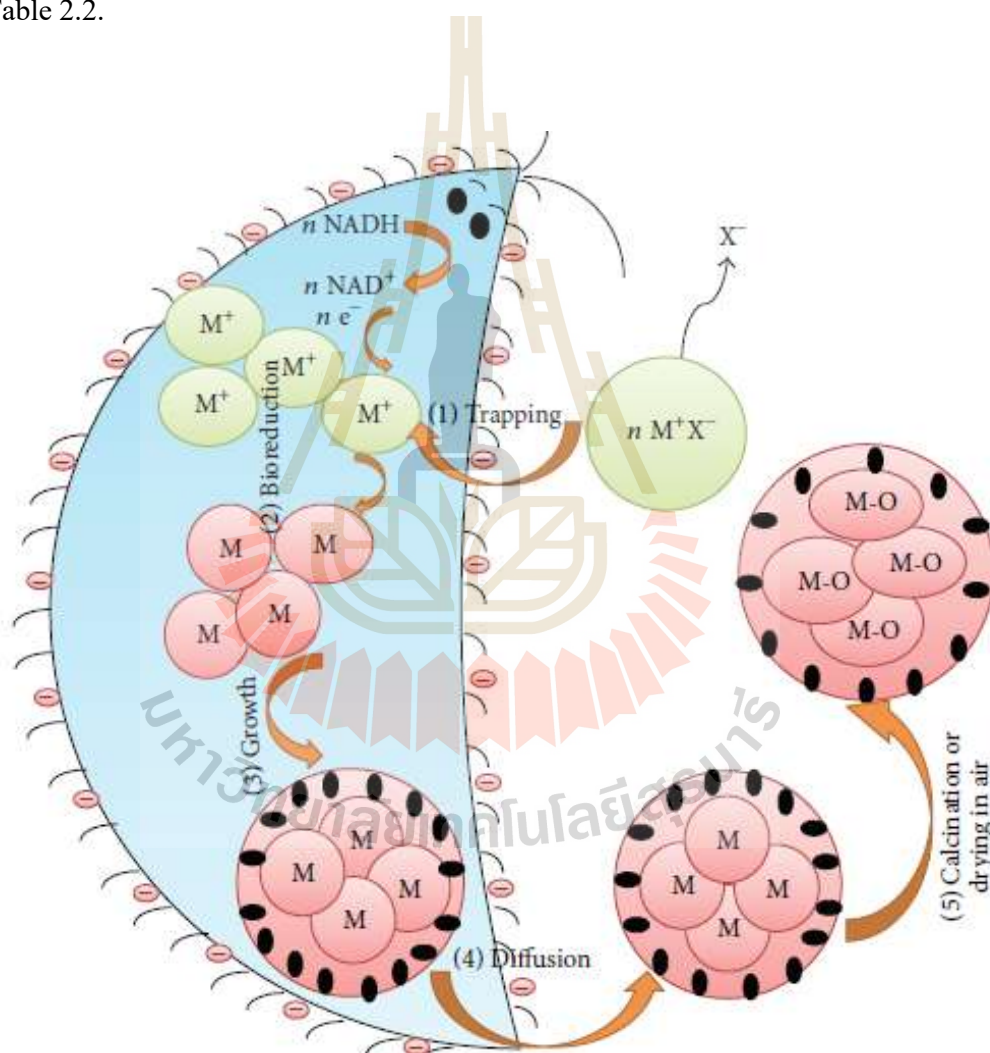


Figure 2.19 Mechanism of microbial-mediated synthesis of metal and metal oxide NPs

(Muhammad and Rani, 2016).

Table 2.2 Intracellular synthesis of metal NPs by various microorganisms.

Microorganisms	Metal NPs	Methods
<i>Rhodopseudomonas capsulate</i>	Au	Reduction
<i>Morganella sp.</i>	Ag	Reduction
<i>Pseudomonas stutzeri</i>	Ag and Cu	Reduction
<i>Rhodococcus sp.</i>	Au	Reduction
<i>Escherichia coli</i>	Pd, Pt, and CdS	Reduction
<i>Plectonema boryanum</i>	Ag	Reduction
<i>Enterococcus faecium</i>	Ag and Pt	Biosorption and reduction
<i>Lactobacillus strains</i>	Ag and Au	Reduction
<i>Rhodococcus sp.</i>	Au	Reduction
<i>Candida glabrata</i>	CdS	Reduction
<i>Schizosaccharomyces pombe</i>	CdS	Reduction
<i>Torulopsis sp.</i>	Pb	Reduction
<i>Cryphonectria sp.</i>	Ag	Enzyme mediated
<i>Bipolaris nodulosa</i>	Ag and Au	Reduction
<i>Pestalotia sp.</i>	Ag	Reduction
<i>Aureobasidium pullulans</i>	Au	Reduction
<i>Neurospora oryzae</i>	Ag	Reduction
<i>Rhizopus oryzae</i>	Au	Reduction
<i>Clostridium thermoaceticum</i>	Ag	Reduction
<i>E.coli K12</i> <i>Geobacillus sp.</i>	Ag	Reduction

Reference: (Khandel and Kumar, 2016)

2.2.2.2 Biomolecule extracts from microbes, plants, and animals

Microbial extracts

A synthesis of metal NPs mediated by microbial extracts was to use the extracts or culture media of bacteria as reducing and/or stabilizing agents (Narayanan and Sakthivel, 2010). The mechanism of extracellular synthesis of metal NPs in fungus was proposed to involve the microbial reductase enzymes that reduce metal ions to metal nanocrystal outer the microbial cells as illustrated in Figure 2.20. (Khandel and Kumar, 2016). The production of extracellular metal NPs by some microbes is summarized in Table 2.3.

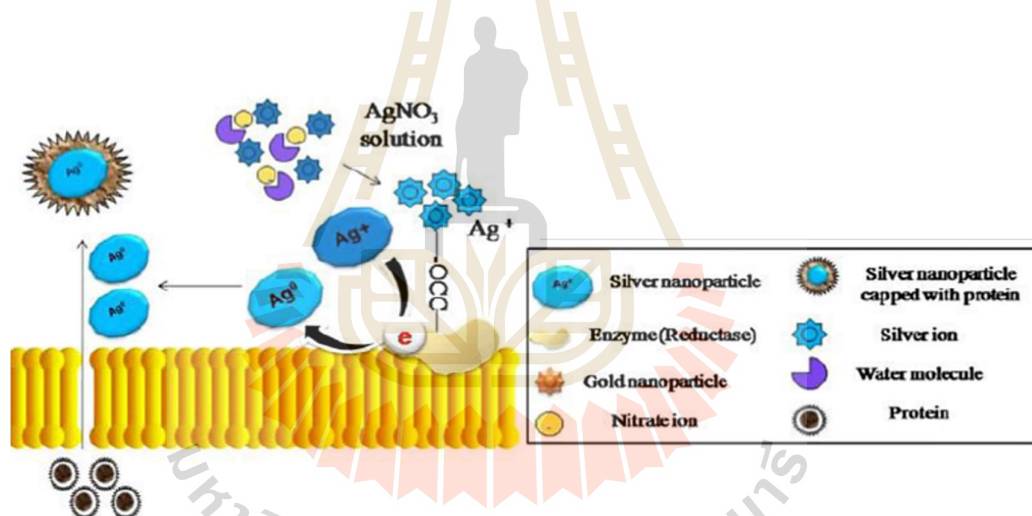


Figure 2.20 Mechanism of extracellular synthesis of AgNPs by fungi (Khandel and Kumar, 2016).

Table 2.3 The extracellular synthesis metal NPs by various microbes.

Microorganisms	Metal NPs	Methods
<i>Verticillium</i> sp.	Ag	Reduction
<i>Escherichia coli</i>	Pd and Pt	Reduction
<i>Rhodopseudomonas capsulata</i>	Au	Reduction
<i>Pseudomonas aeruginosa</i>	Au	Reduction
<i>Delftia acidovorans</i>	Au	Reduction
<i>Shewanella</i> sp.	As	Reduction
<i>Desulfovibrio desulfuricans</i>	Pd	Reduction
<i>Bacillus sphaericus</i> JG-A12	Cu, Pb, Al, and Cd	Biosorption and reduction
<i>Klebsiella pneumonia</i>	Ag	Reduction
<i>Escherichia coli</i>	Ag	Reduction
<i>Enterobacter cloacae</i>	Ag	Reduction
<i>Lactobacillus</i> sp.	Ag	Biosorption and reduction
<i>Enterococcus faecium</i>	Ag	Biosorption and reduction
<i>Lactococcus garvieae</i>	Ag	Biosorption and reduction
<i>Pediococcus pentosaceus</i>	Ag	Biosorption and reduction
<i>Fusarium oxysporum</i>	Cd	Enzyme mediated
<i>Aspergillus fumigatus</i>	Ag	Reduction

Reference: (Thakkar et al., 2010)

Animal extracts

The extracts derived from animal tissues were also reported to facilitate the formation of AgNPs. Khamhaengpol and Siri reported the synthesized colloidal AgNPs using the extract of weaver ant larvae at the 3rd instar stage (Figure 2.21) under the fluorescent irradiation (Khamhaengpol and Siri, 2016). The dominant proteins of 76 and 27 kDa in the extract was proposed to exhibit the reducing and antioxidant activities, thus serving as a good electron donor for reducing Ag⁺ and eventually forming AgNPs. The results revealed the dispersed and spherical AgNPs of approximately 8 nm with the maximum SPR peak at 435 nm. Moreover, this colloidal AgNPs showed antibacterial activity against both *Escherichia coli* and *Staphylococcus aureus*, suggesting their potential use as an effective antibacterial agent (Figure 2.22).

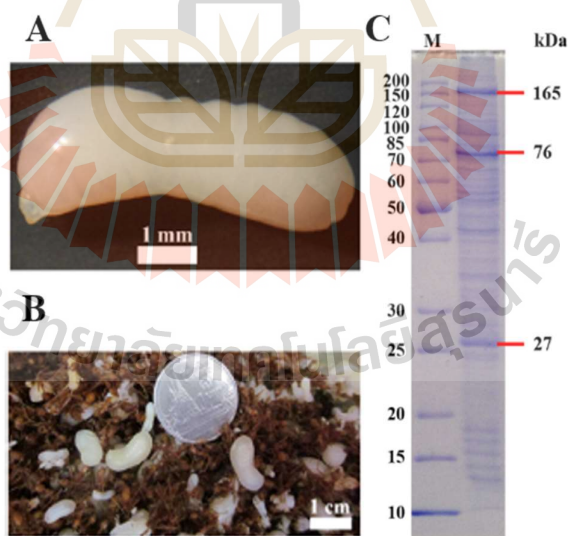


Figure 2.21 Images of (A-B) the weaver ant larvae image at the 3rd instar stage, and (C) their extracted proteins visualized on a 12.5% SDS-PAGE gel (Khamhaengpol and Siri, 2016).

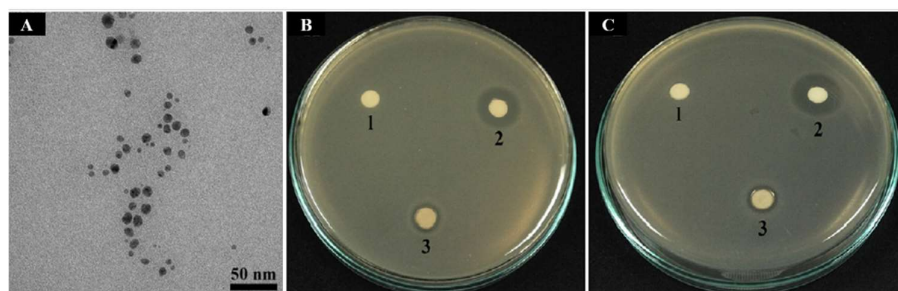


Figure 2.22 Images of (A) TEM analysis of the synthesized AgNPs and (B-C) their growth inhibition zones against *Escherichia coli* and *Staphylococcus aureus*, respectively. 1: the negative control (distilled water), 2: the positive control (ampicillin), and 3: the synthesized AgNPs (25 μg).

Plant extracts

The uses of plant extracts derived from different parts or whole plants have been reported for the production of metal NPs, which the mechanism of plant extracts to mediate synthesis of metal and metal oxide NPs are based on three phases: activation, growth, and NPs formation. The activation phase involves the reduction of metal ions and the metal atoms undergo nucleation. The growth phase involves the spontaneous coalescence of small adjacent NPs into the metal cluster. Finally, the NPs formation is occurred by agglomeration of the growth nanocluster to the stable NPs (Muhammad and Rani, 2016). The end products are obtained after they are air-dried or calcined in air to get final metal NPs. The schematic diagram of the synthesis mechanism of NPs using plant extracts is shown in Figure 2.23. Moreover, the biosynthesis of metal NPs using the extracts of some plant species is presented in Table 2.4.

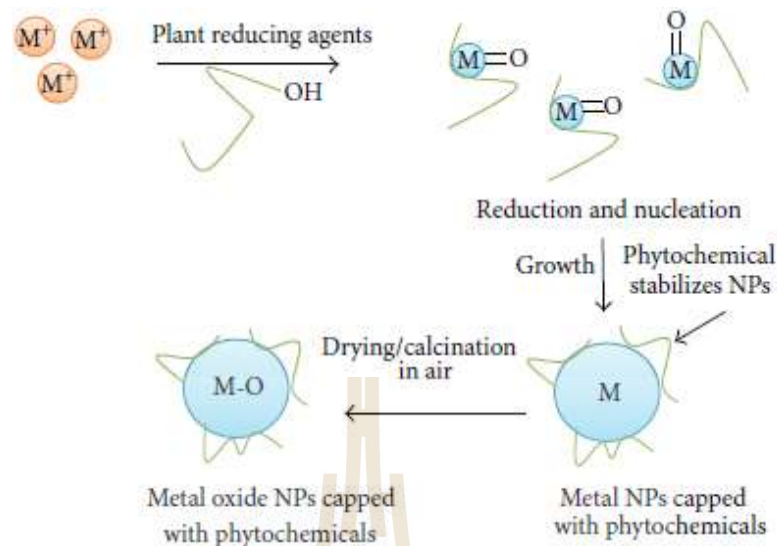


Figure 2.23 Mechanism of plant extracts to mediate the synthesis of metal NPs (Muhammad and Rani, 2016).

Plant extracts have been extensively reported for their potential uses to mediate the synthesis of various metal NPs, which they function as reducing and stabilizing agents. The reaction containing only metal salts and plant extracts under heat or light activation is sufficient to induce the formation of metal NPs. These findings raise our questions such as whether similar reactions can occur in plant cells, whether plant cells can uptake metal ions and transform them into metal NPs, whether plants can produce metal NPs from any metal ions, and where the formation and accumulation of metal NPs occur in the plant cells. Therefore, this work was interested to address these questions and chosen some phytoremediation plants to study since they are efficiently uptake metal ions.

Table 2.4 Biosynthesis of metal NPs using the extraction of plant species.

Species	Parts	NPs	Causative agents
<i>Azadirachta indica</i> A. Juss	Kernel	Au, Ag	Azadirachtin
<i>Camellia sinensis</i> (L.) Kuntze	Leaves	Au	Catechins and arubigins
<i>Jatropha curcas</i> L.	Latex	Pb	Curcacycline A and B
<i>Geranium</i> sp.	Leaves	Ag	Terpenoids (not specified)
<i>Nelumbo nucifera</i> Gaertn.	Leaves	Ag	Not mentioned
<i>Cymbopogon citratus</i> (DC.) Stapf	Leaves	Au	Sugar derivative molecules
<i>Avena sativa</i> L.	Stems	Au	Not mentioned
<i>Aloe vera</i> (L.) Burm.f.	Leaves	Ag	Not mentioned
<i>Syzygium aromaticum</i> (L.) Merrill & Perry.	Flower	Cu	Eugenol
<i>Nephelium lappaceum</i> L.	Peels	NiO	Bioactive compound (not specified)
<i>Cinnamomum camphora</i> (L.) J.S. Presl.	Leaves	Ag, Au	Polyol phenol components and heterocyclic components
<i>Euphorbia esula</i> L.	Leaves	Cu	Flavonoids and phenolic acids
<i>Camellia sinensis</i> Ktze. var. <i>assamica</i> Kitamura	Leaves	Fe ₂ O ₃	Polyphenols

Table 2.4 Biosynthesis of metal NPs using the extraction of plant species (Continued).

Species	Parts	NPs	Causative agents
<i>Pinus eldarica</i> Tenore.	Bark	Ag	Phenolic compounds
<i>Pinus thunbergii</i> Parl.	pine	Ag	Hydroxyl and carbonyl groups
<i>Pinus resinosa</i> Sol. ex Aiton	Bark	Pb	Fulvic acid
<i>Pinus densiflora</i> Siebold & Zucc.	Leaves	Ag	Not mentioned
<i>Ginkgo biloba</i> L.	Leaves	Ag	Proteins and metabolites
<i>Adiantum philippense</i> L.	Leaves	Au, Ag	Not mentioned
<i>Fissidens minutus</i> Thwaites & Mitt.	Thallus	Ag	Not mentioned
<i>Asparagus racemosus</i> Willd.	Cortex	Pd	Bioactive compound (not specified)
<i>Cintella asiatica</i> (L.) Urban	leaves	Au	Polyphenol compounds
<i>Clitoria ternatea</i> L.	Whole plant	MgO	Bioactive compound (not specified)

References: (Das et al., 2017)

2.3 Phytoremediation of Contaminated Heavy Metals in Water

Phytoremediation offers an eco-friendly alternative method to remove contaminated heavy metals in water by plants. Metal hyperaccumulator plants are used to absorb and accumulate heavy metals in aboveground parts. After the plants are harvested, heavy metals are removed and further supplied for industrial uses (Lone et al., 2008). The principle of the phytoremediation system includes phytoextraction, phytodegradation, phytostabilization, phytovolatilization, and rhizofiltration. Phytoextraction is the uptake of heavy metal ions from the soil and direct translocation into the plant biomass. Phytodegradation is the process that some plants can enhance microbial degradation of organic contaminants in the rhizosphere, implied in both soil and water. Phytostabilization is the process that metal ions become less available in the soil due to absorption and precipitation in the roots and root zone, implied in both soil and water (Shafi et al., 2015). Phytovolatilization is the process that plants uptake heavy metal ions (Hg, Se, and volatile hydrocarbons) from the soil and emit them into the air in volatile form through transpiration, implied in both soil and water. Rhizofiltration is the process that metal ions are uptake and removed from contaminated water by plant roots, implied in surface water. Among these, phytoextraction, rhizofiltration, and phytostabilization are commercially important (Thakur et al., 2016). In this work, seven common aquatic plants used for metal phytoremediation were chosen to study their capability to uptake some metal ions and transform them to metal NPs. Important characteristics and metal removal capabilities of these plants are described as following.

2.3.1 *Azolla pinnata* R.Br.

A. pinnata R.Br. (mosquitofern, feathered mosquitofern, or water velvet) is a species of small fern belonging to *Azolla* genus and Salviniaceae family. It is an aquatic plant that grows in or near water and can be classified as emergent, submerged or floating plants. *A. pinnata* R.Br. have been symbiotic relationships with nitrogen-fixing cyanobacteria (*Anabaena azollae*) and was used as a biofertilizer in agriculture worldwide (Qiu and Yu, 2003). The growing *A. pinnata* R.Br. and *A. azollae* are presented in Figure 2.24.

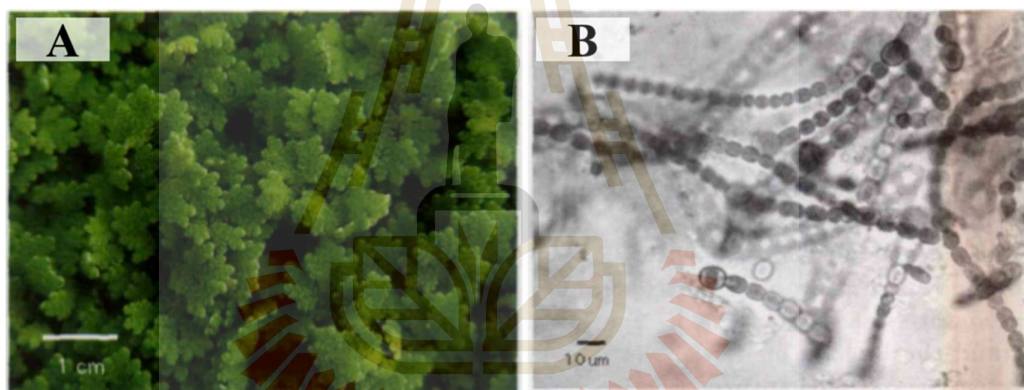


Figure 2.24 Images of (A) the growing *Azolla pinnata* R.Br. and (B) *Anabaena azollae* (Qiu and Yu, 2003).

The aquatic *A. pinnata* R.Br. plants were well recognized for removing heavy metal and herbicide in wastewater (De et al., 2017). In term of the bioremediation of heavy metal, *A. pinnata* R.Br. has been accepted as a hyperaccumulating plant, which is used to remove various metals in contaminated water including mercury, cadmium, lead, zinc, arsenic, and chromium (Jain et al., 1990; Rai, 2008; Sarkar and Jana, 1986; Talebi et al., 2019). Heavy metal pollutant tolerance of this species is due to its high

capability to uptake metals into cell wall and vacuoles through an intensive carrier transporting system as well as an evolution of specific metal resistance enzymes and alteration of cellular metabolites (Abdel et al., 2011).

2.3.2 *Salvinia molesta* D.S. Mitch.

S. molesta D.S. Mitch. (giant salvinia or kariba weed) is a free-floating plant belonging to *Salvinia* genus and Salviniaceae family that has spread to most tropical and sub-tropical countries. Rapid growth rates allow it to blanket still or slow-moving water bodies very quickly, causing environmental, sociological and economic problems (Giardini, 2004). Aquatic *S. molesta* D.S. Mitch. leaves were divided into two types including the emergent and submerged leaves. The emergent leaves have a green color with approximately 2.2 cm long and 1.3 cm wide of maturity. The submerged leaves have a brown color as seen in Figure 2.25 (Titus and Urban, 2009). This plant species was generally used for bioremediation of heavy metal and pollutant in the sewage system due to their fast growing and environmental friendly (Rezania et al., 2016). Heavy metal accumulation in this plant species is quite rapid and involves the passive uptake through adsorption of metal ions onto the plant surface and/or active uptake into plant cells (Abid et al., 2016).



Figure 2.25 The morphology of *Salvinia molesta* D.S. Mitch. (Claudia et al., 2017).

2.3.3 *Lemna minor* L.

L. minor L. (lesser duckweed) is a free-floating aquatic plant belonging to *Lemna* genus and Araceae family, which is generally found in natural lakes and streams (Joshua et al., 2013). Lesser duckweed includes fronds leaves (few leaves) and rootlet (single root) without a stem. The morphology of *L. minor* L. was presented in Figure 2.26. It is widely distributed in the tropics to temperate zones with from the freshwater to brackish water (Ekperusi et al., 2019). This plant is capable of removing heavy metals in contaminated water via different mechanisms such as photodegradation, hydrolysis, plant uptake, and phytodegradation (Zhang et al., 2017). Compared to other duckweed plants, *L. minor* L. is considered as the fast-growing and wide distribution plant that has a high capacity to remove Cd, Cr, and Pb in wastewater treatment pond (Liu et al., 2017; Miretzky et al., 2004). Rezania and colleagues showed that this plant species could remove several heavy metals in wastewater, such as Cr, Pb, Cd, Cu, Zn, As, and Hg (Rezania et al., 2016). In addition, Ohlbaum and colleagues reported its capacity to remove the Se metal in seleniferous soil leachate at the highest amount (97%) as compared with other metals (Ohlbaum et al., 2018).

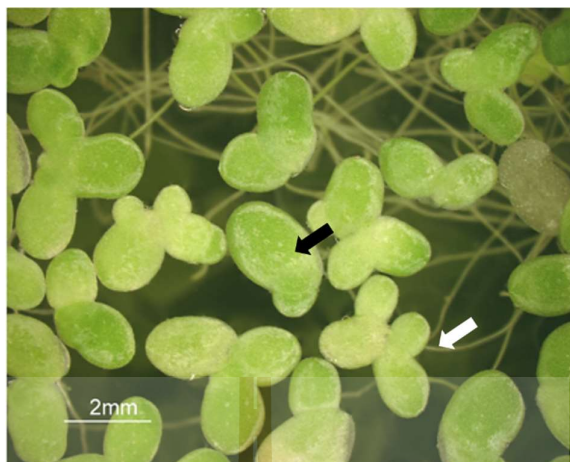


Figure 2.26 The morphology of *Lemna minor* L.; the fronds leaves (black narrow) and rootlet (white narrow) (Khataee et al., 2012).

2.3.4 *Lemna perpusilla* Torr.

L. perpusilla Torr. (minute duckweed) is small floating aquatic herbs belonging to *Lemna* genus and Araceae family. This plant has an approximately 3 cm roots length with only 1.5–4.0 mm of diameter. Leaves of this plant have a pale green color as seen in Figure 2.27 (Azer, 2013). Tang and colleagues proposed that this plant contains a lot of cellulose, lipid, lignin, pentosan, pectin, and minerals, which can be used as biosorbent to remove heavy metals (Tang et al., 2013). The capacity of this aquatic plant to remove potentially toxic heavy metals from water is well documented such as Cd, Pb, Ni, Ag, and Cu (Zhang et al., 2014).



Figure 2.27 The morphology of *Lemna perpusilla* Torr. (Chouhan and Sarma, 2013).

2.3.5 *Spirodela polyrrhiza* (L.) Schleid.

S. polyrrhiza (L.) Schleid. (great duckweed, Figure 2.28) belonging to *Spirodela* genus and Araceae family under the group of monocotyledons was selected for the present study because of its fast growth, wide distribution, short life span, and stability to environmental changes. This plant is considered as the phytoremediation plant capable to remove various heavy metals contaminated in wastewaters and ponds (Chaudhuri et al., 2014; Singh et al., 2016). It was reported for the efficient capability to remove Cd, Co, Cr, Cu, Pb, Ni, and Zn from wastewater (Gaur et al., 1994; Miretzky et al., 2004).



Figure 2.28 The morphology of *Spirodela polyrrhiza* (L.) Schleid. (Cheng et al., 2013).

2.3.6 *Wolffia globosa* (Roxb.) Hartog & Plas

W. globosa (Roxb.) Hartog & Plas (Asian watermeal) in the family of Araceae (duckweed) is a rootless free-floating aquatic plant consisting of small leaves without xylem or phloem cells and considered as the smallest and fastest growing angiosperms. It is distributed globally in aquatic ecosystems and has been used for wastewater treatment. *W. globosa* (Roxb.) Hartog & Plas (Figure 2.29) is very tiny with lesser than a millimeter wide. Generally, this plant is edible and makes nutritious food (Kaplan et al., 2018). Its structural simplicity makes it an interesting model plant for studying elemental behavior (Tel-Or and Forni, 2011). Recent studies showed that this plant efficiently removed Cd, Pb, Sr, and Mg from wastewater (Egila et al., 2011). It also effectively removed As and resisted up to 400 mg As/kg of its dry weight (Abid et al., 2016).



Figure 2.29 The morphology of *Wolffia globosa* (Roxb.) Hartog & Plas (Hartog and Plas, 1970).

2.3.7 *Eichhornia crassipes* (Mart.) Solms

E. crassipes (Mart.) Solms (water hyacinth) grows abundantly throughout the tropical and subtropical regions of the world and is also widely distributed in the southwest regions in Japan. Water hyacinth (Figure 2.30) has thick, glossy, and ovate leaves with the rise above of the water surface as much as 100 cm in height. In addition, the water hyacinth has long, spongy, and bulbous stalks (Reddy and DeBusk, 1984). This plant has also received much attention because of its potential for removal of pollutants when utilized as a biological filtration system (Muramoto and Oki, 1983). Their mechanisms of metal and color removal by biosorption can be classified as extracellular accumulation or precipitation, cell surface sorption or precipitation, and intracellular accumulation. Water hyacinth is one of the most commonly used plants in constructed wetlands because of its fast growth rate and large uptake of nutrients and contaminants. The adsorption efficiency of the water hyacinth to adsorb heavy metals in various forms is listed in Table 2.7, where most of the studies were carried out on the adsorption of heavy metals from the aqueous metal solution (Sanmuga and Senthamil, 2017).



Figure 2.30 The morphology of *Eichhornia crassipes* (Mart.) Solms (Middleton, 2008).

Table 2.5 Capacity of water hyacinth to adsorb heavy metals.

Source of water hyacinth	Metal	Adsorption capacity
Water hyacinth root	Cu and Pb	75% for Cd and more than 90% for Pb
Water hyacinth plant	Pb, Cd and Zn	Sorption capacities of 26.32, 12.60, and 12.55 mg/g for Pb, Cd, and Zn, respectively
Water hyacinth plant	Zn and Cd	0.65 mg/g maximum metal uptake
Water hyacinth roots	As	90% Arsenic removal
Water hyacinth plant	Fe	67.07 mg Fe per 1 kg dry weight
Water hyacinth plant	Al	Phytoremediation efficiency of 63%
Water hyacinth plant	Mn	Phytoextraction of manganese removal
Water hyacinth plant	Cu, Cd, Pb, Zn	98, 99, 98, and 84% for Cd, Cu, Pb, and Zn
Water hyacinth plant	Zn and Cr	95% of Zn, and 84% of Cr
Water hyacinth plant	Fe, Zn, Cu, Cr and Cd	(>90%) of metals; 15 day-experiment
Water hyacinth plant	Cd and Zn	Metal uptake by the plant was dependent upon the concentration of the metal and the duration of the exposure time
Water hyacinth plant	Pb, Cd, and Zn	Metal sorption followed the order Pb>Cd>Zn
Water hyacinth plant	Cd and Zn	Cd in shoots 0.12, roots 2.06 mg/g. Zn in shoots 1.90 mg/g, roots 9.46 mg/g.

Reference: (Sanmuga et al., 2014)

2.4 Review of Related Studies

As mentioned above, several phytoremediator plants are capable to detoxify and store high content of heavy metals but the question remains whether they are able to induce the formation of metal NPs from these uptake metal ions, which is the interest of this research.

Based on the literature review, the accumulation of metal ion in plant cells is proposed to involve the interaction with some polysaccharides, such as pectin and alginic acid, in cell wall of the plant cells, which play a crucial role in defense strategy response to heavy metal (Krzeslowska, 2011). Pectin is a high-molecular-weight carbohydrate that is mainly founded in the plant cell walls (Flutto, 2003). It has negatively charge and can bind to divalent and trivalent metal cations (Figure 2.31).

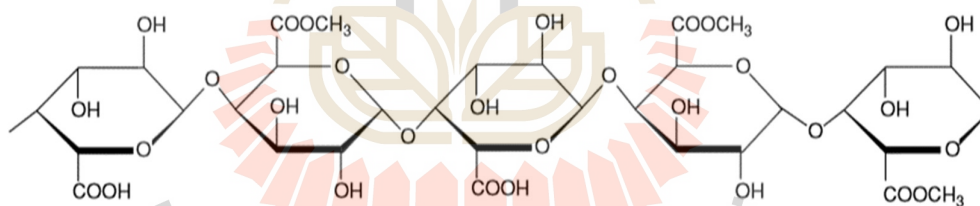


Figure 2.31 Chemical structure of pectin (Flutto, 2003).

The functional groups of carboxylic ($-COOH$), hydroxyl ($-OH$) of pectin and thiol group ($-SH$) of some proteins play a crucial role in heavy metal binding and accumulation in the cell wall (Figure 2.32). These metal-carbohydrate and metal-protein complexes are deposited in the plant cell wall and detected as the electron dense areas, generally having the average size of 200 nm as seen in Figure 2.33. But this metal accumulation was detected after the metal exposure for at least 72 h. Nevertheless, these

metal-carbohydrate and metal-protein complexes were not characterized whether they were metal NPs.

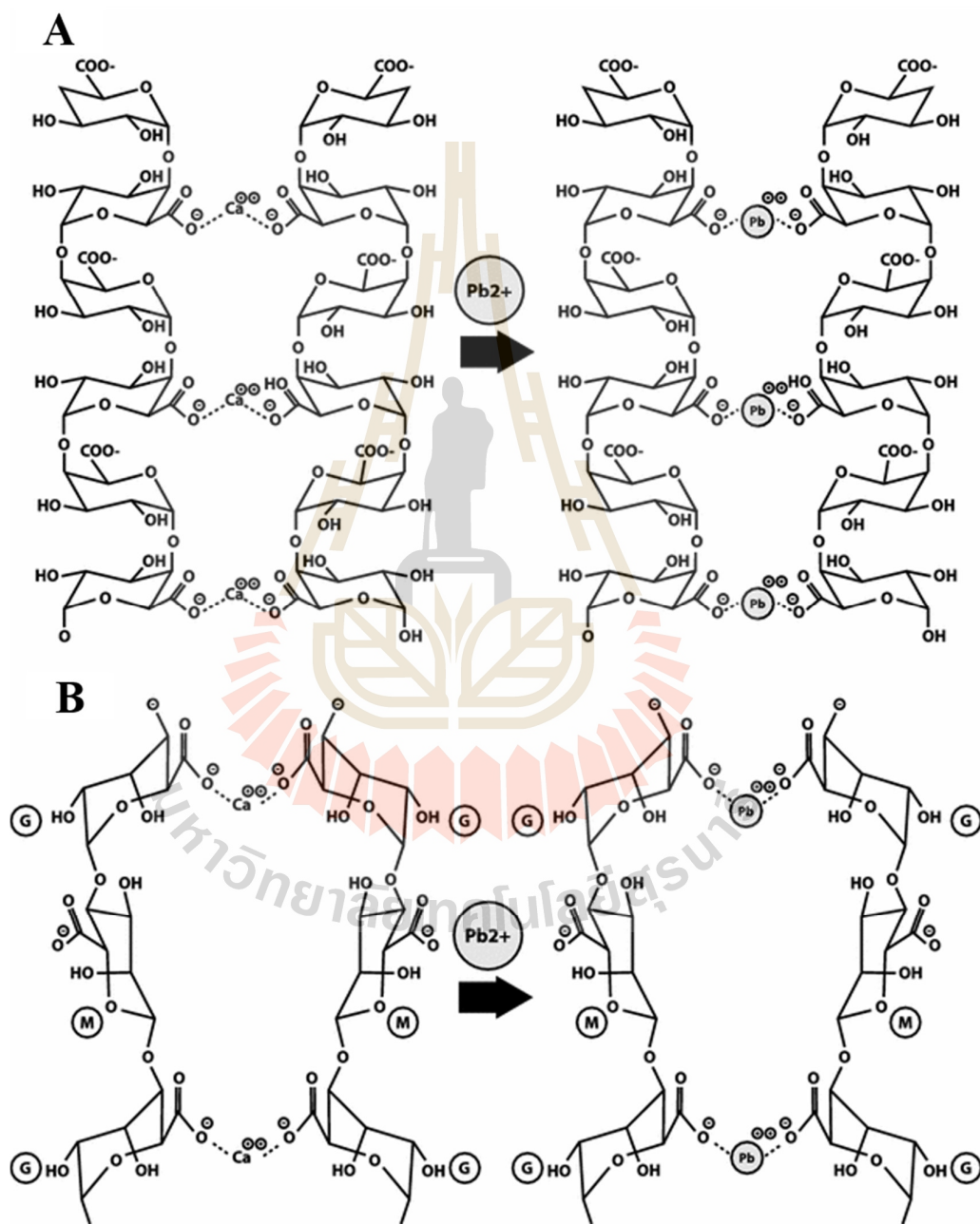


Figure 2.32 The possible cross-linking between metals and (A) pectin and (B) alginate (Krzeslowska, 2011).

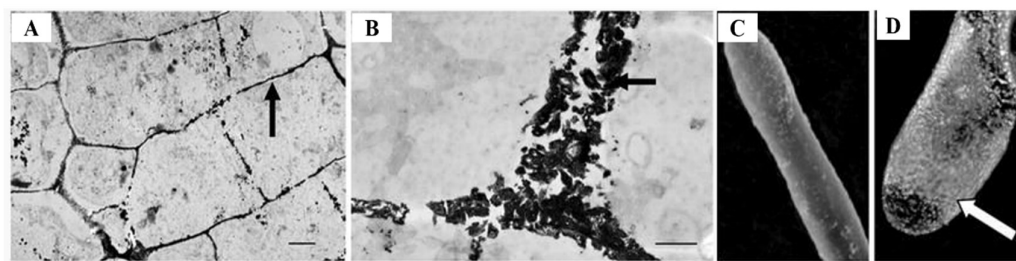


Figure 2.33 TEM images of Pb deposits (*black arrows*) in cell wall of (A) *Funaria hygrometrica* plant, (B) closer view of cell wall (C) SEM images of control *Funaria hygrometrica* plant, and (D) lead deposit on surface of *Funaria hygrometrica* (Krzeslowska, 2011).

In 2014, Taylor and colleagues reported the synthesized gold NPs (AuNPs) in *Arabidopsis thaliana* L. cells from the uptake gold ions with various concentrations. The plant was grown in both hydroponic nutrient and nutrient agar plates for 10 days (Figure 2.34). The results showed that the presence of electron-dense areas in the cell wall, chloroplasts, and vacuoles of cortical and vascular bundle cells of the Au-treated roots as seen in Figure 2.35. The electron dense areas had an average size of 5–100 nm (Taylor et al., 2014). However, the characterization including crystal structure, lattice parameters, and element composition of agglomerated particles in plant cells was still lacking.

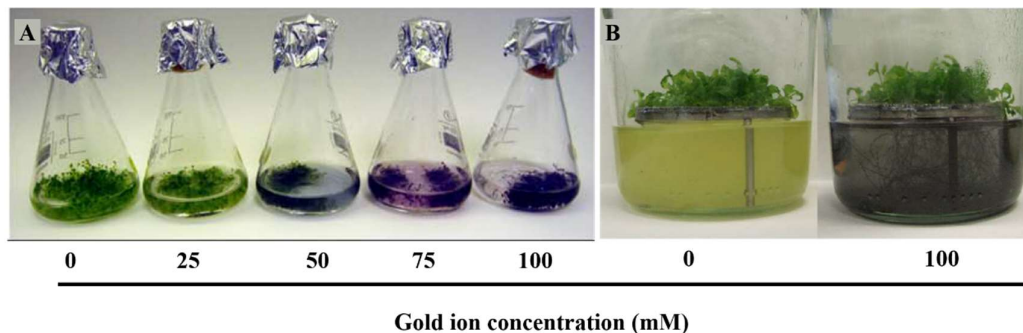


Figure 2.34 The uptake of gold ions by *Arabidopsis* from (A) hydroponic culture and (B) nutrient agar plates (Taylor et al., 2014).

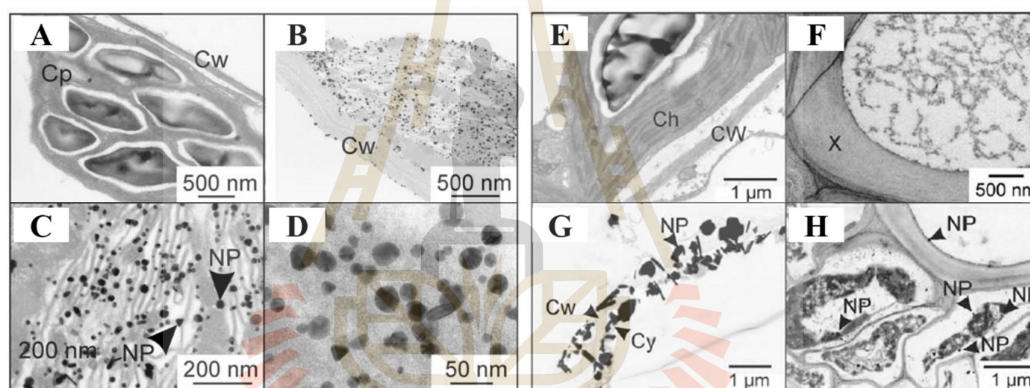


Figure 2.35 TEM images of (A) chloroplasts in cortex of untreated plants and electron dense of gold particles in the treated plants; (B) chloroplast, (C) closer view of chloroplast cell (D) vacuole in cortical cell, (E) chloroplast in vascular bundle from untreated plant, (F) cytoplasm and (G) plasma membrane of the xylem cells, and (H) phloem cells (Taylor et al., 2014).

In 2016, Kouhi research team has studied the anatomical and ultrastructural responses of the *Brassica napus* plant after the long-term exposure to excess zinc ions in a hypotonic system. Results showed that *B. napus* can bio-accumulate zinc metal in its roots and leaves as shown in Figure 2.36. In this work, although the accumulated metal in this plant cells was shown as the electron dense in TEM images, the characterization of these electron dense areas and the formation of metal NPs in this plant species were not studied (Kouhi et al., 2016).

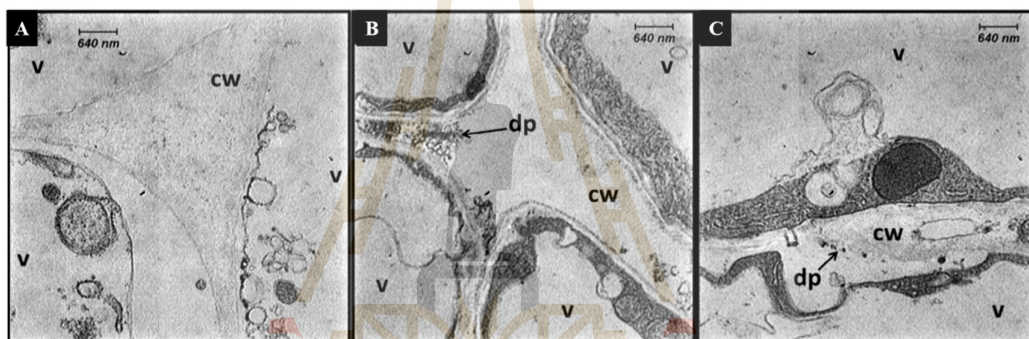


Figure 2.36 TEM micrograph of cross ultrathin sections of the root cortical cells of *Brassica napus* L.; (A) Control plants, (B) plants treated with 300 μM Zn^{2+} and (C) 350 μM Zn^{2+} (Kouhi et al., 2016).

Based on these reviews, the ability of most phytoremediation plants to synthesize metal NPs from the uptake metal ions and the characterization of the produced electron dense areas in the plant cells after exposure to metal ions are still lacking. Therefore, this work is interested to use 7 commonly phytoremediation plants to investigate the above questions.

CHAPTER III

MATERIALS AND METHODS

3.1 Materials

Plant specimens

Seven species of plant samples were collected from the plant nursery at Suranaree University of Technology, Nakhon Ratchasima, Thailand (14°52'37.9"N 102°01'05.4"E); Salvaniaceae (*A. pinnata* R.Br. and *S. molesta* D.S. Mitch.), Araceae (*L. minor* L., *L. perpusilla* Torr., *S. polyrrhiza* (L.) Schleid., and *W. globosa* (Roxb.) Hartog & Plas), and Pontederiaceae (*E. crassipes* (Mart.) Solms). Upon arrival to the laboratory, plant samples were washed with distilled water, followed by incubating in distilled water for 48 h to remove any impurities from the plant surface.

3.2 Experiments

3.2.1 Toxicity analysis

In this experiment, the toxicity of each metal ion to each plant species was determined. The plant samples (5 g) were incubated in 25 mL of each metal ion solution at various concentration (2 – 700 mM) for 12 h. The negative control was deionized (DI) water. The experiments were performed under the condition with a 12/12 h of light/dark diurnal cycle at ambient temperature. The metal solutions used in this experiment were AgNO₃, Cu(NO₃)₂, Fe(NO₃)₃, Ni(NO₃)₂, and Pb(NO₃)₂. The toxicity of each metal solution on each plant was determined by the percent of the

withered, brown leaves of metal-treated plants to the total leaves. Five sets of plant samples were used per treatment to determine the average and standard deviation. The experiments were repeats twice for checking the reproducibility. The toxicity (%) of metal ions in each plant sample was calculated as the followed equation.

$$\text{The toxicity (\%)} = (\text{number of withered, brown leaves} / \text{total leaves}) \times 100$$

The curve fitting and the toxicity 10% (TC10) were determined by OriginPro 2016 software (OriginLab Corporation, Northampton, MA, USA). The TC10 of each metal in each plant species was used in the following experiments as the cellular changes of the metal-treated plant were possibly detected at this concentration point.

3.2.2 Cross-sections of metal-treated roots

The root morphology of each plant sample in response to AgNO_3 , $\text{Cu}(\text{NO}_3)_2$, $\text{Fe}(\text{NO}_3)_3$, $\text{Ni}(\text{NO}_3)_2$, and $\text{Pb}(\text{NO}_3)_2$ solution was determined by the taken images of cross-sectioned roots observed under a bright-field microscope equipped with the BP72 digital camera (Olympus, Tokyo, Japan). Approximately 0.4-mm long root tips of the plant samples were cross-sectioned (15 μm thickness) using an MT-3 plant microtome (Nippon Medical and Chemical Instruments, Osaka, Japan).

3.2.3 Analysis of metal uptake by the plant samples

The uptake of metal ions and the changes of metal elements in the metal-treated roots of seven aquatic plant species were analyzed by energy dispersive X-ray fluorescence (EDXRF) spectroscopy (XGT-5200, Horiba, Japan). Each plant sample was treated with metal solutions at 10% toxicity for 12 h under the condition as previously described. The metal concentration at 10% toxicity was used in this experiment since this condition probably allowed the plants to still maintain regular

activities and be able to transform metal ions to NPs inside the cells. The negative control was the plants incubated in DI water. After 12 h of incubation, the plant samples were rinsed 3 times with 10 mM ethylenediaminetetraacetic acid (EDTA) and rinsed once with DI water to remove any excess ions from the outside of the roots. The modulated levels of metal ions inside the metal-treated roots were compared with the control roots as analyzed by EDXRF spectrometry equipped with an XGT-5200 X-ray analytical microscope (Horiba, Kyoto, Japan). The EDXRF analysis was carried out using a Rh X-ray tube source (voltage 50 kV and current 1 mA), Peltier cooled silicon drift detector (SDD), and 100 s/frame count. Five sets of plant samples were used in each experiment for determining the average data and standard deviation. Two independent experiments were performed to confirm the reproducibility of the experiment.

3.2.4 Analysis of chemical functional groups of biomolecules

To determine the changes of chemical constituents of biomolecules, the metal-treated and control plants was analyzed by the attenuated total reflectance-Fourier transform infrared (ATR-FTIR) spectroscopy equipped by a tensor 27 series (Bruker, Billerica, MA, USA). In this experiment, each plant sample was treated in the metal solution at the concentration of 10% toxicity for 12 h under the condition as previously described. The negative control was the plant samples incubated in DI water. After sequentially rinsing with 10 mM EDTA and DI water, the plant roots were dried in an oven at 70 °C for 24 h before subjecting to analyze by ATR-FTIR. The FTIR analysis was operated at a spectral range of 400 – 4000 cm^{-1} with a resolution of 4 cm^{-1} . Spectral data was processed using the Bruker software system

Opus 7.0 (Bruker, Billerica, MA, USA). Two independent experiments were performed to confirm the reproducibility of the experiment (D'Souza et al., 2008).

3.2.5 Cellular accumulation of nanoparticles in plant cells

The cellular formation of metal NPs in the plant root cells was determined by transmission electron microscope (TEM) analysis. Each plant sample was treated with AgNO_3 , $\text{Cu(NO}_3)_2$, $\text{Fe(NO}_3)_3$, $\text{Ni(NO}_3)_2$, and $\text{Pb(NO}_3)_2$ solution at the concentration of 10% toxicity for 12 h under the condition as previously described. After sequentially rinsing with 10 mM EDTA and DI water, the plant roots were fixed and embedded in the low viscosity Spurr's embedding medium as modified from the method of Kuo (Kuo, 2007). Briefly, the metal-treated root tips of 3-mm length were cut and fixed in 2.5% glutaraldehyde in 100 mM sodium phosphate buffer pH 7.0 at 4 °C for 4 h. For the Fe-treated roots they were required to fix in 5% glutaraldehyde in 100 mM sodium phosphate buffer pH 7.4 at 4 °C for overnight. If the tissues did not sink, they required the additional re-infiltration for 30 min. Then, the samples were rinsed in 100 mM sodium phosphate buffer for 3 times (20 min each) at 4 °C. After that, the post-fixed samples were dehydrated in dilution series of 30% acetone (30 min), 50% acetone (30 min), 75% acetone (overnight), 95% acetone (30 min), and 100% acetone (30 min, twice), respectively. Then, the dehydrated plant samples were infiltrated with the mixture I (Spurr's resin embedding medium and acetone, 1:3 v/v) using a 1:2 w/v ratio in a circular rotary mixer (Neuation Technologies Pvt. Ltd, Gujarat, India) at 10 rpm for 2 – 3 h. The mixture I was replaced with the mixture II (Spurr's resin embedding medium and acetone, 1:2 v/v) and further incubated overnight in a circular rotary mixer (10 rpm). Then, the mixture II was replaced with the mixture III (Spurr's resin embedding medium and acetone, 1:1 v/v) and further

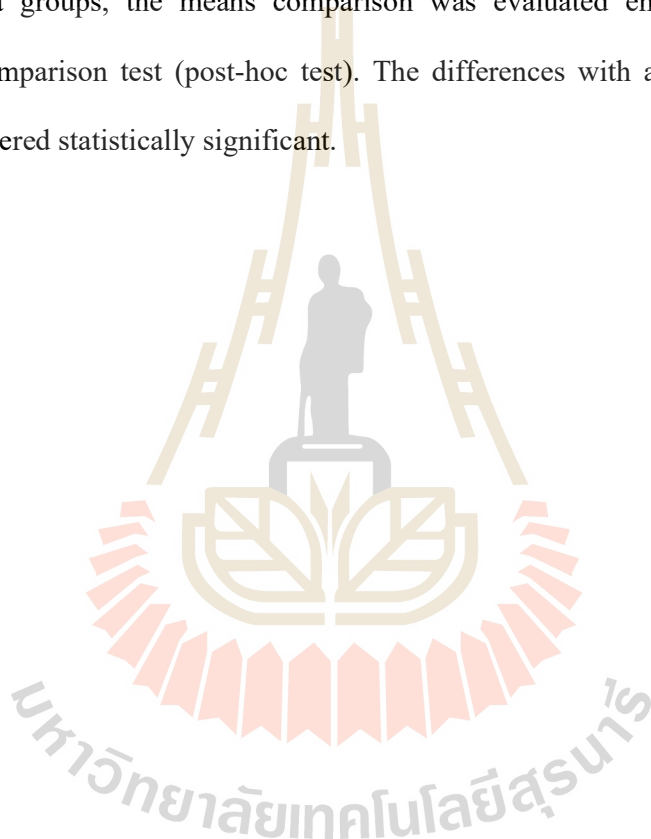
incubated for another 2 – 3 h. The mixture III was replaced with the Spurr's resin embedding medium and incubated for 6 – 12 h depending on the sample sizes. Then, the samples were transferred into a silicone embedding molds (SPI Supplies, West Chester, PA, USA) with the addition of Spurr's resin embedding medium, before drying at 60 °C for 48 h in an oven. Samples were cut by an ultramicrotome PowerTome-XL (RMC Boeckeler, Tucson, AZ, USA) with an ultra-glass knife. The sample sections were placed on the carbon films supported on Cu grids (200 mesh) and air-dried. The presence of NPs was determined by a TEM using an accelerating electron source of 120 kV with LaB6 filament. The images were captured by the equipped Orius 200 CCD Camera (Gatan, Pleasanton, CA, USA) (Khamhaengpol et al., 2016). The size distribution and average size of each NP in the plant root cells was analyzed by ImageJ software (National Institutes of Health, Bethesda, MD, USA), which 100 particles were randomly picked and measured their diameters.

3.2.6 Characterization of metal nanoparticles

To analyze the crystalline nature of the nanoparticles, the ultrathin sections of the metal-treated and control roots were analyzed by selected area electron diffraction (SAED) and high resolution (HR) TEM using a Tecnai G2 S-Twin TEM operating at an accelerating electron source of 200 kV with LaB6 filament. The images were taken by the equipped Gatan Orius 200 CCD Camera. Elemental composition of the accumulated NPs was characterized by energy-dispersive X-ray (EDX) spectroscopy carried out on a Tecnai G2 20 S-Twin TEM equipped with an EDAXr-TEM SUTW detector operating at an accelerating voltage of 15 kV (Janthima et al., 2018).

3.2.7 Statistical analysis

The data were represented as the average \pm standard deviation. The experimental data were statistically analyzed using SPSS version 18.0 for Windows software (SPSS, Inc., Somers, NY, USA). Statistical comparisons were performed using the one-way analysis of variance (ANOVA). To identify significant difference among data groups, the means comparison was evaluated employing a Tukey's multiple comparison test (post-hoc test). The differences with a value of $p < 0.05$ were considered statistically significant.



CHAPTER IV

RESULTS AND DISCUSSION PART I

Salviniaceae family: The ability of *Azolla pinnata* R.Br. and *Salvinia molesta* D.S. Mitch. to absorb and transform metal ions to metal nanoparticles

4.1 Toxicity Test

Heavy metals at optimal concentrations are important for promoting plant growth and development. However, at the excess concentrations, they are toxic to plants and lead to their death. The toxicity of heavy metals varies upon plant species, metal types, and metal concentrations (Ackova, 2018). In this part, two common aquatic plant species belonging to the same family (Salviniaceae) were used as the studied species; *A. pinnata* R.Br. and *S. molesta* D.S. Mitch. In this work, five metals were chosen as they were mostly contaminated in the environment; Ag^+ , Cu^{2+} , Fe^{3+} , Ni^{2+} , and Pb^{2+} . The dominant silver ions in the contaminated water are monocationic ions (Pelkonen et al., 2003). Most copper, nickel, and lead ions that contaminated in the environment are in a divalent cationic form (Santhosh et al., 2017; Turhanen et al., 2015). In addition, trivalent of iron ions is also mainly found in the contaminated water (Turhanen et al., 2015). The toxicity of 5 heavy metals (Ag, Cu, Fe, Ni, and Pb) at various concentrations was determined after incubating with each plant species for 12 h including AgNO_3 (0.5, 1, 1.5, 2, 3, 4, 6, 8, 10, and 20 mM), $\text{Cu}(\text{NO}_3)_2$ (10, 20, 30, 40, 50, 60, 70, and 80 mM),

Fe(NO₃)₃ (10, 20, 30, 40, 50, 60, 70, 80, 100, 120, and 140 mM), Ni(NO₃)₂ (100, 150, 200, 300, 400, 500, and 600 mM), and Pb(NO₃)₂ (100, 150, 200, 300, 400, 500, and 600 mM). The metal toxicity was reported as the percent of toxicity concentration (TC) values, which referred to the concentration of heavy metal that cause the withered and brown leaves in response to the metal treatment. The results showed that %TC of all heavy metals were increased according to the increased metal concentrations (dose-dependent response) as the data were reported in APPENDIX C.

In *A. pinnata* R.Br., withered and brown leaves in response to metal treatment were clearly seen in all metal treatments (Figure 4.1A). These morphological changes of leaves are likely due to the plasmolysis and chlorosis effects of metal solutions at the higher concentration than the acceptable level in *A. pinnata* R.Br. The TC10, the metal concentration causing 10% toxicity, was also determined as shown in Figure 4.1B. The TC10 values of AgNO₃, Cu(NO₃)₂, Fe(NO₃)₃, Ni(NO₃)₂, and Pb(NO₃)₂ on *A. pinnata* R.Br. were 1.5 ± 0.9 , 13.5 ± 1.7 , 31.0 ± 3.5 , 152.8 ± 1.14 , and 149.1 ± 2.4 mM, respectively. Ni(NO₃)₂ had the highest concentration at TC10 as compared with the other metal solutions, whereas AgNO₃ had the lowest concentration at TC10. Thus, these results suggested that *A. pinnata* R.Br. was more tolerant to Ni²⁺ treatment, while it was quite sensitive to Ag⁺ treatment.

In *S. molesta* D.S. Mitch., the changes of leaf colors from green to brown were clearly seen in the metal-treated plant samples, which more numbers of affected leaves were detected according to the increasing concentrations of metal solutions (Figure 4.2A). The TC10 values of AgNO₃, Cu(NO₃)₂, Fe(NO₃)₃, Ni(NO₃)₂, and Pb(NO₃)₂ were detected at 1.3 ± 2.1 , 18.5 ± 1.0 , 31.3 ± 3.1 , 94.8 ± 0.4 , and 152.2 ± 4.3 mM, respectively (Figure 4.2B). Similar to *A. pinnata* R.Br., *S. molesta* D.S. Mitch. was very

sensitive to Ag^+ treatment. Unlike *A. pinnata* R.Br., *S. molesta* D.S. Mitch. was more tolerant to Pb^{2+} than Ni^{2+} treatments.

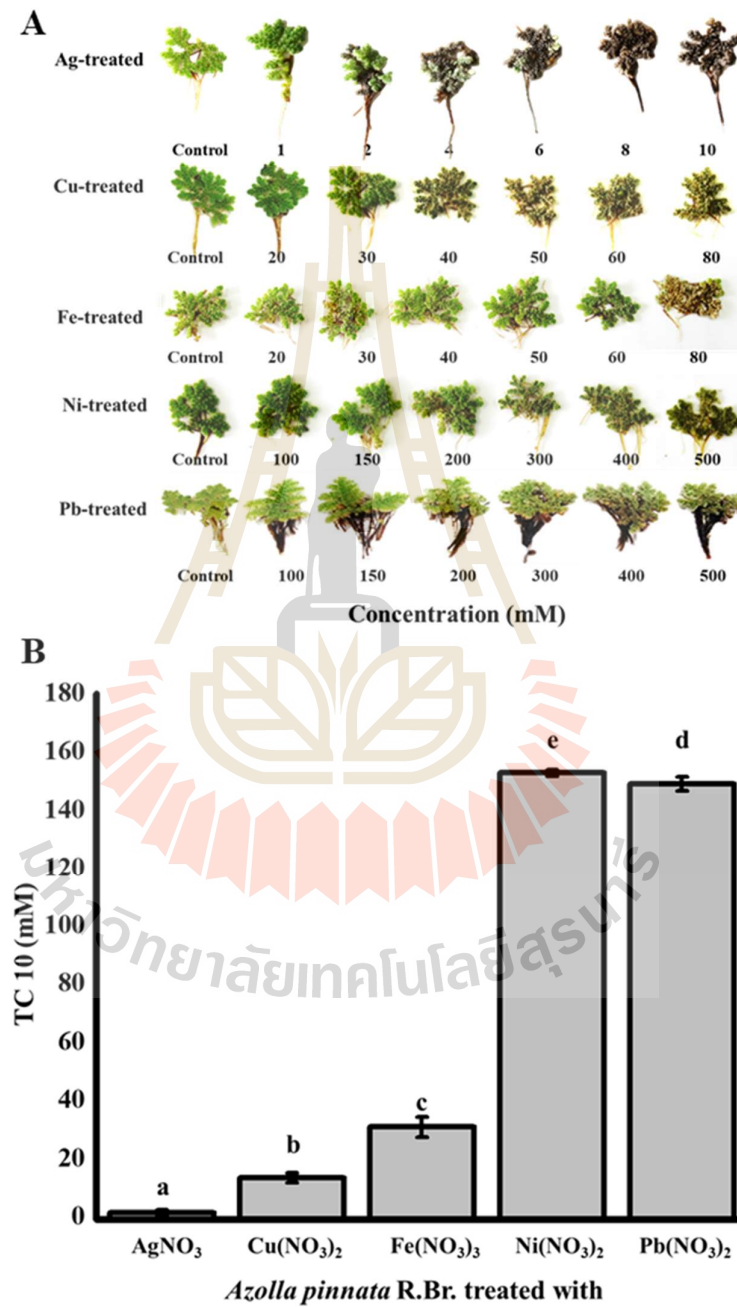


Figure 4.1 The toxicity effects of 5 metal ions on *Azolla pinnata* R.Br.; (A) the morphology changes of leaves and (B) the TC10 values.

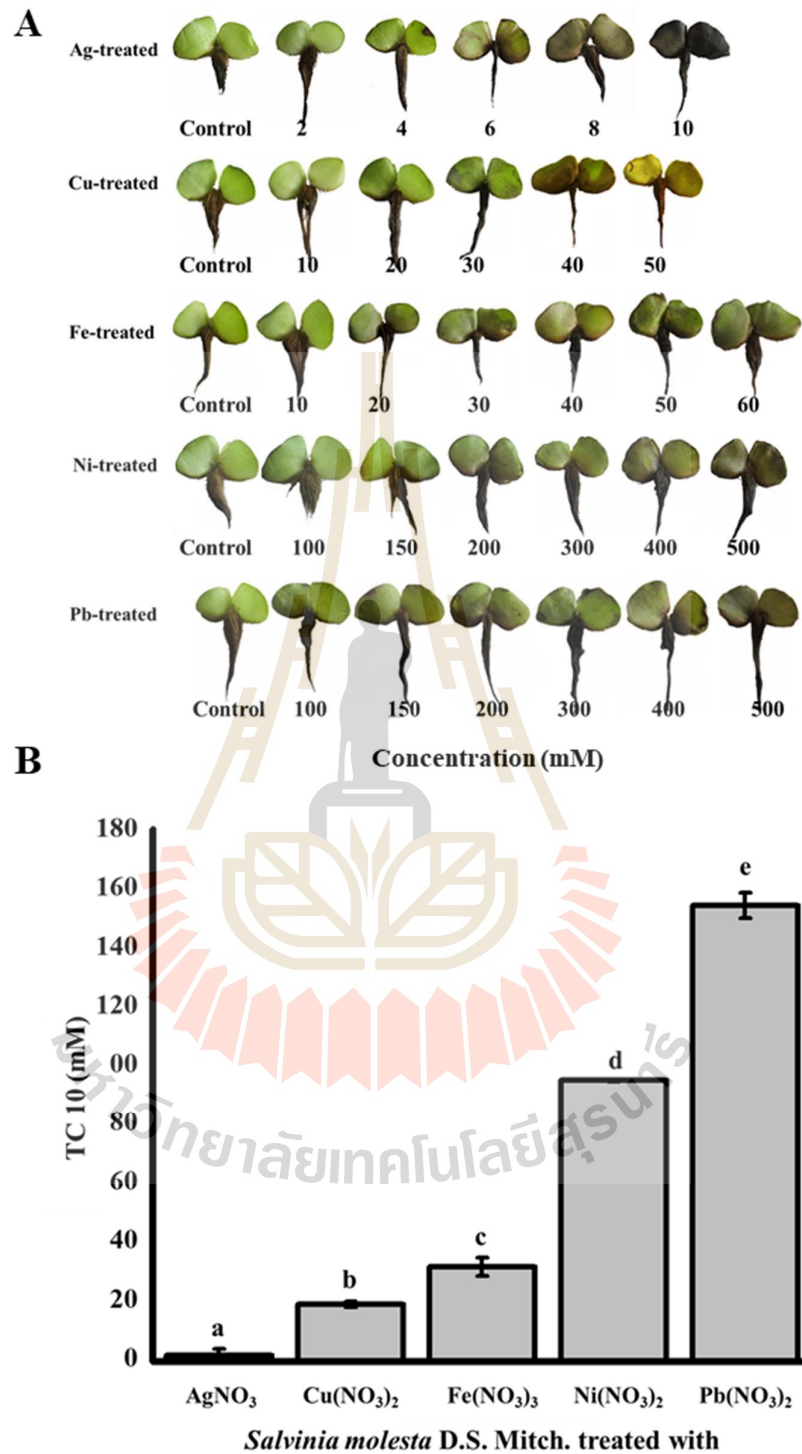


Figure 4.2 The toxicity effects of 5 metal ions on *Salvinia molesta* D.S. Mitch.; (A) the morphology changes of leaves and (B) the TC10 values.

The above results, both plant species are very sensitive to AgNO_3 , which its toxicity in the plants is likely due to the following actions. Similar to other cations (such as Co^{2+} , Cu^{2+} , Fe^{2+} , Mn^{2+} , Mo^{2+} , Ni^{2+} , Pb^{2+} , and Zn^{2+} ions), Ag^+ ions can enter the plant cells via apoplastic and/or symplastic pathways, which its high concentration level inside the cells leads to cellular damage, high production level of reactive oxygen species (ROS), interference of the normal metabolic reactions by altering the enzymatic activities, reduction of growth and biomass, alteration of chlorophyll content, injury of shoot and root, stimulation of leaf chlorosis, suppression of root nodules, and eventually induction of cell death (Arif et al., 2016).

For $\text{Cu(NO}_3)_2$ treatment, Cu^{2+} ions at low concentration facilitate several cellular processes such as photosynthesis and electron transport. However, they generate the toxic effect when exceed the optimized concentration in cells such as growth inhibition (Arif et al., 2016; Chen et al., 2009).

For $\text{Fe(NO}_3)_3$ treatment, Connolly and Guerinot reported that a low concentration of Fe showed the adverse effect as the essential nutrient for plants, which play an importance role in the electron-transport chains of photosynthesis and respiration processes. But its negative effects to plant occurred when it accumulated at high levels in the plant cells. Its generation of hydroxyl radicals ($\cdot\text{OH}$), also known as the Fenton reaction, could damage lipids, proteins and DNA in the plant cells (Connolly and Guerinot, 2002).

For $\text{Ni(NO}_3)_2$ treatment, its toxicity effect was likely due to the chlorosis and necrosis effects of Ni^{2+} ions, which eventually reduced the photosynthesis rate of the plants (Kushwaha et al., 2018). As mentioned before, the TC10 of $\text{Ni(NO}_3)_2$ on *A. pinnata* R.Br. was higher than the other metal solutions, suggesting that this plant

species was more tolerant to Ni^{2+} uptake level than the other tested ions. This result was in a good agreement with the report by Lokuge and colleagues that revealed the highest uptake level of Ni^{2+} ion as compared with the other studied metal ions (Cr^{3+} , Cd^{2+} , and Pb^{2+}) by *A. pinnata* R.Br. Therefore, *A. pinnata* R.Br. was considered as the good hyperaccumulation plant for Ni^{2+} ions (Lokuge, 2016).

For toxicity effect of $\text{Pb}(\text{NO}_3)_2$, Sharma and Dubey reported that Pb^{2+} ions at low concentration predominantly entered the plant cells via an apoplastic system and bound with some phytochemicals in a cell wall such as pectin and alginic acid and forms non-toxic metal complexes. Thus, plants were tolerant and survived under the low Pb^{2+} exposure (Sharma and Dubey, 2005). As mentioned before, the TC_{10} of $\text{Pb}(\text{NO}_3)_2$ on *S. molesta* D.S. Mitch. was higher than the other metal solutions, suggested that *S. molesta* D.S. Mitch. was more resistant to Pb^{2+} ions than Ag^+ , Cu^{2+} , Fe^{3+} , and Ni^{2+} . Nevertheless, the toxicity of Pb^{2+} exposure was reported as follows. Kramer and colleagues reported that Pb^{2+} ions at a high concentration passively entered the cells via the apoplastic and symplastic pathways, and membrane-transport protein channels (Krämer et al., 2007). The primary toxic effect of Pb^{2+} ions was via the electrostatic interaction of Pb-divalent with sulfur atom of sulfhydryl groups, mainly found in proteins, which caused the inhibition of enzyme activities. Moreover, Pb^{2+} ions induced the ROS species, which caused the production of oxidative stress in plants, affecting a long list of physiological and biological processes in plants leading to the cell death (Hadi and Aziz, 2015; Pourrut et al., 2011).

In general, the optimized pH range for metal ion absorption by plants varies on the metal type; Ag^+ (pH 4 – 8), Fe^{3+} (pH 3 – 8), Cu^{2+} (pH 6.3 – 7.8), Ni^{2+} (pH 6.4 – 7.3), and Pb^{2+} (pH 5 – 7.2) (Chaney, 1989; Kukier et al., 2004; Rieuwerts et al., 1998; Saleeb

et al., 2019) In this experiment, the pH values of AgNO_3 , $\text{Cu(NO}_3)_2$, $\text{Fe(NO}_3)_3$, $\text{Ni(NO}_3)_2$, and $\text{Pb(NO}_3)_2$ in the experiments were 5, 6, 7, 7, and 7, respectively, which were in the optimal ranges for plant to uptake.

4.2 The Elemental Mass Profile Analysis

The elemental mass profiles of *A. pinnata* R.Br. and *S. molesta* D.S. Mitch. roots exposed to AgNO_3 , $\text{Cu(NO}_3)_2$, $\text{Fe(NO}_3)_3$, $\text{Ni(NO}_3)_2$, and $\text{Pb(NO}_3)_2$ solutions were determined by EDXRF analysis. The EDXRF images showed the significantly different levels of ^{15}P , ^{16}S , ^{19}K , ^{20}Ca , ^{26}Fe , ^{28}Ni , ^{29}Cu , ^{47}Ag , and ^{82}Pb of the treated roots as compared with the control roots (Figure 4.3 and Figure 4.4). For each metal treatment, the results clearly showed the high level of the treated metal in the plant roots, whereas no detection of that metal in the control roots. Interestingly, the treated roots showed the reduction levels of ^{19}K and ^{20}Ca elements as compared with the control, suggesting that each metal treatment caused the cellular ^{19}K and ^{20}Ca levels in the root cells (Table 4.1).

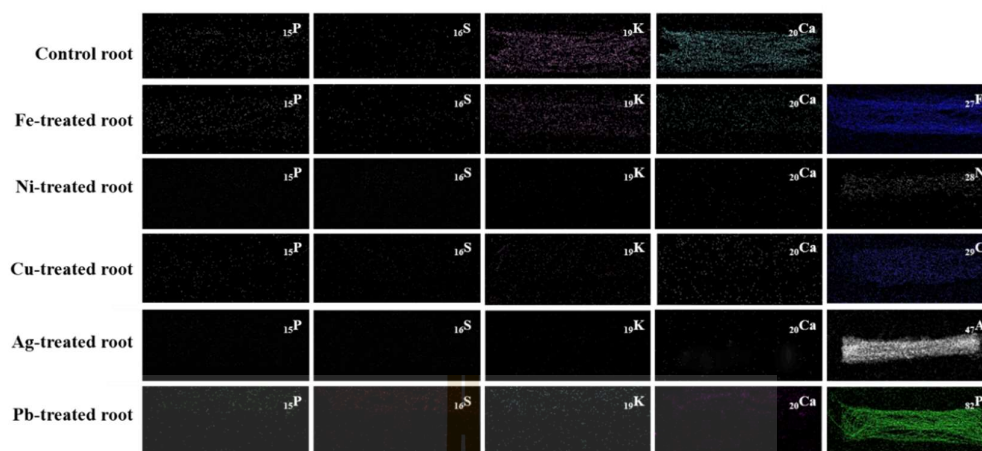


Figure 4.3 The EDXRF mapping images of *Azolla pinnata* R.Br. roots treated with AgNO_3 , $\text{Cu}(\text{NO}_3)_2$, $\text{Fe}(\text{NO}_3)_3$, $\text{Ni}(\text{NO}_3)_2$, and $\text{Pb}(\text{NO}_3)_2$ solutions.

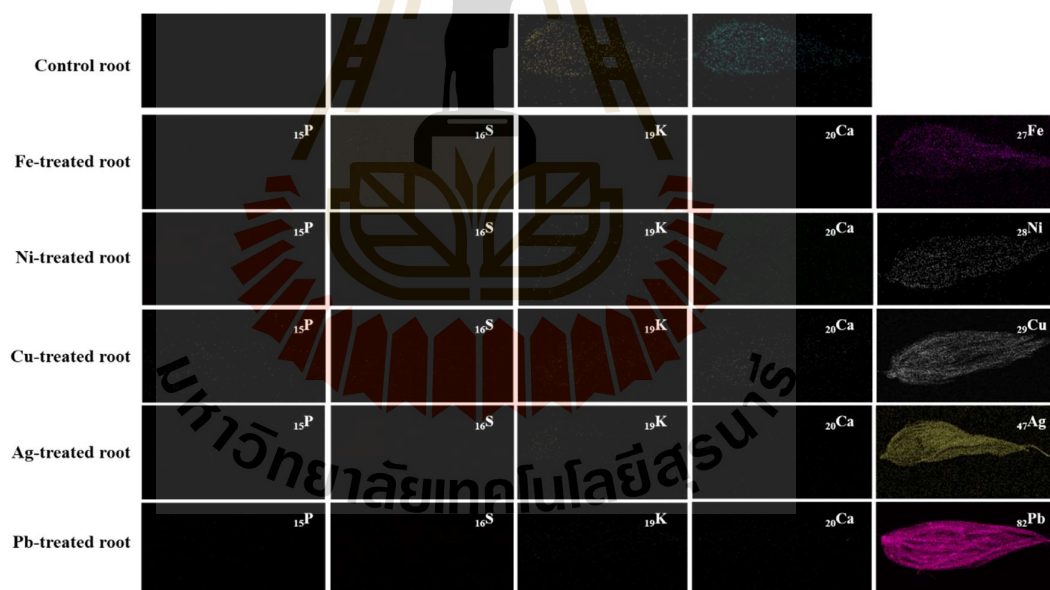


Figure 4.4 The EDXRF mapping images of *Salvinia molesta* D.S. Mitch. roots treated with AgNO_3 , $\text{Cu}(\text{NO}_3)_2$, $\text{Fe}(\text{NO}_3)_3$, $\text{Ni}(\text{NO}_3)_2$, and $\text{Pb}(\text{NO}_3)_2$ solutions.

The quantitative levels of each element are shown in Table 4.2. The treated *A. pinnata* R.Br. roots with AgNO_3 , $\text{Cu}(\text{NO}_3)_2$, $\text{Fe}(\text{NO}_3)_3$, $\text{Ni}(\text{NO}_3)_2$, and $\text{Pb}(\text{NO}_3)_2$ solutions showed the high levels of the treated metals, which were 80.3% (^{47}Ag), 72.9% (^{29}Cu), 73.2% (^{26}Fe), 61.8% (^{28}Ni), and 87.8% (^{82}Pb), respectively. In addition, the levels of ^{19}K and ^{20}Ca in *A. pinnata* R.Br. were significantly reduced in response to all metal treatments. Similarly, the treated *S. molesta* D.S. Mitch. roots with AgNO_3 , $\text{Cu}(\text{NO}_3)_2$, $\text{Fe}(\text{NO}_3)_3$, $\text{Ni}(\text{NO}_3)_2$, and $\text{Pb}(\text{NO}_3)_2$ solutions showed the high levels of the treated metals, which were 94.6% (^{47}Ag), 75.5% (^{29}Cu), 71.2% (^{26}Fe), 61.6% (^{28}Ni), and 98.1% (^{82}Pb), respectively. For both plant species, their highest accumulated element was Pb^{2+} , followed by Ag^+ , while Ni^{2+} was the lowest accumulated element in their roots. Similar to the results of treated *A. pinnata* R.Br., the treated *S. molesta* D.S. Mitch. had the significant reduction levels of ^{19}K and ^{20}Ca .

It was likely that the transport of each metal ion into plant cells was via several transporters. The transport of Cu^{2+} was via the zinc-responsive transporter/iron-responsive transporter-like protein (ZIP) family and Cu-transporter protein (COPT) family (Yruela, 2009). The transport of Fe^{3+} was via the iron-nicotianamine transporters and ZIP family (Aydemir and Cousins, 2018). The transport of Pb^{2+} was via the plant natural resistance associated macrophage protein (NRAMP) family and ZIP family (Thomine et al., 2000). The transport of Ni^{2+} was via the high-affinity Ni transport protein, metallothionein and metallochaperones. The transport of Ag^+ was via the NRAMP and ZIP family (Chen et al., 2009). The reduction levels of ^{19}K and ^{20}Ca in all metal treatments were hypothesized to cause by the competition between these ions and other metal ions that shared the same transporting routes, resulting in limiting the Ca^{2+} and K^+ influx (Ahmad et al., 2016).

Table 4.1 The quantitative levels of metal elements in *Azolla pinnata* R.Br. roots by EDXRF analysis.

Metal Elements	Control root	% Element mass in the treated roots with				
		AgNO ₃	Cu(NO ₃) ₂	Fe(NO ₃) ₃	Ni(NO ₃) ₂	Pb(NO ₃) ₂
¹⁵ P	2.6 ± 2.3 ^a	2.3 ± 0.8 ^b	3.7 ± 1.7 ^{c,d}	4.1 ± 0.9 ^{d,e}	4.8 ± 0.8 ^e	0.8 ± 0.1 ^f
¹⁹ K	45.9 ± 11.6 ^a	1.1 ± 0.1 ^e	2.9 ± 7.6 ^d	4.4 ± 0.4 ^c	7.7 ± 3.3 ^b	4.8 ± 0.2 ^c
²⁰ Ca	38.3 ± 9.7 ^a	0.3 ± 0.3 ^f	3.7 ± 4.1 ^d	5.6 ± 0.2 ^c	8.8 ± 3.9 ^b	2.2 ± 1.9 ^e
²⁶ Fe	1.7 ± 2.1 ^a	2.4 ± 1.0 ^b	1.9 ± 0.7 ^{a,b}	73.2 ± 0.7^d	2.3 ± 2.1 ^b	5.6 ± 0.6 ^c
²⁸ Ni	2.1 ± 2.4 ^a	1.0 ± 0.2 ^c	2.3 ± 0.6 ^a	2.3 ± 0.7 ^a	61.8 ± 3.3^b	2.0 ± 0.2 ^a
²⁹ Cu	3.1 ± 2.6 ^a	0.5 ± 0.3 ^d	72.9 ± 9.5^c	0.3 ± 0.3 ^d	3.0 ± 1.5 ^a	4.1 ± 0.9 ^b
⁴⁷ Ag	2.0 ± 0.3 ^a	80.3 ± 1.0^c	2.6 ± 0.2 ^{a,b}	2.5 ± 1.5 ^{a,b}	2.9 ± 1.9 ^b	3.0 ± 0.6 ^b
⁸² Pb	2.1 ± 1.3 ^a	1.3 ± 0.5 ^{c,d}	0.6 ± 0.3 ^d	0.8 ± 0.6 ^d	0.4 ± 0.2 ^d	87.7 ± 1.2^b

n = 7, p < 0.05, significant difference of each metal was compared among different metal-treated roots.

Table 4.2 The quantitative levels of metal elements in *Salvinia molesta* D.S. Mitch. roots by EDXRF analysis.

Metal Elements	% Element mass in the treated roots with					
	Control root	AgNO ₃	Cu(NO ₃) ₂	Fe(NO ₃) ₃	Ni(NO ₃) ₂	Pb(NO ₃) ₂
¹⁵ P	7.4 ± 1.5 ^a	9.3 ± 0.7 ^b	0.2 ± 0.3 ^c	0.1 ± 0.1 ^c	0.5 ± 0.4 ^c	0.1 ± 0.17 ^c
¹⁹ K	33.4 ± 1.9 ^a	0.1 ± 0.1 ^d	0.7 ± 0.6 ^{c,d}	7.1 ± 0.4 ^b	0.9 ± 0.3 ^c	0.1 ± 0.4 ^d
²⁰ Ca	54.4 ± 2.4 ^a	0.2 ± 0.2 ^f	1.0 ± 1.2 ^e	10.4 ± 0.9 ^b	5.4 ± 0.4 ^c	0.8 ± 0.7 ^{d,e}
²⁶ Fe	0.6 ± 0.1 ^a	0.4 ± 0.2 ^a	4.2 ± 1.3 ^c	71.2 ± 1.3^d	3.6 ± 1.9 ^c	2.3 ± 1.2 ^b
²⁸ Ni	0.6 ± 0.2 ^a	0.1 ± 0.2 ^a	0.4 ± 0.1 ^a	0.3 ± 0.1 ^a	61.6 ± 0.5^c	1.5 ± 0.5 ^b
²⁹ Cu	1.1 ± 2.6 ^a	0.3 ± 0.2 ^b	75.5 ± 0.5^c	0.2 ± 0.1 ^b	1.1 ± 1.2 ^a	1.2 ± 0.1 ^a
⁴⁷ Ag	0.5 ± 0.6 ^a	94.6 ± 1.2^b	0.1 ± 0.2 ^a	0.3 ± 0.3 ^a	0.1 ± 0.1 ^a	0.2 ± 0.1 ^a
⁸² Pb	0.6 ± 0.9 ^a	1.6 ± 1.2 ^b	0.2 ± 0.3 ^a	0.3 ± 0.4 ^a	0.3 ± 0.1 ^a	98.1 ± 1.3^c

n = 7, p < 0.05, significant difference of each metal was compared among different metal-treated roots.

4.3 Changed Profiles of Biomolecules in Response to Metal

Treatments

The biochemical changes of the functional groups of biomolecules in *A. pinnata* R.Br. and *S. molesta* D.S. Mitch. roots exposed to AgNO_3 , $\text{Cu(NO}_3)_2$, $\text{Fe(NO}_3)_3$, $\text{Ni(NO}_3)_2$, and $\text{Pb(NO}_3)_2$ solutions at TC10 values were analyzed by ATR-FTIR, which the results were summarized in Table 4.3 and Table 4.4, respectively. The ATR-FTIR spectra of each metal exposure in both plants were shown in APPENDIX C. The ATR-FTIR profiles revealed the changes of cellular biomolecules, which were determined by their characteristic functional groups. The results clearly showed that both metal-treated plants induced the syntheses of proteins and nucleic acids in response to each metal treatment as determined by the emerging of new spectral peaks as compared with those of the control plant. The presences of new proteins and nucleic acids were determined by the presence of spectral peaks of C=O of amide I ($1800 - 1630 \text{ cm}^{-1}$), C-N of amide II ($1395 - 1370 \text{ cm}^{-1}$), N-H of protein ($1000 - 800 \text{ cm}^{-1}$), and N-C of nucleic acid ($800 - 515 \text{ cm}^{-1}$) (Suresh et al., 2016a; 2016b).

In *A. pinnata* R.Br., all four spectral peaks were detected in response to Cu-treatment and Pb-treatment. Three spectral peaks, C-N of amide II, N-H of protein, and N-C of nucleic acid, were detected in Ag-treated plants. In Fe-treatment, three spectral peaks were detected; C=O of amide I, C-N of amide II, and N-C of nucleic acid. Interestingly, only single spectral peak of N-C of nucleic acid was detected in Ni-treatment, implying the lower toxicity of Ni^{2+} as compared with other treated metal ions since no significant levels of new protein synthesis was detected.

In *S. molesta* D.S. Mitch., two spectral peaks (C=O of amide I and C–N of amide II) were detected under the condition of Ag- and Fe-treatments. However, there was no detection of spectral peak for nucleic acids, suggesting that most cellular responses occurred at the protein regulation level, not the gene expression level. In Pb-treatment, all four spectral peaks were detected, suggesting that the cellular effects of Pb²⁺ ions were at both protein and gene expression levels. The changes of protein and gene expression in response to metal treatment in both plant species were in a good agreement with the previous reports. Cvjetko and colleagues reported that plants exposure to heavy metals (As, Cd, Cr, Cu, Fe, Hg, Mn, Mo, Ni, Pb, and Zn) exhibited the change of protein expression pattern as well as the quantitative change of protein and mRNA levels (Cvjetko et al., 2014). Hasan and colleagues reported the induction of some amino acids and proteins (i.g. proline, phytochelatins, and metallothioneins) in tomato treated with Cu²⁺ and Fe³⁺. These biomolecules played the important roles for metal detoxification by the chelation of metal ions (Hasan et al., 2017). Mendoza-Soto's research team suggested the induction of gene expression in response to Ag, Cu, Cd, Ni, Mn, and Pb exposures, such as the cytochrome c6 and carboxypeptidase X genes that encode for cytochrome c(6) and the carboxypeptidase family proteins, respectively (Mendoza-Soto et al., 2012). Also, Puig and colleagues reported the induction of arabidopsis H⁺-ATPase gene that plays important role to produce ferric chelate reductase enzyme important for an Fe transport process (Puig et al., 2007).

Table 4.3 The summary of the ATR-FTIR spectral peaks of *Azolla pinnata* R.Br. roots treated with AgNO₃, Cu(NO₃)₂, Fe(NO₃)₃, Ni(NO₃)₂, and Pb(NO₃)₂.

No.	Standard reference	Wave number (cm ⁻¹)					Functional groups	Biological compounds	
		Ctrl	Treated roots						
			Ag-	Cu-	Fe-	Ni-			Pb-
1	1800–1630	nd	1731	1735	1731	1730	1731	C=O	Amine I proteins
2	1395–1370	nd	1371	1376	1348	nd	1371	C–N	Amide II proteins
3	1000–800	nd	nd	911	nd	nd	811	N–H	Proteins
4	800–515	nd	626	611	612	611	632	N–C	Nucleic acids

nd: not detected

Table 4.4 The summary of the ATR-FTIR spectral peaks of the *Salvinia molesta* D.S. Mitch. roots in response to metal exposures.

No.	Standard reference	Wave number (cm ⁻¹)					Functional groups	Biological compounds	
		Ctrl	Treated roots						
			Ag-	Cu-	Fe-	Ni-			Pb-
1	1800–1630	nd	nd	nd	1631	1725	C=O	Amine I proteins	
2	1395–1370	nd	1383	1386	1386	nd	1380	C–N	Amide II proteins
3	1000–800	nd	nd	nd	nd	nd	811	N–H	Proteins
4	800–515	nd	nd	nd	nd	nd	632	N–C	Nucleic acids

nd: not detected

4.4 Accumulation of Metal Nanoparticles

4.4.1 Accumulation of metal nanoparticles in *Azolla pinnata* R.Br.

Since roots are the primary tissues to expose and uptake heavy metals, this study focuses on the transformation of the uptake metal ions to metal NPs in root tissues, especially in the cell division zone of the root tip where the cell division and enzymatic metabolisms are highly active (Haegeman et al., 2012). TEM images of ultrathin cross-sections of the *A. pinnata* R.Br. roots revealed the localization of AgNPs, CuNPs, FeNPs, and PbNPs from the uptake Ag^+ , Cu^{2+} , Fe^{3+} , and Pb^{2+} ions, but no observed NiNPs. In cortical tissue (Figure 4.5), each NPs was dominantly detected near the plasma membrane as isolated and agglomerated NPs. Similarly, morphology of AgNPs, CuNPs, and FeNPs were spherical, which their average diameters were 13.46 ± 3.67 , 14.07 ± 2.80 , and 15.76 ± 2.91 , respectively. Unlike other detected NPs, the morphology of PbNPs was short rod with 12.25 ± 2.41 nm in width and 16.02 ± 3.11 nm in length. The size distribution of each NPs is shown in Figure 4.6 as determined from 100 particles.

The possible mechanism of the produced metal NPs is still unclear, especially the formation of different-shaped metal NPs. In this work, we hypothesize that the formation of spherical metal NPs in plants is as follows. After the metal ions enter to the plant cells, the metal ions were reduced by some cellular molecules possessing reducing activity (such as phenolic and anionic compounds), resulting in zero-valent metal nuclei (Edge et al., 2007; Jan et al., 2010). These metal nuclei can grow into metal clusters and eventually NPs with the assistance of complex phytochemicals that help to stabilize the formed NPs in the plant cells (Kawamura et al., 2013). For a formation of rod NPs, it is hypothesized that the metal ions are reduced by weak reducing agents

such as tannic acid and glucose in the plant cells, which is also mediated the formation of twinned-seed structure (Ahmad, 2014; Sivaraman et al., 2009). Also with the appropriate cellular stabilizing agents, the growth of metal-seed nuclei prefers in a (100) plane, thus leading to an elongation of rod NPs (Abedini et al., 2016).

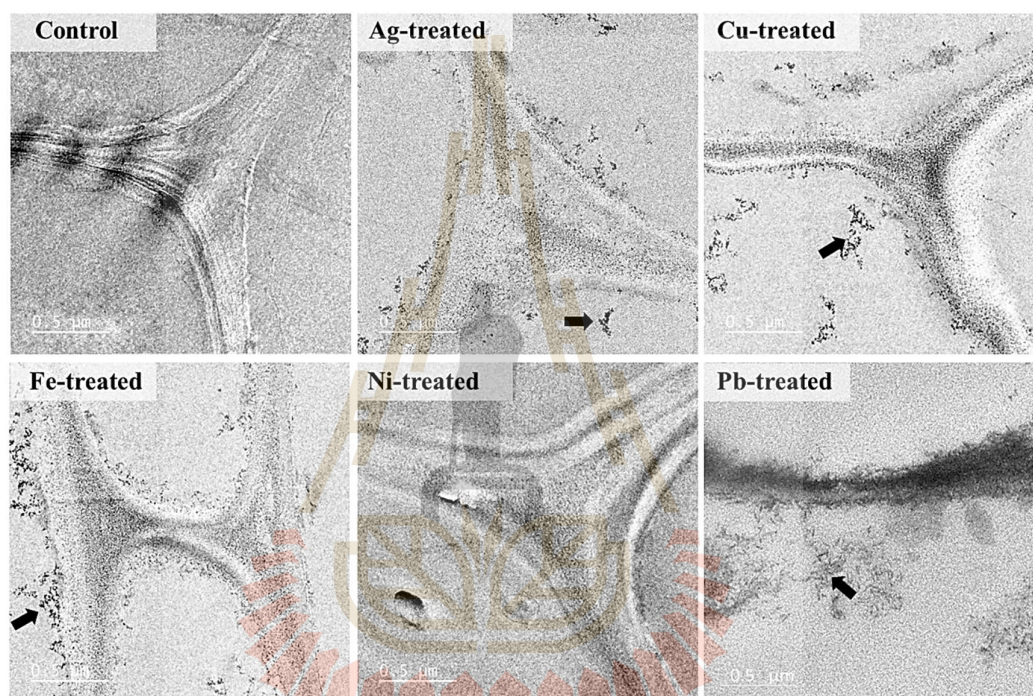


Figure 4.5 TEM images of cross-sections of cortical tissues of *Azolla pinnata* R.Br. roots. Arrows indicate metal NPs.

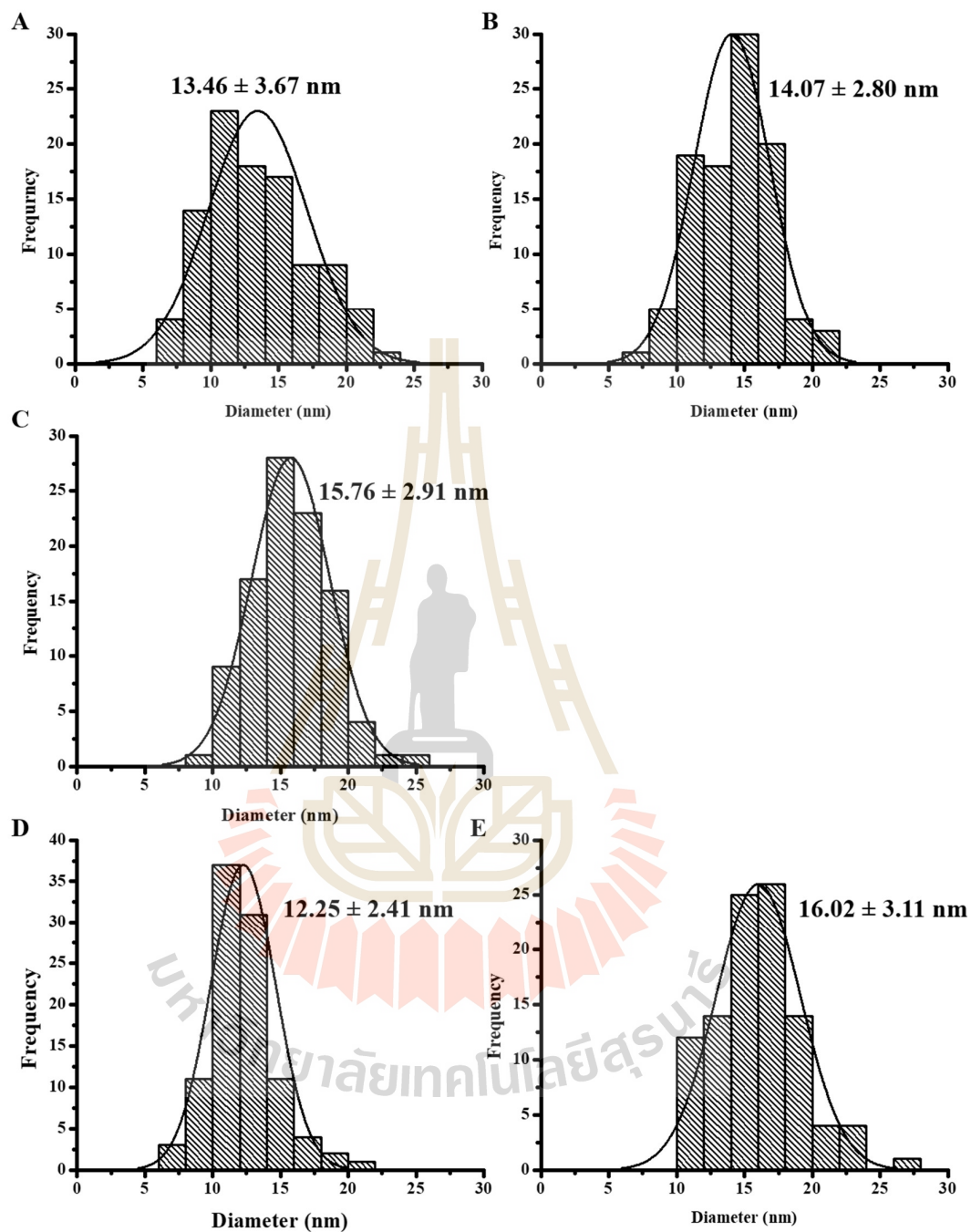
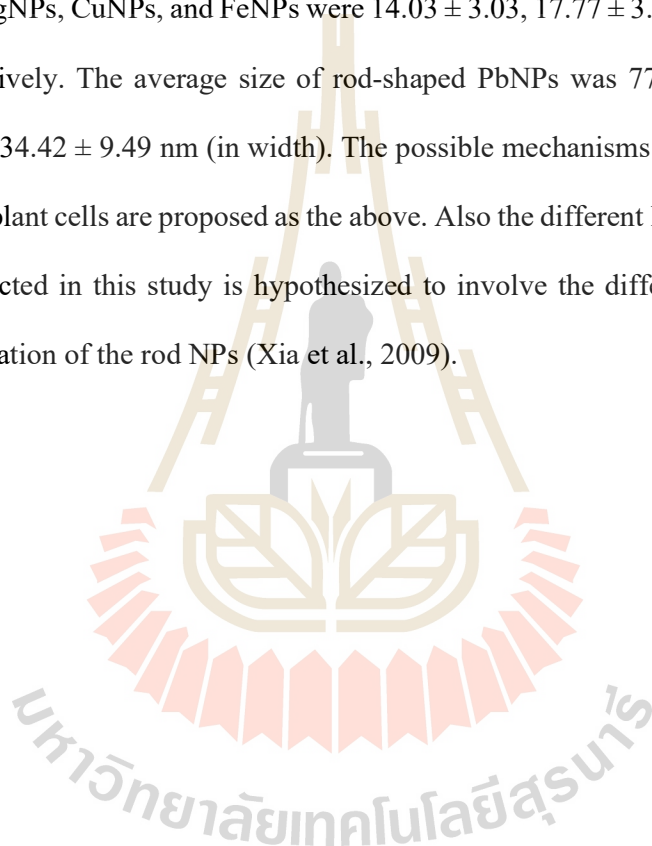


Figure 4.6 Size distribution of metal NPs detected in cortical tissues of *Azolla pinnata*

R.Br. roots; (A) spherical AgNPs, (B) spherical CuNPs, (C) spherical FeNPs, (D) rod PbNPs (width), and (E) rod PbNPs (length).

In vascular tissues, the isolated and agglomerated spherical AgNPs, CuNPs, and FeNPs were dominantly detected near the plasma membrane of xylem cells and some were detected in cytoplasm. Unlike the above NPs, PbNPs had the rod shape and mainly distributed near in phloem and procambium cells (Figure 4.7). The average diameter and size distribution of each NP are shown in Figure 4.8. The average sizes of spherical AgNPs, CuNPs, and FeNPs were 14.03 ± 3.03 , 17.77 ± 3.59 , and 20.09 ± 4.27 nm, respectively. The average size of rod-shaped PbNPs was 77.51 ± 29.59 nm (in length) and 34.42 ± 9.49 nm (in width). The possible mechanisms of the spherical and rod NPs in plant cells are proposed as the above. Also the different length of rod-shaped PbNPs detected in this study is hypothesized to involve the different aging times to allow elongation of the rod NPs (Xia et al., 2009).



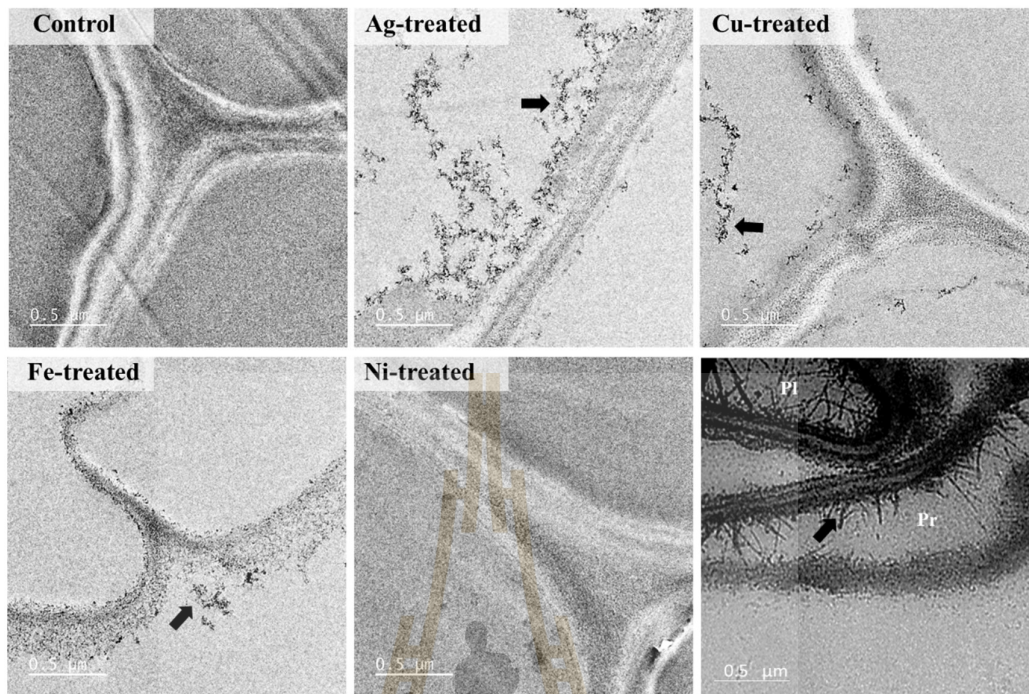


Figure 4.7 TEM images of cross-sections of xylem tissues of *Azolla pinnata* R.Br. roots. Abbreviation list: phloem (pl) and procambium (pr). Arrows indicated metal NPs.

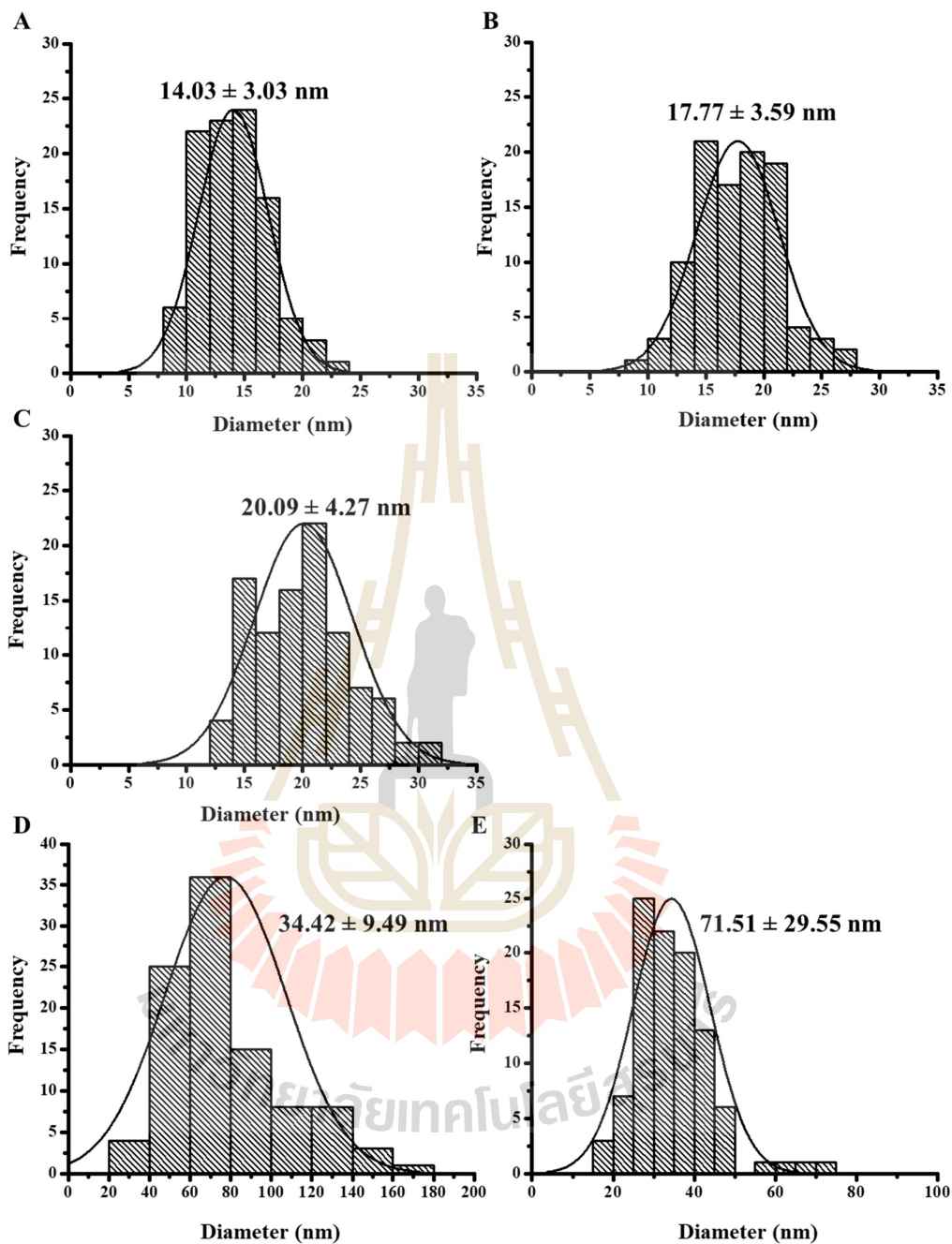


Figure 4.8 Average sizes and size distribution of metal NPs in xylem tissues of *Azolla pinnata* R.Br. roots; (A) spherical AgNPs, (B) spherical CuNPs, (C) spherical FeNPs, (D) rod PbNPs (width), and (E) rod PbNPs (length).

4.4.2 Accumulation of metal nanoparticles in *Salvinia molesta* D.S. Mitch.

Figure 4.9 shows TEM images of ultrathin cross-sections of the control, Ag, Cu, Ni, Fe, and Pb-treated roots of *S. molesta* D.S. Mitch. The isolated and aggregated spherical AgNPs, FeNPs, and PbNPs were clearly detected in the cortical tissue. Interestingly, the formation of rod-shaped PbNPs was not detected in the root cells of *S. molesta* D.S. Mitch. Also, no clear observation of CuNPs was in the treated plant, instead only electron dense area was found. Similar to *A. pinnata* R.Br., no detection of NiNPs was in *S. molesta* D.S. Mitch. The average diameters of AgNPs, FeNPs, and PbNPs were 19.43 ± 7.51 , 20.44 ± 4.16 , and 33.27 ± 11.66 nm, respectively (Figure 4.10). In addition, some isolated and aggregated spherical NPs of Ag, Fe, and Pb can also be found at the plasma membrane of the xylem tissue while founded in form of electron dense of Cu treatment. The diameter and size distribution of each NP in plant cells was showed in Figure 4.12. Average size of Ag, Fe, and Pb were 72.71 ± 25.82 , 95.61 ± 35.55 , and 106.22 ± 45.28 nm, respectively.

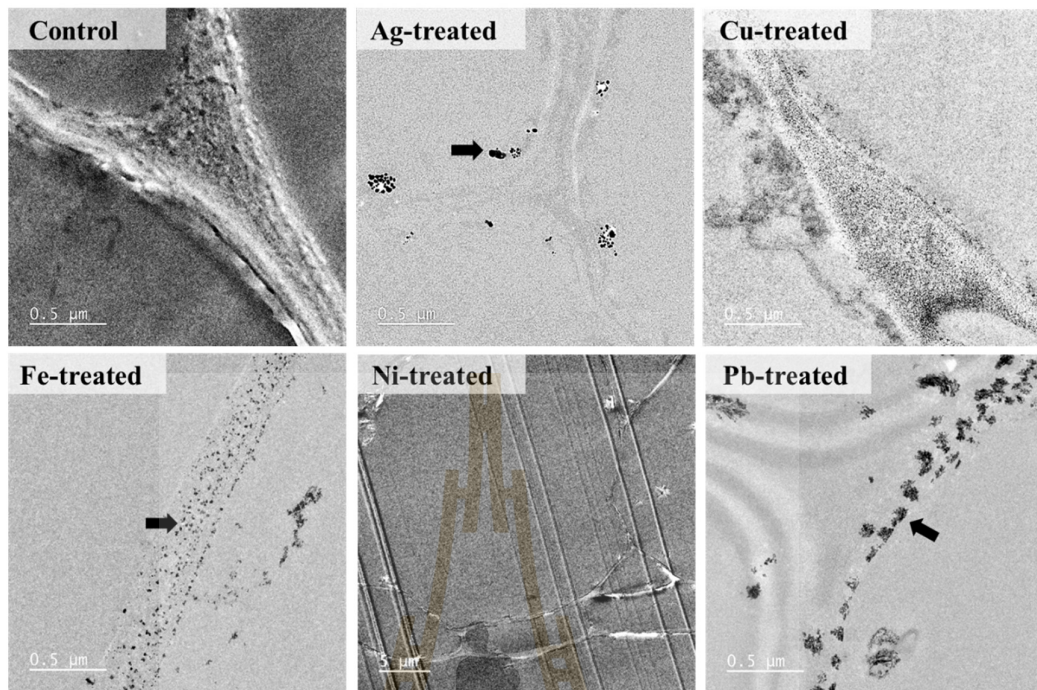


Figure 4.9 TEM images of cross-sections of cortical tissues of *Salvinia molesta* D.S.

Mitch. roots. Arrows indicate metal NPs.



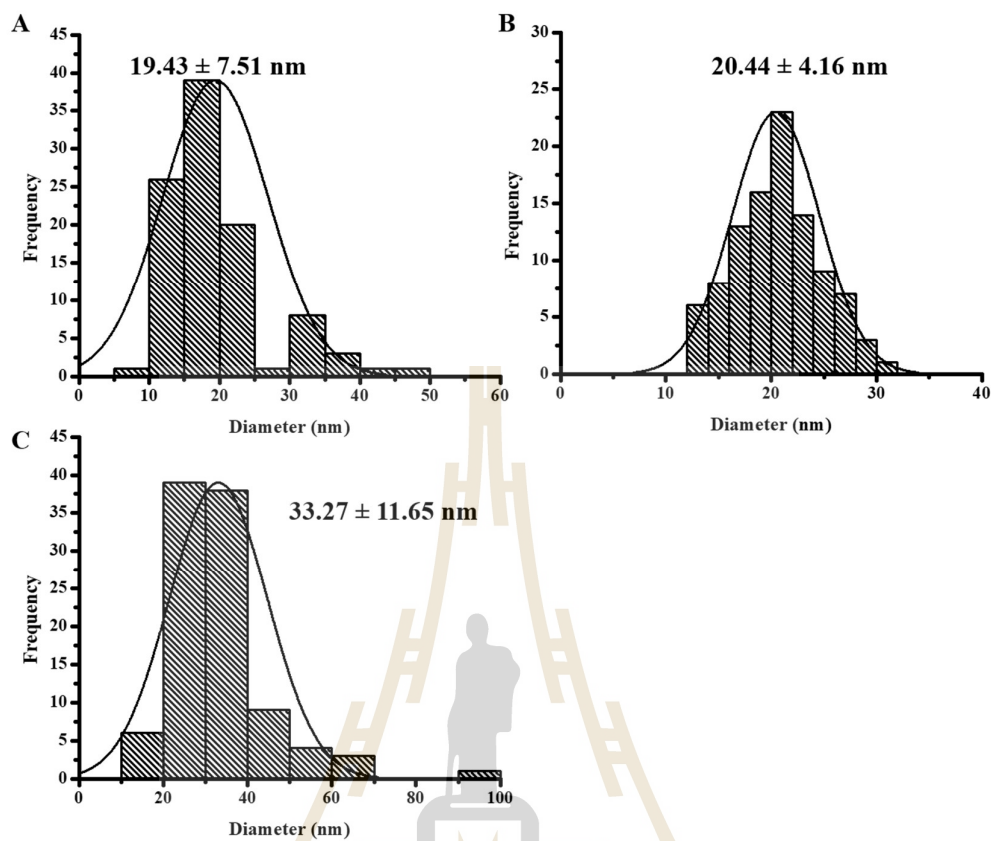


Figure 4.10 Average sizes and size distribution of metal NPs in cortical tissues of *Salvinia molesta* D.S. Mitch. roots; (A) spherical AgNPs, (B) spherical FeNPs, and (C) spherical PbNPs.

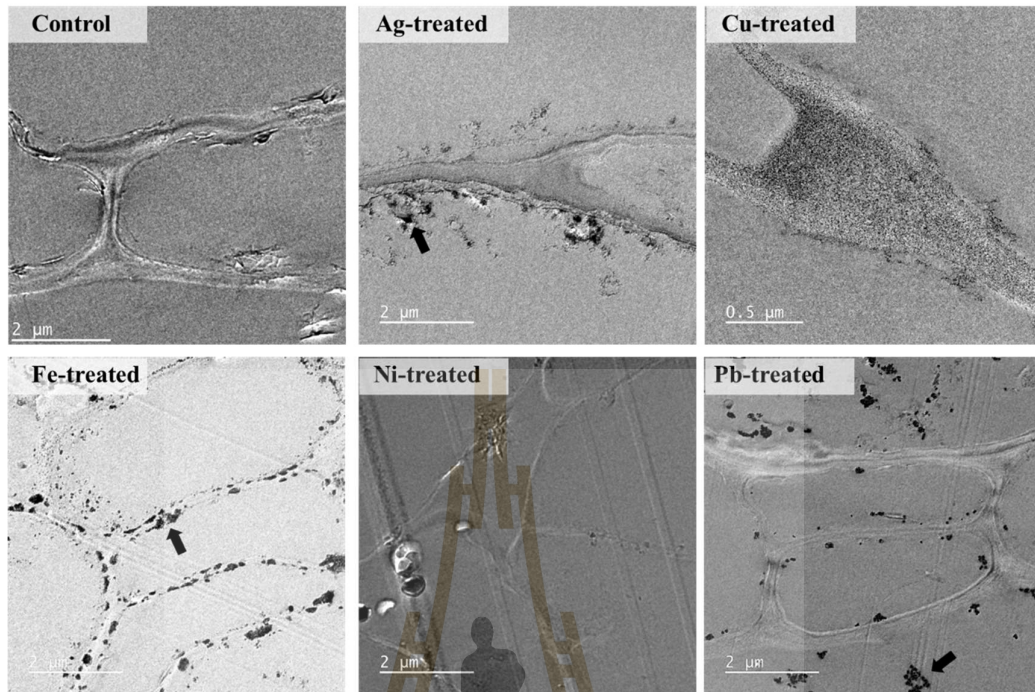


Figure 4.11 TEM images of cross-sections of vascular tissues of *Salvinia molesta* D.S.

Mitch. roots. Arrows indicate metal NPs.



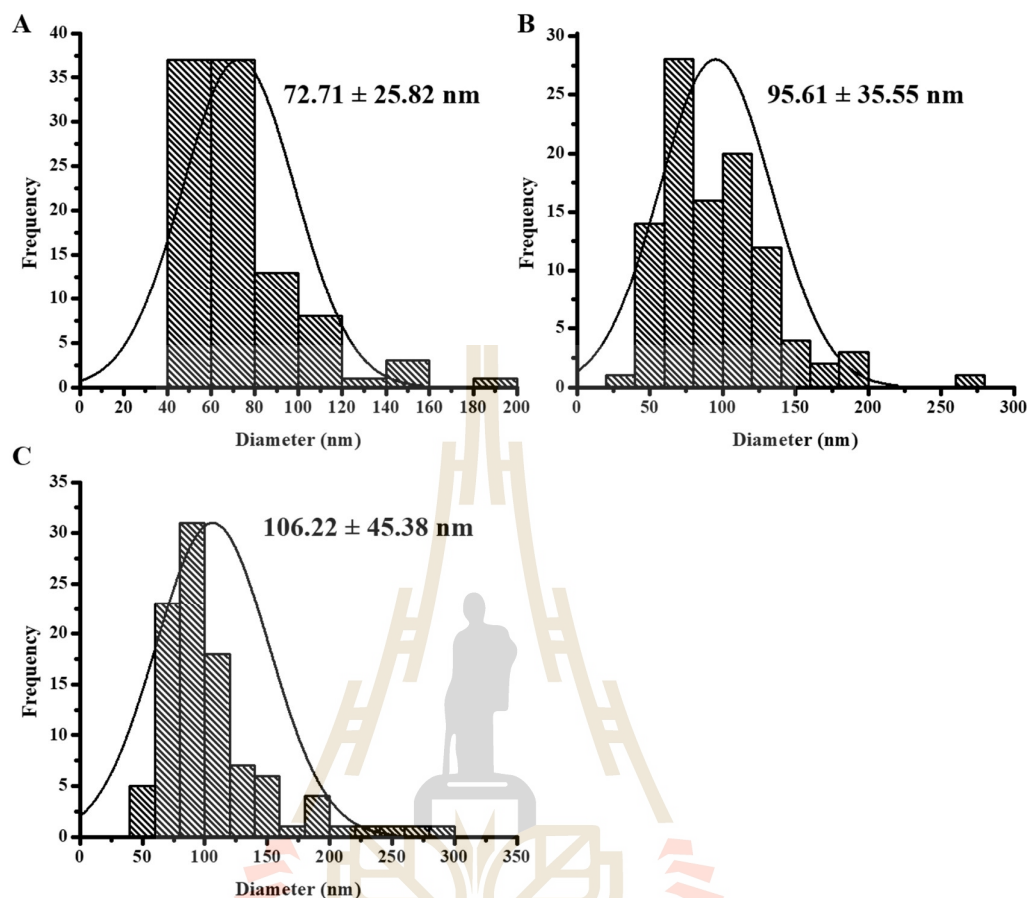


Figure 4.12 Average diameters and size distribution of metal NPs in vascular tissues of *Salvinia molesta* D.S. Mitch. roots; (A) spherical AgNPs, (B) spherical FeNPs, and (C) spherical PbNPs.

4.5 Characterization of Metal Nanoparticles in the Plant Cells

The SAED-TEM and EDX analyses were carried out to determine the identity of the accumulated metal NPs in the root cells.

4.5.1 SAED-TEM analyses

Figure 4.13 shows the representative SAED-TEM images of the accumulated NPs in the *A. pinnata* R.Br. roots exposed to AgNO_3 , $\text{Cu}(\text{NO}_3)_2$, $\text{Fe}(\text{NO}_3)_3$, $\text{Ni}(\text{NO}_3)_2$,

and $\text{Pb}(\text{NO}_3)_2$ solutions. The Ag-treated root cells showed the presence of the concentric diffraction rings at 2.36, 2.04, 1.45, 1.23, 1.02, and 0.83 Å, that corresponded to the hlk planar of (111), (200), (220), (311), (400), and (422) of FCC structure of Ag, based on the database of Joint Committee on Powder Diffraction Standards (JCPDS) number 01-1167 (Balakumaran et al., 2015). In the Cu-treated roots, the concentric diffraction rings were 2.08, 1.81, 1.28, 1.04, and 0.91 Å, corresponding to the hlk planar of (111), (200), (220), (222), and (400) of the FCC structure of Cu (Wang et al., 2014). For the Fe-treated root cells, the concentric diffraction rings of 2.53, 1.17, and 0.88 Å suggested the hlk planar of (311), (211), and (416) of Fe_2O_3 (Shao et al., 2011), while the concentric diffraction rings of 2.97 and 0.97 Å corresponded to the hlk planar of (220) and (324) of Fe_3O_4 (Iyengar et al., 2014). For Pb-treated root cells, the SAED-TEM pattern of the accumulated particles showed the concentric diffraction rings at 2.55, 1.97, 1.64, 1.31, 1.12, and 0.97 Å corresponding to the hlk planar of (200), (200), (003), (220), (312), and (323) of the body-centered tetragonal of PbO as compared with the databases of JCPDS number 01-0797 (McMurdie et al., 1986).

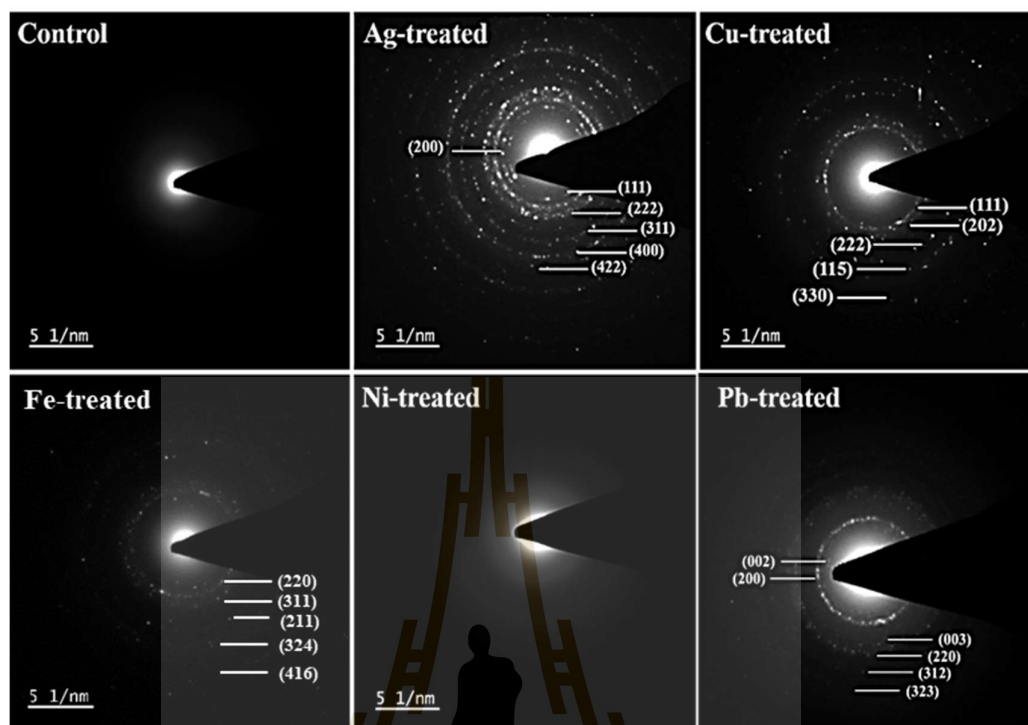


Figure 4.13 SAED-TEM analyses of metal NPs in the Ag-, Cu-, Fe-, Ni-, and Pb-treated roots of *Azolla pinnata* R.Br. as compared with the control root.

The SAED-TEM images of the accumulated NPs in *S. molesta* D.S. Mitch. roots exposed to Ag, Fe, and Pb ions was presented in Figure 4.14. The Ag-treated root cells showed the presence of the concentric diffraction rings at 2.37, 2.05, 1.44, 1.23, and 0.91Å, that correspond to the hlk planar of (111), (200), (220), (311), and (420) of the FCC structure of Ag as based on the database of JCPDS number 01-1167 (Balakumaran et al., 2015). In the Fe-treated roots, the concentric diffraction rings were 2.08, 1.81, 1.28, 1.04, and 0.91Å, corresponding to the hlk planar of (111), (200), (220), (222), and (400) of the FCC structure of Fe (Wang et al., 2014). In the Pb-treated roots, the concentric diffraction rings was 2.81, 1.86, 1.67, and 1.27Å, corresponding to the hlk planar of (111), (201), (003), and (004) of the cubic structure of Pb as compared

with the databases of JCPDS number 01–0976 (McMurdie et al., 1986). However, there was no detection of the concentric diffraction ring in the area of electron dense in Cu-treated roots, suggesting no formation of CuNPs in *S. molesta* D.S. Mitch. root cells. Also, the control root cells showed no detection of the concentric diffraction ring by TEM-SAED analysis.

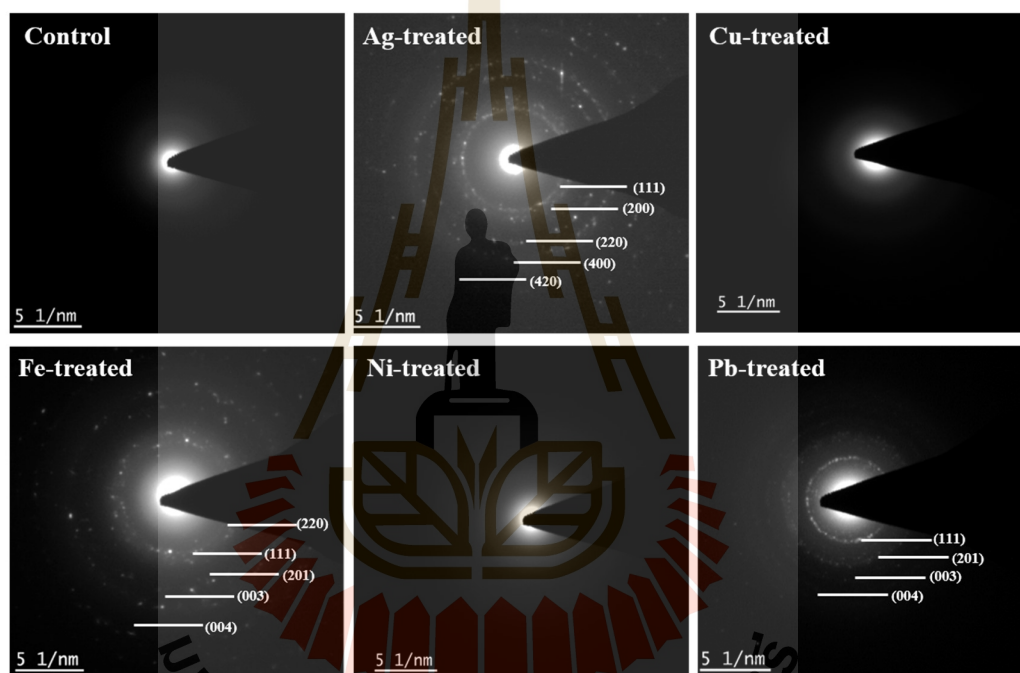


Figure 4.14 SAED-TEM analyses of the Ag-, Cu-, Fe-, and Pb-treated roots of *Salvinia molesta* D.S. Mitch. as compared with the control root.

4.5.2 EDX analyses

Figure 4.15 shows the EDX-TEM analysis of the elemental composition of the Ag-, Cu-, Fe-, and Pb-treated roots of *A. pinnata* R.Br. The result clearly showed that each treated metal was predominantly detected in the plant roots, suggesting that each metal was uptake and accumulate in the plant roots. In Ag-treated roots, Ag

element was as high as 64.21% mass. In Cu-treated root, Cu element was detected as high as 21.38% mass. The content of Fe was 17.63% mass in Fe-treated roots. The detection of Pb was also as high as 51.26% mass in Pb-treated roots. The presences of C and O in all samples could be explained by the organic materials, which were the major components in living organisms. It was also noted that the grids used to hold the sample were the carbon-coated Cu grid, thus the detection of Cu was due to the grid composition (Janthima et al., 2018). For Cu-treated roots, the carbon coated Fe grid was used instead, thus resulting in the detection of Fe in this sample. Interestingly, in Ni-treated roots, no significantly detection of Ni element in the roots. Thus, it was possible that no detection of NiNPs in *A. pinnata* R.Br. was potentially due to the translocation of Ni^{2+} ions to other parts of the plants.

Figure 4.16 shows the EDX-TEM analysis of the elemental composition of the Ag-, Cu-, Fe-, and Pb-treated roots of *S. molesta* D.S. Mitch. Similar results were detected in metal-treated *S. molesta* D.S. Mitch. roots, which Ag (48.26% mass), Cu (20.31% mass), Fe (15.23% mass), and Pb (48.26% mass) elements were detected in Ag-, Cu-, Fe-, and Pb-treated roots, respectively. These elements were not detected if the plant samples were not incubated in these metal solutions. However, only Ni element was not significantly detected in *S. molesta* D.S. Mitch. roots incubated with $\text{Ni}(\text{NO}_3)_2$ solution. It was possible that the content of Ni in the plant root was less than 0.1% mass, which is the detection limit of EDX-TEM in this work. It is important to note that the previous EDXRF analysis showed the detected level of Ni element in the plant roots exposed to $\text{Ni}(\text{NO}_3)_2$ since this technique has the higher detection level in the range of ppm (Strüder, 2000).

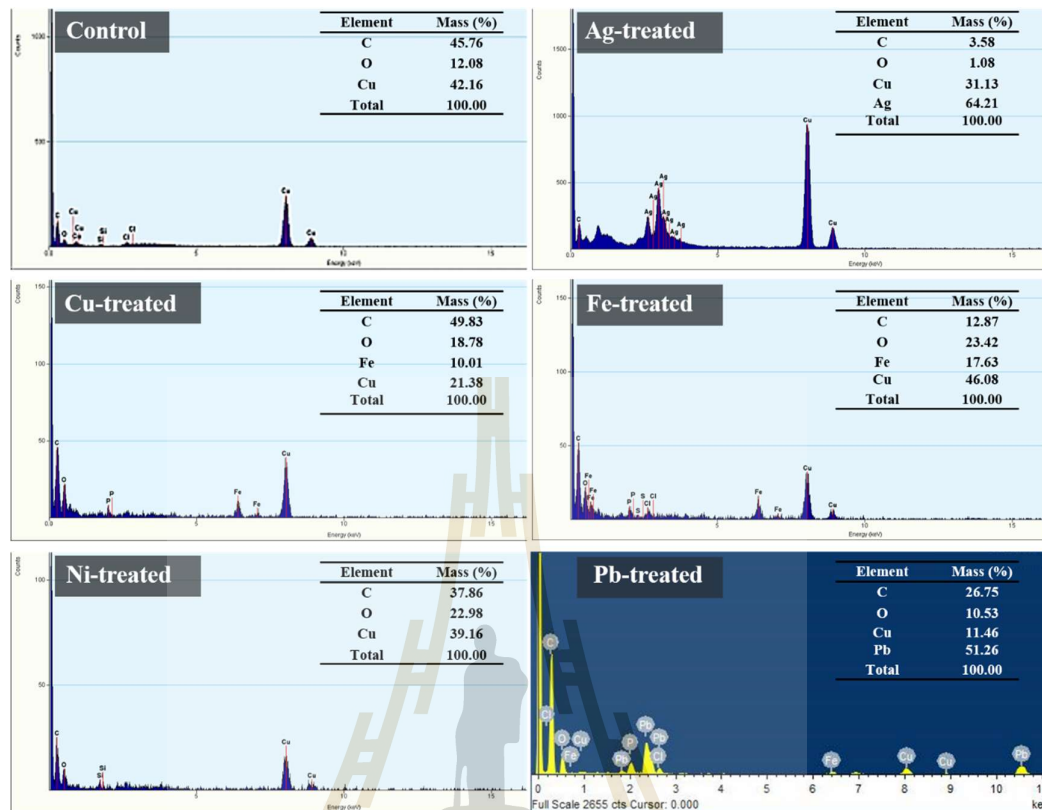


Figure 4.15 EDX-TEM analyses of the Ag-, Cu-, Fe-, Ni-, and Pb-treated roots of *Azolla pinnata* R.Br. as compared with the control root.

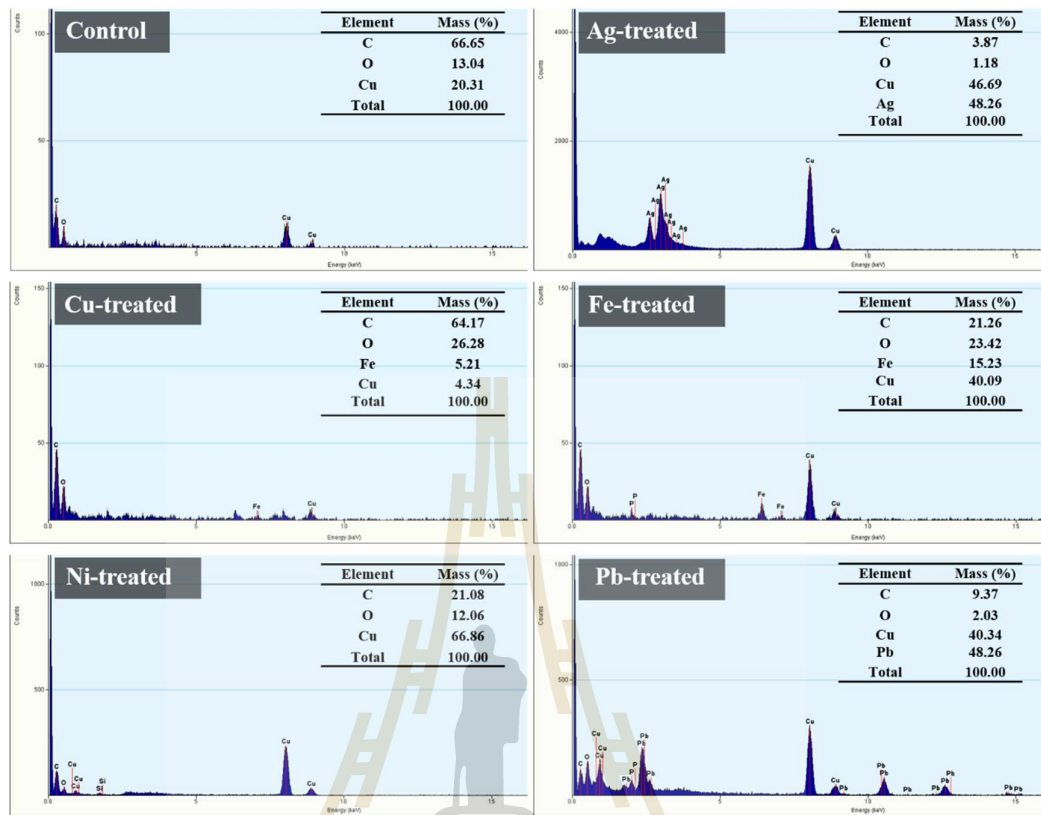


Figure 4.16 EDX-TEM analyses of the Ag-, Cu-, Fe-, Ni-, and Pb-treated roots of *Salvinia molesta* D.S. Mitch. as compared with the control root.

In this section, the abilities of *A. pinnata* R.Br. and *S. molesta* D.S. Mitch., belonging to the same Salviniaceae family, to absorb and transform five metal ions (Ag, Cu, Fe, Ni, and Pb) to metal NPs were reported. The result showed that both plant species could absorb these metal ions. Similarly, both plant species were highly sensitive to Ag^+ ions but more tolerant to Pb^{2+} ions. In addition, the reduction levels of ^{19}K and ^{20}Ca in metal-treated plants could be the metal-stress response in these plant species. ATR-FTIR results also suggested the metal responses in the plant roots via the induction levels of phosphorus-containing biomolecules, lipids, soluble sugars, gene expression and protein synthesis. Interestingly, TEM image suggested that the formation of metal NPs depended on the types of uptake metal ions and plant species. The formation of AgNPs, CuNPs, FeNPs, and PbNPs, except NiNPs, was detected in *A. pinnata* R.Br. roots. Unlike *A. pinnata* R.Br., *S. molesta* D.S. Mitch. root cells could assist the formation of only AgNPs, FeNPs, and PbNPs, but not CuNPs, and NiNPs. In addition, the shape of metal NPs could be different depending on the plant species. In this work, *A. pinnata* R.Br. root cells clearly showed the formation of rod-shaped PbNPs, whereas spherical PbNPs were detected in *S. molesta* D.S. Mitch. The identity of metal NPs was confirmed by SAED-TEM, which AgNPs, CuNPs, FeNPs (Fe_2O_3 and Fe_3O_4), and PbNPs (Pb and PbO) were detected.

The responses of *A. pinnata* R.Br. and *S. molesta* D.S. Mitch. to five metal ions as well as their capabilities to uptake and transform these metal ions into metal NPs are summarized in Table 4.5.

Table 4.5 Data summary of *Azolla pinnata* R.Br. and *Salvinia molesta* D.S. Mitch. in response to five metal ions and their capability to produce metal NPs.

Topics	Aquatic plants	Metal ion treatments				
		Ag ⁺	Cu ²⁺	Fe ³⁺	Ni ²⁺	Pb ²⁺
TC10 (mM)	<i>Azolla pinnata</i> R.Br.	1.5 ± 0.9	13.5 ± 1.7*	31.0 ± 3.5	152.8 ± 1.1*	149.1 ± 2.4*
	<i>Salvinia molesta</i> D.S. Mitch.	1.3 ± 2.1	18.5 ± 1.0	31.3 ± 3.1	94.8 ± 0.4	152.2 ± 4.3
Metal uptake capability (% mass)	<i>Azolla pinnata</i> R.Br.	80.3 ± 1.0*	72.9 ± 9.5*	73.2 ± 0.7*	61.8 ± 3.3	87.8 ± 1.2*
	<i>Salvinia molesta</i> D.S. Mitch.	94.6 ± 1.2	75.5 ± 0.5	71.2 ± 1.3	61.6 ± 0.5	98.1 ± 1.3
Formation of NPs	<i>Azolla pinnata</i> R.Br.	AgNPs	CuNPs	FeNPs	nd	PbNPs
	<i>Salvinia molesta</i> D.S. Mitch.	AgNPs	nd, ED	FeNPs	nd	PbNPs
Shapes of NPs	<i>Azolla pinnata</i> R.Br.	Sphere	Sphere	Sphere	-	Rod
	<i>Salvinia molesta</i> D.S. Mitch.	Sphere	-	Sphere	-	Sphere
Identity of NPs	<i>Azolla pinnata</i> R.Br.	FCC of AgNPs	FCC of CuNPs	Cubic of Fe ₂ O ₃ NPs	-	Body-centered tetragonal of PbONPs
	<i>Salvinia molesta</i> D.S. Mitch.	FCC of AgNPs	-	FCC of FeNPs	-	FCC of PbNPs

Note: $p < 0.05$ (*); nd: NP was not detected; ED: electron dense.

CHAPTER V

RESULTS AND DISCUSSION PART II

Araceae family: The ability of *Lemna minor* L., *Lemna perpusilla* Torr., *Spirodela polyrhiza* (L.) Schleid., and *Wolffia globosa* (Roxb.) Hartog & Plas to absorb and transform metal ions to metal nanoparticles.

In this work, four plant species in a subfamily of Lemnaceae (in a family of Araceae) were used for the study. Lemnaceae is a subfamily of duckweeds, are well-known as the smallest, fastest growing, and simplest flowering monocot plants. Globally, at least 33 species are distributed, which belong to only five genera; *Spirodela*, *Landoltia*, *Lemna*, *Wolffiella*, and *Wolffia*. Based on their evolution, *Spirodela* is the oldest inherited species, while *Wolffia* is the youngest derived one (Wang et al., 2011). Four species from three genera of duckweeds were studied and compared in this work; *L. minor* L., *L. perpusilla* Torr., *S. polyrhiza* (L.) Schleid., and *W. globosa* (Roxb.) Hartog & Plas.

5.1 Toxicity Study

Ag, Cu, Fe, Ni, and Pb are considered as ones of dangerous metal pollutants in ecotoxicology and environment regarding to their toxicity effects on organisms (Rainbow, 2018). The toxic effects of heavy metals on plants depends on several factor

including type and concentration of metal ions, and susceptibility of the plant species (Ackova, 2018). Therefore, in this section, the toxicity effects of AgNO_3 (1, 2, 3, 4, and 5 mM), $\text{Cu}(\text{NO}_3)_2$ (10, 20, 30, 40, and 50 mM), $\text{Fe}(\text{NO}_3)_3$ (10, 20, 30, 40, and 50 mM), $\text{Ni}(\text{NO}_3)_2$ (100, 200, 300, 400, and 500 mM), and $\text{Pb}(\text{NO}_3)_2$ (100, 200, 300, 400, and 500 mM) on four aquatic plant species in the same family were investigated; *L. minor* L., *L. perpusilla* Torr., *S. polyrhiza* (L.) Schleid., and *W. globosa* (Roxb.) Hartog & Plas. The changes of withered and brown leaves of these plant species in response to metal treatments were determined and reported as the percentage of toxicity concentration (%TC).

5.1.1 Toxicity of the tested metal solutions to *Lemna minor* L. and *Lemna perpusilla* Torr.

In this work, since *L. minor* L. and *L. perpusilla* Torr. belong to the same genus, their responses to metal treatments are reported in comparison. The morphological changes of *L. minor* L. and *L. perpusilla* Torr. leaves in response to AgNO_3 , $\text{Cu}(\text{NO}_3)_2$, $\text{Fe}(\text{NO}_3)_2$, $\text{Ni}(\text{NO}_3)_2$, and $\text{Pb}(\text{NO}_3)_2$ at various concentrations are shown in Figure 5.1. Both plant species exhibited the morphological changes in response to all metal solution, which the changes of leaves color were clearly seen. With increasing concentration of metal solutions, colors of leaves were changed from green to yellow, except for AgNO_3 -treatment which the leaves color was changed to dark brown. The appearance of yellow leaves could be resulted from the chlorosis effect of the metals on plants (Arif et al., 2016). Dark blue color of leaves and roots in Ag-treated plants was likely due to the color of accumulated AgNO_3 in the leaf and root tissues. Also, both plant species were sensitive to AgNO_3 , $\text{Cu}(\text{NO}_3)_2$, and $\text{Fe}(\text{NO}_3)_2$ than $\text{Ni}(\text{NO}_3)_2$, and $\text{Pb}(\text{NO}_3)_2$ as determined by the concentrations of metal solution to cause the changes of leaves colors.

TC10 values of AgNO_3 , $\text{Cu(NO}_3)_2$, $\text{Fe(NO}_3)_3$, $\text{Ni(NO}_3)_2$, and $\text{Pb(NO}_3)_2$ in *L. minor* L. and *L. perpusilla* Torr. were also determined as the toxicity of metal solution caused 10% of morphological changes (based on leaves color changes) as shown in Figure 5.2. The TC10 values of AgNO_3 , $\text{Cu(NO}_3)_2$, $\text{Fe(NO}_3)_3$, $\text{Ni(NO}_3)_2$, and $\text{Pb(NO}_3)_2$ in *L. minor* L. were 1.23 ± 0.9 , 10.25 ± 3.40 , 20.13 ± 5.12 , 200.64 ± 6.21 , and 300.96 ± 12.34 mM, respectively. Those in *L. perpusilla* Torr. were 1.04 ± 2.30 , 20.19 ± 2.13 , 30.16 ± 10.32 , 300.17 ± 6.12 , and 400.02 ± 2.39 mM, respectively. These results indicated that both plant species were most sensitive to AgNO_3 , followed by $\text{Cu(NO}_3)_2$, $\text{Fe(NO}_3)_2$, $\text{Ni(NO}_3)_2$, and $\text{Pb(NO}_3)_2$, respectively. It was hypothesized that Ag^+ ions was most toxic to the plants because it interacts to organic molecules (e.g. thiol group of proteins and sulphate group of nucleic acids) and also affect photosynthetic and respiratory processes (Tripathi et al., 2017). As compared with *L. perpusilla* Torr., *L. minor* L. was more sensitive to $\text{Ni(NO}_3)_2$, and $\text{Pb(NO}_3)_2$ as indicated by the lower concentrations of $\text{Ni(NO}_3)_2$ and $\text{Pb(NO}_3)_2$ at TC10 values.

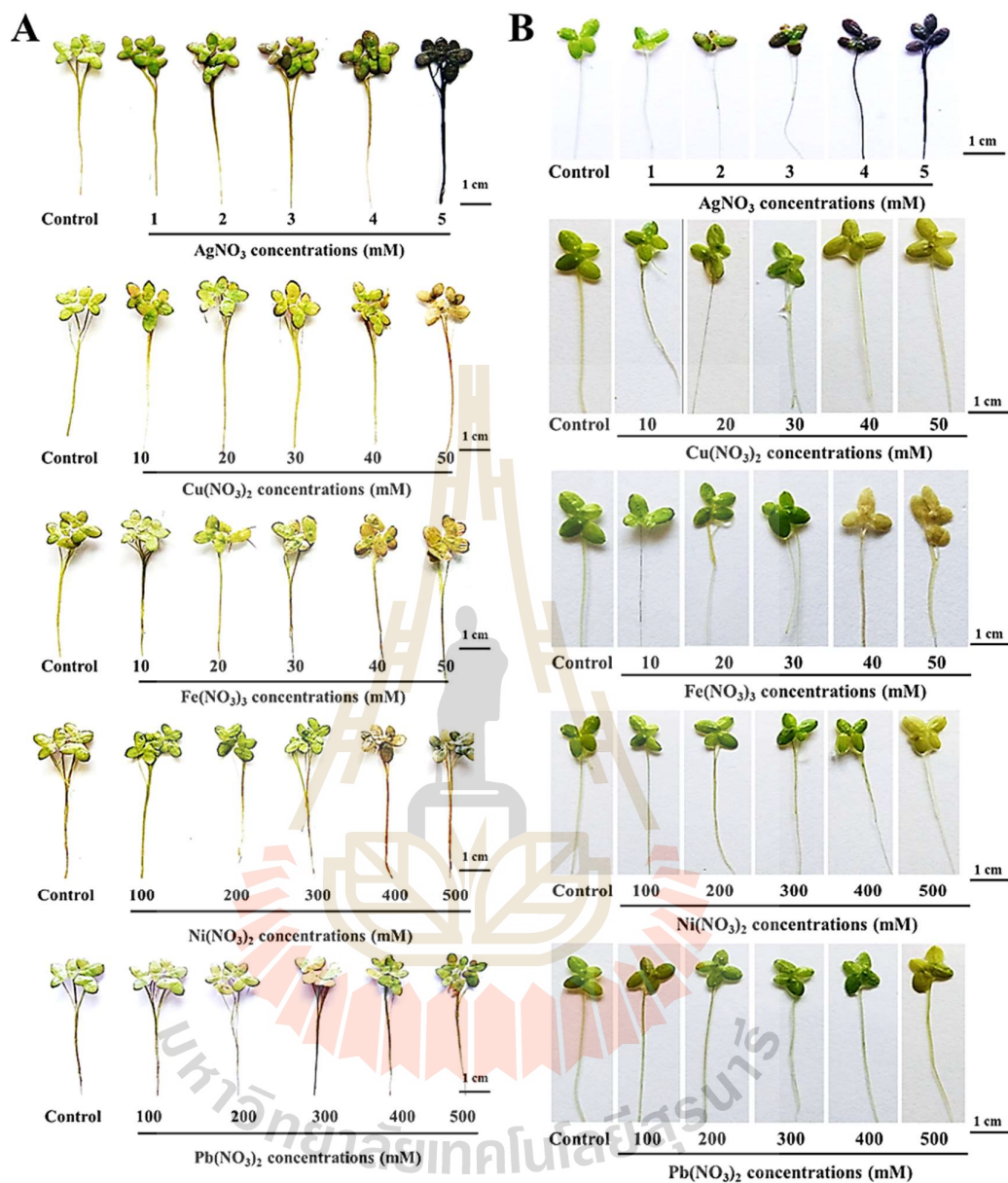


Figure 5.1 The morphological changes of *Lemna minor* L. (A) and *Lemna perpusilla* Torr. (B) in response to AgNO₃, Cu(NO₃)₂, Fe(NO₃)₂, Ni(NO₃)₂, and Pb(NO₃)₂ treatments.

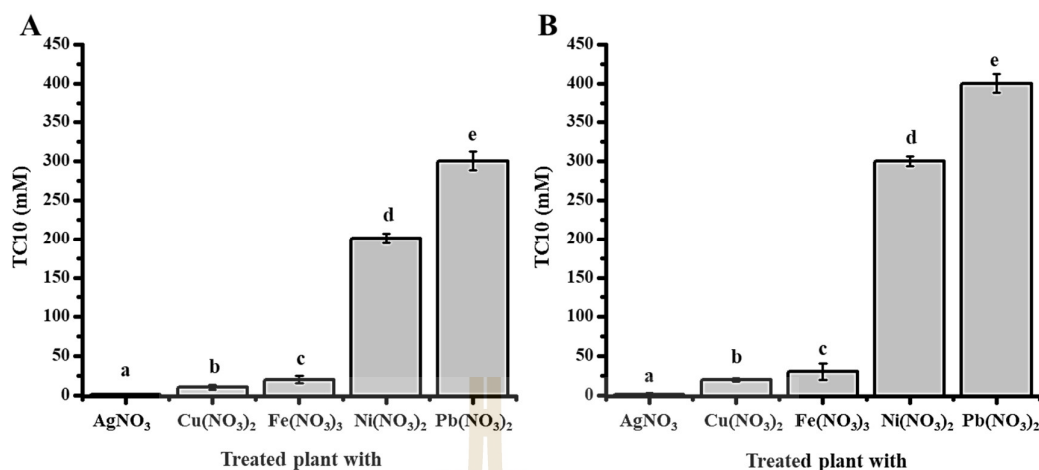


Figure 5.2 TC10 values of AgNO₃, Cu(NO₃)₂, Fe(NO₃)₃, Ni(NO₃)₂, and Pb(NO₃)₂ as determined in (A) *Lemna minor* L. and (B) *Lemna perpusilla* Torr.

5.1.2 Toxicity of the tested metal solutions to *Spirodela polyrhiza* (L.) Schleid

Similar to *L. minor* L. and *L. perpusilla* Torr., *S. polyrhiza* (L.) Schleid. exposed to AgNO₃, Cu(NO₃)₂, Fe(NO₃)₂, Ni(NO₃)₂, and Pb(NO₃)₂ for 12 h resulted in the changes of leaves color from green to pale yellow and dark brown colors according to increasing concentrations of the treated solutions (Figure 5.3A). The TC10 values of AgNO₃, Cu(NO₃)₂, Fe(NO₃)₂, Ni(NO₃)₂, and Pb(NO₃)₂ were at 1.01 ± 0.60 , 20.16 ± 5.13 , 20.89 ± 6.21 , 300.79 ± 12.40 , and 300.69 ± 21.06 mM, respectively (Figure 5.3B). Unlike *L. minor* and *L. perpusilla* Torr., *S. polyrhiza* (L.) Schleid. had the similar TC10 values of Ni(NO₃)₂, and Pb(NO₃)₂ solutions.

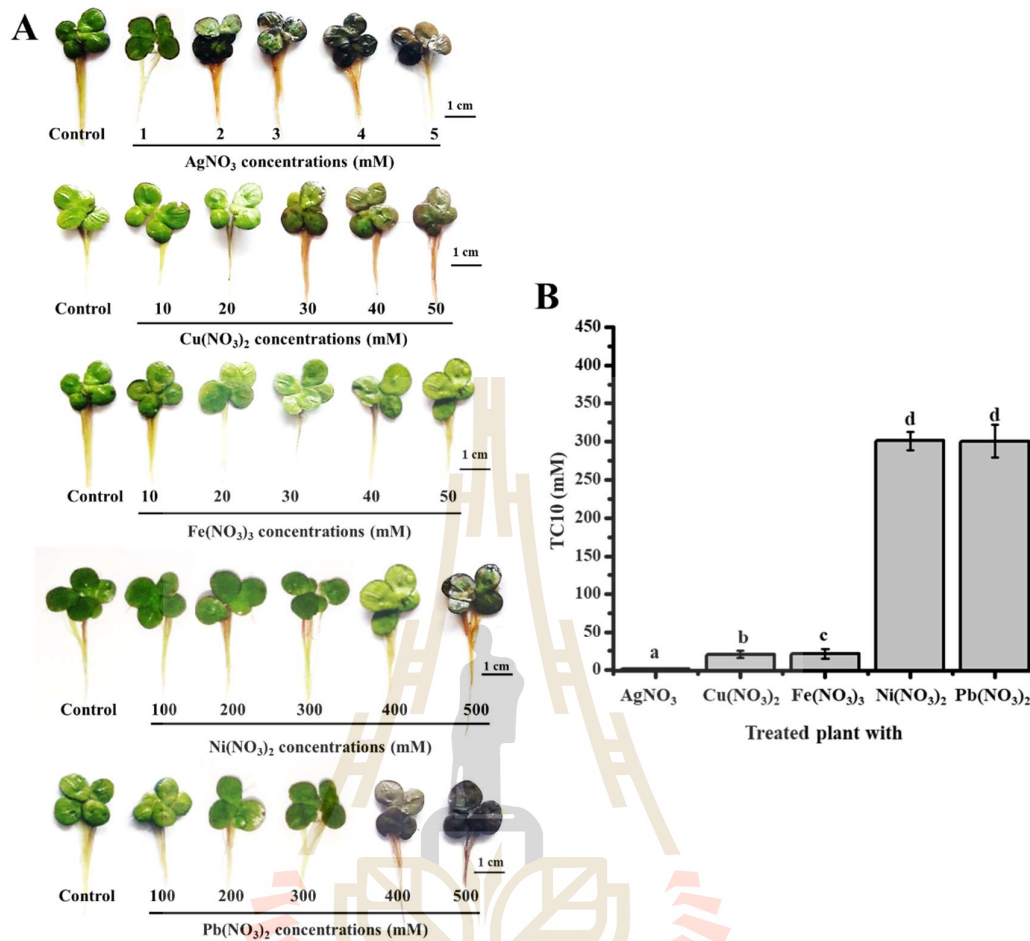


Figure 5.3 The morphological changes (A) and TC10 values (B) of *Spirodela polyrhiza* (L.) Schleid. plant in response to AgNO₃, Cu(NO₃)₂, Fe(NO₃)₂, Ni(NO₃)₂, and Pb(NO₃)₂ treatments.

5.1.3 Toxicity of the tested metal solutions to *Wolffia globosa* (Roxb.) Hartog & Plas

Similar to *Lemna*, *W. globosa* (Roxb.) Hartog & Plas exposed to AgNO₃, Cu(NO₃)₂, Fe(NO₃)₂, Ni(NO₃)₂, and Pb(NO₃)₂ for 12 h resulted in the changes of plant color from green to pale yellow and dark brown colors according to increasing concentrations of the treated solutions (Figure 5.4A). The TC10 values of AgNO₃,

$\text{Cu}(\text{NO}_3)_2$, $\text{Fe}(\text{NO}_3)_2$, $\text{Ni}(\text{NO}_3)_2$, and $\text{Pb}(\text{NO}_3)_2$ were at 0.96 ± 0.16 , 21.06 ± 12.64 , 10.94 ± 12.16 , 300.89 ± 16.14 , and 200.69 ± 21.49 , respectively (Figure 5.4B). Unlike *Lemma* species and *S. polyrhiza* (L.) Schleid., the TC10 values of $\text{Ni}(\text{NO}_3)_2$, and $\text{Pb}(\text{NO}_3)_2$ solutions in *W. globosa* (Roxb.) Hartog & Plas were tolerance to $\text{Ni}(\text{NO}_3)_2$ than $\text{Pb}(\text{NO}_3)_2$.

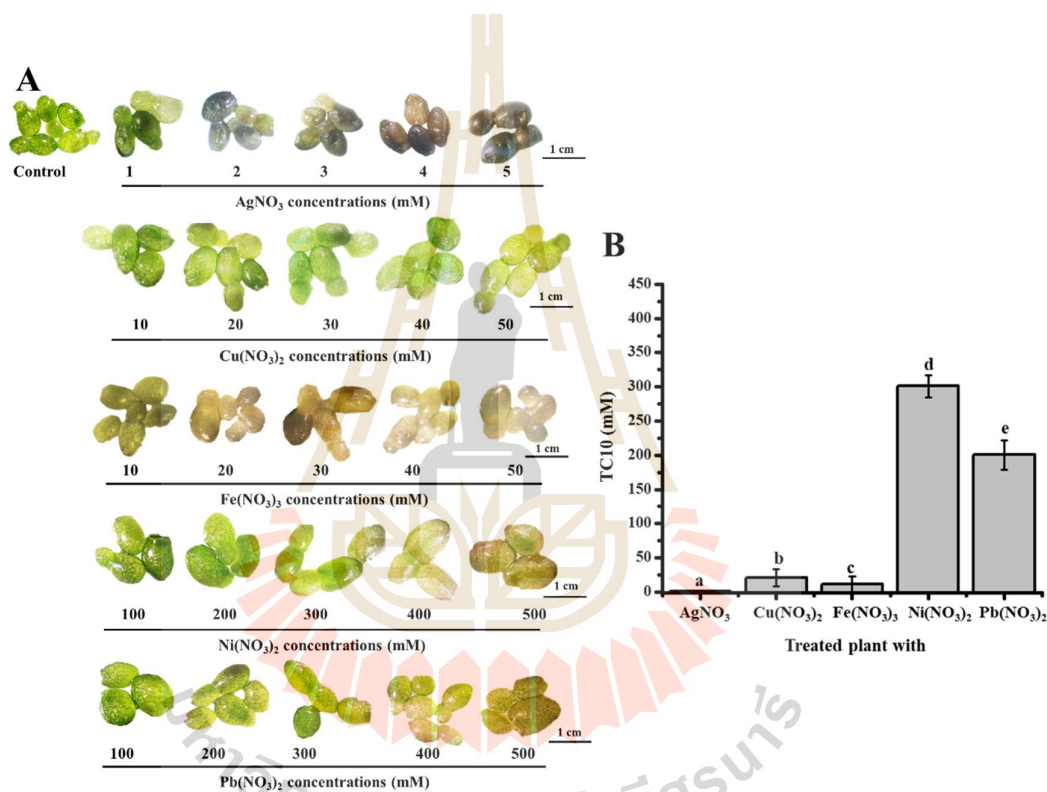


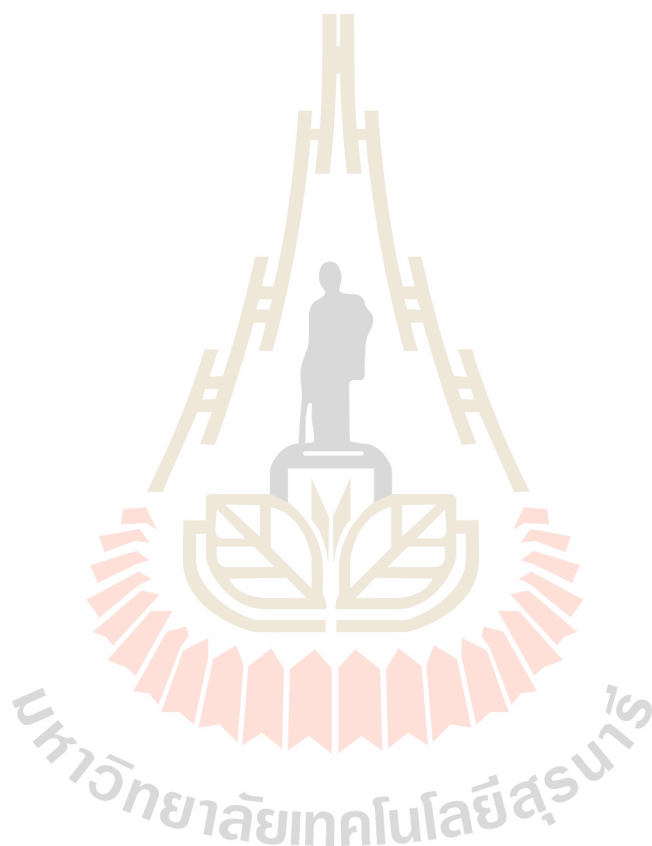
Figure 5.4 The morphological changes (A) and TC10 values (B) of *Wolffia globosa* (Roxb.) Hartog & Plas in response to AgNO_3 , $\text{Cu}(\text{NO}_3)_2$, $\text{Fe}(\text{NO}_3)_2$, $\text{Ni}(\text{NO}_3)_2$, and $\text{Pb}(\text{NO}_3)_2$ treatments.

5.2 The Elemental Mass Profiles

5.2.1 *Lemna minor* L. and *Lemna perpusilla* Torr.

The elemental analysis of mass profiles in *L. minor* L. and *L. perpusilla* Torr. roots exposed to AgNO_3 , $\text{Cu}(\text{NO}_3)_2$, $\text{Fe}(\text{NO}_3)_3$, $\text{Ni}(\text{NO}_3)_2$, and $\text{Pb}(\text{NO}_3)_2$ solutions were determined using EDXRF analysis. The representative EDXRF mapping images of detected metal elements in five metal-treated roots of *L. minor* L. and *L. perpusilla* Torr. were showed in Figure 5.5 and Figure 5.6, respectively. EDXRF mapping images revealed the significantly different levels of seven elements as compared with the control: ^{19}K , ^{20}Ca , ^{26}Fe , ^{28}Ni , ^{29}Cu , ^{47}Ag , and ^{82}Pb . The quantitative evaluation of each element is shown in Table 5.1 and Table 5.2. Among five metal solutions, both plants could uptake Pb^{2+} ions at the highest level, which were 99.41 ± 0.31 and $94.18 \pm 0.01\%$ mass in *L. minor* L. and *L. perpusilla* Torr., respectively. For *L. minor* L., the levels of ^{47}Ag , ^{29}Cu , ^{26}Fe , and ^{28}Ni in the roots treated with AgNO_3 , $\text{Cu}(\text{NO}_3)_2$, $\text{Fe}(\text{NO}_3)_3$, and $\text{Ni}(\text{NO}_3)_2$ solutions were 71.91 ± 0.57 , 67.85 ± 3.31 , 82.70 ± 4.70 , and $44.92 \pm 3.50\%$ mass, respectively. For *L. perpusilla* Torr., those were 84.82 ± 0.80 , 50.90 ± 12.80 , 70.14 ± 3.97 , and $49.80 \pm 9.44\%$ mass, respectively. The highest uptake level of Pb^{2+} ions by both plant species suggested their potential applications for Pb^{2+} -remediation. The uptake and translocation of metal ions in plant roots are via apoplastic and symplastic pathways and several protein transporters (Pourrut et al., 2011; Printz et al., 2016; Thomine et al., 2000). For examples, Cu can be transported via ZIP family and Cu-transporter protein family (Yruela, 2009). Fe transport was via the Fe-nicotianamine transporter and ZIP family (Aydemir and Cousins, 2018). For Ag transport, it was via the high affinity transport protein, metallothionein, metallochaperones, NRAMP family, and ZIP family (Chen et al., 2009). Also, in this work, all metal-treated roots showed

the reduced levels of ^{19}K and ^{20}Ca as compared with the control. It was hypothesized that the tested metal ions might enter the root cells via the same routes of Ca^{2+} and K^{+} cationic ions, including channels and protein transporters, thus competing with their transports and limiting their influx (Ahmad et al., 2016).



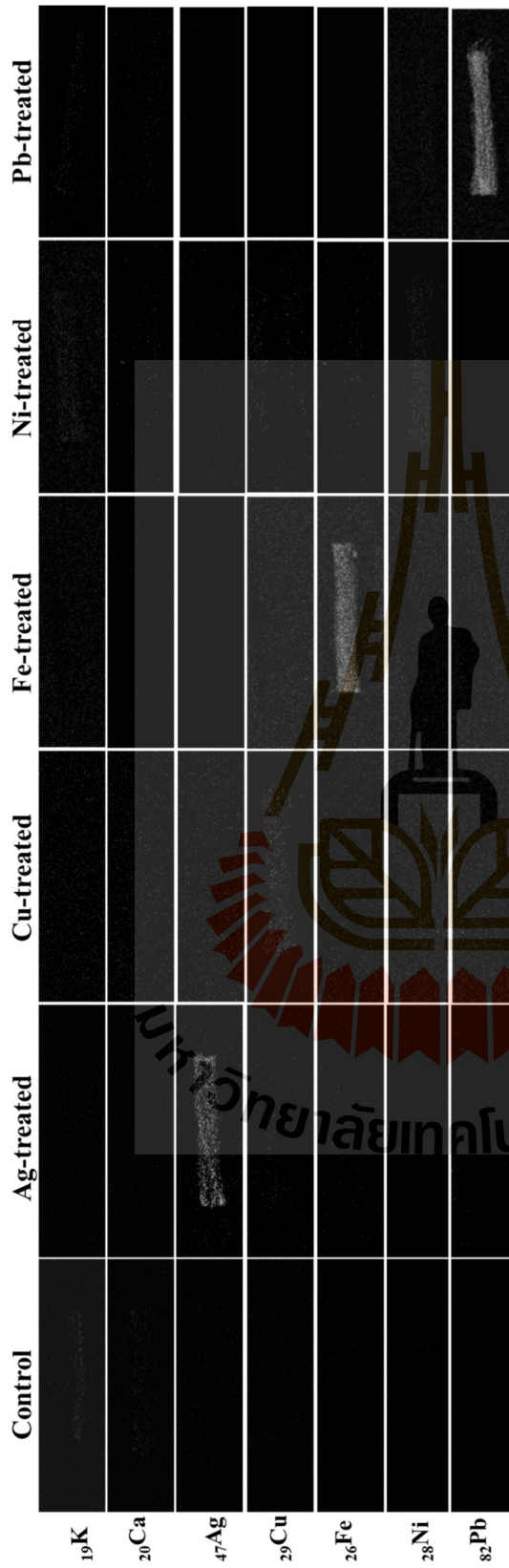


Figure 5.5 EDXRF mapping analysis of *Lemna minor* L. exposed to AgNO_3 , $\text{Cu}(\text{NO}_3)_2$, $\text{Fe}(\text{NO}_3)_2$, $\text{Ni}(\text{NO}_3)_2$, and $\text{Pb}(\text{NO}_3)_2$ solutions.

Table 5.1. Elemental mass quantification of the roots of *Lemna minor* L. in response to metal exposures by EDXRF analysis.

Metal elements	% Element mass in the treated roots with					
	Ctrl	AgNO ₃	Cu(NO ₃) ₂	Fe(NO ₃) ₂	Ni(NO ₃) ₂	Pb(NO ₃) ₂
¹⁹ K	23.46 ± 0.39 ^d	9.97 ± 1.39 ^c	8.84 ± 0.74 ^{b,c}	7.09 ± 1.07 ^b	46.03 ± 2.63 ^e	0.00 ± 0.00 ^a
²⁰ Ca	59.77 ± 1.29 ^e	7.67 ± 1.44 ^c	9.05 ± 2.04 ^{c,d}	10.55 ± 2.64 ^d	5.69 ± 6.78 ^b	0.00 ± 0.00 ^a
²⁹ Cu	1.55 ± 2.05 ^b	1.98 ± 0.80 ^b	67.85 ± 3.3^d	3.64 ± 2.49 ^c	2.49 ± 1.98 ^{b,c}	0.02 ± 0.02 ^a
¹⁶ Fe	3.54 ± 0.45 ^c	2.56 ± 0.53 ^{b,c}	5.31 ± 1.86 ^d	82.70 ± 4.70^e	1.29 ± 0.87 ^b	0.43 ± 0.26 ^a
⁸² Pb	0.84 ± 0.87 ^a	0.37 ± 0.45 ^a	0.61 ± 0.93 ^a	0.68 ± 0.45 ^a	0.20 ± 0.22 ^a	99.41 ± 0.31^b
²⁸ Ni	0.61 ± 0.34 ^a	1.29 ± 0.86 ^{a,b}	2.26 ± 0.81 ^b	0.36 ± 0.13 ^a	44.92 ± 3.50^c	0.12 ± 0.03 ^a
⁴⁷ Ag	0.13 ± 0.18 ^a	71.91 ± 0.57^c	0.12 ± 0.21 ^a	0.07 ± 0.12 ^a	1.04 ± 0.45 ^{a,b}	0.01 ± 0.00 ^a

p < 0.05 (compared with the control), significant difference of each metal was compared among different metal-treated roots.

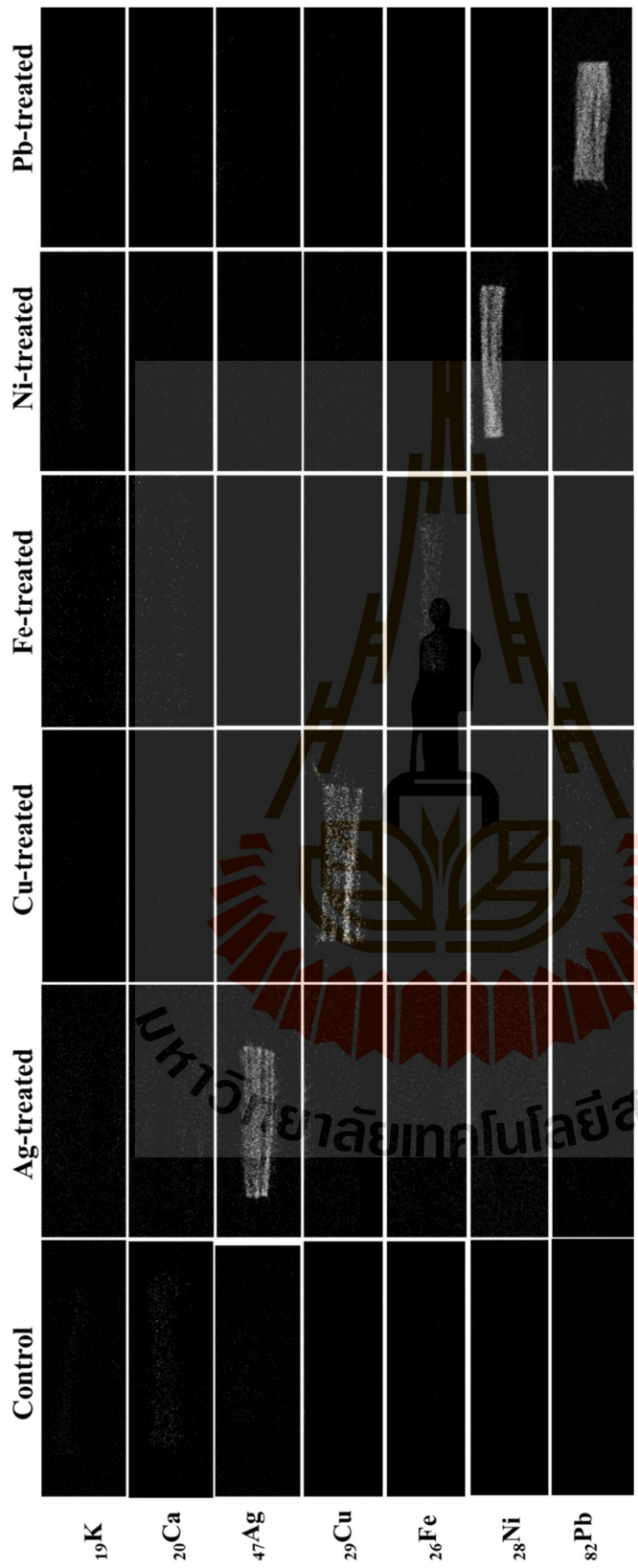


Figure 5.6 EDXRF mapping analysis of *Lemna perpusilla* Torr. exposed to AgNO_3 , $\text{Cu}(\text{NO}_3)_2$, $\text{Fe}(\text{NO}_3)_2$, $\text{Ni}(\text{NO}_3)_2$, and $\text{Pb}(\text{NO}_3)_2$ solutions.

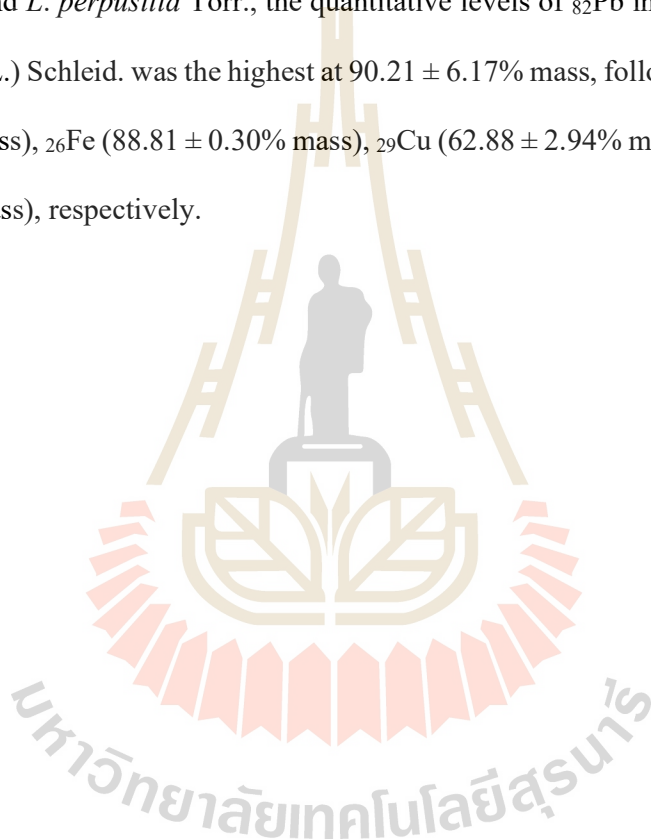
Table 5.2. Elemental mass quantification of the roots of *Lemna perpusilla* Torr. in response to metal exposures by EDXRF analysis.

Metal elements	% Element mass in the treated roots with					
	Ctrl	AgNO ₃	Cu(NO ₃) ₂	Fe(NO ₃) ₂	Ni(NO ₃) ₂	Pb(NO ₃) ₂
¹⁹ K	51.84 ± 9.54 ^e	0.00 ± 0.00 ^a	14.63 ± 2.53 ^b	9.84 ± 0.76 ^c	26.10 ± 3.39 ^d	0.23 ± 0.39 ^a
²⁰ Ca	25.08 ± 8.73 ^d	8.29 ± 1.02 ^{b,c}	16.16 ± 10.39 ^c	11.81 ± 2.88 ^{b,c}	14.30 ± 10.15 ^c	3.55 ± 1.27 ^a
²⁹ Cu	1.89 ± 1.66 ^{a,b}	2.07 ± 0.64 ^b	50.90 ± 12.80^d	4.48 ± 1.86 ^c	2.34 ± 0.60 ^b	0.41 ± 0.54 ^a
¹⁶ Fe	6.76 ± 2.13 ^c	2.98 ± 0.55 ^b	4.94 ± 0.85 ^a	70.14 ± 3.97^d	4.84 ± 1.09 ^c	0.56 ± 0.77 ^a
⁸² Pb	0.56 ± 0.39 ^a	0.00 ± 0.00 ^a	0.02 ± 0.02 ^a	0.09 ± 0.13 ^a	0.00 ± 0.00 ^a	94.18 ± 0.01^b
²⁸ Ni	1.78 ± 1.16 ^{a,b}	2.16 ± 0.52 ^b	1.12 ± 0.09 ^a	0.75 ± 0.29 ^a	49.80 ± 9.44^c	0.01 ± 0.69 ^a
⁴⁷ Ag	0.25 ± 0.41 ^a	84.82 ± 0.80^b	0.06 ± 0.09 ^a	0.07 ± 0.07 ^a	0.37 ± 0.48 ^a	1.26 ± 1.76 ^a

p < 0.05 (compared with the control), significant difference of each metal was compared among different metal-treated root

5.2.2 *Spirodela polyrhiza* (L.) Schleid.

EDXRF analyses of *S. polyrhiza* (L.) Schleid. roots in response to AgNO_3 , $\text{Cu}(\text{NO}_3)_2$, $\text{Fe}(\text{NO}_3)_2$, $\text{Ni}(\text{NO}_3)_2$, and $\text{Pb}(\text{NO}_3)_2$ are shown in Figure 5.7. The elemental distribution mapping images revealed the significantly different profiles of 7 elements (^{19}K , ^{20}Ca , ^{26}Fe , ^{28}Ni , ^{29}Cu , ^{47}Ag , and ^{82}Pb) as compared with the control. Similar to *L. minor* L., and *L. perpusilla* Torr., the quantitative levels of ^{82}Pb in the Pb-treated of *S. polyrhiza* (L.) Schleid. was the highest at $90.21 \pm 6.17\%$ mass, followed by ^{47}Ag ($89.30 \pm 4.11\%$ mass), ^{26}Fe ($88.81 \pm 0.30\%$ mass), ^{29}Cu ($62.88 \pm 2.94\%$ mass), and ^{28}Ni ($40.85 \pm 5.80\%$ mass), respectively.



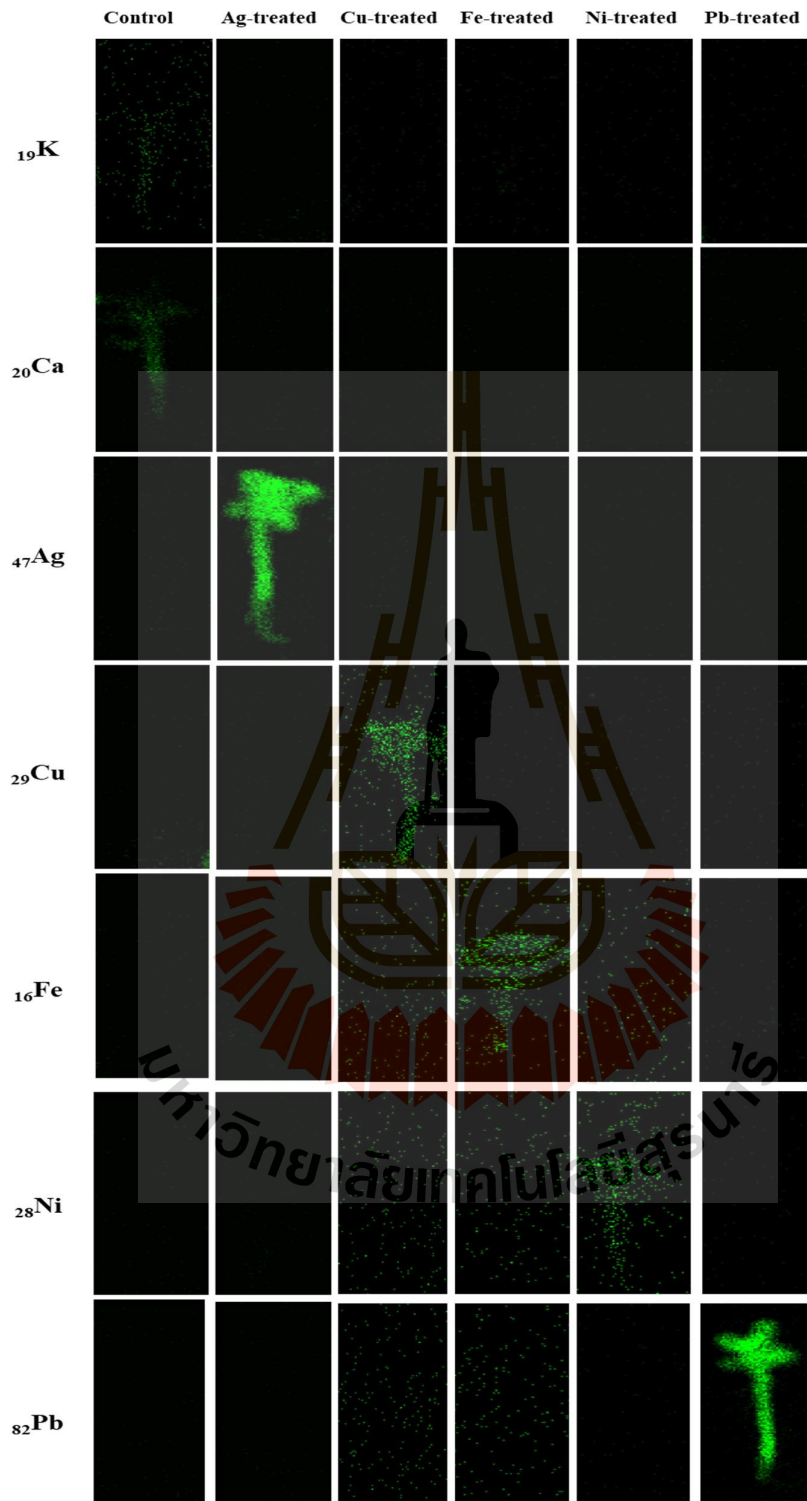


Figure 5.7 EDXRF mapping analysis of *Spirodela polyrhiza* (L.) Schleid. exposed to AgNO_3 , $\text{Cu}(\text{NO}_3)_2$, $\text{Fe}(\text{NO}_3)_2$, $\text{Ni}(\text{NO}_3)_2$, and $\text{Pb}(\text{NO}_3)_2$ solutions.

Table 5.3. Elemental mass quantification of the roots of *Spirodela polyrhiza* (L.) Schleid. in response to metal exposures by EDXRF analysis.

Metal elements	% Element mass in the treated roots with					
	Ctrl	AgNO ₃	Cu(NO ₃) ₂	Fe(NO ₃) ₂	Ni(NO ₃) ₂	Pb(NO ₃) ₂
¹⁹ K	60.37 ± 15.93 ^e	4.48 ± 3.21 ^b	21.23 ± 8.44 ^c	0.00 ± 0.01 ^a	34.41 ± 3.86 ^d	0.06 ± 0.85 ^a
²⁰ Ca	32.29 ± 17.51 ^e	3.96 ± 1.78 ^b	18.18 ± 10.74 ^d	1.19 ± 0.71 ^{a,b}	12.12 ± 0.41 ^c	0.45 ± 2.04 ^a
²⁹ Cu	0.02 ± 0.01 ^a	1.63 ± 1.4 ^{a,b}	62.88 ± 2.94^d	1.99 ± 0.77 ^b	4.43 ± 1.98 ^c	0.79 ± 0.42 ^a
¹⁶ Fe	5.05 ± 1.41 ^c	0.16 ± 0.03 ^a	3.86 ± 1.71 ^b	88.81 ± 0.30^e	7.90 ± 1.14 ^d	4.34 ± 2.23 ^{b,c}
⁸² Pb	0.49 ± 0.15 ^a	0.67 ± 0.50 ^a	0.01 ± 0.04 ^a	0.12 ± 0.11 ^a	0.58 ± 1.00 ^a	90.21 ± 6.17^b
²⁸ Ni	1.79 ± 0.40 ^{a,b}	0.02 ± 0.0 ^a	2.77 ± 0.46 ^{a,b}	3.06 ± 2.05 ^b	40.85 ± 5.80^b	1.31 ± 0.48 ^a
⁴⁷ Ag	0.02 ± 0.11 ^a	89.30 ± 4.1^c	0.33 ± 0.02 ^a	1.03 ± 0.91 ^b	0.47 ± 0.40 ^a	0.16 ± 0.21 ^a

p < 0.05 (compared with the control), significant difference of each metal was compared among different metal-treated root

5.2.3 *Wolffia globosa* (Roxb.) Hartog & Plas

The elemental mapping images and quantitative element mass of *W. globosa* (Roxb.) Hartog & Plas in response to AgNO_3 , $\text{Cu}(\text{NO}_3)_2$, $\text{Fe}(\text{NO}_3)_2$, $\text{Ni}(\text{NO}_3)_2$, and $\text{Pb}(\text{NO}_3)_2$ as determined by EDXRF are shown in Figure 5.8 and Table 5.4, respectively. As expected, the high level of each uptake metal was shown in the plant, which the level of ^{82}Pb was the highest ($92.40 \pm 4.31\%$ mass), followed by followed by ^{26}Fe ($83.65 \pm 3.81\%$ mass), ^{47}Ag ($76.71 \pm 3.71\%$ mass), ^{29}Cu ($69.22 \pm 6.49\%$ mass), and ^{28}Ni ($64.17 \pm 1.08\%$ mass), respectively. Similar to the previous data, the significant reduction of ^{19}K and ^{20}Ca was detected in *W. globosa* (Roxb.) Hartog & Plas, which was hypothesized as one of the metal-stress responses in aquatic plants.



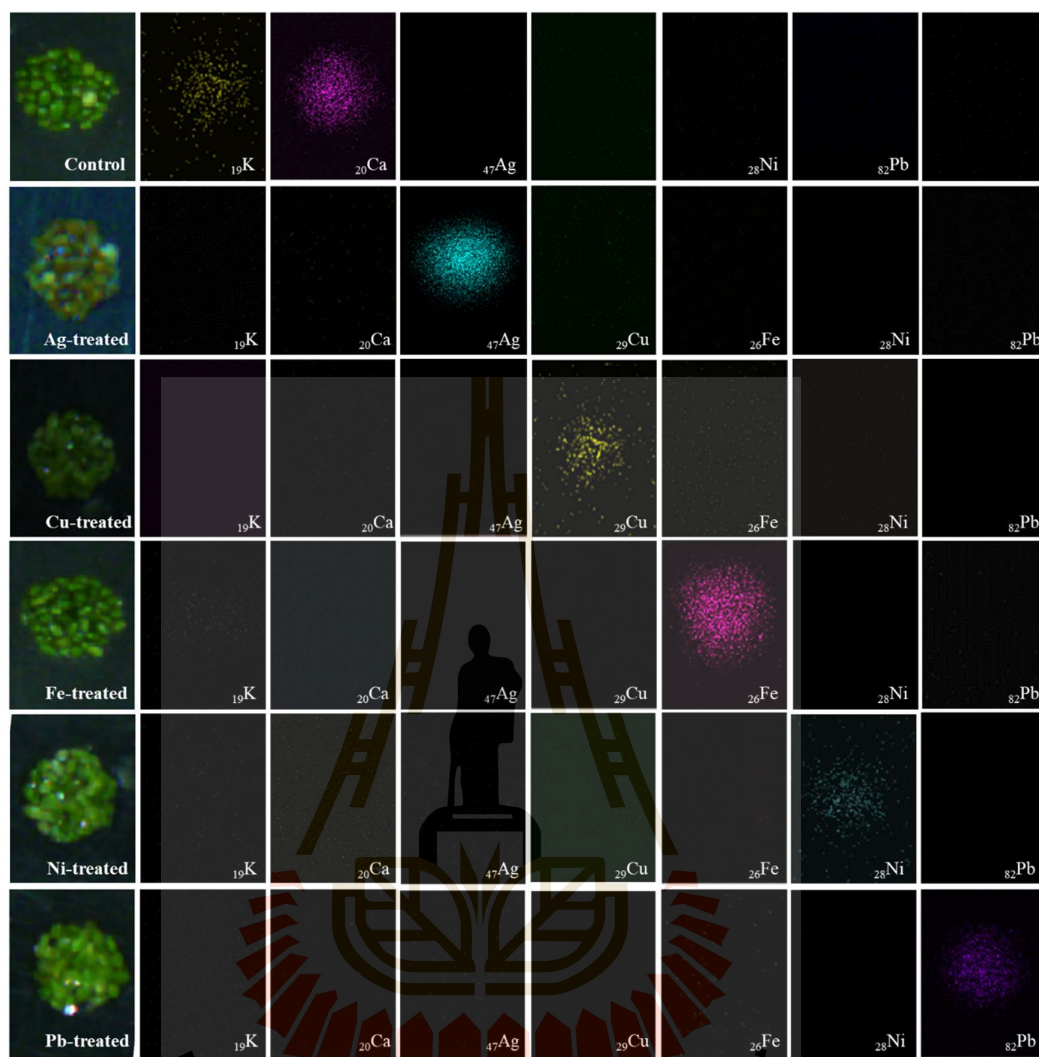


Figure 5.8 EDXRF mapping analysis of *Wolffia globosa* (Roxb.) Hartog & Plas exposed to AgNO_3 , $\text{Cu}(\text{NO}_3)_2$, $\text{Fe}(\text{NO}_3)_2$, $\text{Ni}(\text{NO}_3)_2$, and $\text{Pb}(\text{NO}_3)_2$ solutions.

Table 5.4. Elemental mass quantification of the roots of *Wolffia globosa* (Roxb.) Hartog & Plas in response to metal exposures by EDXRF analysis.

Metal elements	% Element mass in the treated roots with					
	Ctrl	AgNO ₃	Cu(NO ₃) ₂	Fe(NO ₃) ₂	Ni(NO ₃) ₂	Pb(NO ₃) ₂
¹⁹ K	41.39 ± 4.45 ^c	5.92 ± 0.80 ^{b,c}	6.03 ± 2.36 ^c	3.55 ± 1.26 ^b	12.98 ± 0.78 ^d	1.31 ± 0.45 ^a
²⁰ Ca	56.82 ± 4.71 ^d	9.55 ± 0.24 ^b	12.04 ± 1.80 ^c	9.41 ± 0.55 ^b	11.55 ± 1.63 ^c	2.39 ± 1.46 ^a
²⁹ Cu	0.22 ± 0.16 ^a	0.51 ± 0.64 ^a	69.22 ± 6.49^b	0.22 ± 0.22 ^a	0.18 ± 0.31 ^a	0.42 ± 0.72 ^a
¹⁶ Fe	1.11 ± 0.65 ^{a,b}	2.42 ± 0.57 ^{a,b}	2.97 ± 1.16 ^b	83.65 ± 3.81^c	0.91 ± 1.09 ^a	0.46 ± 0.43 ^a
⁸² Pb	0.35 ± 0.31 ^a	0.18 ± 0.06 ^a	1.66 ± 1.85 ^a	0.51 ± 0.53 ^a	0.02 ± 0.03 ^a	92.40 ± 4.31^b
²⁸ Ni	0.15 ± 0.19 ^a	0.31 ± 0.05 ^a	0.35 ± 0.54 ^a	0.13 ± 0.10 ^a	64.17 ± 1.08^b	0.67 ± 0.91 ^a
⁴⁷ Ag	0.02 ± 0.04 ^a	76.71 ± 3.71^b	0.32 ± 0.27 ^a	0.06 ± 0.10 ^a	0.180 ± 0.29 ^a	0.28 ± 0.49 ^a

p < 0.05 (compared with the control), significant difference of each metal was compared among different metal-treated root.

5.3 ATR-FTIR Profiles in Response to Metal Treatments

5.3.1 *Lemna minor* L. and *Lemna perpusilla* Torr.

ATR-FTIR analysis was used to investigate the changes of cellular biomolecules of *L. minor* L. and *L. perpusilla* Torr. roots exposed to AgNO_3 , $\text{Cu}(\text{NO}_3)_2$, $\text{Fe}(\text{NO}_3)_2$, $\text{Ni}(\text{NO}_3)_2$, and $\text{Pb}(\text{NO}_3)_2$ solutions as determined by the changed vibrations of functional groups of the biomolecules in the mid-infrared region of $4000 - 400 \text{ cm}^{-1}$. The ATR-FTIR spectra of these plants in response to metal treatments as compared with the control are shown in Figure 5.9 and 5.10, respectively. The ATR-FTIR profiles revealed the changes of spectral peaks, which were the reduced intensity, increased intensity, emergence, and absence of spectral peaks.

The spectral peaks with intensity reduction as compared with the control were detected in a range of $3600 - 3300 \text{ cm}^{-1}$, $1800 - 1630 \text{ cm}^{-1}$, and $1000 - 800 \text{ cm}^{-1}$ in *L. minor* L., while single spectral peak with intensity reduction ($1800 - 1630 \text{ cm}^{-1}$) was detected in *L. perpusilla* Torr. The spectral peak in a range $3600 - 3300 \text{ cm}^{-1}$ was assigned to O–H stretching vibration of phenolic compounds and carbohydrates such as cellulose, hemicellulose, pectin, and lignin. It is possibly that the intensity reduction of this spectral peak is the result of the interaction between the divalent cation of metal ions to O–H moieties of these phenolic compounds and carbohydrates, especially some flavonoids that play an important role to reduce the metal toxicity in plants (Mira et al., 2002). The spectral peak in a range of $1800 - 1630 \text{ cm}^{-1}$ was assigned to C–ONHR stretching vibrations of amide I of proteins (Yang et al., 2014). The spectral peak in a range of $1000 - 800 \text{ cm}^{-1}$ was attributed to the N–H group of proteins (Suresh et al., 2016a). Thus, the ATR-FTIR results suggested the reduction of protein levels in metal-treated plants, which were possibly due to the effect of metal ions to interfere a protein

folding, leading to aggregation and denaturation of proteins under the metal-stress condition in plant cells (Xia et al., 2019).

The increased spectral peaks was detected in a range 1395 – 1370 cm^{-1} in both plants, which this spectral peak was corresponded to C–N stretching of amide II proteins (Suresh et al., 2016a; 2016b). This result suggested that some protein level might be increased in response to metal-stress, which potentially related to a group of metal detoxification proteins in plants (Wang et al., 2020).

In this work, only single spectral peak at 1400 – 1250 cm^{-1} was disappeared in the ATR-FTIR of *L. minor* L. treated with $\text{Pb}(\text{NO}_3)_2$. This spectral peak was assigned to ester moieties (C–OR vibration) of carbohydrate and lipid (Papageorgiou et al., 2019), thus suggesting the inhibition of production or changed structure of some carbohydrates and lipids in response to Pb-treatment.

For the emergence of new spectral peaks, the spectral peak at 1730 cm^{-1} was detected only in the Ag-, Fe-, and Pb-treated roots of *L. perpusilla* Torr., which was corresponded to C=O stretching vibration of amide I groups of proteins (Yang et al., 2014). Therefore, new protein induction was suggested in the metal-treated plant. In addition, the new spectral peak at 800 – 515 cm^{-1} was detected in both plants treated with $\text{Ni}(\text{NO}_3)_2$ and $\text{Pb}(\text{NO}_3)_2$, which was assigned to N–C group of nucleic acid. This result suggested the possible induction of gene expression in response to metal exposures, which could relate to metal detoxification and stress response genes (Puig et al., 2007). Also, the new spectral peak at 775 – 420 cm^{-1} was detected in Pb-treated plants, corresponding to the metal-organic groups. Therefore, this result suggested the interaction between Pb^{2+} and organic compounds, which was one of the metal-detoxification process in plant cells (Xu et al., 2017).

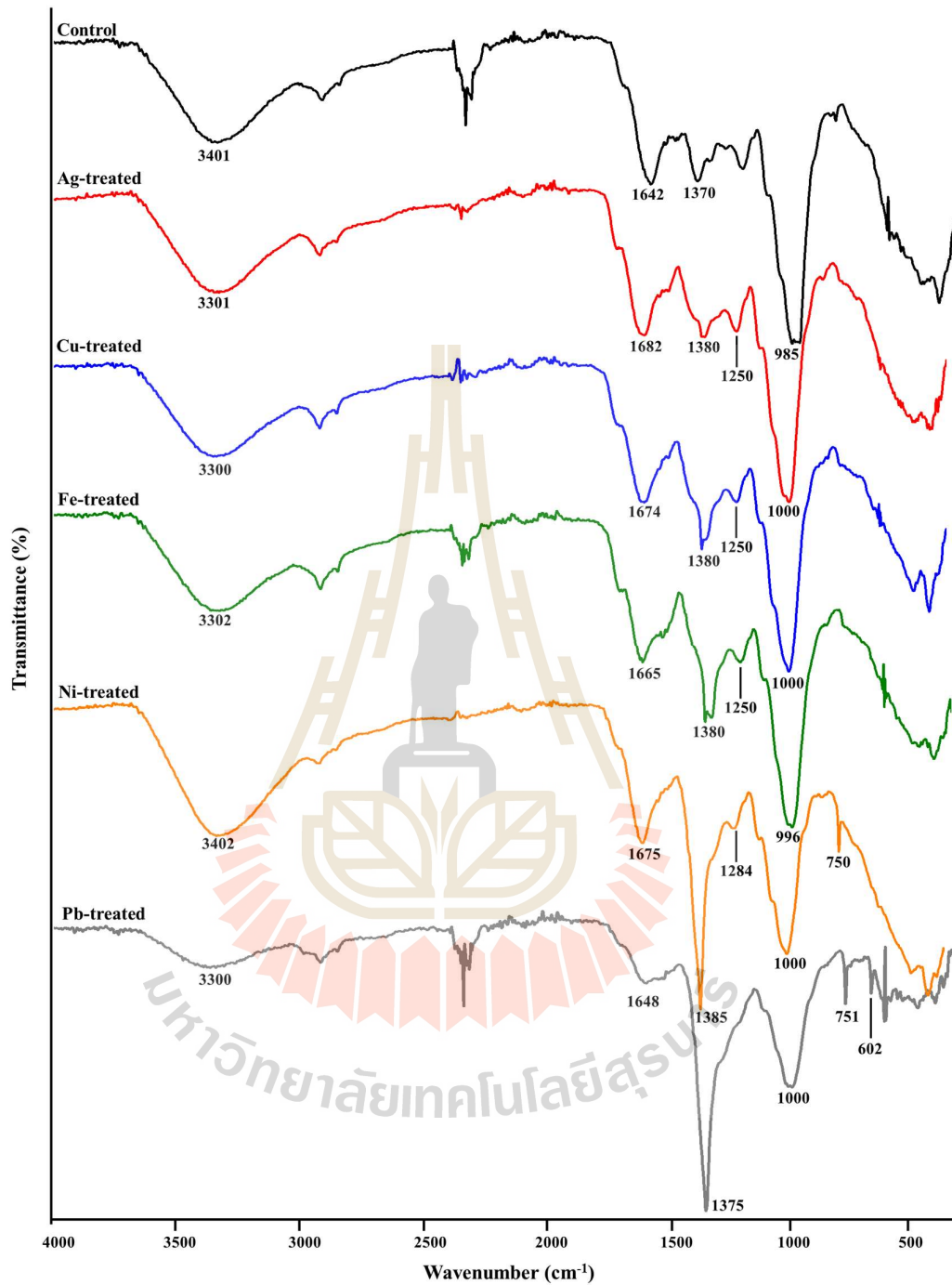


Figure 5.9 ATR-FTIR spectra of the control and metal-treated of *Lemna minor* L. roots as determined in the wavelength range of 4000 – 400 cm⁻¹.

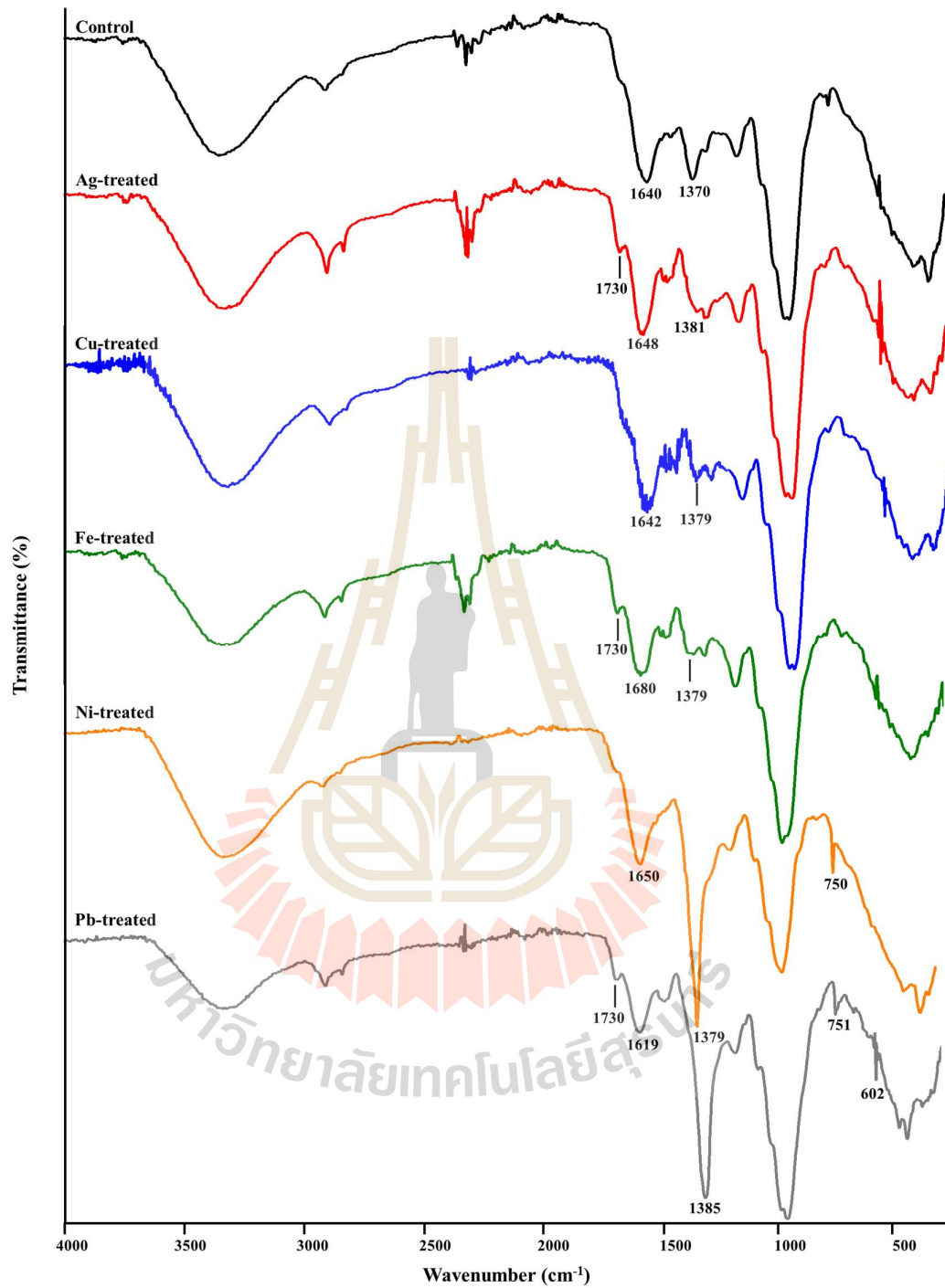


Figure 5.10 ATR-FTIR spectra of the control and metal-treated of *Lemna perpusilla*

Torr. roots as determined in the wavelength range of $4000 - 400 \text{ cm}^{-1}$.

Table 5.5. The summary of the FTIR spectral peaks of two aquatic roots in response to metal exposures.

No.	Standard reference	Wave number (cm ⁻¹)					Functional groups	Biological compounds	
		Ctrl	Treated roots with						
			Ag	Cu	Fe	Ni			Pb
<i>Lemna minor</i> L.									
1	3600–3300	3401	3301	3300	3302	3402	3300	O–H	Carbohydrate, phenolic
2	1800–1630	1642	1705	1704	1705	1705	1705	C–ONHR	Amine I proteins
3	1395–1370	1370	1380	1380	1380	1385	1375	C–N	Amide II proteins
4	1400–1250	1250	1250	nd	1541	nd	1540	C–OR	Carbohydrate, lipid
5	1000–800	985	1000	1000	996	1000	1000	N–H	Proteins
6	800–515	nd	nd	nd	nd	750	751	N–C	Nucleic acids
7	775–420	nd	nd	nd	nd	nd	612	Me–organic	Metal-binding organic compound
<i>Lemna perpusilla</i> Torr.									
1	1800–1630	nd	1730	nd	1730	nd	1730	C=O	Amine I proteins
2	1800–1630	1640	1648	1642	1680	1650	1619	C–ONHR	Amine I proteins
3	1395–1370	1370	1381	1379	1379	1375	1385	C–N	Amide II proteins
4	800–515	nd	nd	nd	nd	750	nd	N–C	Nucleic acids
5	775–420	nd	nd	nd	nd	751	602	Me–organic	Metal-binding organic compound

nd; not detected

5.3.2 *Spirodela polyrhiza* (L.) Schleid.

ATR-FTIR spectra of the control and the metal-treated roots of *S. polyrhiza* (L.) Schleid. exposed with AgNO_3 , $\text{Cu}(\text{NO}_3)_2$, $\text{Fe}(\text{NO}_3)_2$, $\text{Ni}(\text{NO}_3)_2$, and $\text{Pb}(\text{NO}_3)_2$ solutions are showed in Figure 5.11. Similar to *Lemna* results, the changes of cellular biomolecule levels in *S. polyrhiza* (L.) Schleid. were detected, including the increased intensity, new emergence, and absence of spectral peaks. The increased intensity of spectral peaks was detected at $1800 - 1630 \text{ cm}^{-1}$ (C=ONHR group of the amide I of proteins), $1000 - 800 \text{ cm}^{-1}$ (the N-H group of proteins), and $1395 - 1370 \text{ cm}^{-1}$ (C-N stretching of amide II proteins), which suggested the induction of protein synthesis in response to metal-stress. As compared with the control, the spectral peak at $1400 - 1250 \text{ cm}^{-1}$ was not detected in the metal-treated sample, which this peak correlated to C-OR vibration of carbohydrate and lipids. Also, the new spectral peak was detected at $800 - 515 \text{ cm}^{-1}$ (N-C group of nucleic acid), suggesting the induction of gene expression in response to metal-stress in this plant.

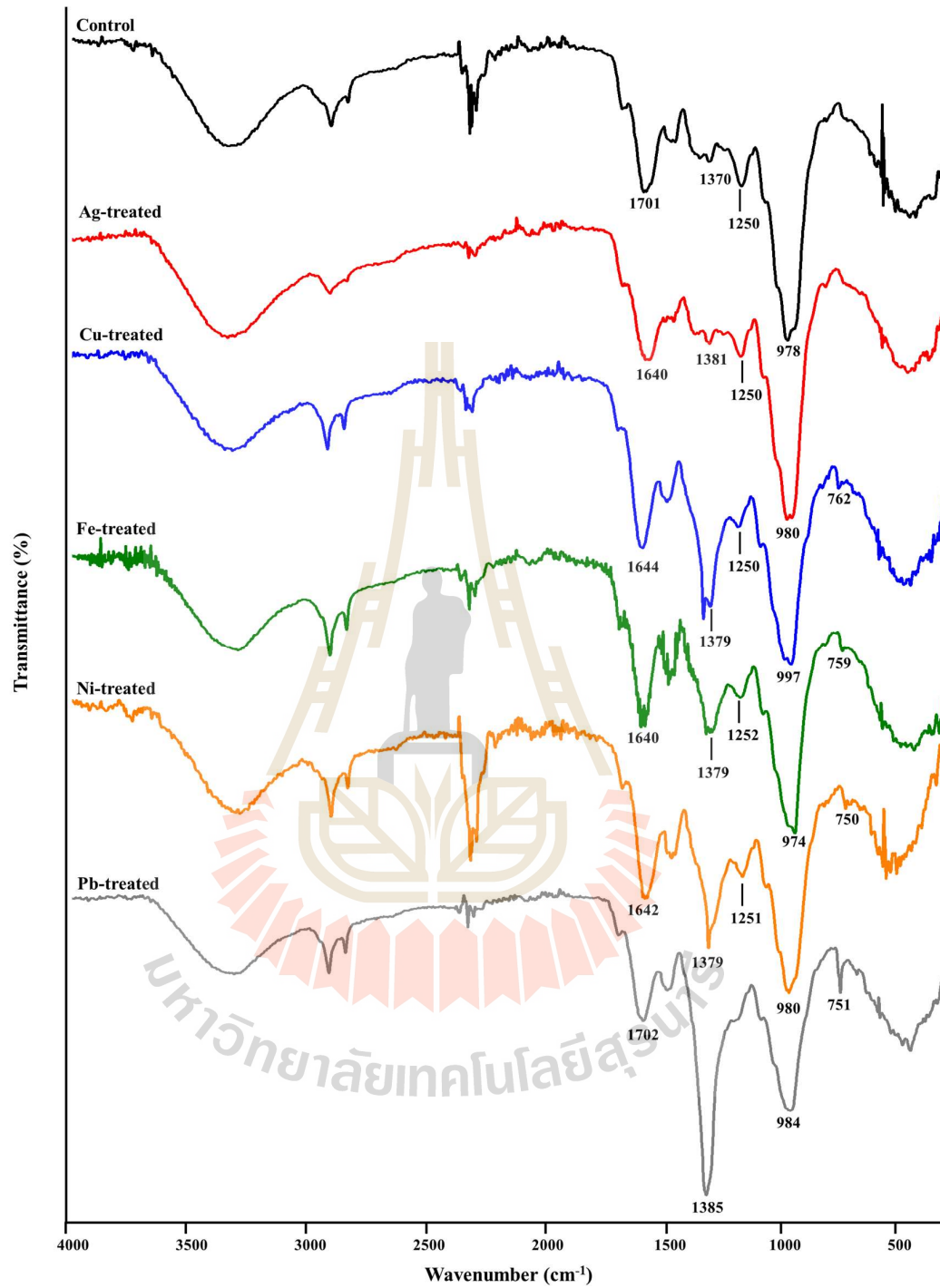


Figure 5.11 ATR-FTIR spectra of the control and metal-treated of *Spirodela polyrhiza* (L.) Schleid. roots as determined in the wavelength range of 4000 – 400 cm⁻¹.

Table 5.6 The summary of ATR-FTIR spectral peaks of *Spirodela polyrhiza* (L.) Schleid. roots in response to metal exposures.

No.	Wave number (cm ⁻¹)						Functional groups	Biological compounds	
	Standard reference	Ctrl	Treated roots with						
			Ag	Cu	Fe	Ni			Pb
1	1800–1630	1700	1640	1644	1640	1642	1702	C–ONHR	Amine I proteins
2	1400–1250	1250	1250	1250	1252	1251	nd	C–OR	Carbohydrate, lipid
3	1395–1370	1370	1381	1379	1379	1379	1385	C–N	Amide II proteins
4	1000–800	978	980	997	974	980	984	N–H	Proteins
5	800–515	nd	nd	762	759	750	751	N–C	Nucleic acids

nd: not detected

5.3.3 *Wolffia globosa* (Roxb.) Hartog & Plas

ATR-FTIR spectra of the Ag-, Cu-, Fe-, Ni-, and Pb-treated roots of *W. globosa* (Roxb.) Hartog & Plas as compared with the control are shown in Figure 5.12. Similar to the previous studies, the changes of cellular biomolecules in response to metal treatments were detected, which were the reduction of spectral peaks at 3600 – 3300 and 1000 – 800 cm⁻¹, the disappeared spectral peak at 1400 – 1250 cm⁻¹, and the new spectral peak at 800 – 515 and 775 – 420 cm⁻¹. Unlike the previous studies, the increased intensity of the spectral peak at 1500 – 1000 cm⁻¹ was detected in metal-treated *W. globosa* (Roxb.) Hartog & Plas, which was assigned to the “fingerprint” region of amine III of proteins (Wei et al., 2009). In addition, the new spectral peaks at 3700 – 3500, 3450 – 3350, and 750 – 720 cm⁻¹ were detected. The spectral peaks at 3700 – 3500 and 3450–3350 cm⁻¹ were attributed to the –NH₂ stretching vibrations

(non-bounded) of a primary amine (Souza et al., 2008). This primary amine might be related to newly synthesized proteins such as phytochelatins and metallothionein in metal-detoxification responses in plant cells (Hasan et al., 2017). Also, the ATR-FTIR spectral peak at $750 - 720 \text{ cm}^{-1}$ was detected in the metal-treated plant, which was correspond to the C–C stretching in the ring vibration of phenolic compounds such as phenylpropanoid and triterpenoid (Guerrero et al., 2014). According to Kisa and co-workers, one of the metal-stress responses of plants was to induce the synthesis of some metabolites that could associate with heavy metals including phenolic acids, flavonoids, coumarins, and lignins (Kisa et al., 2019).



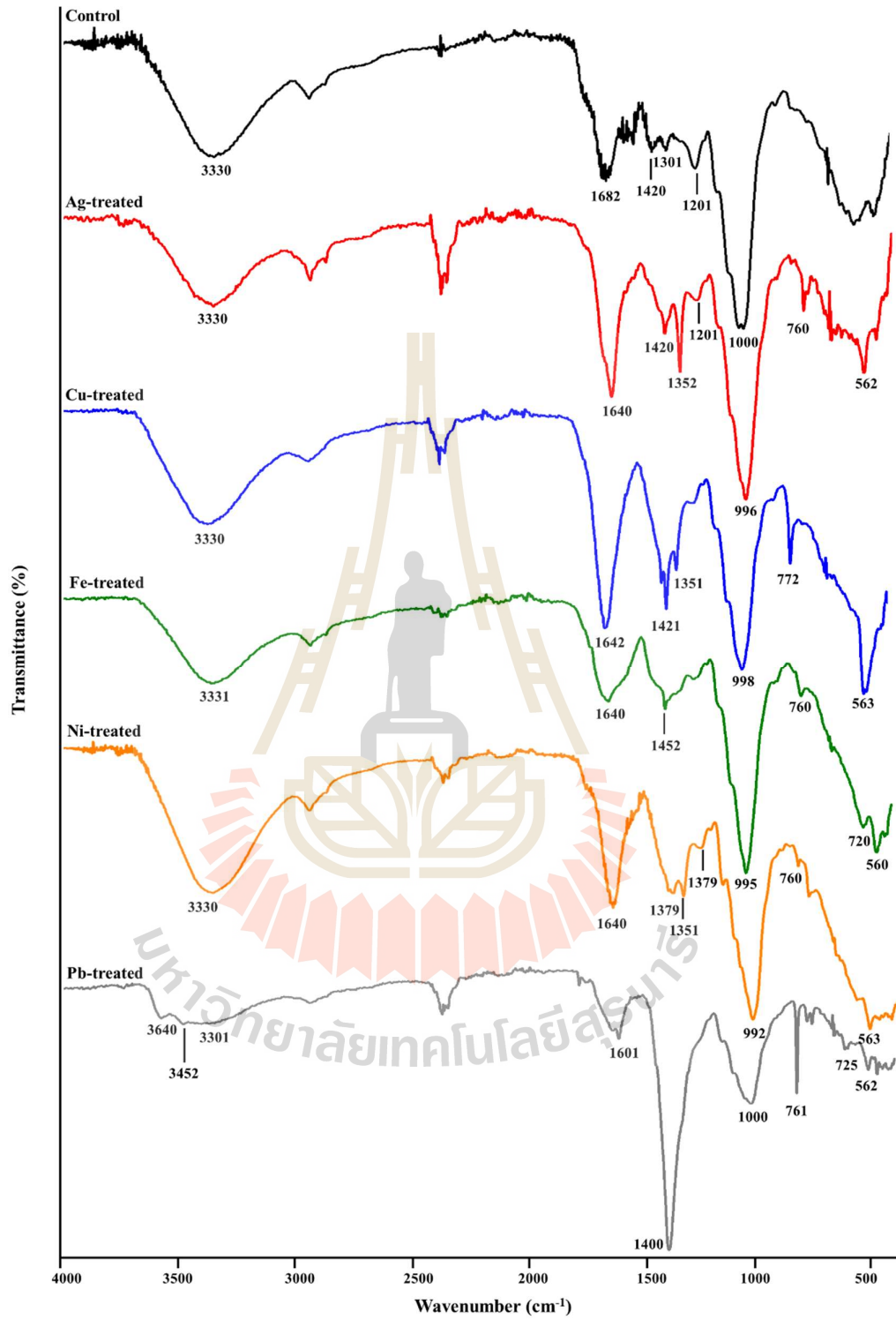


Figure 5.12 ATR-FTIR spectra of the control and metal-treated *Wolffia globosa* (Roxb.) Hartog & Plas as determined in the wavelength range of 4000 – 400 cm^{-1} .

Table 5.7 The summary of the ATR-FTIR spectral peaks of *Wolffia globosa* (Roxb.) Hartog & Plas in response to metal exposures.

No.	Standard reference	Wave number (cm^{-1})					Functional groups	Biological compounds	
		Ctrl	Treated roots with						
		Ag	Cu	Fe	Ni	Pb			
1	3700–3500	nd	nd	nd	nd	nd	3640	–NH ₂	Amine I (non-bound)
	3450–3350	nd	nd	nd	nd	nd	3452	–NH ₂	proteins
2	3600–3300	3330	3330	3330	3331	3335	3301	O–H	Carbohydrate, phenolic
3	1800–1630	1682	1640	1642	1640	1640	1601	C=O	Amine I proteins
4	1500–1000	1420	1420	1420	1452	1397	1400	C–ONHR	Amine I proteins
5	1395–1370	1372	1371	1370	1372	1370	1371	C–N	Amine II proteins
6	1400–1250	1301	1352	1351	1351	1351	nd	C–N	Amine III proteins
7	1000–800	1000	996	998	995	992	1000	N–H	Proteins
8	800–515	nd	760	772	760	760	761	N–C	Nucleic acids
9	750–720	nd	nd	nd	nd	720	725	C–C	Phenolic compounds
10	775–420	nd	562	563	560	563	562	Me–organic	Metal-binding organic compound

nd: not detected

5.4 Accumulation and Characterization of Metal Nanoparticles

5.4.1 *Lemna minor* L.

TEM images were used to determine the production and localization of metal NPs in roots of *L. minor* L. that exposed in AgNO_3 , $\text{Cu}(\text{NO}_3)_2$, $\text{Fe}(\text{NO}_3)_3$, $\text{Ni}(\text{NO}_3)_2$, and $\text{Pb}(\text{NO}_3)_2$ solutions. The results showed similar accumulation of metal NPs in both cortical and vascular tissues, which only AgNPs, FeNPs, and PbNPs were detected, but not CuNPs and NiNPs.

Representative TEM images of cortical cells of *L. minor* L. are shown in Figure 5.13). Agglomerated and free AgNPs were predominantly detected in cytoplasm and some were near the plasma membrane (black arrow). In addition to plasma membrane, FeNPs were detected in an ectosome (red box). For PbNPs, they agglomerated near plasma membrane and intercellular space. As all metal NPs, not the electron dense, were detected near plasma membrane, it was hypothesized that the metal ions were reduced by phyto-compounds and form metal nuclei leading to a synthesis of metal NPs. These phyto-compounds were likely accumulated near the plasma membrane. thus, it was the major location to accumulate metal NPs in cortical cells. Since the accumulation of FeNPs were detected in an ectosome, suggested that several proteins such as matrix metalloproteins, glycoprotein type GP1b, and adhesion proteins P-selectin contained in ectosome assist the formation of metal FeNPs (Meldolesi, 2018). The detection of PbNPs in the intercellular space area also suggested that metal ions between cells could be transformed into metal NPs. Therefore, the phyto-compounds that assist the formation of metal NPs were present both inside and between cells.

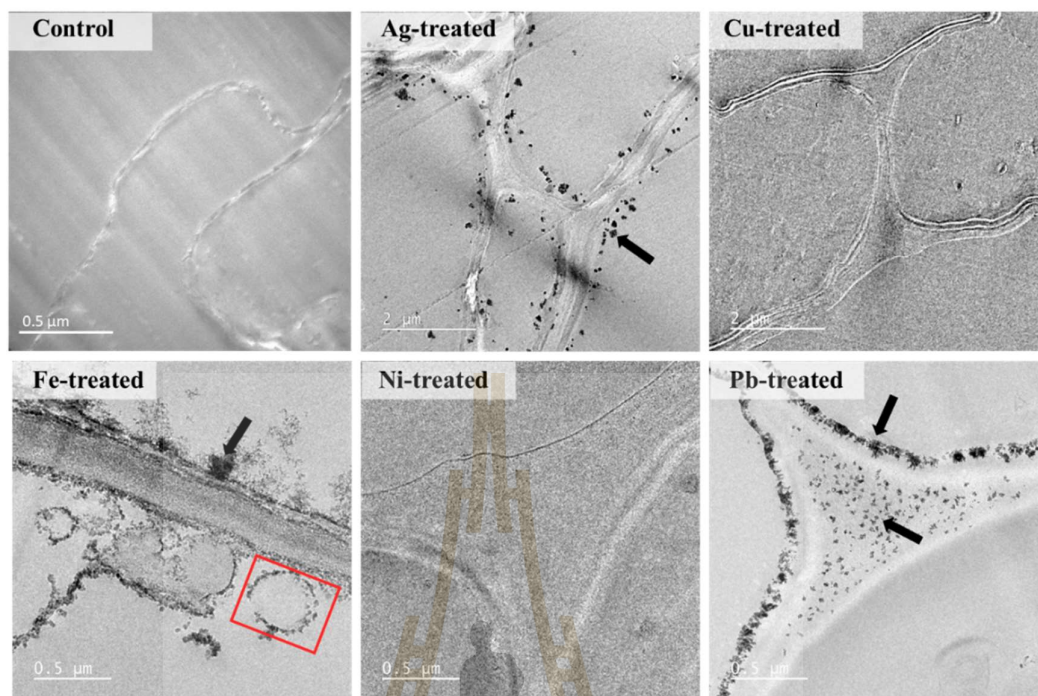


Figure 5.13 TEM images of metal NPs in cortical cells of the Ag-, Cu-, Fe-, Ni-, and Pb-treated roots of *Lemna minor* L. Dark arrow: NPs. Red box: ectosome.

The average diameters of spherical AgNPs, FeNPs, and PbNPs in cortical cells were measured from 100 NPs in TEM images and the size distribution histogram was plotted as shown in Figure 5.14. The average sizes of AgNPs, FeNPs, and PbNPs were 32.42 ± 16.46 , 9.68 ± 4.95 , and 69.96 ± 24.59 nm, respectively. The distributed sizes of AgNPs, FeNPs, and PbNPs were 11.79 – 100.21, 7.64 – 34.16, and 37.71 – 165.51 nm, respectively.

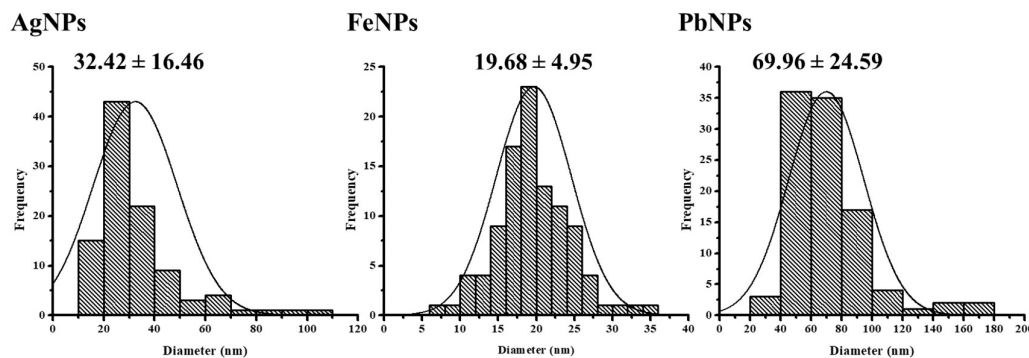


Figure 5.14 Size distribution histograms and average sizes of AgNPs, FeNPs, and PbNPs in cortical cells of *Lemna minor* L. roots.

In vascular bundle, representative TEM images of Ag-, Cu-, Fe-, Ni-, and Pb-treated roots of *L. minor* L. exposed to AgNO_3 , $\text{Cu}(\text{NO}_3)_2$, $\text{Fe}(\text{NO}_3)_3$, $\text{Ni}(\text{NO}_3)_2$, and $\text{Pb}(\text{NO}_3)_2$ solutions are shown in Figure 5.15. AgNPs were detected near the plasma membrane of the xylem tissue (Figure 5.15B). This result suggested the translocation of Ag^+ ions from the outmost to central tissues of roots. Also, phyto-compounds to assist the formation of metal NPs were present in vascular cells. Similar to the result in cortical cells, FeNPs were detected near the plasma membrane (black arrow) and in ectosome (red box) in the xylem tissue. Kim and Guerinot reported that Fe ions could transport from the outer to inner layers of the plant cells via two strategy. Strategy I, Fe^{3+} ions transport via the chelate reduction, which is reduced the trivalent Fe to divalent Fe by ferric-chelate reductase defective 1 (frd1) in plasma membrane. Strategy II, Fe^{2+} ions transport via the Fe-regulated transporter 1, a member of the metal transporter family (Kim and Guerinot, 2007). Also, trivalent Fe has the high binding affinity to mugineic acid, the member in a family of phytosiderophores, as the metal-complexes (Mori, 1999). Unlike the other detected NPs, the detected PbNPs in xylem

cells were in spherical and rod shapes, suggesting that the environment in xylem tissue was suitable for assisting the growth of anisotropic NPs.

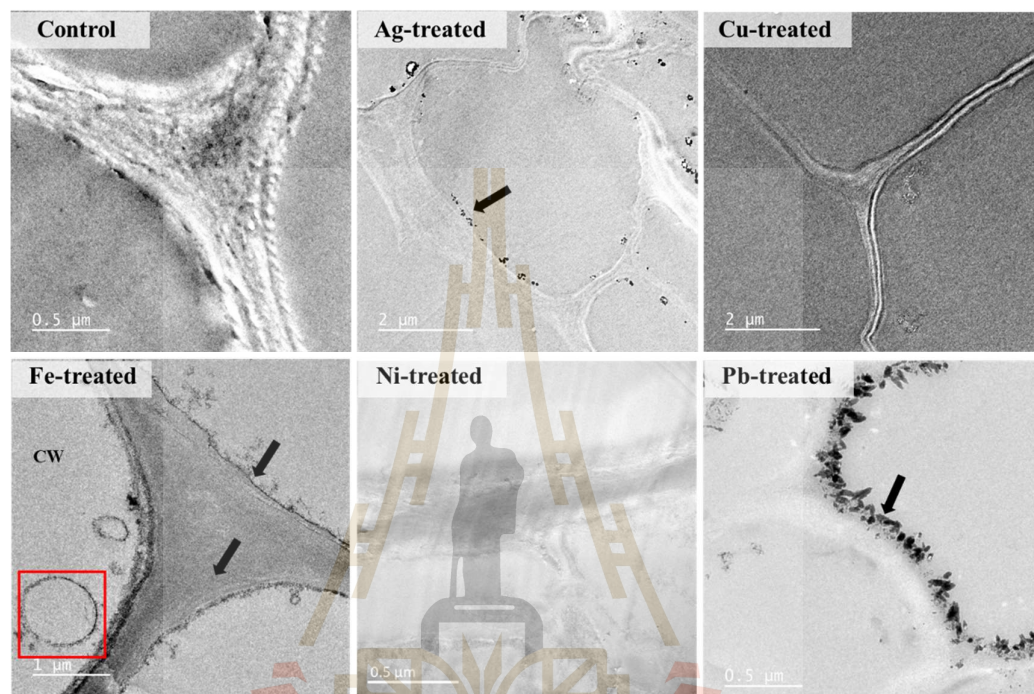


Figure 5.15 TEM images of metal NPs in vascular tissues of the Ag-, Cu-, Fe-, Ni-, and Pb-treated roots of *Lemna minor* L.: Dark arrow and red box indicate NPs and ectosome, respectively.

Average diameters and size distribution histograms of AgNPs, FeNPs, and PbNPs in vascular tissues are shown in Figure 5.16. The average sizes of AgNPs, FeNPs, and PbNPs were 65.77 ± 36.00 , 22.25 ± 6.98 , and 58.63 ± 22.83 nm, respectively. The distributed sizes of AgNPs, FeNPs, and PbNPs were 25.13 – 176.30, 8.33 – 49.52, and 28.06 – 147.00 nm, respectively.

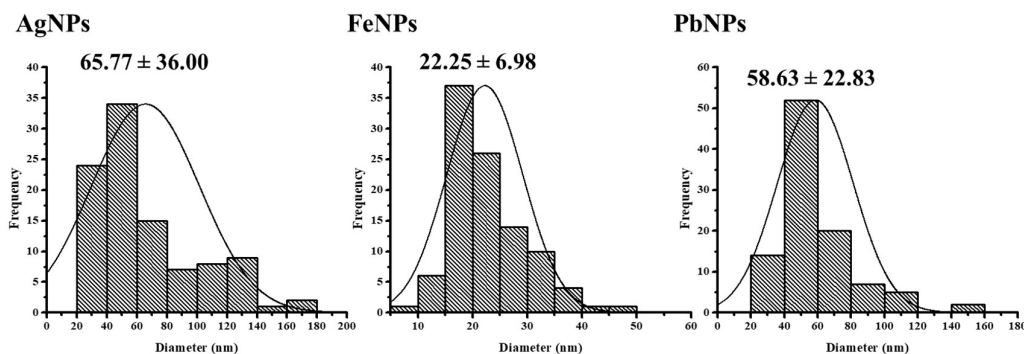


Figure 5.16 Size distribution histograms and average diameters of AgNPs, FeNPs, and PbNPs in vascular tissues of the Ag-, Fe-, and Pb-treated roots of *Lemna minor* L.

Identity of metal NPs in *L. minor* L. were determined by SAED-TEM and EDX-TEM analyses. The formation of AgNPs in the Ag-treated roots was confirmed by SAED-TEM images (Figure 5.17), which revealed the presence of the concentric diffraction rings at 2.37, 2.06, 1.44, 1.24, 1.18, 0.94, and 0.91 Å. These values were corresponded to the hlk planar of (111), (200), (220), (311), (222), (331), and (420) of the FCC structure of Ag according to JCPDS number 01–1164 (Mollick et al., 2015). In Fe-treated roots, the concentric diffraction ring was detected at 2.40 Å, corresponding to the hlk planar of (111) of the FCC structure of FeO structure based on the JCPDS number 02–1186 (Agale et al., 2017). Besides, the concentric diffraction rings were detected at 2.93 and 2.51 Å, corresponding to the hlk planar of (220) and (311) of the FCC structure of Fe₂O₃ based on the JCPDS number 02–1047 (Shao et al., 2011). Moreover, the concentric diffraction ring was detected at 2.43 Å, attributing to the hlk planar of (222) of the FCC structure of Fe₃O₄ based on the JCPDS number 02–1035. Thus, three forms of FeNPs were produced in the plant cells: FeO, Fe₂O₃, and Fe₃O₄ NPs. In Pb-treated roots, the concentric diffraction rings were detected at 2.81,

2.43, 1.72, 1.41, 1.13, and 1.01 Å, corresponding to the hkl planar of (111), (200), (220), (222), (331), and (422) of the cubic (Fm3m) lattice of Pb structure based on the JCPDS number 01-0995 (Davey, 1925). Similar to other results, a concentric diffraction ring was not detected in the Cu- and Ni-treated roots, suggesting no formation of CuNPs and NiNPs in the plant roots.

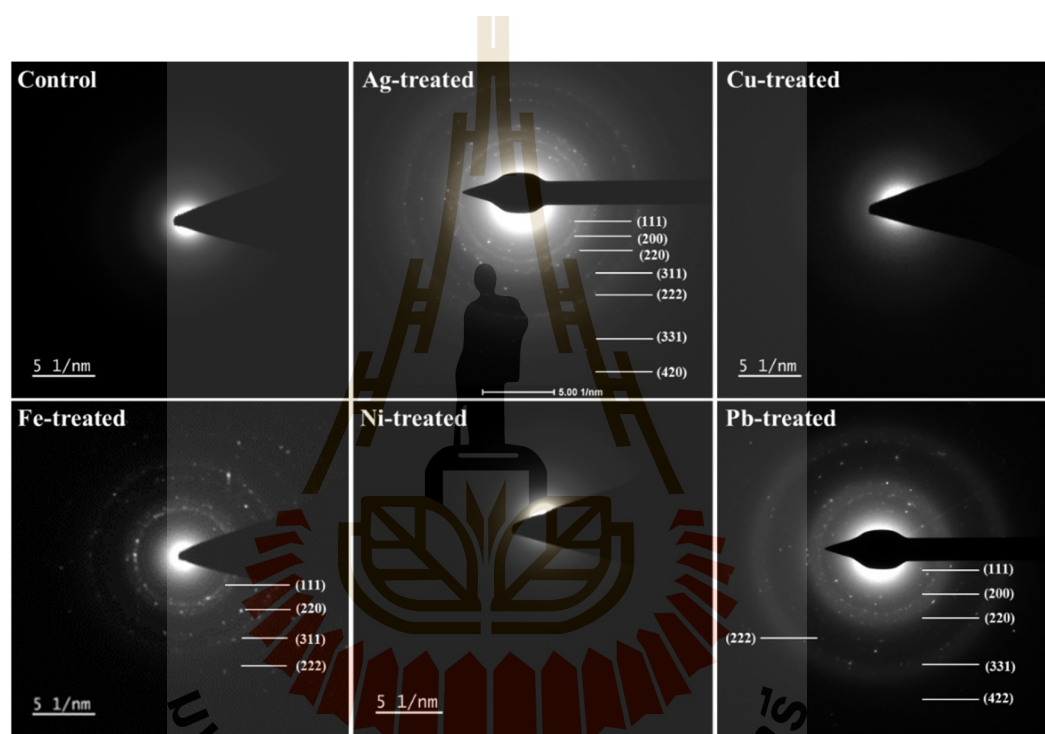


Figure 5.17 SAED-TEM analyses of the Ag-, Cu-, Fe-, Ni-, and Pb-treated roots as compared with the control.

In this work, EDX-TEM analysis was also employed to identify the elemental profiles of the metals in Ag-, Cu-, Fe-, Ni-, and Pb-treated roots as shown in Figure 5.18. The EDX-TEM profiles showed that the presence of Ag, Fe, and Pb elements in the Ag-, Fe-, and Pb-treated roots; 59.07, 5.03, and 54.92% mass, respectively. No detectable level of Cu and Ni was in the Cu- and Ni-treated roots, which was well-

corresponded to the absence of both metal NPs in the roots. It was pointed out that the detected levels of C, O, and P were likely from the organic materials in plant tissues (Elnaggar et al., 2015). Also, the presence of Cu in all samples was resulted from the carbon-coated Cu grids using to hold the samples (Janthima et al., 2018).

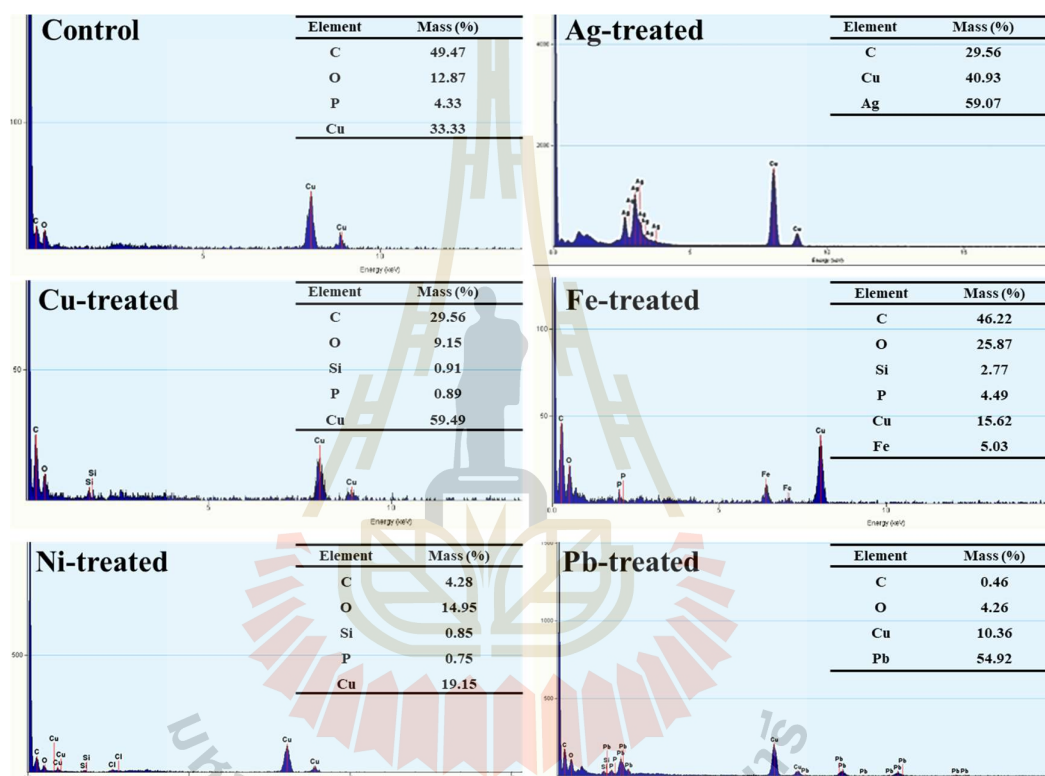


Figure 5.18 EDX-TEM analyses of the Ag-, Cu-, Fe-, Ni-, and Pb-treated roots as compared with the control.

5.4.2 *Lemna perpusilla* Torr.

The accumulation of metal NPs (Ag, Cu, Fe, Ni, and Pb) in *L. perpusilla* Torr. was determined by TEM images. Figure 5.19 shows TEM images of cortical cells of the Ag-, Cu-, Fe-, Ni-, and Pb-treated roots. In Ag- and Pb-treated roots, the agglomerated and free NPs were dominantly in a vicinity the plasma membrane. In Fe-

treated roots, only electron dense area was detected, but not metal NPs. The average diameters of AgNPs and PbNPs were 29.43 ± 14.20 and 130.67 ± 53.45 nm, respectively (Figure 5.20). The distributed sizes of AgNPs and PbNPs were 10.31 – 89.46 and 1.02 – 350.14 nm, respectively. In Fe-treated roots, the agglomerated FeNPs were also detected, but could not determine their sizes due to unclear images.

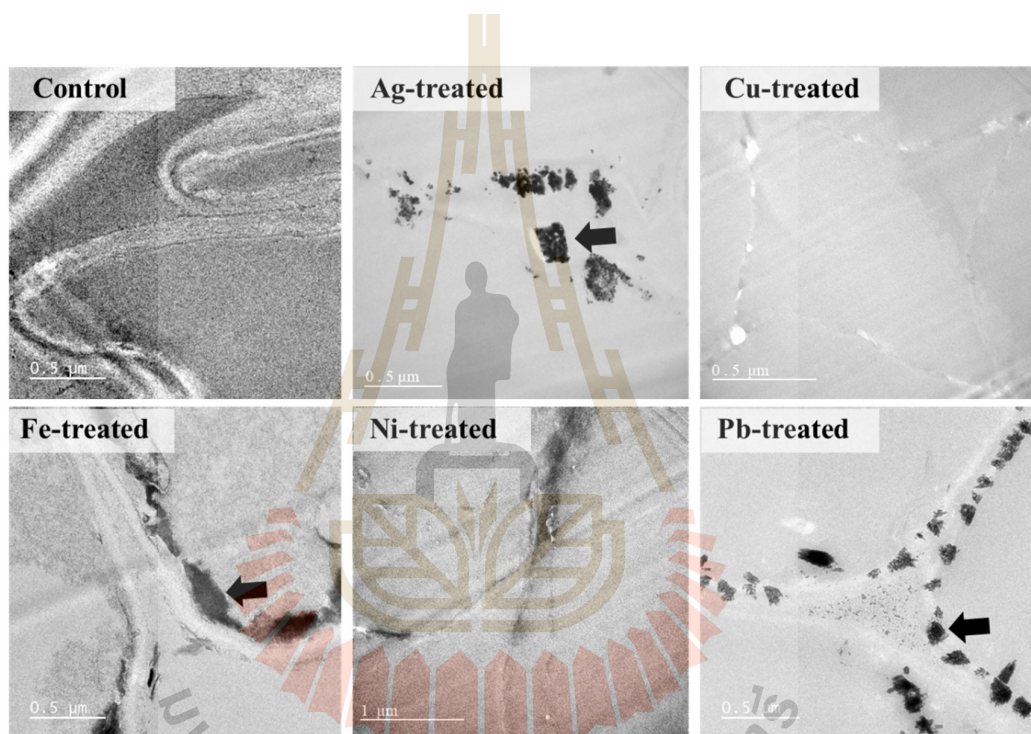


Figure 5.19 TEM images of metal NPs in cortical tissue of the Ag-, Cu-, Fe-, Ni-, and Pb-treated roots of *Lemna perpusilla* Torr. Dark arrow: NPs.

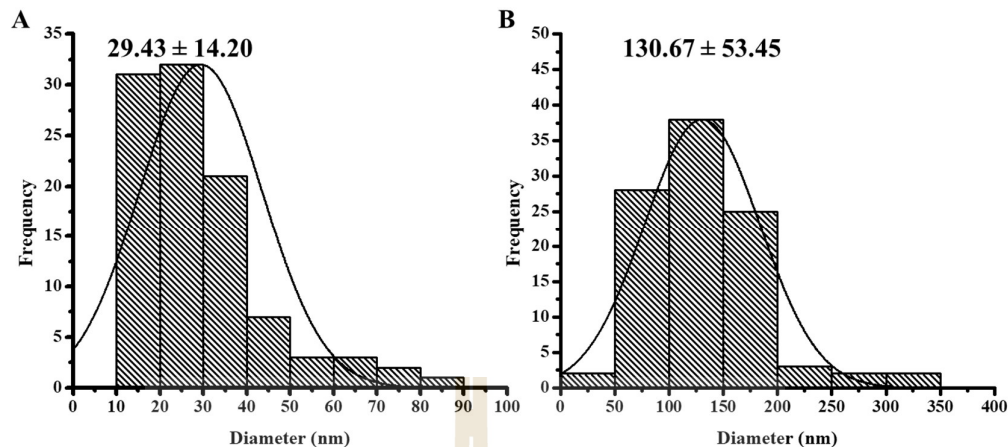


Figure 5.20 Size distribution histograms and average diameters of (A) AgNPs and (B) PbNPs in cortical tissue of the Ag- and Pb-treated roots of *Lemna perpusilla* Torr.

TEM images of vascular tissues of Ag-, Cu-, Fe-, Ni-, and Pb-treated roots are shown in Figure 5.21. Similar to cortical tissues, AgNPs and PbNPs were dominantly detected near the plasma membrane. Unlike cortical tissues, in vascular tissues there was the detection of FeNPs in a vesicle near the plasma membrane. The average diameters of AgNPs and PbNPs were 37.92 ± 16.85 and 85.84 ± 39.76 nm, respectively (Figure 5.22). Also, the average size of FeNPs could not determine due to unclear images.

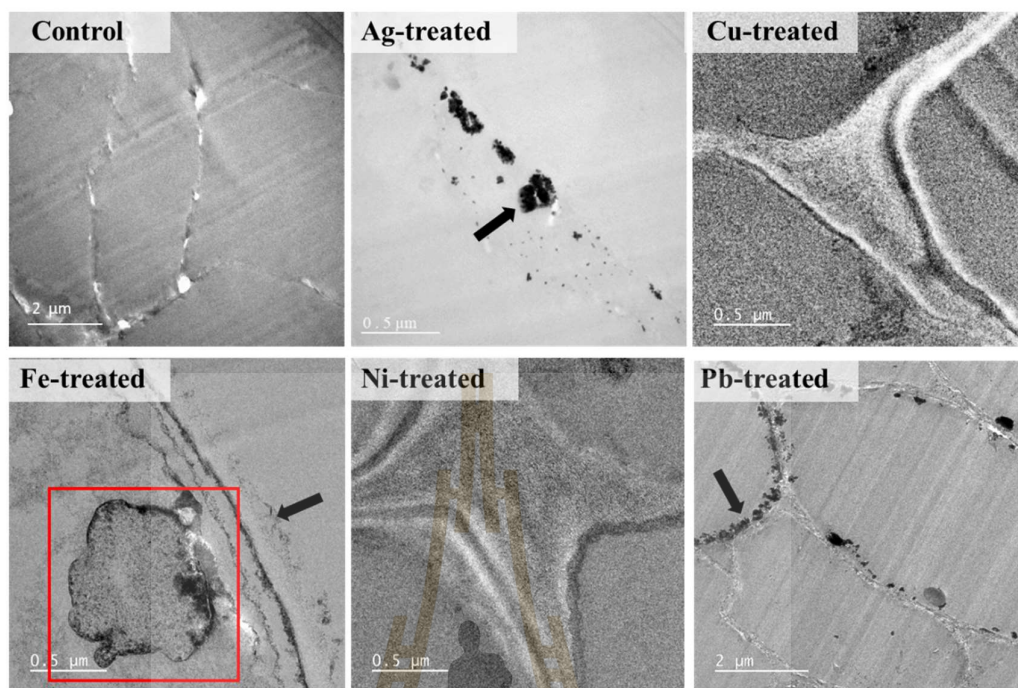


Figure 5.21 TEM images of metal NPs in vascular tissues of the Ag-, Cu-, Fe-, Ni-, and Pb-treated roots of *Lemna perpusilla* Torr. Dark arrow and red box indicate NPs and ectosome, respectively.

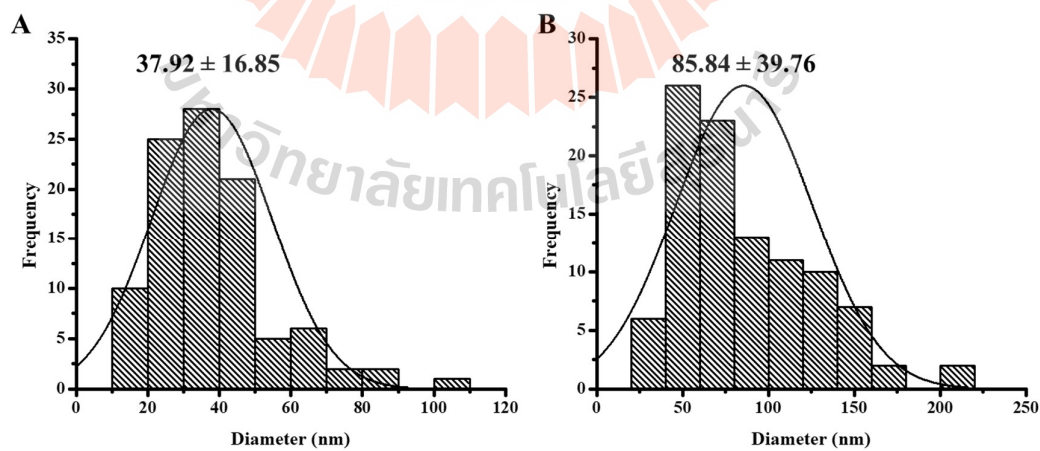


Figure 5.22 Size distribution histograms and average diameters of (A) AgNPs and (B) PbNPs in vascular tissues of the Ag- and Pb-treated roots of *Lemna perpusilla* Torr.

The crystallography and chemical profiles of the accumulated NPs in roots of *L. perpusilla* Torr. were determined by SAED-TEM and EDX analyses. SAED-TEM images (Figure 5.23) revealed that the concentric diffraction rings at 2.37, 2.05, 1.43, 1.23, and 1.18 Å in the Ag-treated roots. These rings were correspond to the hlk planar of (111), (200), (220), (311), and (222) of the FCC structure of Ag, based on the JCPDS number 03–0652871 (Ushamani and Renuka, 2017). In Fe-treated roots, the concentric diffraction rings were detected at 4.85 and 2.97 Å, corresponding to the hlk planar of (111) and (220) of the FCC structure of FeO structure based on the JCPDS number 02–1186) (Agale et al., 2017). In Pb-treated roots, the concentric diffraction rings were detected at 2.85 and 1.49 Å, corresponding to the hlk planar of (111) and (311) of the cubic (Fm3m) lattice of Pb structure (based on the JCPDS number 01-1972) (Roy and Bysakh, 2011). Moreover, the concentric ring was detected at 1.86 Å, corresponding to the hlk planar of (201) of the tetragonal (P4/nm129) of PbO structure (based on the JCPDS number 01–0796) (Klaytae et al., 2013). Similar to other results, there was no detection of any concentric diffraction rings in the Cu- and Ni-treated roots, suggesting no formation of CuNPs and NiNPs in the plant roots.

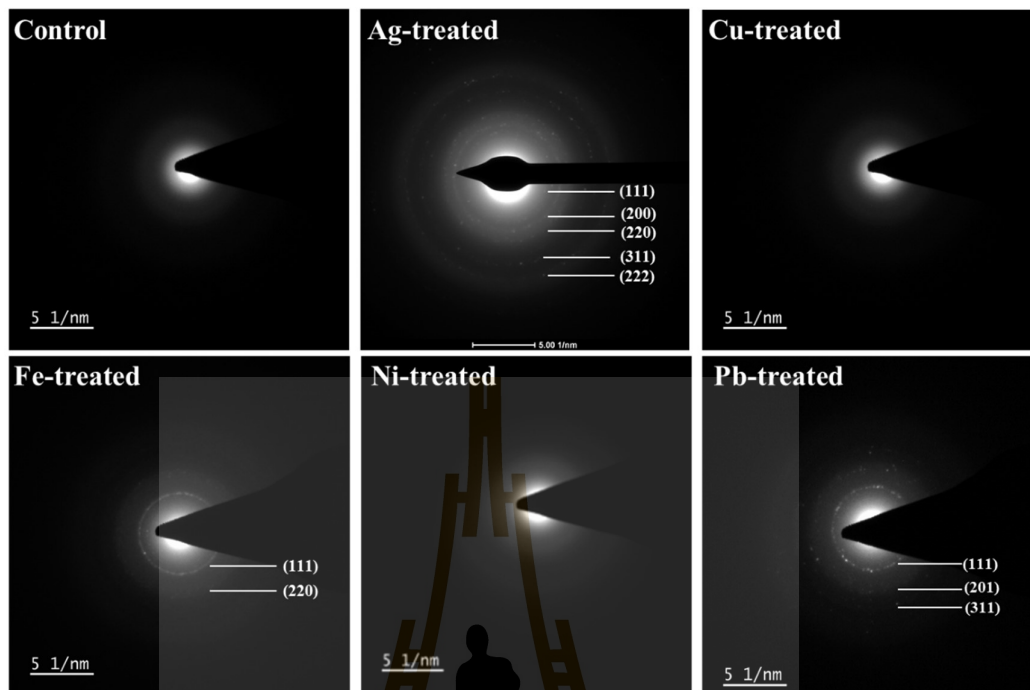


Figure 5.23 SAED-TEM analyses of the Ag-, Cu-, Fe-, Ni-, and Pb-treated roots of *Lemna perpusilla* Torr. as compared with the control.

Figure 5.24 shows the EDX-TEM analysis, which was estimated the level of elemental profiles in Ag-, Cu-, Fe-, Ni-, and Pb-treated root cells. The contents of Ag, Fe, and Pb elements were 68.69, 29.46, and 50.96% mass in the Ag-, Fe-, and Pb-treated roots, respectively. These results were well-corresponded to the detection of these metal NPs in the plant cells. Also, no detection of Cu and Ni elements in the Cu- and Ni-treated roots, which were well related to TEM images showing no detection of both metal NPs in the plant roots. It was noted that the detection of C, O, and P was contributed from the organic materials in the plants (Elnaggar et al., 2015). Also, the detected Cu in all samples was resulted from the sample holder, the carbon-coated Cu grid (Janthima et al., 2018).

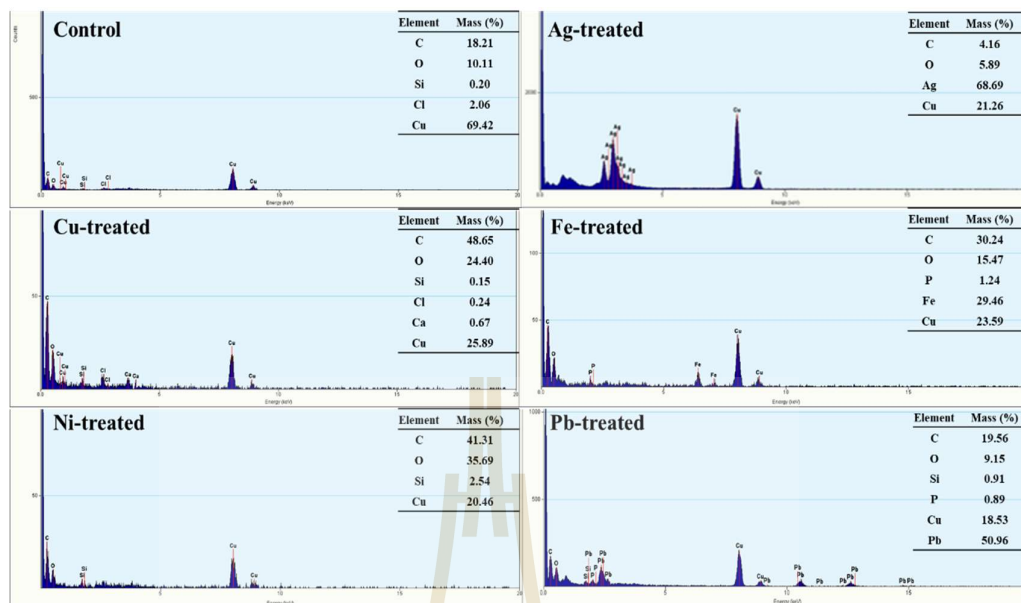


Figure 5.24 EDX-TEM analyses of the Ag-, Cu-, Fe-, Ni-, and Pb-treated roots of *Lemna perpusilla* Torr. as compared with the control.

5.4.3 *Spirodela polyrhiza* (L.) Schleid.

The accumulation of metal NPs (Ag, Cu, Fe, Ni, and Pb) in roots of *S. polyrhiza* (L.) Schleid. was analyzed from TEM images. In cortical tissues, TEM images (Figure 5.25) revealed the clear images of AgNPs and PbNPs in the Ag- and Pb-treated plants. FeNPs and CuNPs were not clearly detected as the images showed electron dense areas in the Fe- and Cu-treated plants. For Ni-treated plant, there was no detection of metal NPs.

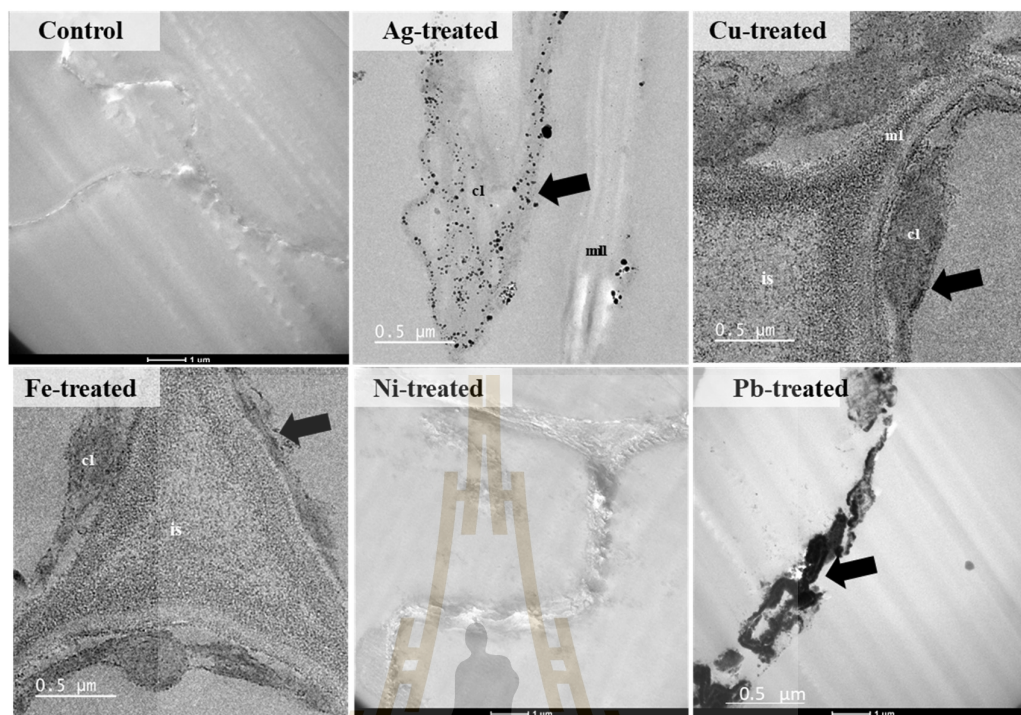


Figure 5.25 TEM images of metal NPs in cortical tissues of the Ag-, Cu-, Fe-, Ni-, and Pb-treated roots of *Spirodela polyrhiza* (L.) Schleid. Abbreviation: cl = chloroplast, is = intercellular space, and ml = middle lamella. Dark arrow: NPs.

Average diameters and size distributions of AgNPs and PbNPs are shown in Figure 5.26. The average diameters of AgNPs and PbNPs in cortical cells of *S. polyrhiza* (L.) Schleid. were 24.65 ± 9.45 and 60.77 ± 28.01 nm, respectively. The distributed sizes of AgNPs and PbNPs were 11.06 – 9.45 and 19.41 – 221.05 nm, respectively.

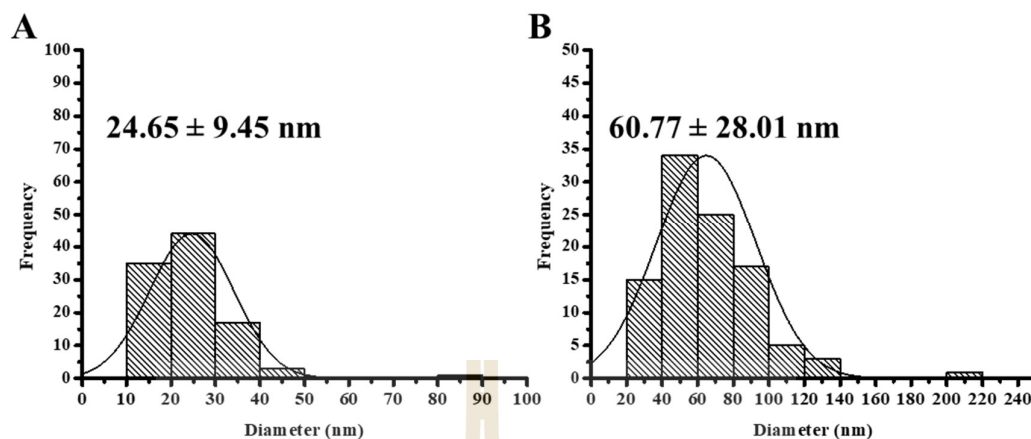


Figure 5.26 Size distribution histograms and average diameters of (A) AgNPs and (B) PbNPs in cortical tissues of the Ag- and Pb-treated roots of *Spirodela polyrhiza* (L.) Schleid.

TEM images of metal NPs (Ag, Cu, Fe, Ni, and Pb) in vascular tissues of roots of *S. polyrhiza* (L.) Schleid. are shown in Figure 5.27. Similar to cortical cells, AgNPs and PbNPs were clearly detected near the plasma membrane in the Ag- and Pb-treated roots, while the electron dense areas were detected in the Fe- and Cu-treated roots. Also, PbNPs was also detected at the plasma membrane of xylem cells.

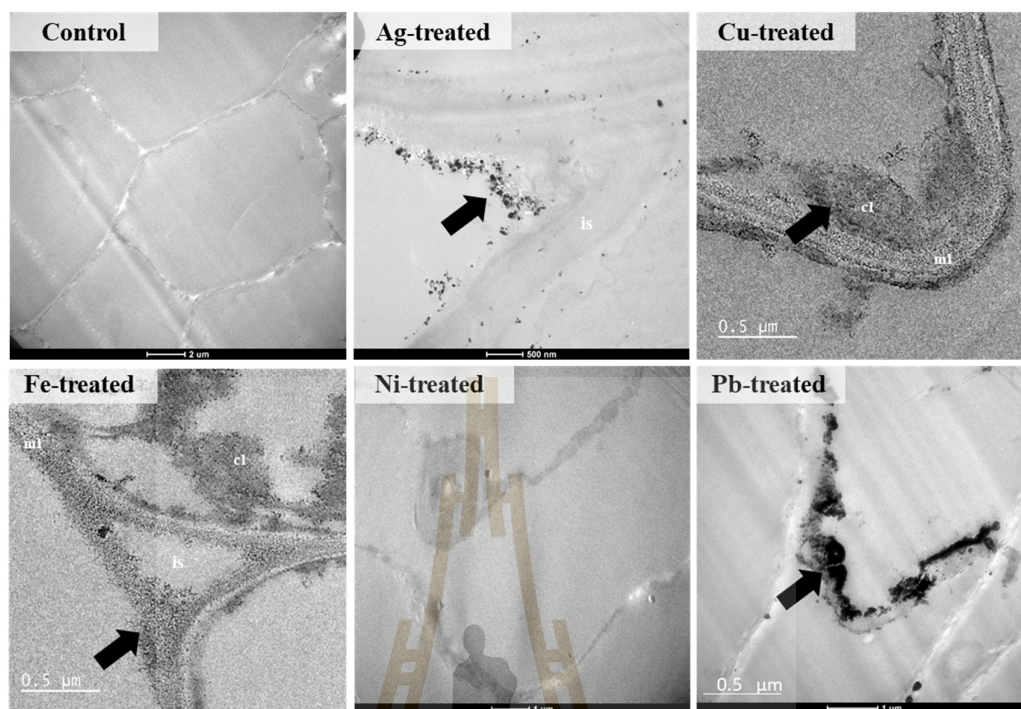


Figure 5.27 TEM images of metal NPs in vascular tissues of the Ag-, Cu-, Fe-, Ni-, and Pb-treated roots of *Spirodela polyrhiza* (L.) Schleid. Abbreviation: cl = chloroplast, is = intercellular space, and ml = middle lamella. Dark arrow: NPs.

Average diameters and size distributions of AgNPs and PbNPs are shown in Figure 5.28. The average diameters of AgNPs and PbNPs in vascular tissues of *S. polyrhiza* (L.) Schleid. were 52.92 ± 15.09 and 144.52 ± 58.13 nm, respectively. The distributed sizes of AgNPs and PbNPs were 19.61 – 140.62 and 2.04 – 351.42 nm, respectively.

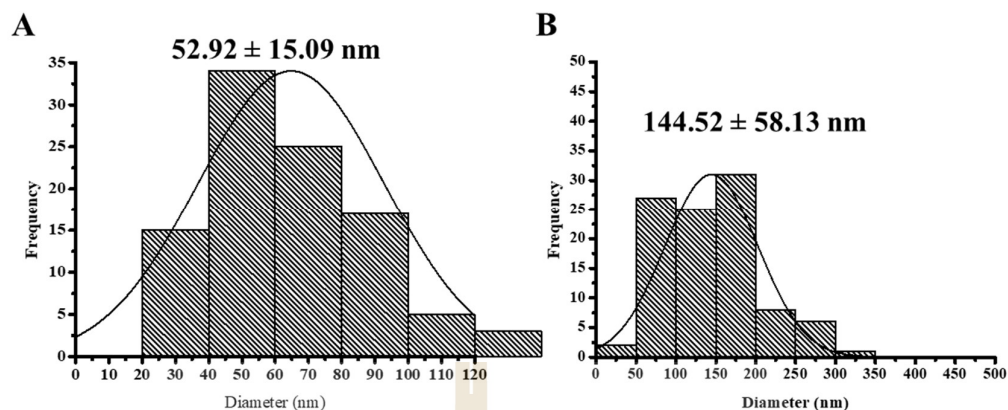


Figure 5.28 Size distribution histograms and average diameters of (A) AgNPs and (B) PbNPs in vascular tissues of the Ag- and Pb-treated roots of *Spirodela polyrhiza* (L.) Schleid.

The identity of NPs in the roots of *S. polyrhiza* (L.) Schleid. was determined by SAED-TEM and EDX analyses. SAED-TEM images (Figure 5.29) revealed that in the Ag-treated roots, the detected concentric diffraction rings were at 2.38, 2.06, 1.46, 1.24, 1.19, and 0.92 Å, attributing to the hkl planar of (111), (200), (220), (311), (222), and (420) of the FCC structure of Ag based on the JSPDS number 65–8428 (Kumar et al., 2014). In the Cu-treated roots, the concentric diffraction rings were detected at 2.47 and 2.14 Å, corresponding to the hkl planar of (111) and (200) of the cubic (Fm3m) structure of CuO based on the JCPDS number 01–1223 (Ali et al., 2018). In the Fe-treated roots, the concentric diffraction rings were marked at 2.05, 1.01, and 0.91 Å, corresponding to the hkl planar of (110), (220), and (310) of the cubic (Fm3m) structure of Fe based on the JCPDS number 01–1252 (Guo et al., 2006). In the Pb-treated roots, the concentric diffraction rings were observed at 2.82, 2.44, and 1.48 Å, corresponding to the hkl planar of (111), (200), and (311) of the cubic (Fm3m) lattice of Pb structure based on JCPDS number 02–0811 (Klaytae et al., 2013).

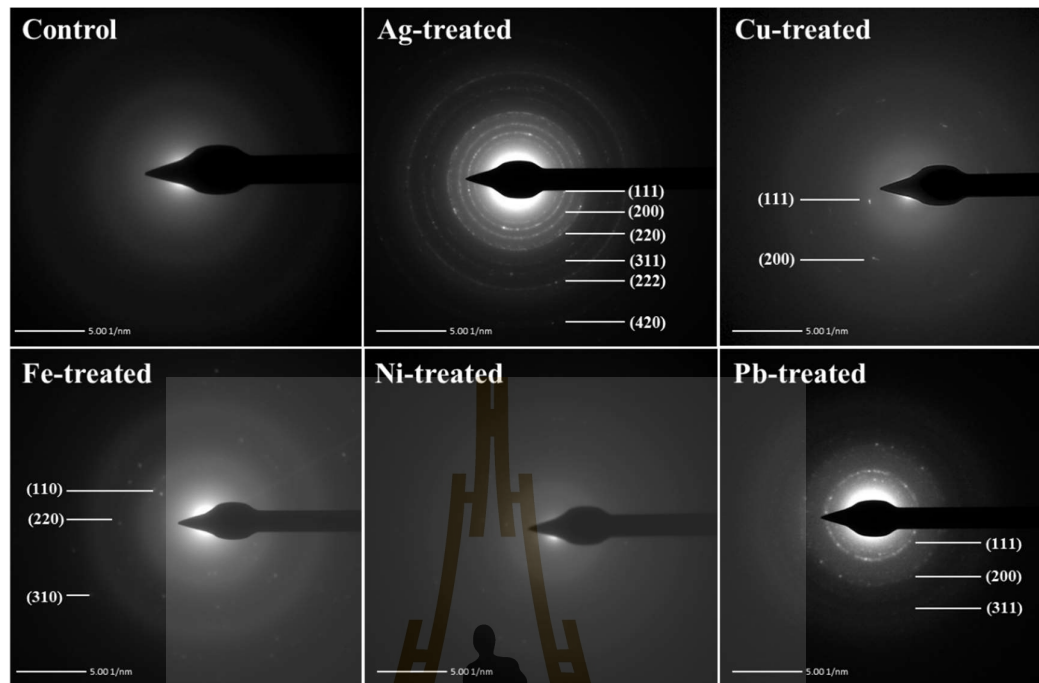


Figure 5.29 SAED-TEM analyses of the Ag-, Cu-, Fe-, Ni-, and Pb-treated roots of *Spirodela polyrhiza* (L.) Schleid. as compared with the control.

EDX-TEM analyses (Figure 5.30) revealed the detection of Ag, Cu, Fe, and Pb elements at 57.40, 58.53, 51.06, and 69.59% mass in the Ag-, Cu, Fe-, and Pb-treated roots, respectively. These results supported the SAED-TEM and TEM analyses for the presence of AgNPs, CuNPs, FeNPs, and PbNPs in the metal-treated roots of *S. polyrhiza* (L.) Schleid. Similar to the previous data, there were the detected levels of C, O, and P due to the organic contents in the samples (Elnaggar et al., 2015). Also, the detected level of Cu was due to the sample holder that contained Cu, the carbon-coated Cu grid (Janthima et al., 2018).

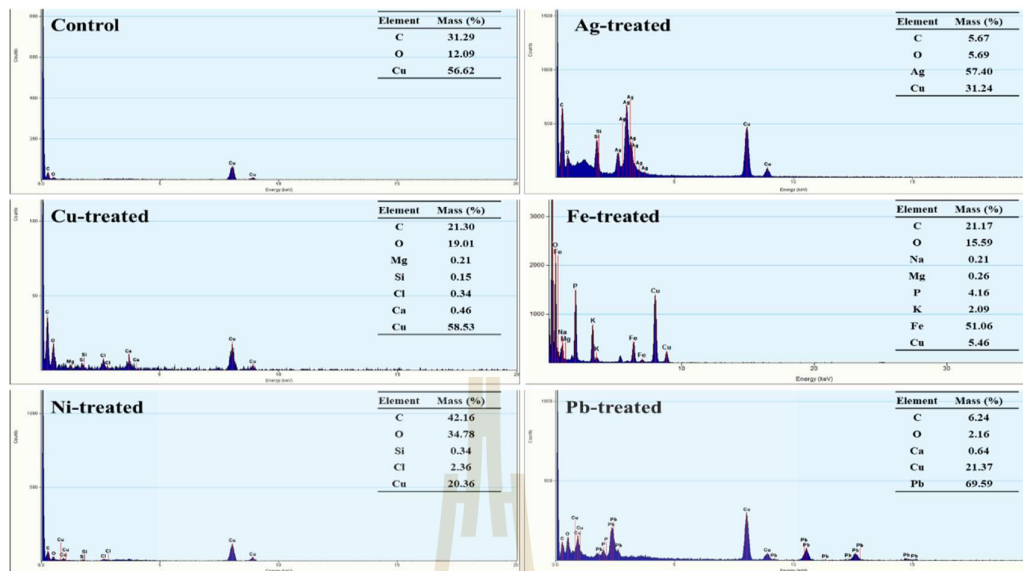


Figure 5.30 EDX-TEM analyses of the Ag-, Cu-, Fe-, Ni-, and Pb-treated roots of *Spirodela polyrhiza* (L.) Schleid. as compared with the control.

5.4.4 *Wolffia globosa* (Roxb.) Hartog & Plas

The formation of metal NPs in *W. globosa* (Roxb.) Hartog & Plas was determined by TEM images. TEM images (Figure 5.31) revealed the presence of spherical AgNPs, FeNPs, and PbNPs was widely distributed in the chloroplast cells of Ag-, Fe, and Pb-treated plant. Average diameter and size distribution of spherical AgNPs, FeNPs, and PbNPs in cortical cell was measured from TEM images using ImageJ software (Abràmoff et al., 2004) and origin program with 100 particles. The results showed that average diameter of AgNPs, FeNPs, and PbNPs were 32.42 ± 16.46 , 9.68 ± 4.95 , and 69.96 ± 24.59 nm, respectively (Figure 5.32).

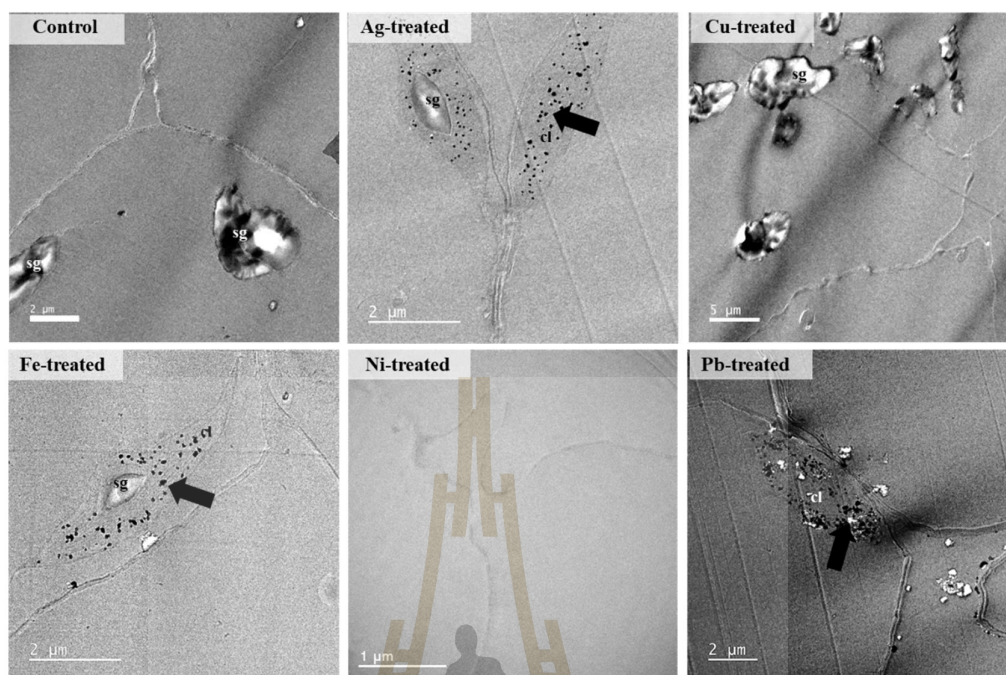


Figure 5.31 TEM images of metal NPs in the Ag-, Cu-, Fe-, Ni-, and Pb-treated *Wolffia globosa* (Roxb.) Hartog & Plas. Dark arrow: NPs.

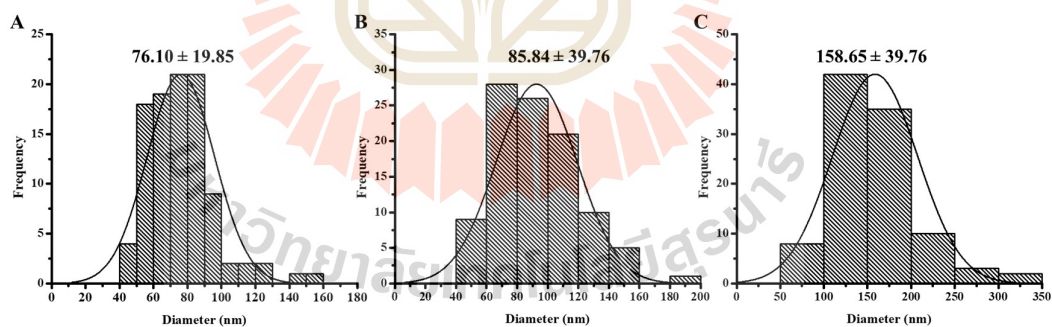


Figure 5.32 Size distribution histograms and average diameters of (A) AgNPs, (B) FeNPs, and (C) PbNPs in the Ag-, Fe-, and Pb-treated *Wolffia globosa* (Roxb.) Hartog & Plas.

The identity of metal NPs in *W. globosa* (Roxb.) Hartog & Plas was analyzed by SAED-TEM and EDX. SAED-TEM images (Figure 5.33) revealed the presence of

metal NPs in Ag-, Fe-, and Pb-treated plants. In the Ag-treated plants, SAED-TEM images showed the presence of the concentric diffraction rings at 2.35, 2.04, 1.44, 1.23, 1.79, 0.93, and 0.91 Å that corresponded to the hkl planar of (111), (200), (220), (311), (222), (331), and (420) of the FCC structure of Ag based on the JSPDS number 65–2871 (Shobha et al., 2018). For the Fe-treated plants, the concentric diffraction rings were detected at 4.85, 2.97, and 2.53 Å, corresponding to the hkl planar of (111), (220), and (311) of the structure of Fe₃O₄ structure based on the JCPDS number 01–1111 (Hedayati et al., 2017). The additional concentric diffraction ring was detected at 0.83 Å, corresponding to the hkl planar of (222) of the FCC structure of Fe (based on JCPDS number 01–1262) (Oliver, 2012). In the Pb-treated plants, the concentric diffraction rings were marked at 2.82, 2.44, 1.74, 1.48, and 1.42 Å, corresponding to the hkl planar of (111), (200), (220), (311), and (222) of the cubic (Fm3m) lattice of Pb structure based on the JCPDS number 01–0811 (Mahmoud et al., 2015).

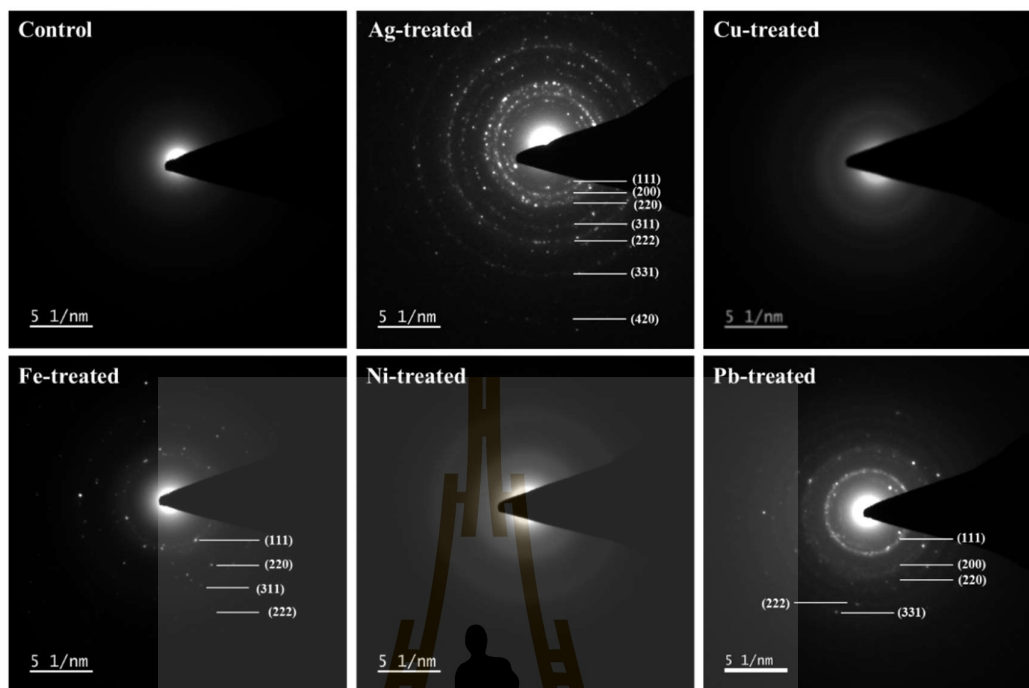


Figure 5.33 SAED-TEM analyses of the Ag-, Cu-, Fe-, Ni-, and Pb-treated *Wolffia globosa* (Roxb.) Hartog & Plas as compared with the control.

EDX-TEM analysis was also employed to identify the elemental profiles of the metals in Ag-, Cu-, Fe-, Ni-, and Pb-treated roots (Figure 3.34). The EDX-TEM profiles showed the presence of Ag, Fe, and Pb of 51.67, 34.67, and 55.89 % mass in the Ag-, Fe-, and Pb-treated samples, respectively. These data were well related to the SAED-TEM and TEM analyses, which suggested the formation of AgNPs, FeNPs, and PbNPs, but not CuNPs and NiNPs in *W. globosa* (Roxb.) Hartog & Plas. The detection of C, O, and P, Cu in some samples was previously explained.

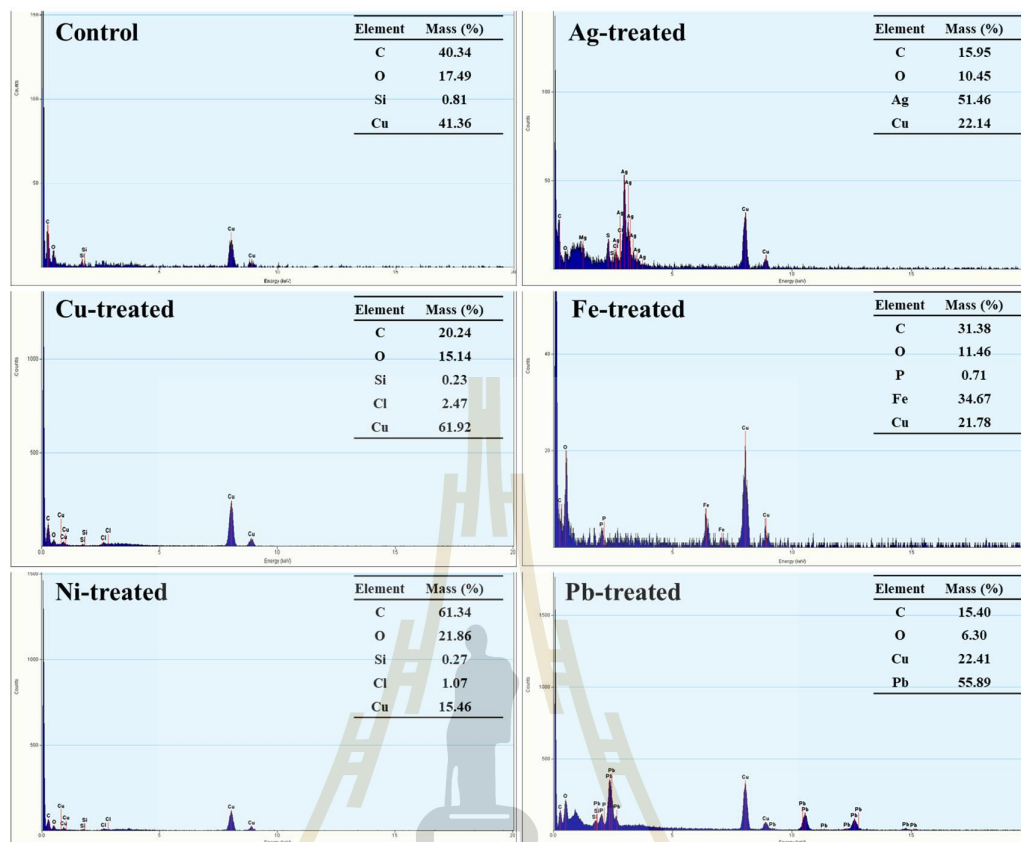


Figure 5.34 EDX-TEM analyses of the Ag-, Cu-, Fe-, Ni-, and Pb-treated *Wolffia globosa* (Roxb.) Hartog & Plas as compared with the control.

In this section, the abilities of four aquatic plant species, belonging to the same Araceae family, to transform the uptake metal ions (Ag, Cu, Fe, Ni, and Pb) to metal NPs were reported: *L. minor* L., *L. perpusilla* Torr., *S. polyrhiza* (L.) Schleid., and *W. globosa* (Roxb.) Hartog & Plas. The results showed that these plant species efficiently absorb these metal ions as determined by EDXRF analysis. Among five metal ions, they were most sensitive to Ag⁺ ions. Moreover, all metal-treated plants showed the similar response in which the ¹⁹K and ²⁰Ca levels were decreased in response to all metal treatments. ATR-FTIR results also suggested the metal responses in the plant roots via the induction levels of phosphorus-containing biomolecules,

lipids, soluble sugars, gene expression, and protein synthesis. Interestingly, TEM images suggested that the formation of metal NPs depended on the types of uptake metal ions and plant species. The formation of AgNPs, CuNPs, FeNPs, and PbNPs, except NiNPs, was detected in *S. polyrhiza* (L.) Schleid. roots. Unlike *S. polyrhiza* (L.) Schleid roots, *L. minor* L., *L. perpusilla* Torr., and *W. globosa* (Roxb.) Hartog & Plas root cells could assist the formation of only AgNPs, FeNPs, and PbNPs, but not CuNPs, and NiNPs. In addition, the shape of metal NPs was different, depending on the plant species. In this work, *L. minor* L. root cells clearly showed the formation of short rod-shaped PbNPs, whereas spherical PbNPs were detected in *L. perpusilla* Torr., *S. polyrhiza* (L.) Schleid., and *W. globosa* (Roxb.) Hartog & Plas. The identity of metal NPs was confirmed by SAED-TEM, which AgNPs, CuNPs (Cu and CuO), FeNPs (Fe, FeO, Fe₂O₃ and Fe₃O₄), and PbNPs (Pb and PbO) were detected. In comparison, the summary data of these four plant species are shown in Table 5.7.

Table 5.8 Summary data of *Lemna minor* L., *Lemna perpusilla* Torr., *Spirodela polyrhiza* (L.) Schlel., and *Wolffia globosa* (Roxb.) Hartog & Plas in response to five metal ions and their capability to produce metal NPs.

Topics	Aquatic plants	Metal ion treatments				
		Ag ⁺	Cu ²⁺	Fe ³⁺	Ni ²⁺	Pb ²⁺
TC10 (mM)	<i>Lemna minor</i> L.	1.23 ± 0.9 ^b	10.25 ± 3.40 ^a	20.13 ± 5.12 ^b	200.64 ± 6.21 ^a	300.96 ± 12.34 ^b
	<i>Lemna perpusilla</i> Torr.	1.04 ± 2.30 ^a	20.19 ± 2.13 ^b	30.16 ± 10.32 ^c	300.17 ± 6.12 ^b	400.02 ± 2.39 ^c
	<i>Spirodela polyrhiza</i> (L.) Schlel.	1.01 ± 0.60 ^a	20.16 ± 5.13 ^b	20.89 ± 6.21 ^b	300.79 ± 12.40 ^b	300.69 ± 21.06 ^b
	<i>Wolffia globosa</i> (Roxb.) Hartog & Plas	0.96 ± 0.16 ^a	21.06 ± 12.64 ^c	10.94 ± 12.16 ^a	300.89 ± 16.14 ^b	200.69 ± 21.49 ^a
Metal uptake analysis (% mass)	<i>Lemna minor</i> L.	71.91 ± 0.57 ^a	67.85 ± 3.31 ^c	82.70 ± 4.70 ^b	44.92 ± 3.50 ^b	99.41 ± 0.31 ^d
	<i>Lemna perpusilla</i> Torr.	84.82 ± 0.80 ^c	50.90 ± 12.80 ^a	70.14 ± 3.97 ^a	94.18 ± 0.01 ^d	94.18 ± 0.01 ^c
	<i>Spirodela polyrhiza</i> (L.) Schlel.	89.30 ± 4.11 ^d	62.88 ± 2.94 ^b	88.81 ± 0.30 ^d	40.85 ± 5.80 ^a	90.21 ± 6.17 ^a
	<i>Wolffia globosa</i> (Roxb.) Hartog & Plas	76.71 ± 3.71 ^b	69.22 ± 6.49 ^d	83.65 ± 3.81 ^c	64.17 ± 1.08 ^c	92.40 ± 4.31 ^b
Formation of NPs	<i>Lemna minor</i> L.	AgNPs	nd	FeNPs	nd	PbNPs
	<i>Lemna perpusilla</i> Torr.	AgNPs	nd	FeNPs	nd	PbNPs
	<i>Spirodela polyrhiza</i> (L.) Schlel.	AgNPs	CuNPs	FeNPs	nd	PbNPs
	<i>Wolffia globosa</i> (Roxb.) Hartog & Plas	AgNPs	nd	FeNPs	nd	PbNPs

Table 5.7 Summary data of *Lemna minor* L., *Lemna perpusilla* Torr., *Spirodela polyrhiza* (L.) Schlel., and *Wolffia globosa* (Roxb.) Hartog & Plas in response to five metal ions and their capability to produce metal NPs (Continued).

Topics	Aquatic plants	Metal ion treatments				
		Ag ⁺	Cu ²⁺	Fe ³⁺	Ni ²⁺	Pb ²⁺
Shapes of NPs	<i>Lemna minor</i> L.	Sphere	-	Sphere	-	Short rod
	<i>Lemna perpusilla</i> Torr.	Sphere	-	Sphere	-	Sphere
	<i>Spirodela polyrhiza</i> (L.) Schlel.	Sphere	Sphere	Sphere	-	Sphere
	<i>Wolffia globosa</i> (Roxb.) Hartog & Plas	Sphere	Sphere	Sphere	-	Sphere
Identity of NPs		FCC of AgNPs	-	FCC of FeONPs, Cubic of Fe ₂ O ₃ NPs Cubic of Fe ₃ O ₄ NPs	-	Tetragonal of PbONPs
	<i>Lemna minor</i> L.					
	<i>Lemna perpusilla</i> Torr.	FCC of AgNPs	-	FCC of FeNPs	-	FCC of PbNPs
	<i>Spirodela polyrhiza</i> (L.) Schlel.	FCC of AgNPs	Cubic (CuO)	FCC of FeNPs	-	Cubic of PbNPs
	<i>Wolffia globosa</i> (Roxb.) Hartog & Plas	FCC of AgNPs	-	Cubic of FeONPs	-	Cubic of PbNPs
				Cubic of Fe ₃ O ₄ NPs		

nd = not detection.

(a-c) = Significant differences of each metal level were compared among different plant species.

CHAPTER VI

RESULTS AND DISCUSSION PART III

Pontederiaceae family: The ability of *Eichhornia crassipes* (Mart.)

Solms to absorb and transform metal ions to metal nanoparticles

In this part, the ability of *E. crassipes* (Mart.) Solms to absorb and transform metal ions to metal NPs were investigated since this plant species is widely distributed in natural water and it is suggested as a good contaminant-absorbing plant.

6.1 Toxicity Test

The effects of five metal ions: AgNO_3 , $\text{Cu(NO}_3)_2$, $\text{Fe(NO}_3)_3$, $\text{Ni(NO}_3)_2$, and $\text{Pb(NO}_3)_2$, on water hyacinth were determined by the changed morphology of its leaves (withered and brown leaves) that was calculated as %toxicity and toxicity concentration (TC) at 10%, 20%, 50%, and 80% (Table 6.1). The results showed that the values of TC10, TC20, TC50, and TC80 of all metal treatments increased according to the increasing metal concentrations, which is also known as the dose-dependent response. Among five metal ions, the TC value was highest for Pb^{2+} , followed by Ni^{2+} , whereas the lowest was Ag^+ , suggesting that this plant was highly tolerant to Pb^{2+} , followed by Ni^{2+} but very sensitive to Ag^+ .

Table 6.1 Toxicity concentrations of five metal ions on water hyacinth.

Treatment	Toxicity concentration (mM)			
	TC10	TC20	TC50	TC80
AgNO ₃	2.79 ± 1.17	3.67 ± 3.18	5.82 ± 0.16	9.24 ± 2.34
Cu(NO ₃) ₂	27.17 ± 1.06	32.13 ± 8.11	42.67 ± 2.56	56.66 ± 1.06
Fe(NO ₃) ₃	28.46 ± 0.99	32.46 ± 4.74	40.53 ± 1.63	50.60 ± 1.27
Ni(NO ₃) ₂	307.99 ± 0.74	350.04 ± 21.53	434.49 ± 38.15	539.29 ± 2.57
Pb(NO ₃) ₂	281.85 ± 1.46	370.57 ± 4.36	588.24 ± 3.65	933.77 ± 5.26

N = 5, $p < 0.05$, two replications

In addition to the leave morphology, the root morphology in response to metal treatment was determined under a light microscope. Based on images of cross-sectioned roots, the presence of dark particles was detected in cell wall, aerenchyma chamber, endodermis, xylem, and phloem. We hypothesized that these metal ions penetrated into the roots passing through cell wall and plasma membrane of epidermis, exodermis, and aerenchyma chamber, and finally reached the vascular system. In the cortex tissue (Figure 6.1), the accumulation of dark particles was clearly seen in Ag-, Cu-, Fe-, and Pb-treated roots, but not in Ni-treated roots. Similarly, the accumulation of dark particles was also detected in the vascular tissues of Ag-, Cu-, Fe-, and Pb-treated roots, but not in Ni-treated roots (Figure 6.2). These results suggested the penetration of these metal ions from the outermost layer of the root cells into a vascular system and the possible transport to other parts of the plant. In addition, more accumulated particles were observed as the higher concentrations of metal ions were used (data in APPENDIX C).

The withered and brown leaves as well as dark brown roots and stems in response to these metal treatments were hypothesized to involve the plasmolysis and toxicity effects of these metal ions. Under a metal exposure, the plant cells were affected by the metal toxicity, leading to cellular damage, high level of reactive oxygen species, disruption of normal metabolic reactions, reduction of growth, inhibition of seed germination, alteration of chlorophyll content, injury of shoot and root, leaf chlorosis, suppression of root nodules and death (Arif et al., 2016). It was noted that in this work the leave morphology was changed in response to Ni-treatment, however no dark particles were observed in the cross-sectioned roots, raising the question whether water hyacinth can accumulate Ni^{2+} as metal NPs inside their roots.

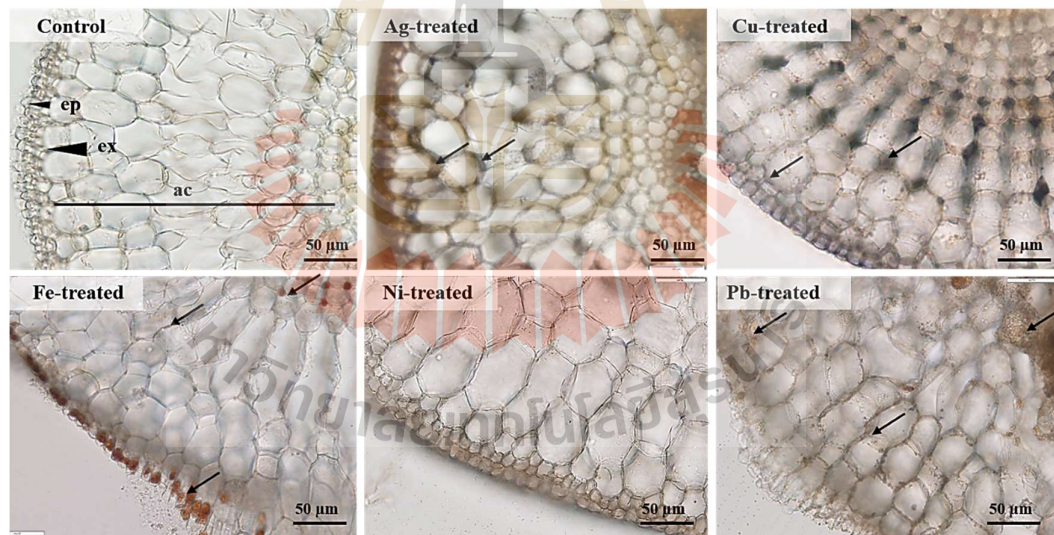


Figure 6.1 Cross-sections in cortex tissue of water hyacinth roots exposed to AgNO_3 , $\text{Cu}(\text{NO}_3)_2$, $\text{Fe}(\text{NO}_3)_3$, $\text{Ni}(\text{NO}_3)_2$, and $\text{Pb}(\text{NO}_3)_2$ solutions observed under a light microscope. Abbreviation lists; ac (aerenchyma chamber), ep (epidermis), and ex (exodermis).

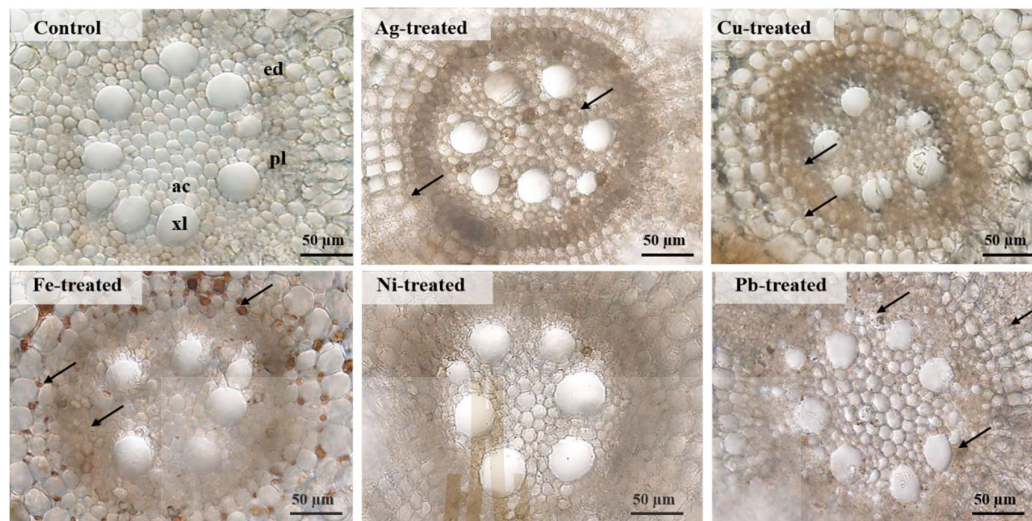


Figure 6.2 Cross-sections in the vascular tissue of water hyacinth roots exposed to AgNO_3 , $\text{Cu(NO}_3)_2$, $\text{Fe(NO}_3)_3$, $\text{Ni(NO}_3)_2$, and $\text{Pb(NO}_3)_2$ solutions observed under a light microscope. Abbreviation lists: ed (endodermis), pl (phloem), and xl (xylem).

6.2 The Elemental Mass Profiles

The elemental profiles of water hyacinth roots in response to Ag-, Cu-, Fe-, Ni-, and Pb-treatments was analyzed by EDXRF. The representative images of some elemental mapping were presented in Figure 6.3. The results showed that the treated roots showed the significantly different levels of 9 elements (^{15}P , ^{16}S , ^{19}K , ^{20}Ca , ^{26}Fe , ^{28}Ni , ^{29}Cu , ^{47}Ag , and ^{82}Pb) as compared with the control roots. Table 1 shows the corresponding quantification of these elements in the treated roots. The quantitative level of ^{26}Fe in the treated roots was highest (81.68% mass), followed by ^{82}Pb (81.12% mass), ^{29}Cu (78.88% mass), ^{47}Ag (62.17% mass), and ^{28}Ni (59.26% mass), respectively. As compared with the studies of other plants in this research, water hyacinth has a broader tolerance to metal ions as determined by the high accumulated elements in its

roots. In addition, the significant reduction levels of ^{19}K and ^{20}Ca were detected in all metal treatments. Also, the significant induction of ^{15}P was detected only in Ni- and Ag-treated roots.

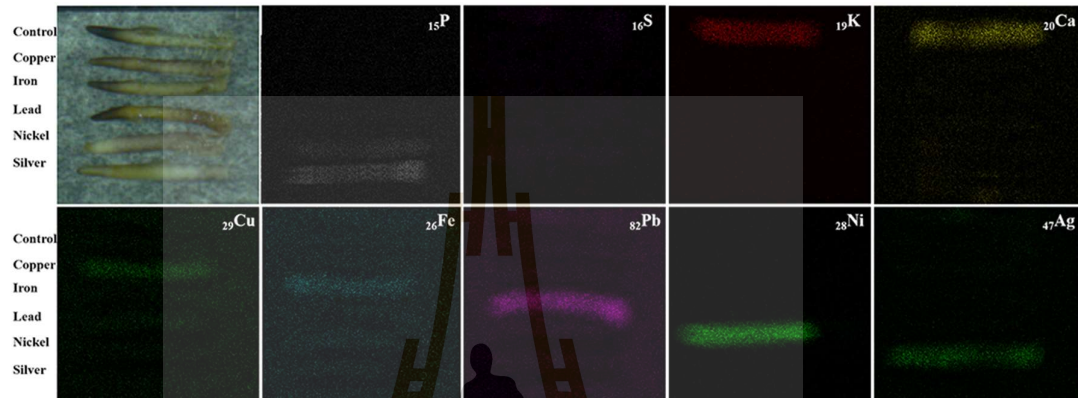


Figure 6.3 EDXRF elemental mapping of the water hyacinth roots treated with AgNO_3 , $\text{Cu}(\text{NO}_3)_2$, $\text{Fe}(\text{NO}_3)_3$, $\text{Ni}(\text{NO}_3)_2$, and $\text{Pb}(\text{NO}_3)_2$ solutions.



Table 6.2 Elemental mass of water hyacinth roots in response to metal exposures.

Metal Elements	Control root	% Element mass in the treated roots with					
		AgNO ₃	Cu(NO ₃) ₂	Fe(NO ₃) ₃	Ni(NO ₃) ₂	Pb(NO ₃) ₂	
¹⁵ P	1.2 ± 1.0 ^a	37.9 ± 1.5 ^c	1.6 ± 0.1 ^a	0.5 ± 1.2 ^a	31.4 ± 3.5 ^b	2.0 ± 2.6 ^a	
¹⁶ S	0.2 ± 0.1 ^a	0.0 ± 0.0 ^a	0.6 ± 0.8 ^a	0.8 ± 1.2 ^a	0.3 ± 0.5 ^a	0.2 ± 0.4 ^a	
¹⁹ K	64.4 ± 4.3 ^b	0.6 ± 1.2 ^a	1.3 ± 0.3 ^a	1.6 ± 1.3 ^a	0.9 ± 1.2 ^a	1.5 ± 1.8 ^a	
²⁰ Ca	55.4 ± 1.9 ^b	0.8 ± 0.4 ^a	0.4 ± 0.3 ^a	1.2 ± 0.8 ^a	1.3 ± 0.6 ^a	1.5 ± 0.3 ^a	
²⁹ Cu	0.3 ± 0.4 ^a	1.7 ± 0.9 ^a	78.9 ± 2.7^b	1.9 ± 0.5 ^a	0.3 ± 0.2 ^a	0.4 ± 0.2 ^a	
¹⁶ Fe	0.9 ± 1.0 ^a	1.7 ± 2.4 ^a	0.5 ± 0.4 ^a	81.7 ± 3.6^b	0.9 ± 0.4 ^a	1.9 ± 0.3 ^a	
⁸² Pb	0.0 ± 0.0 ^a	0.0 ± 0.0 ^a	0.1 ± 0.0 ^a	1.1 ± 0.7 ^a	2.0 ± 1.8 ^a	81.1 ± 4.1^b	
²⁸ Ni	0.0 ± 0.1 ^a	0.1 ± 0.1 ^a	0.1 ± 0.1 ^{a,b}	1.3 ± 0.3 ^{a,b}	59.3 ± 3.8^c	3.2 ± 0.6 ^{a,b}	
⁴⁷ Ag	0.1 ± 0.2 ^a	62.2 ± 3.4^b	0.9 ± 0.8 ^a	0.9 ± 0.9 ^a	0.1 ± 0.1 ^a	0.1 ± 0.1 ^a	

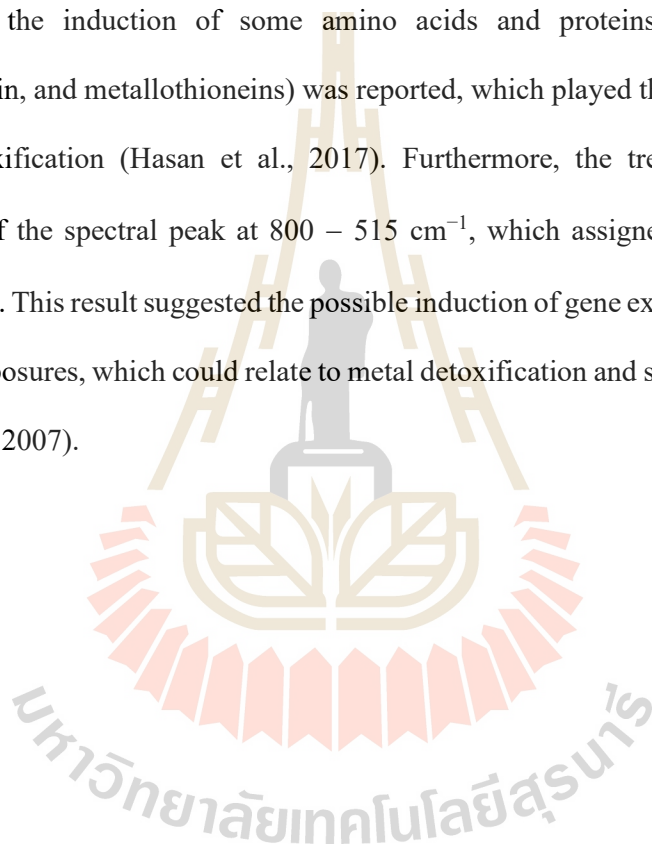
N = 5, *p* < 0.05 (compared with the control root).

The transports of metal ions to root tissues were reported to mediate via several transporters such as the ZIP family and COPT family for Cu transport (Yruela, 2009), the Fe-nicotianamine transporters and ZIP family for Fe transport (Aydemir and Cousins, 2018), the plant NRAMP family and ZIP family for Pb transport (Thomine et al., 2000), the high affinity Ni transport protein, metallothionein and metallochaperones for Ni transport and the NRAMP and ZIP family for Ag transport (Chen et al., 2009). As the reduction levels of ^{19}K and ^{20}Ca were detected in all metal treatments, we hypothesized that the treated metal ions might enter the root cells via the same routes of Ca^{2+} and K^{+} ions, including channels and protein transporters, thus competing with Ca^{2+} and K^{+} transports and limiting their influxes (Ahmad et al., 2016). Furthermore, the increased level of ^{15}P in the Ni-, and Ag-treated roots was possibly due to the production of polyphosphates, which was produced to cap metal ions, forming the osmotically inert polyphosphate bodies, to detoxify these metal ions in plant cells (Guasch et al., 2004; Luo et al., 2014).

6.3 The ATR-FTIR Profiles of Water Hyacinth Roots

The modulation levels of cellular biomolecules in Ag-, Cu-, Fe-, Ni-, and Pb-treated roots as compared with the control roots was analysed by ATR-FTIR (Figure 6.4 and Table 6.3). The roots treated with AgNO_3 , $\text{Cu}(\text{NO}_3)_2$, $\text{Fe}(\text{NO}_3)_3$, $\text{Ni}(\text{NO}_3)_2$, and $\text{Pb}(\text{NO}_3)_2$ solutions had the intensity reduction of the spectral peak in a range of $3600\text{--}3300\text{ cm}^{-1}$. This spectral peak corresponded to O–H stretching vibration of phenolic compounds and carbohydrates such as cellulose, hemicellulose, pectin, and lignin. The decrease of free O–H groups of these compounds might relate to their interaction to metal ions, especially some flavonoids that chelated heavy metal ions to

reduce their toxicity (Mira et al., 2002). However, the reduction of this peak intensity was not detected in Fe-treated roots. The new emerging peaks at 1800 – 1630, 1500–1395, and 1000 – 800 cm^{-1} in the treated plants were detected, referring to C=O stretching of carbonyl compounds of the amine I, C–N group of the amide II, and N–H group of proteins, respectively (Suresh et al., 2016a; 2016b). In response to metal treatments, the induction of some amino acids and proteins (such as proline, phytochelatin, and metallothioneins) was reported, which played the important roles in metal detoxification (Hasan et al., 2017). Furthermore, the treated roots had the induction of the spectral peak at 800 – 515 cm^{-1} , which assigned to N–C group of nucleic acid. This result suggested the possible induction of gene expression in response to metal exposures, which could relate to metal detoxification and stress response genes (Puig et al., 2007).



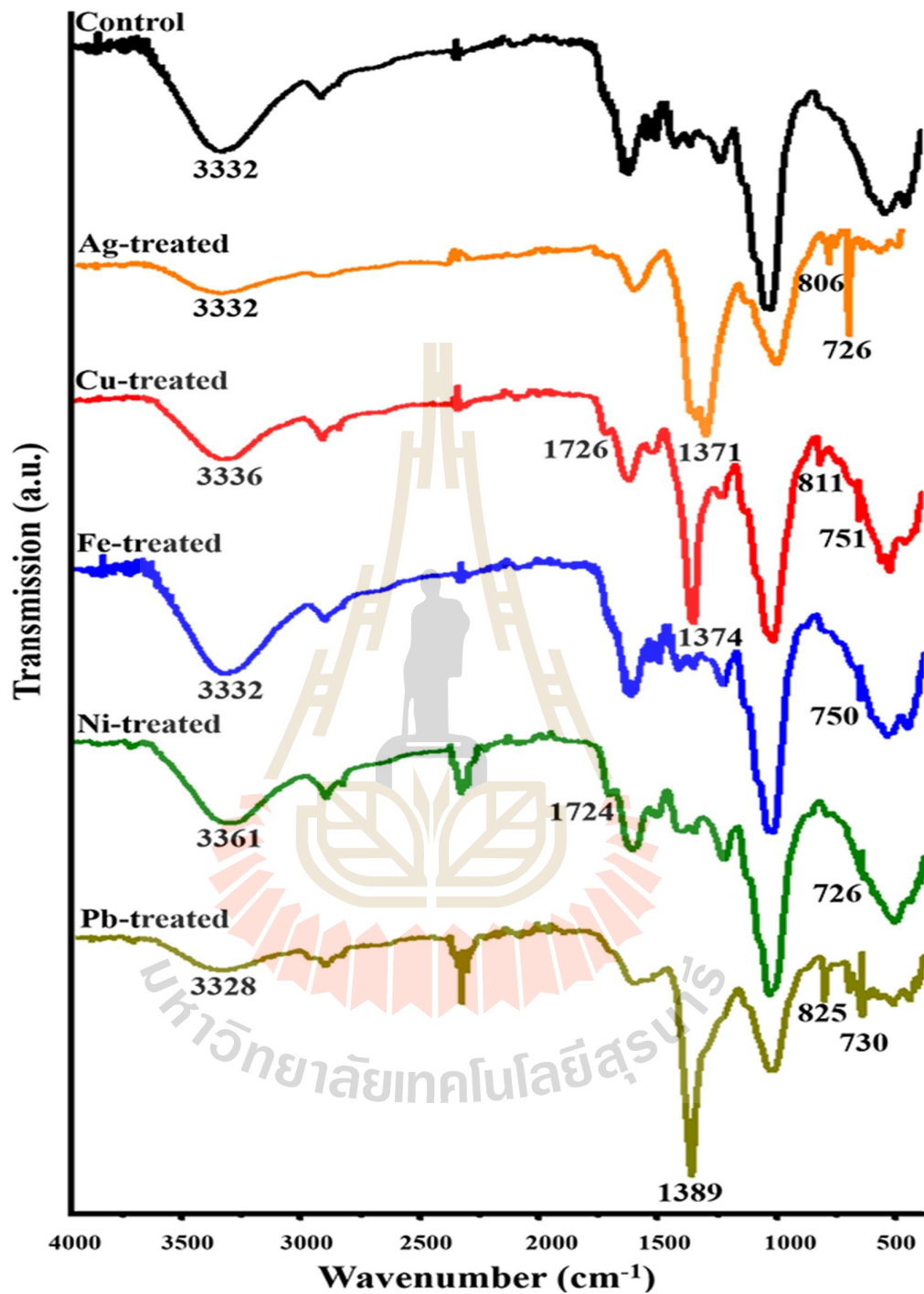


Figure 6.4 ATR-FTIR spectra of the control and metal-treated roots of water hyacinth in the wavelength range of 4000 – 400 cm^{-1} .

Table 6.3 The summary of ATR-FTIR spectral peaks of the metal-treated roots of water hyacinth.

No.	Standard reference	Wave number (cm ⁻¹)						Functional groups	Biological compounds
		Ctrl	Treated roots						
			Ag	Cu	Fe	Ni	Pb		
1	3600–3300	3332	3332	3336	3332	3361	3328	O–H	Carbohydrate, phenolic
2	1800–1630	nd	nd	1726	nd	1724	nd	C=O	Amine I proteins
3	1395–1370	nd	1371	1374	nd	nd	1389	C–N	Amide II proteins
5	1000–800	nd	806	811	nd	nd	825	N–H	Proteins
6	800–515	nd	726	751	750	726	730	N–C	Nucleic acids

nd: no detected

6.4 Accumulation of Metal Nanoparticles

The accumulation of AgNPs, CuNPs, FeNPs, NiNPs, and PbNPs in water hyacinth roots was determined by TEM analysis. In Figure 6.5, TEM images revealed the accumulated NPs in cortical cells of water hyacinth only in the Ag-, Cu-, Fe-, and Pb-treated roots, but not Ni-treated and control roots. The deposition of metal NPs predominantly near the plasma membrane, but the deposition of AgNPs mostly located in cytoplasm. The average diameters of deposited AgNPs, CuNPs, FeNPs, and PbNPs were 56.54 ± 1.58 , 32.97 ± 1.09 , 31.88 ± 8.02 , and 24.19 ± 9.71 nm, respectively.

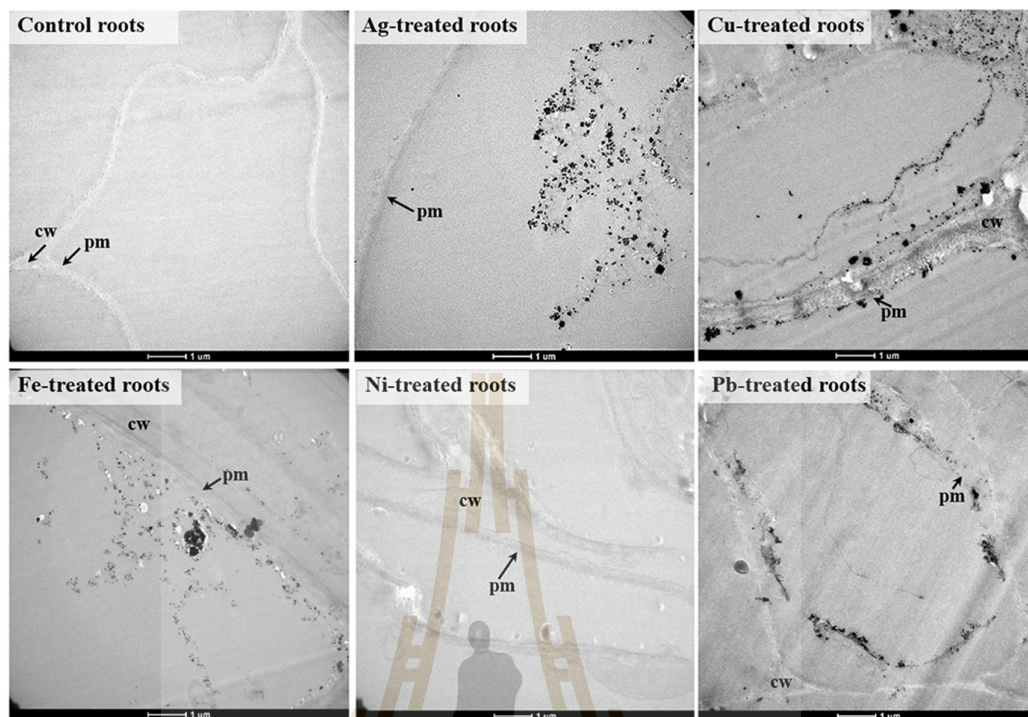


Figure 6.5 TEM images of cortical cells of the Ag-, Cu-, Fe-, Ni-, and Pb-treated roots.

Abbreviation lists: pm (plasma membrane) and cm (cell wall).

In Figure 6.6, the representative TEM images also revealed the deposition of AgNPs, CuNPs, FeNPs, and PbNPs, but not NiNPs, in xylem of the treated water hyacinth roots. The localization of the NPs was predominantly near the plasma membrane and some distributed in the cytoplasm. The average diameter of the AgNPs, CuNPs, and PbNPs were 34.14 ± 9.01 , 28.05 ± 9.70 , and 26.03 ± 1.21 nm, respectively. Interestingly, two distinct sizes of FeNPs were detected; 19.33 ± 7.77 , and 122.31 ± 68.90 nm, where the small size was detected at the plasma membrane of small xylem vessels and the large size was detected at the plasma membrane of large xylem vessels.

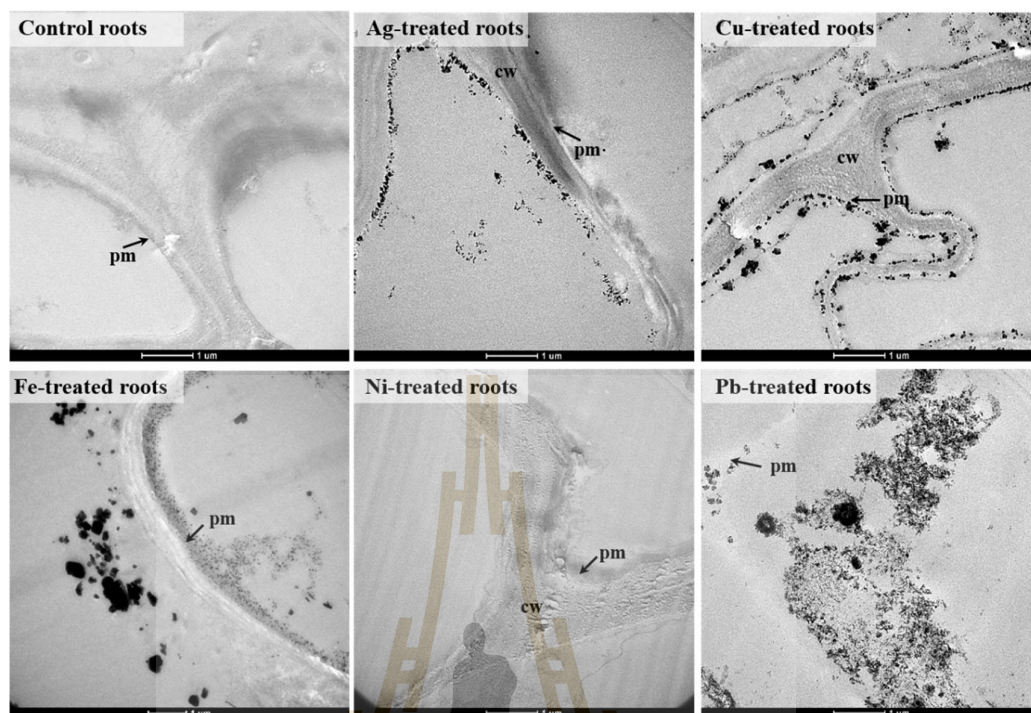


Figure 6.6 TEM images of xylem of the Ag-, Cu-, Fe-, Ni-, and Pb-treated roots of water hyacinth. Abbreviation lists: pm (plasma membrane) and cm (cell wall).

6.5 Characterization of Metal Nanoparticles

The HR-TEM, SAED-TEM, and EDX analyses were carried out to determine the identity of the accumulated NPs in water hyacinth roots. Figure 6.7 shows the representative HR-TEM images of the accumulated NPs in the water hyacinth roots exposed to AgNO_3 , $\text{Cu}(\text{NO}_3)_2$, $\text{Fe}(\text{NO}_3)_3$, $\text{Ni}(\text{NO}_3)_2$, and $\text{Pb}(\text{NO}_3)_2$ solutions. In the Ag-treated roots, the lattice spacing analysis revealed the d -spacing value of 0.241 ± 0.053 nm, well corresponding to the (111) plane of the FCC lattice of Ag (Balakumaran et al., 2015). In the Cu-treated roots, the detected d -spacing value was 0.210 ± 0.064 nm, corresponding to the (111) plane of the FCC lattice of Cu (Wang et al., 2014). In the

Fe-treated roots, the detected d -spacing values were 0.151 ± 0.044 and 0.296 ± 0.031 nm, suggesting the (220) and (400) planes of the Fe_2O_3 and Fe_3O_4 , respectively (Iyengar et al., 2014). In the Pb-treated roots, the detected d -spacing value was 0.249 ± 0.042 nm, well corresponding to the (200) of the cubic (Fm3m) lattice of Pb structure (Roy and Bysakh, 2011). In a good agreement with TEM images, the HR-TEM results showed no detection of d -spacing value in the Ni-treated roots, suggesting no formation of NiNPs.

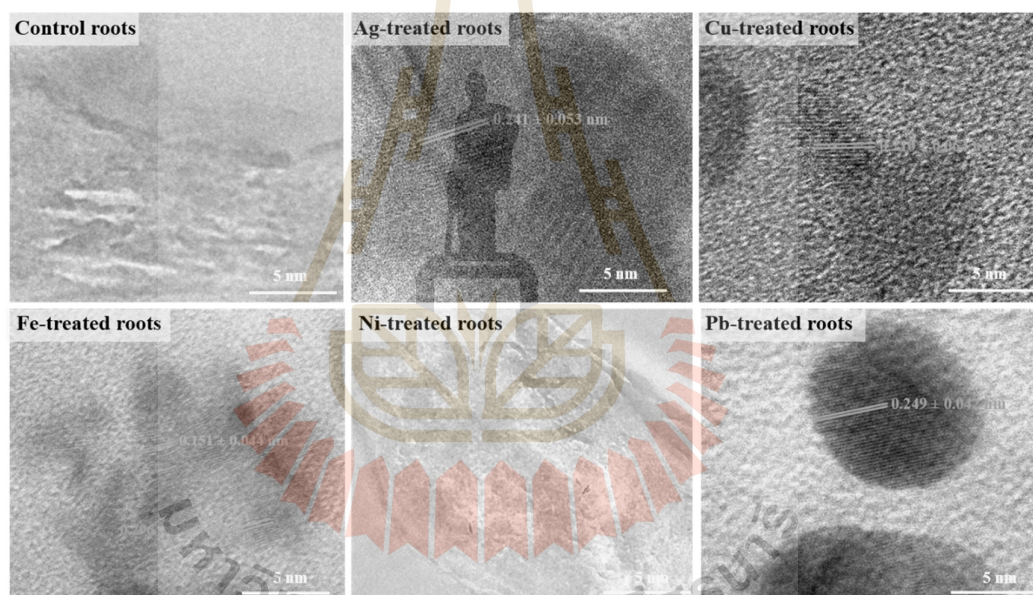


Figure 6.7 HR-TEM analyses of the Ag-, Cu-, Fe-, Ni-, and Pb-treated roots as compared with the control root.

Figure 6.8 shows the representative SAED-TEM analyses of the accumulated NPs in the root cells after exposure to AgNO_3 , $\text{Cu}(\text{NO}_3)_2$, $\text{Fe}(\text{NO}_3)_3$, $\text{Ni}(\text{NO}_3)_2$, and $\text{Pb}(\text{NO}_3)_2$ solutions. The SAED-TEM analysis of the NPs deposited in the Ag-treated root cells showed the presence of the concentric diffraction rings at 2.11, 2.02, 1.48,

1.28, and 0.94 Å that corresponded to the hlk planar of (111), (200), (220), (311), and (331) of the FCC structure of Ag as based on the database of Joint Committee on JCPDS number 04–0783 (Balakumaran et al., 2015). For the NPs deposited in the Cu-treated root cells, the concentric diffraction rings were 3.00, 2.72, 1.41, and 0.93 Å, corresponding to the hlk planar of (111), (200), (220), and (331) of the FCC structure of Cu (Wang et al., 2014). In Fe-treated roots, the concentric diffraction rings of 3.66 and 1.46 Å were detected, suggesting the hlk planar of (311) and (400) of Fe_2O_3 (Shao et al., 2011), while the concentric diffraction rings of 4.84, 2.00, 1.27, and 1.50 Å corresponded to the hlk planar of (111), (110), (400), and (220) of Fe_3O_4 (Iyengar et al., 2014). For the NPs deposited in the Pb-treated root cells, the concentric diffraction rings were 1.49, 2.46, and 2.86 Å, corresponding to the hlk planar of (311), (200), and (111) of the cubic (Fm3m) lattice of Pb structure (JCPDS number 01–0972) (Roy and Bysakh, 2011). Similar to other results, no detection of concentric diffraction ring was in the Ni-treated roots, suggesting no production of NiNPs.

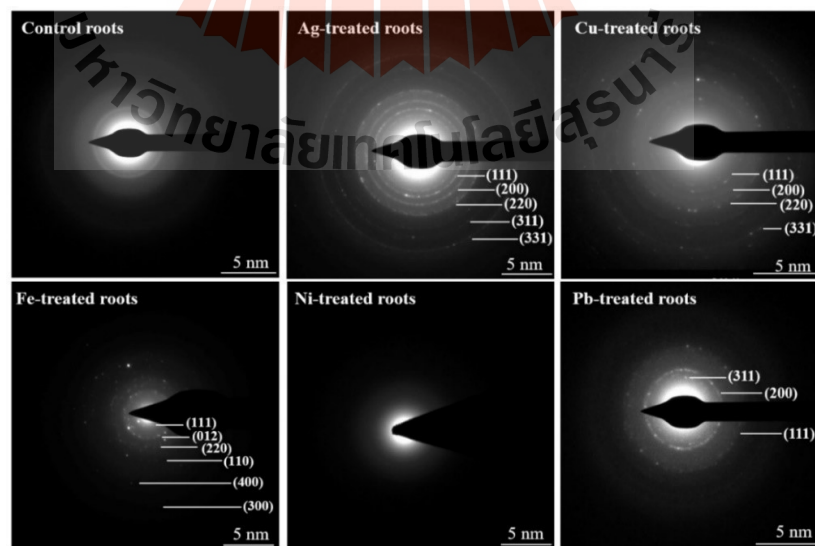


Figure 6.8 SAED-TEM analyses of metal-treated roots of water hyacinth.

Figure 6.9 shows the EDX spectra of elemental composition profiles of the water hyacinth roots treated with AgNO_3 , $\text{Cu(NO}_3)_2$, $\text{Fe(NO}_3)_3$, $\text{Ni(NO}_3)_2$, and $\text{Pb(NO}_3)_2$ solutions. The results showed that Ag (65.19% mass), Cu (12.16% mass), Fe (15.81% mass), and Pb (41.07% mass) elements were detected in Ag-, Cu-, Fe-, and Pb-treated roots, respectively. However, these elements were not detected in the control plant. In this result, Ni element was not detected in Ni-treated roots, possibly due to the low level Ni element than 0.1% mass, which is the detection limit of EDX-TEM analysis (Strüder, 2000). The low accumulation of Ni in plant roots may be explained by the translocation process, which some trace elements such as Ca, Ni, Mn, and Zn can form low molecular weight cationic and anionic complexes (500 – 10,000 molecular weight) and transport to leaves via symplastic pathway (Cataldo and Wildung, 1978). It is noted that although the Ni element could not be detected in Ni-treated roots via EDX analysis, it was detected by EDXRF due to its higher detection limit in a range of ppm (Strüder, 2000). In all samples, the detection of carbon and oxygen was likely from the organic materials in the plant and the carbon-coated Cu grid with 200 mesh used in this analysis (Janthima et al., 2018).

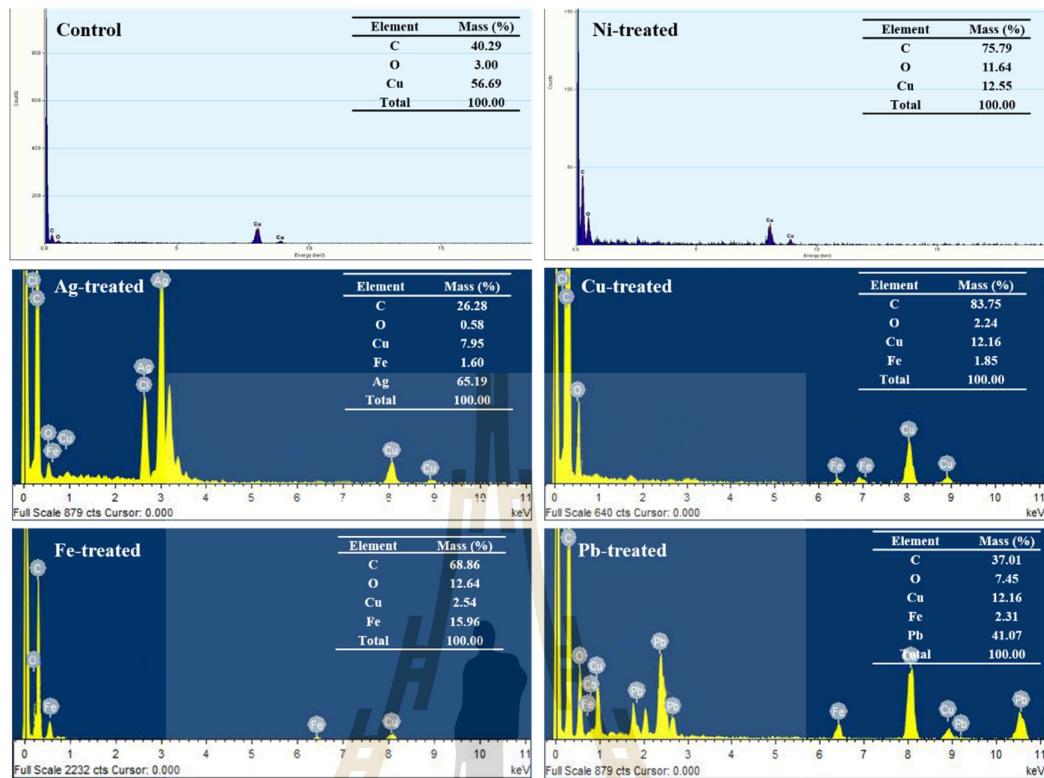


Figure 6.9 EDX-TEM analyses of the Ag-, Cu-, Fe-, Ni-, and Pb-treated roots as compared with the control root.

In this section, the ability of water hyacinth (*E. crassipes* (Mart.) Solms) to uptake and transform five metal ions (Ag^+ , Cu^{2+} , Fe^{3+} , Ni^{2+} , and Pb^{2+}) to metal NPs were reported. Water hyacinth had the high efficacy to uptake all five metal ions and most sensitive to Ag^+ as determined by its TC10 value. In response to all metal exposures, the reduction levels of ^{19}K and ^{20}Ca were detected, which could be the metal-stress response in this plant species. ATR-FTIR results also suggested the metal responses in its cellular biomolecules as indicated by the induction levels of phosphorus-containing biomolecules, lipids, soluble sugars, gene expression, and protein synthesis. TEM images revealed that the formation of metal NPs, which depended on the types of uptake metal ions. The formation of AgNPs, CuNPs, FeNPs, and PbNPs, except NiNPs, was detected in water hyacinth roots near the plasma membrane and cytoplasm of cortical and/or vascular tissues. The identity of metal NPs was identified by SAED-TEM, which cellular AgNPs, CuNPs, FeNPs (Fe_2O_3 and Fe_3O_4), and PbNPs (PbO) were confirmed. The responses of water hyacinth to five metal ions as well as its capability to uptake and transform these metal ions into metal NPs are summarized in Table 6.4.

Table 6.4 Data summary of water hyacinth in response to five metal ions and its capability to produce metal NPs.

Topics	Metal ion treatments				
	Ag ⁺	Cu ²⁺	Fe ³⁺	Ni ²⁺	Pb ²⁺
TC10 (mM)	2.8 ± 0.2	27.2 ± 1.1	28.5 ± 0.1	307.9 ± 0.7	281.9 ± 1.5
Metal uptake analysis (% mass)	62.2 ± 3.4	78.9 ± 2.7	81.7 ± 3.6	59.3 ± 3.8	81.1 ± 4.1
Formation of NPs	AgNPs	CuNPs	FeNPs	nd	PbNPs
Shapes of NPs	Sphere	Sphere	Sphere	-	Sphere
Identity of NPs	FCC of AgNPs	FCC of CuNPs	Cubic of Fe ₂ O ₃ NPs	-	Cubic of PbNPs

nd = not detected.

CHAPTER VII

RESULTS AND DISCUSSION PART VII

Comparison of seven plant species to uptake and transform metal ions into nanoparticles

As the capability of the studied plants to uptake and transform metal ions into NPs are the main investigation of this research. Thus, this chapter compares the data of these seven plant species to uptake metal ions and transform them into metal NPs as follows.

7.1 Metal Uptake

The EDXRF elemental mass analyses of each metal in seven plant species exposed to AgNO_3 , $\text{Cu}(\text{NO}_3)_2$, $\text{Fe}(\text{NO}_3)_3$, $\text{Ni}(\text{NO}_3)_2$, and $\text{Pb}(\text{NO}_3)_2$ is shown in Figure 7.1. All species could uptake these metal ions with high efficacy. Among seven species, *S. molesta* D.S. Mitch. showed the greatest capability to uptake ^{47}Ag . In addition, *S. molesta* D.S. Mitch. and *E. crassipes* (Mart.) Solms had the greatest capability to uptake ^{29}Cu . For ^{26}Fe analysis, *S. polyrrhiza* (L.) Schleid. had the highest uptake level of ^{26}Fe . Furthermore, *A. pinnata* R.Br., *S. molesta* D.S. Mitch., and *W. globosa* (Roxb.) Hartog & Plas have the greatest capability to uptake ^{28}Ni . For ^{82}Pb , *L. minor* L. have the highest capacity to uptake this element in the root cells.

It was noted that *S. molesta* D.S. Mitch. showed the greatest capability to uptake ^{47}Ag , ^{29}Cu , and ^{28}Ni , while its capability to uptake ^{82}Pb and ^{26}Fe was also high even not the highest. Therefore, *S. molesta* D.S. Mitch. was considered as the most suitable species for uptake most metal ions in this work.

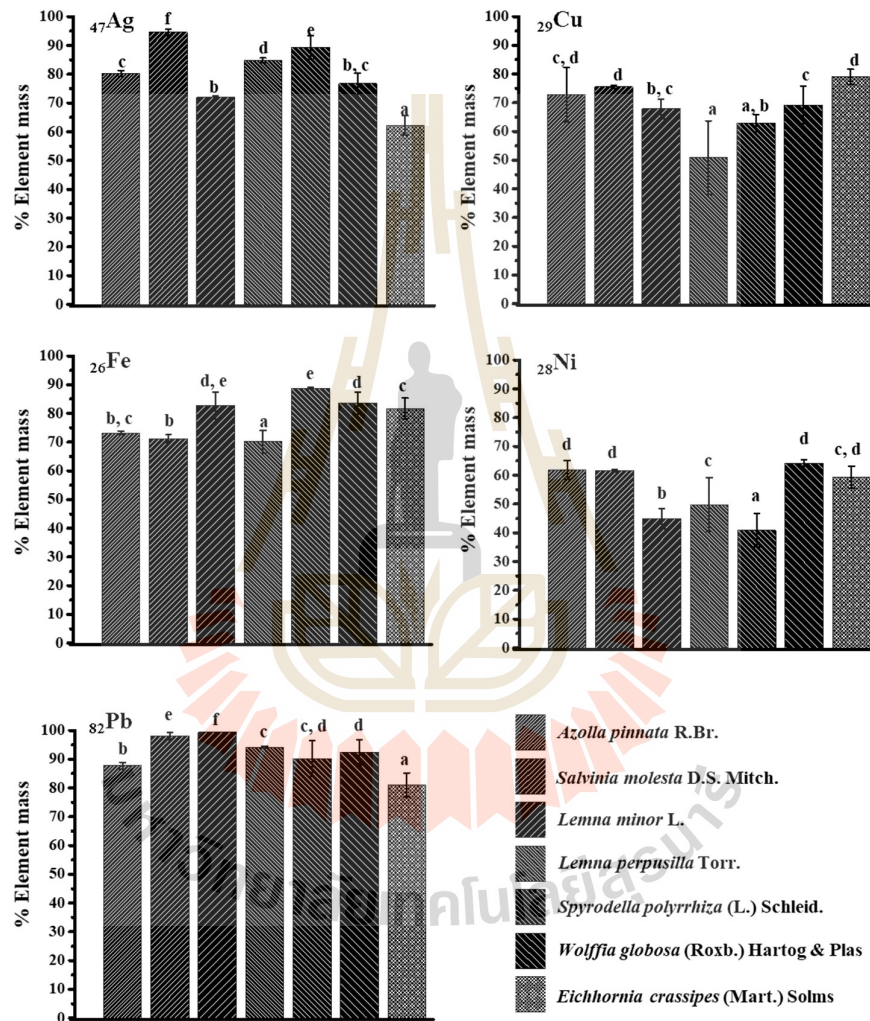


Figure 7.1 The quantitative metal-uptake analysis of ^{47}Ag , ^{29}Cu , ^{26}Fe , ^{28}Ni , and ^{82}Pb in roots of seven aquatic plants treated with AgNO_3 , $\text{Cu}(\text{NO}_3)_2$, $\text{Fe}(\text{NO}_3)_3$, $\text{Ni}(\text{NO}_3)_2$, and $\text{Pb}(\text{NO}_3)_2$ solutions, respectively.

7.2 Formation of Metal Nanoparticles

The formation of metal NPs in the roots of seven plant species is compared as follows.

7.2.1 Formation of silver nanoparticles

All seven plant species could transform silver ions into spherical AgNPs. These AgNPs can also be found at the plasma membrane of the cortex and vascular tissue in six aquatic plant species, except *W. globosa* (Roxb.) Hartog & Plas, which AgNPs were detected in chloroplasts (Table 7.1).

Table 7.1 Formation of AgNPs in seven plant species.

Plant species	Formation of AgNPs	Morphology	Localization
<i>Azolla pinnata</i> R.Br.	Yes	Spherical	Plasma membrane of cortex and vascular tissues
<i>Salvinia molesta</i> D.S. Mitch.	Yes	Spherical	Plasma membrane of cortex and vascular tissues
<i>Lemna minor</i> L.	Yes	Spherical	Plasma membrane of cortex and vascular tissues
<i>Lemna perpusilla</i> Torr.	Yes	Spherical	Plasma membrane of cortex and vascular tissues
<i>Spirodela polyrrhiza</i> (L.) Schleid.	Yes	Spherical	Plasma membrane of cortex and vascular tissues
<i>Wolffia globosa</i> (Roxb.) Hartog & Plas	Yes	Spherical	Chloroplasts
<i>Eichhornia crassipes</i> (Mart.) Solms	Yes	Spherical	Plasma membrane of cortex and vascular tissues

7.2.3 Formation of copper nanoparticles

For the formation of CuNPs, only three plant species could transform copper ions into CuNPs; *A. pinnata* R.Br., *S. polyrrhiza* (L.) Schleid., and *E. crassipes* (Mart.) Solms. The spherical CuNPs were dominantly detected at the plasma membrane of the cortex and vascular tissues (Table 7.2).

Table 7.2 Formation of CuNPs in seven plant species.

Plant species	Formation of CuNPs	Morphology	Localization
<i>Azolla pinnata</i> R.Br.	Yes	Spherical	Plasma membrane of cortex and vascular tissues
<i>Salvinia molesta</i> D.S. Mitch.	No	Electron dense	Plasma membrane of cortex and vascular tissues
<i>Lemna minor</i> L.	No	-	-
<i>Lemna perpusilla</i> Torr.	No	-	-
<i>Spirodela polyrrhiza</i> (L.) Schleid.	Yes	Spherical	Plasma membrane of cortex and vascular tissues
<i>Wolffia globosa</i> (Roxb.) Hartog & Plas	No	-	-
<i>Eichhornia crassipes</i> (Mart.) Solms	Yes	Spherical	Plasma membrane of cortex and vascular tissues

7.2.4 Formation of iron nanoparticles

For the formation of FeNPs, all seven plant species could transform copper ions into CuNPs (Table 7.3). The spherical FeNPs were found at the plasma membrane of the cortex and vascular tissues in the roots of *A. pinnata* R.Br., *S. molesta* D.S. Mitch., *S. polyrrhiza* (L.) Schleid., and *E. crassipes* (Mart.) Solms. In addition, FeNPs could be founded in ectosomes in cortex and vascular tissues in two aquatic plant species; *L. minor* L. and *L. perpusilla* Torr. Furthermore, FeNPs was also detected in the chloroplasts of *W. globosa* (Roxb.) Hartog & Plas.

Table 7.3 Formation of FeNPs in seven plant species.

Plant species	Formation of FeNPs	Morphology	Localization
<i>Azolla pinnata</i> R.Br.	Yes	Spherical	Plasma membrane of cortex and vascular tissues
<i>Salvinia molesta</i> D.S. Mitch.	Yes	Spherical	Plasma membrane of cortex and vascular tissues
<i>Lemna minor</i> L.	Yes	Spherical	Plasma membrane and ectosome of cortex and vascular tissues
<i>Lemna perpusilla</i> Torr.	Yes	Spherical	Plasma membrane of cortex and vascular tissues
<i>Spirodela polyrrhiza</i> (L.) Schleid.	Yes	Spherical	Plasma membrane of cortex and vascular tissues
<i>Wolffia globosa</i> (Roxb.) Hartog & Plas	Yes	Spherical	Chloroplasts
<i>Eichhornia crassipes</i> (Mart.) Solms	Yes	Spherical	Plasma membrane of cortex and vascular tissues

7.2.5 Formation of nickel nanoparticles

For the formation of NiNPs, all seven plant species could not form NiNPs in their root cells.

7.2.6 Formation of lead nanoparticles

The formation of PbNPs in seven aquatic plant species is summarized in Table 7.4, which all species could form PbNPs. The morphology of these PbNPs were either spherical or rod shapes depending on the plant species. Spherical PbNPs were detected in the plasma membrane of cortex and vascular tissues of *S. molesta* D.S. Mitch., *L. perpusilla* Torr., *S. polyrrhiza* (L.) Schleid., *W. globosa* (Roxb.) Hartog & Plas, and *E. crassipes* (Mart.) Solms. But rod PbNPs were detected only in *A. pinnata* R.Br. and *L. minor* L.

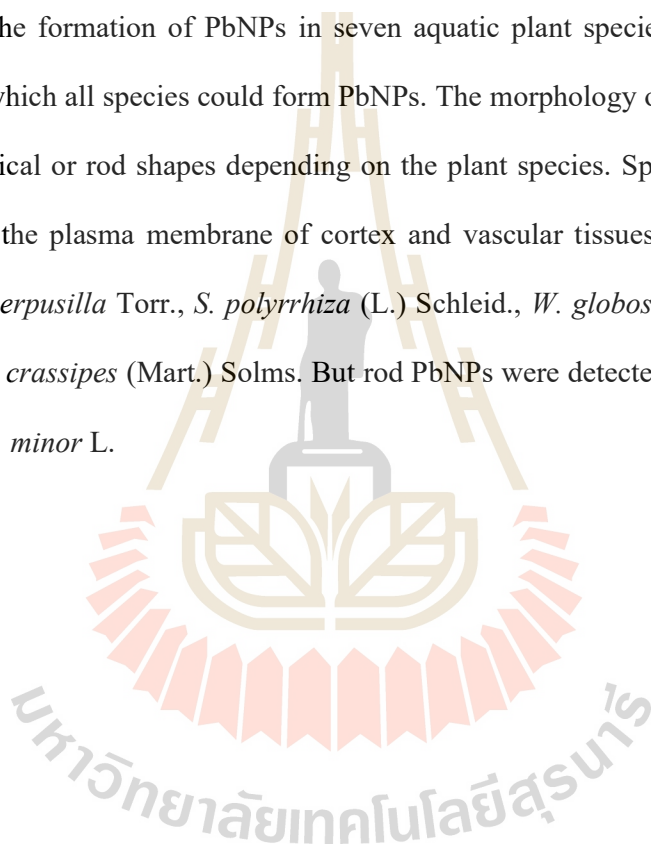


Table 7.4 Formation of PbNPs in seven plant species

Plant species	Formation of PbNPs	Morphology	Localization
<i>Azolla pinnata</i> R.Br.	Yes	Rod	Plasma membrane of cortex tissue, phloem, and procambium cells
<i>Salvinia molesta</i> D.S. Mitch.	Yes	Spherical	Plasma membrane of cortex and vascular tissues
<i>Lemna minor</i> L.	Yes	Short rod	Plasma membrane of cortex and vascular tissues
<i>Lemna perpusilla</i> Torr.	Yes	Spherical	Plasma membrane of cortex and vascular tissues
<i>Spirodela polyrrhiza</i> (L.) Schleid.	Yes	Spherical	Plasma membrane of cortex and vascular tissues
<i>Wolffia globosa</i> (Roxb.) Hartog & Plas	Yes	Spherical	Chloroplasts
<i>Eichhornia crassipes</i> (Mart.) Solms	Yes	Spherical	Plasma membrane of cortex and vascular tissues

7.3 Proposed Mechanism of the Formation of Metal Nanoparticles

The mechanism of the formation of these metal NPs is not known. This work hypothesizes that the possible mechanism may relate to the metal phytoremediation and detoxification process as well as the reducing phytochemicals in plants as depicted in Figure 7.2.

Metal ions can enter root cells via apoplast and symplastic pathways and/or specialized proteins embedded in the plant cell membrane (such as ZIP family, ATP-binding cassette ABC, NRAMPs, CTR family, and MTP family). Inside the cell, the metal ions may bind to phytochelatins and metallothioneins, organic acids, amino acids, and proteins, thus forming metal-complex molecules in the cytosol, which may deposit near cell membrane or translocate to storage vesicles. These metal-complex molecules are likely detected as the electron-dense area in the cells, but not as metal NPs. It is possible that at the suitable concentrations of metal ions and/or the sufficient ratio of metal ions and reducing phytochemicals, some metal ions may be reduced, leading to a formation of small metal seeds by the activity of reducing phytochemicals inside the cells. These metal seeds can grow into clusters and subsequently form metal NPs, in which the complex phytochemicals assist this process as the capping agents. The balance and imbalance growths of each lattice plane result in spherical and rod morphology of the metal NPs. As a result, the spherical and rod metal NPs were detected in epidermal, aerenchyma and xylem cells of plant roots. In this work, the formation of NiNPs was not detected in the roots of all seven plant species. It was hypothesized that the levels of Ni (and/or the ratio of Ni and reducing phytochemicals) was not suitable to initiate the formation of zero-valent metal seeds, thus no formation of NiNPs could occur. This low content of Ni in the root could be explained by the

common Ni translocation process in plants. In general, the uptake Ni was mostly translocated to leaves as it complexed with other phytochemicals to form low molecular weight cationic or anionic complexes (500 – 10,000 MW) and transport to leaves via a symplastic pathway.

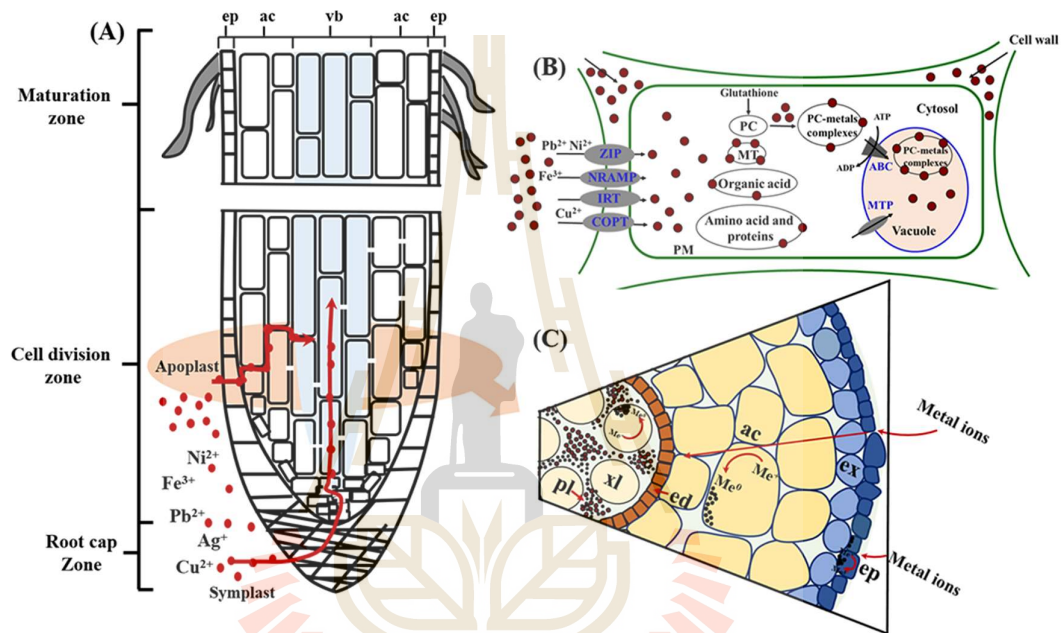


Figure 7.2 The proposed mechanism of the formation of metal NPs in plant root cells.

A) the uptake of metal ions into root cells. B) the entry of metal ions into the cells. C) the translocation of metal ions from epidermal to vascular layers resulting in the presence of metal NPs in these tissues.

CHAPTER VIII

CONCLUSION

In this study, the formation of metal NPs from the uptake Ag^+ , Cu^{2+} , Fe^{3+} , Ni^{2+} , and Pb^{2+} ions was investigated in root tissues of seven plant species belonging to three Families; Family Salvanaceae: *A. pinnata* R.Br., *S. molesta* D.S. Mitch., Family Araceae: *L. minor* L., *L. perpusilla* Torr., *S. polyrrhiza* (L.) Schleid., *W. globosa* (Roxb.) Hartog & Plas, and Family Pontederiaceae: *E. crassipes* (Mart.) Solms.

Salvanaceae is a family of heterosporous ferns, which contains only two genera; *Azolla* and *Salvinia*. In this work, *A. pinnata* R.Br. and *S. molesta* D.S. Mitch. were chosen as the studied plants as they are commonly found in Southeast Asia. The results showed that both plant species could absorb Ag^+ , Cu^{2+} , Fe^{3+} , Ni^{2+} , and Pb^{2+} through their roots as suggested by EDXRF analyses. In response to these metals, the reduced levels of ^{19}K and ^{20}Ca in Ag-, Cu-, Fe-, Ni-, and Pb-treated roots were significantly detected. ATR-FTIR results also suggested the induction levels of phosphorus-containing biomolecules, lipids, gene expression and protein synthesis in response to all metal treatments. The formation of metal NPs in both plants was observed in TEM images, which depended on types of metal ions and plant species. Cellular productions of AgNPs, CuNPs, FeNPs, and PbNPs, but not

NiNPs, were detected in *A. pinnata* R.Br. roots. However, *S. molesta* D.S. Mitch. root cells could assist the formation of only AgNPs, FeNPs, and PbNPs, but not CuNPs and NiNPs. Although most metal NPs in roots were dominantly spherical, short- and long-rod PbNPs were detected in different tissues of *A. pinnata* R.Br., but not in *S. molesta* D.S. Mitch. SAED-TEM analyses also indicated the structures of metal NPs formed in root cells as AgNPs, CuNPs, FeNPs (Fe_2O_3 and Fe_3O_4), and PbNPs (PbO).

Araceae is a family of monocotyledonous flowering plants, which in this work four species of common aquatic freshwater plants were selected to study; *L. minor* L., *L. perpusilla* Torr., *S. polyrrhiza* (L.) Schleid., and *W. globose* (Roxb.) Hartog & Plas. All four plant species had the great capability to absorb Ag^+ , Cu^{2+} , Fe^{3+} , Ni^{2+} , and Pb^{2+} via their roots and they were highly sensitive to Ag^+ ions. Similarly, the diminished levels of ^{19}K and ^{20}Ca in Ag-, Cu-, Fe-, Ni-, and Pb-treated plants was significantly detected in response to the metal-stress. ATR-FTIR profiles also showed the induction of some functional peaks suggesting the production of phosphorus-containing biomolecules, lipids, and proteins in response to the metal treatments. In this group of plants, only spherical NPs were detected. Similarly, the formation of AgNPs, FeNPs, CuNPs, and PbNPs was detected, but not NiNPs. Interestingly, the formation of FeNPs and CuNPs was not detected in all studied plants in this group. The identity of metal NPs was confirmed by SAED-TEM, which AgNPs, CuNPs (Cu and CuO), FeNPs (FeO, Fe_2O_3 , and Fe_3O_4), and PbNPs (Pb and PbO) were detected.

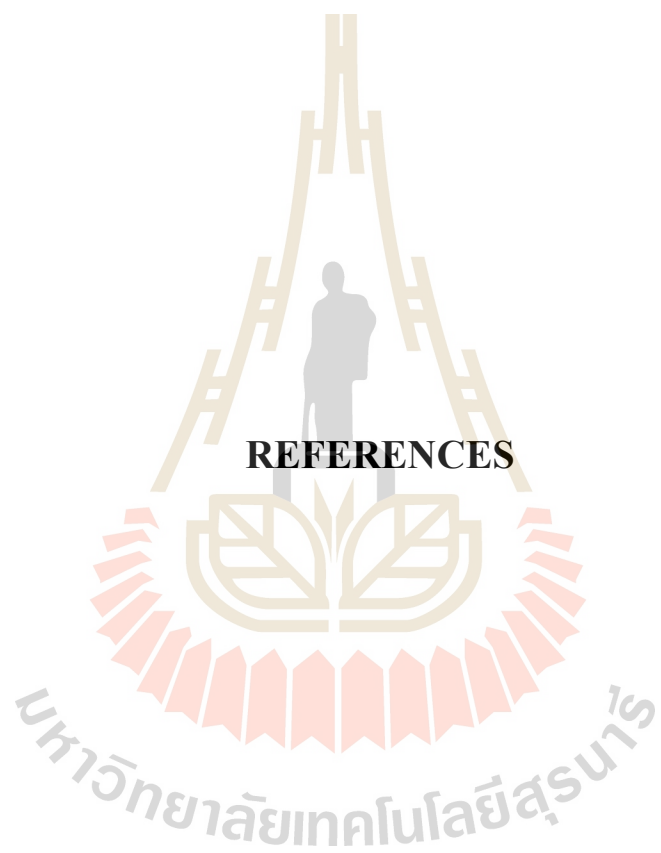
Pontederiaceae is a family of flowering plants, which contains six genera. In this work, only water hyacinth (*E. crassipes* (Mart.) Solms) was chosen for the study as it is the wide-spreading invasive species in natural water resources. EDXRF analysis revealed that water hyacinth had the great ability to absorb Ag^+ , Cu^{2+} , Fe^{3+} , Ni^{2+} , and

Pb²⁺ by its roots. It is sensitive to Ag⁺ ions but more tolerant of Ni²⁺ ions. In addition to the reduced levels of ¹⁹K and ²⁰Ca, the induction levels of phosphorus-containing biomolecules, lipids, gene expression, and protein synthesis were detected in root tissues, suggesting the metal-stress response in this plant. Similar to most studied plants, water hyacinth formed spherical AgNPs, CuNPs, FeNPs, and PbNPs, but not NiNPs in its root tissues. The identity of metal NPs was confirmed by SAED-TEM, which AgNPs, CuNPs, FeNPs (Fe₂O₃ and Fe₃O₄), and PbNPs (PbO) were detected.

In comparison, seven plant species in this study showed different capability to uptake and transform metal ions into NPs. Among seven plant species, *S. polyrrhiza* (L.) Schleid. was the most suitable plant to uptake Ag⁺, Cu²⁺, Fe³⁺, Ni²⁺, and Pb²⁺ ions as it contained the high mass levels of these metals in its roots based on the EDXRF analysis. The ATR-FTIR analysis data suggested the similar metal responses in all seven plant species, which were the reduction levels of ¹⁹K and ²⁰Ca and the induction levels of phosphorus-containing biomolecules, lipids, gene expression, and protein synthesis. Interestingly, the results of this work clearly showed that the formation of metal NPs and their shapes depended on the plant species and the metal types. Spherical AgNPs, FeNPs, CuNPs, and PbNPs were dominantly detected in most plant species, except rod PbNPs that occurred only in *A. pinnata* R.Br. These metal NPs were dominantly detected near plasma membrane, which were hypothesized that cellular reducing phytochemicals were mostly localized at the plasma membrane such as mugineic acid, alginic acid, tannic acid, and phenolic, and flavonoid compounds. Thus, these phytochemicals reduced metal ions and finally induced the formation of metal NPs, resulting in the presence of metal NPs predominantly near the plasma membrane. It was noted that the formation of NiNPs was not detected in the roots of all seven plant

species in this study. It was hypothesized that the levels of Ni in the roots was too low and insufficient to induce the formation of NiNPs. In general, the uptake Ni was mostly translocated to leaves as it complexed with other phytochemicals to form low molecular weight cationic or anionic complexes (500 – 10,000 MW) and transport to leaves via a symplastic pathway.

The mechanism of the formation of these metal NPs is not known. This work hypothesizes that the possible mechanism may involve the reducing phytochemicals and relate to the metal phytoremediation and detoxification systems in plants. When metal ions enter root cells, via apoplast and symplastic pathways and/or transport proteins, they interact with the reducing phytochemicals (such as proteins, glycoproteins, phospholipid, lipids, and metal-chelating agents (such as phytochelatins and metallothioneins, organic acids, amino acids, and proteins) at the plasma membrane, thus forming zero-valent metal seeds and finally cluster into metal NPs. As the results, most metal NPs deposit near cell membrane, while few may translocate to storage vesicles.



REFERENCES

REFERENCES

- Abdel, A., Azza, A., Elham, M., and Hassanein, A.M. (2011). Bioaccumulation of heavy metals by the water fern *Azolla pinnata*. **Egyptian Journal of Agricultural Research**. 89(4): 1261-1275.
- Abedini, A., Bakar, A.A., Larki, F., Menon, P.S., Islam, M.S., and Shaari, S. (2016). Recent advances in shape-controlled synthesis of noble metal nanoparticles by radiolysis route. **Nanoscale Research Letters**. 11(1): 287-294.
- Abeywickrama, T.M., Hassan, A., and Snee, P.T. (2018). Colloidal synthesis of bulk-bandgap lead selenide nanocrystals. **Frontiers in Chemistry**. 6(562): 1-9.
- Abid, A., Gill, S.S., and Gill, R. (2016). Phytoremediation: Management of environmental contaminants. Springer International Publishing, Picassoplatz, Basel, Switzerland. 409 p.
- Abou El-Nour, K.M.M., Eftaiha, A., Al-Warthan, A., and Ammar, R.A.A. (2010). Synthesis and applications of silver nanoparticles. **Arabian Journal of Chemistry**. 3(3): 135-140.
- Abràmoff, M.D., Magalhães, P.J., and Ram, S.J. (2004). Image processing with imageJ. **Biophotonics International**. 11(7): 36-42.
- Ackova, D. (2018). Heavy metals and their general toxicity for plants. **Plant Science Today**. 5(1): 14-18.

- Agale, A.A., Janjal, S.M., Gaikwad, S.T., and Rajbhoj, A.S. (2017). A versatile route for the synthesis of iron oxide nanostructures by electrochemical reduction method and their antibacterial application. **Journal of Cluster Science**. 28(1): 477-488.
- Agnihotri, S., Mukherji, S., and Mukherji, S. (2014). Size-controlled silver nanoparticles synthesized over the range 5–100 nm using the same protocol and their antibacterial efficacy. **The Royal Society of Chemistry Advances**. 4(8): 3974-3983.
- Ahmad, M.S., and Ashraf, M. (2011). Essential roles and hazardous effects of nickel in plants. **Reviews of Environmental Contamination and Toxicology**. 214: 125-167.
- Ahmad, P., Abdel Latef, A.A., Abd Allah, E.F., Hashem, A., Sarwat, M., Anjum, N. A., and Gucel, S. (2016). Calcium and potassium supplementation enhanced growth, osmolyte secondary metabolite production, and enzymatic antioxidant machinery in cadmium-exposed chickpea (*Cicer arietinum* L.). **Frontiers in Plant Science**. 7: 513-527.
- Ahmad, T. (2014). Reviewing the tannic acid mediated synthesis of metal nanoparticles. *Journal of Nanotechnology*. 2014(1): 1-11.
- Albrecht, R., Hunger, J., Block, T., Pöttgen, R., Senyshyn, A., Doert, T., and Ruck, M. (2019). Oxo-hydroxoferrate $K(2-x)Fe(4)O(7-x)(OH)(x)$: Hydroflux synthesis, chemical and thermal instability, crystal and magnetic structures. **Chemistry Open**. 8(1): 74-83.

- Ali, A., Bashir, F., Raza, R., Rafique, A., Ullah, M., Alvi, F., Afzal, M., Ghauri, M., and Belova, L. (2018). Electrochemical study of composite materials for coal-based direct carbon fuel cell. **International Journal of Hydrogen Energy**. 43(28): 12900-12908.
- Amcoff, Ö., and Holényi, K. (1996). Mineral formation on metallic copper in a future repository site environment. Swedish Nuclear Power Inspectorate, University of Uppsala, Institute of Earth Sciences, Sweden. 49 p.
- Arif, N., Yadav, V., Singh, S., Singh, S., Ahmad, P., Mishra, R.K., Sharma, S., Tripathi, D.K., Dubey, N.K., and Chauhan, D.K. (2016). Influence of high and low levels of plant-beneficial heavy metal ions on plant growth and development. **Frontiers in Environmental Science**. 4(69): 1-11.
- Aydemir, T.B., and Cousins, R.J. (2018). The multiple faces of the metal transporter ZIP14 (SLC39A14). **The Journal of Nutrition**. 148(2): 174-184.
- Azer, S.A. (2013). Taxonomic revision of genus *Lemna* (Lemnaceae Gray) in Egypt. **Annals of Agricultural Sciences**. 58(2): 257-263.
- Aziz, H.A., Adlan, M.N., and Ariffin, K.S. (2008). Heavy metals (Cd, Pb, Zn, Ni, Cu and Cr(III)) removal from water in Malaysia: Post treatment by high quality limestone. **Bioresource Technology**. 99(6): 1578-1583.
- Balakumaran, M.D., Ramachandran, R., and Kalaichelvan, P.T. (2015). Exploitation of endophytic fungus, *Guignardia mangiferae* for extracellular synthesis of silver nanoparticles and their in vitro biological activities. **Microbiological Research**. 178(Supplement C): 9-17.

- Bhattacharai, B., Zaker, Y., and Bigioni, T.P. (2018). Green synthesis of gold and silver nanoparticles: Challenges and opportunities. **Current Opinion in Green and Sustainable Chemistry**. 12: 91-100.
- Cataldo, D.A., and Wildung, R.E. (1978). Soil and plant factors influencing the accumulation of heavy metals by plants. **Environmental Health Perspectives**. 27: 149-159.
- Chaney, R. (1989). Kinetics of ferric chelate reduction by roots of iron-deficient peanut (*Arachis hypogea*). **Acta Botanica Neerlandica**. 38(2): 155-163.
- Chatterjee, A., Chakraborty, R., and Basu, T. (2014). Mechanism of antibacterial activity of copper nanoparticles. **International Journal of Nanoscience**. 25: 1-22.
- Chaudhuri, D., Majumder, A., Misra, A.K., and Bandyopadhyay, K. (2014). Cadmium removal by *Lemna minor* and *Spirodela polyrhiza*. **International Journal of Phytoremediation**. 16(11): 1119-1132.
- Chen, C., Huang, D., and Liu, J. (2009). Functions and toxicity of nickel in plants: Recent advances and future prospects. **Clean**. 37(4-5): 304-313.
- Cheng, T.-S., Hung, M.-J., Cheng, Y.-I., and Cheng, L.-J. (2013). Calcium-induced proline accumulation contributes to amelioration of NaCl injury and expression of glutamine synthetase in greater duckweed (*Spirodela polyrhiza* L.). **Aquatic Toxicology**. 144: 265-274.
- Chifiriuc, M.C., and Grumezescu, A.M. (2016). Chapter 9 - Iron oxide nanomaterials for functional imaging. In: Grumezescu, A.M. (ed). *Nanobiomaterials in Medical Imaging*. William Andrew Publishing, London, UK. pp. 279-301.

- Chouhan, A.P.S., and Sarma, A.K. (2013). Biodiesel production from *Jatropha curcas* L. oil using *Lemna perpusilla* Torrey ash as heterogeneous catalyst. **Biomass and Bioenergy**. 55(1): 386-389.
- Claudia, Z., Isabelle C., Rodrigues D.S., Matthias, M., Maryna, K., Wilhelm, B., and Hendrik, H. (2017). Plant surfaces: Structures and functions for biomimetic innovations. **Nano-Micro Letters**. 9(2): 9-23.
- Connolly, E.L., and Guerinot, M. (2002). Iron stress in plants. **Genome Biology**. 3(8): 1-5.
- Cortalezzi, M.M., Rose, J., Wells, G.F., Bottero, J.-Y., Barron, A.R., and Wiesner, M. R. (2003). Ceramic membranes derived from ferroxane nanoparticles: A new route for the fabrication of iron oxide ultrafiltration membranes. **Journal of Membrane Science**. 227(1): 207-217.
- Cutton, J.A. (2018). Face centered cubic structure (FCC). IOP Publishing Ltd, The Pennsylvania State University, Pennsylvania, USA. 408 p.
- Cvjetko, P., Zovko, M., and Balen, B. (2014). Proteomics of heavy metal toxicity in plants. **Archives of Industrial Hygiene and Toxicology**. 65(1): 1-18.
- D'Souza, L., Devi, P., Shridhar, D.M. P., and Naik, C.G. (2008). Use of fourier transform infrared (FTIR) spectroscopy to study cadmium-induced changes in *Padina tetrastratica* (Hauck). **Analytical Chemistry Insights**. 3: 135-143.
- Das, R.K., Pachapur, V.L., Lonappan, L., Naghdi, M., Pulicharla, R., Maiti, S., Cledon, M., Dalila, L.M.A., Sarma, S.J., and Brar, S.K. (2017). Biological synthesis of metallic nanoparticles: Plants, animals and microbial aspects. **Nanotechnology for Environmental Engineering**. 2(1): 1-18.

- Davey, W.P. (1925). Precision measurements of the lattice constants of twelve common metals. **Physical Review**. 25(6): 753-761.
- De, A.K., Sarkar, B., and Adak, M.K. (2017). Physiological explanation of herbicide tolerance in *Azolla pinnata* R.Br. **Annals of Agrarian Science**. 15(3): 402-409.
- Domènech, B., Bastos-Arrieta, J., Alonso, A., Macanás, J., Muñoz, M., and Muraviev, D.N. (2012). Bifunctional polymer-metal nanocomposite ion exchange materials. In: Kilislioglu, A. (ed). Ion Exchange Technologies. IntechOpen Limited, London, UK. pp. 1-3.
- Duan, H., Wang, D., and Li, Y. (2015). Green chemistry for nanoparticle synthesis. **Chemical Society Reviews**. 44(16): 5778-5792.
- Edge, R., El-Agamey, A., Land, E.J., Navaratnam, S., and George, T.T. (2007). Studies of carotenoid one-electron reduction radicals. **Archives of Biochemistry and Biophysics**. 458(2): 104-110.
- Egila, J., Dauda, B., Iyaka, Y., and Jimoh, T. (2011). Agricultural waste as a low cost adsorbent for heavy metal removal from wastewater. **International Journal of Physical Sciences**. 6(8): 2152-2157.
- Ekperusi, A.O., Sikoki, F.D., and Nwachukwu, E.O. (2019). Application of common duckweed (*Lemna minor*) in phytoremediation of chemicals in the environment: State and future perspective. **Chemosphere**. 223: 285-309.
- El-Kemary, M., Nagy, N., and El-Mehasseb, I. (2013). Nickel oxide nanoparticles: Synthesis and spectral studies of interactions with glucose. **Materials Science in Semiconductor Processing**. 16(6): 1747-1752.

- Elnaggar, A., Fitzsimons, P., Nevin, A., Osticioli, I., and Watkins, K. (2015). Investigation of ultrafast picosecond laser system for cleaning of metal decorations of 17th C. gloves of king charles I. **E-Preservation Science**. 12: 14-19.
- Fendler, J.H., and Tian, Y. (2007). Nanoparticles and nanostructured films: Current accomplishments and future prospects. In: Fendler, J.H. (ed). *Nanoparticles and Nanostructured Films*. Wiley-VCH Verlag, Weinheim, Germany. pp. 429-461.
- Firdhouse, M.J., and Lalitha, P. (2015). Biosynthesis of silver nanoparticles and its applications. **Journal of Nanotechnology**. 2015: 829526-829534.
- Flutto, L. (2003). Pectin: Properties and determination. **Encyclopedia of Food Sciences and Nutrition**. 2(1): 4440-4449.
- Frey, P.A., and Reed, G.H. (2012). The ubiquity of iron. **American Chemical Society Chemical Biology**. 7(9): 1477-1481.
- Fu, C., and Ravindra, N.M. (2012). Magnetic iron oxide nanoparticles: Synthesis and applications. **Bioinspired, Biomimetic and Nanobiomaterials**. 1(4): 229-244.
- Gao, D., Zhang, J., Zhu, J., Qi, J., Zhang, Z., Sui, W., Shi, H., and Xue, D. (2010). Vacancy-mediated magnetism in pure copper oxide nanoparticles. **Nanoscale Research Letters**. 5(4): 769-772.
- Gao, X., Lan, Y., Pan, G., Wu, F., Qu, J., Song, D., and Shen, P. (2001). Electrochemical hydrogen storage by carbon nanotubes decorated with metallic nickel. *Electrochemical and Solid-State Letters*. 4(10): A173-A175.

- Gaur, J.P., Noraho, N., and Chauhan, Y.S. (1994). Relationship between heavy metal accumulation and toxicity in *Spirodela polyrhiza* (L.) Schleid. and *Azolla pinnata* R.Br. **Aquatic Botany**. 49(2): 183-192.
- Gerdes, F., Volkmann, M., Schliehe, C., Bielewicz, T., and Klinke, C. (2015). Sculpting of lead sulfide nanoparticles by means of acetic acid and dichloroethane. **International Journal of Research in Physical Chemistry and Physics**. 229(1-2): 139-189.
- Giardini, M. (2004). *Salvinia molesta* D.S. Mitchell (Salviniaceae): The second record for Italy (Latium) and consideration about the control of this invasive species. **Webbia**. 59(2): 457-467.
- Guasch, H., Navarro, E., Serra, A., and Sabater, S. (2004). Phosphate limitation influences the sensitivity to copper in periphytic algae. **Freshwater Biology**. 49(4): 463-473.
- Guo, L., Huang, Q.-J., Li, X.-Y., and Yang, S. (2006). PVP-coated iron nanocrystals: Anhydrous synthesis, characterization, and electrocatalysis for two species. **Langmuir**. 22(18): 7867-7872.
- Hadi, F., and Aziz, T. (2015). A mini review on lead (Pb) toxicity in plants. **Journal of Biology and Life Science**. 6(2): 1-91.
- Haegeman, A., Kyndt, T., Gheysen, G., Trooskens, G., Denil, S., De Meyer, T., and Crieckinge, W.V. (2012). Transcriptome analysis of rice mature root tissue and root tips in early development by massive parallel sequencing. **Journal of Experimental Botany**. 63(5): 2141-2157.
- Hartog, C., and Plas, F. (1970). A synopsis of the Lemnaceae. **Blumea**. 18(2): 355-368.

- Hasan, M.K., Cheng, Y., Kanwar, M.K., Chu, X.-Y., Ahammed, G.J., and Qi, Z.-Y. (2017). Responses of plant proteins to heavy metal stress-A review. **Frontiers in Plant Science**. 8: 1492-1492.
- Hassan, M.S., and Edwards, P. (1992). Evaluation of duckweed (*Lemna perpusilla* and *Spirodela polyrrhiza*) as feed for Nile tilapia (*Oreochromis niloticus*). **Aquaculture**. 104(3-4): 315-326.
- Hedayati, K., Goodarzi, M., and Ghanbari, D. (2017). Hydrothermal synthesis of Fe₃O₄ nanoparticles and flame resistance magnetic poly styrene nanocomposite. **Journal of Nanostructures**. 7(1): 32-39.
- Hegazi, H.A. (2013). Removal of heavy metals from wastewater using agricultural and industrial wastes as adsorbents. **Housing and Building National Research Center Journal**. 9(3): 276-282.
- Helmlinger, J., Sengstock, C., Heitfeld, C., Mayer, C., Schildhauer, T.A., Köller, M., and Epple, M. (2016). Silver nanoparticles with different size and shape: Equal cytotoxicity, but different antibacterial effects. **The Royal Society of Chemistry Advances**. 6(22): 18490-18501.
- Heredia-Guerrero, J.A., Benítez, J.J., Domínguez, E., Bayer, I.S., Cingolani, R., Athanassiou, A., and Heredia, A. (2014). Infrared and raman spectroscopic features of plant cuticles: A review. **Frontiers in Plant Science**. 5: 305-305.
- Hirunsit, P., Soodsawang, W., and Limtrakul, J. (2015). CO₂ electrochemical reduction to methane and methanol on copper-based alloys: Theoretical insight. **The Journal of Physical Chemistry C**. 119(15): 8238-8249.

- Huang, H.H., Yan, F.Q., Kek, Y.M., Chew, C.H., Xu, G.Q., Ji, W., Oh, P.S., and Tang, S.H. (1997). Synthesis, characterization, and nonlinear optical properties of copper nanoparticles. **Langmuir**. 13(2): 172-175.
- Huber, D.L. (2005). Synthesis, properties, and applications of iron nanoparticles. **Small**. 1(5): 482-501.
- Iyaka, Y. (2011). Nickel in soils: A review of its distribution and impacts. **Scientific Research and Essays**. 6(33): 1-11.
- Iyengar, S.J., Joy, M., Ghosh, C.K., Dey, S., Kotnala, R.K., and Ghosh, S. (2014). Magnetic, X-ray and mössbauer studies on magnetite/maghemite core-shell nanostructures fabricated through an aqueous route. **Royal Society of Chemistry Advances**. 4(110): 64919-64929.
- Jain, S.K., Vasudevan, P., and Jha, N.K. (1990). *Azolla pinnata* R.Br. and *lemna minor* L. for removal of lead and zinc from polluted water. **Nano Letters**. 24(2): 177-183.
- Jan, A.T., Kamli, M.R., Murtaza, I., Singh, J.B., Ali, A., and Haq, Q.M.R. (2010). Dietary flavonoid quercetin and associated health benefits—An overview. **Food Reviews International**. 26(3): 302-317.
- Janthima, R., Khamhaengpol, A., and Siri, S. (2018). Egg extract of apple snail for eco-friendly synthesis of silver nanoparticles and their antibacterial activity. **Artificial Cells, Nanomedicine, and Biotechnology**. 46(2): 361-367.
- Jiang, X., Du, B., Huang, Y., and Zheng, J. (2018). Ultrasmall noble metal nanoparticles: Breakthroughs and biomedical implications. **Nano Today**. 21: 106-125.

- Joshua, C., Cheshier, M., and Madsen, W.D. (2013). The susceptibility of duckweed (*Lemna minor* L.) to fluridone and penoxsulam. **Journal of Aquatic Plant Management**. 49(1): 50-52.
- Jozefczak, M., Remans, T., Vangronsveld, J., and Cuypers, A. (2012). Glutathione is a key player in metal-induced oxidative stress defenses. **International Journal of Molecular Sciences**. 13(3): 3145-3175.
- Kaplan, A., Zelicha, H., Tsaban, G., Yaskolka Meir, A., Rinott, E., Kovsan, J., Novack, L., Thiery, J., Ceglarek, U., Burkhardt, R., Willenberg, A., Tirosh, A., Cabantchik, I., Stampfer, M.J., and Shai, I. (2018). Protein bioavailability of *Wolffia globosa* duckweed, a novel aquatic plant: A randomized controlled trial. **Clinical Nutrition**: 2576-2582.
- Kawamura, G., Nogami, M., and Matsuda, A. (2013). Shape-controlled metal nanoparticles and their assemblies with optical functionalities. **Journal of Nanomaterials**. 2013: 1-17.
- Keat, C.L., Aziz, A., Eid, A.M., and Elmarzugi, N.A. (2015). Biosynthesis of nanoparticles and silver nanoparticles. **Bioresources and Bioprocessing**. 2(1): 47-56.
- Khamhaengpol, A., and Siri, S. (2016). Fluorescent light mediated a green synthesis of silver nanoparticles using the protein extract of weaver ant larvae. **Journal of Photochemistry and Photobiology B: Biology**. 163: 337-344.
- Khandel, P., and Kumar, S.S. (2016). Microbes mediated synthesis of metal nanoparticles: Current status and future prospects. **International Journal of Nanomaterials and Biostructures**. 6(1): 1-25.

- Khataee, A.R., Movafeghi, A., Torbati, S., Salehi Lisar, S.Y., and Zarei, M. (2012). Phytoremediation potential of duckweed (*Lemna minor* L.) in degradation of C.I. Acid Blue 92: Artificial neural network modeling. **Ecotoxicology and Environmental Safety**. 80: 291-298.
- Kim, C., Kim, C., Lee, K., and Lee, H. (2014). Shaped nickel nanoparticles with an unconventional HCP crystalline structure. **Chemical Communications**. 50(48): 6353-6356.
- Kim, S.A., and Guerinot, M.L. (2007). Mining iron: Iron uptake and transport in plants. **Federation of European Biochemical Societies Letters**. 581(12): 2273-2280.
- Kisa, D., Kayir, O., Saglam, N., Şahin, S., Öztürk, L., and Elmastaş, M. (2019). Changes of phenolic compounds in tomato associated with the heavy metal stress. **Bartın University International Journal of Natural and Applied Sciences**. 2: 35-43.
- Klaytae, T., Panthong, P., and Thountom, S. (2013). The effect of fuel content on the characteristic of lead titanate fine powders prepared by sol-gel combustion method. **Ferroelectrics**. 455(1): 43-48.
- Kouhi, S., Lahouti, M., and Ganjeali, A. (2016). Anatomical and ultrastructural responses of *Brassica napus* after long-term exposure to excess zinc. **Turkish Journal of Biology**. 40(3): 652-660.
- Krämer, U., Talke, I.N., and Hanikenne, M. (2007). Transition metal transport. **Federation of European Biochemical Societies Letters**. 581(12): 2263-2272.

- Krzeslowska, M. (2011). The cell wall in plant cell response to trace metals: Polysaccharide remodeling and its role in defense strategy. **Acta Physiologiae Plantarum**. 33(1): 35-51.
- Kukier, U., Peters, C.A., Chaney, R.L., Angle, J.S., and Roseberg, R.J. (2004). The effect of pH on metal accumulation in two *Alyssum* species. **Journal of Environmental Quality**. 33(6): 2090-2102.
- Kumar, B., Smita, K., Cumbal, L., Debut, A., and Pathak, R. (2014). Sonochemical synthesis of silver nanoparticles using starch: A comparison. **Bioinorganic chemistry and applications**. 2014: 784268-784276.
- Kuo, J. (2007). Electron microscopy: Methods and protocols. Springer Science & Business Media, Berlin, Heidelberg, Germany. 283 p
- Kushwaha, A., Hans, N., Kumar, S., and Rani, R. (2018). A critical review on speciation, mobilization and toxicity of lead in soil-microbe-plant system and bioremediation strategies. **Ecotoxicology and Environmental Safety**. 147: 1035-1045.
- Kwon, Y., Lee, H., and Lee, J. (2011). Autonomous interfacial creation of nanostructured lead oxide. **Nanoscale**. 3(12): 4984-4988.
- Lee, K.-S. (2015). Coupling graphene sheets with iron oxide nanoparticles for energy storage and microelectronics. **The Journal of Hannam University**. 1(1): 1-35.
- Liu, C., Dai, Z., and Sun, H. (2017). Potential of duckweed (*Lemna minor*) for removal of nitrogen and phosphorus from water under salt stress. **Journal of Environmental Management**. 187: 497-503.

- Lokuge, U.M.L. (2016). A study on the phytoremediation potential of *Azolla pinnata* under laboratory conditions. **Journal of Tropical Forestry and Environment**. 6(1): 36-49.
- Lone, M.I., He, Z.-l., Stoffella, P.J., and Yang, X.-e. (2008). Phytoremediation of heavy metal polluted soils and water: Progresses and perspectives. **Journal of Zhejiang University Science B: Biomedicine & Biotechnology**. 9(3): 210-220.
- Lumpkin, T.A. (1983). Taxonomy, physiology, and agronomic potential of *Azolla* sp. **Applied Biochemistry and Biotechnology**. 47: 777-780.
- Luo, Z.-B., Wu, C., Zhang, C., Li, H., Lipka, U., and Polle, A. (2014). The role of ectomycorrhizas in heavy metal stress tolerance of host plants. **Environmental and Experimental Botany**. 108: 47-62.
- Magaye, R., and Zhao, J. (2012). Recent progress in studies of metallic nickel and nickel-based nanoparticles' genotoxicity and carcinogenicity. **Environmental Toxicology and Pharmacology**. 34(3): 644-650.
- Mahmoodi, S., Elmi, A., and Hallaj Nezhadi, S. (2018). Copper nanoparticles as antibacterial agents. **Journal of Molecular Pharmaceutics and Organic Process Research**. 6(1): 1-7.
- Mahmoud, Z., Hannora, A., and Sherif, M. (2015). Preparation of lead-polymer nano composite for nuclear shielding applications. **International Journal for Research in Applied Science & Engineering Technology**. 3: 1046-1049.
- Kerracher, R., León, C.P., Wills, R.G., Shah, A.A., and Walsh, F. (2015). A review of the iron–air secondary battery for energy storage. **ChemPlusChem**. 80: 323-335.

- Murdie, H.F., Morris, M.C., Evans, E.H., Paretzkin, B., Wong-Ng, W., Ettlinger, L., and Hubbard, C.R. (1986). Standard X-Ray diffraction powder patterns from the JCPDS research associateship. **Powder Diffraction**. 1(2): 64-77.
- Meldolesi, J. (2018). Exosomes and ectosomes in intercellular communication. **Current Biology**. 28(8): R435-R444.
- Mendoza-Soto, A., Sanchez, F., and Hernandez, G. (2012). Micro RNAs as regulators in plant metal toxicity response. **Frontiers in Plant Science**. 3(105): 1-5.
- Middleton, B.A. (2008). Invasive species A2 - Jørgensen, Sven Erik. In: Fath, B.D. (ed). Encyclopedia of Ecology. Academic Press, Oxford, UK. pp. 2020-2028.
- Mira, L., Fernandez, M.T., Santos, M., Rocha, R., Florencio, M.H., and Jennings, K. R. (2002). Interactions of flavonoids with iron and copper ions: A mechanism for their antioxidant activity. **Free Radical Research**. 36(11): 1199-1208.
- Miretzky, P., Saralegui, A., and Cirelli, A.F. (2004). Aquatic macrophytes potential for the simultaneous removal of heavy metals (Buenos Aires, Argentina). **Chemosphere**. 57(8): 997-1005.
- Moacă, E.-A., Coricovac, E.D., Soica, C.M., Pinzaru, I.A., Păcurariu, C.S., and Dehelean, C.A. (2018). Iron Ores and Iron Oxide Materials. IntechOpen Limited, London, UK. 353 p.
- Mody, V.V., Siwale, R., Singh, A., and Mody, H.R. (2010). Introduction to metallic nanoparticles. **Journal of Pharmacy and Bioallied Sciences**. 2(4): 282-289.
- Mohindroo, J.J., Garg, U.K., and Sharma, A.K. (2016). Optical properties of stabilized copper nanoparticles. **American Institute of Physics Conference Proceedings**. 1728(1): 020534-020538.

- Mollick, M.M.R., Rana, D., Dash, S.K., Chattopadhyay, S., Bhowmick, B., Maity, D., Mondal, D., Pattanayak, S., Roy, S., Chakraborty, M., and Chattopadhyay, D. (2015). Studies on green synthesized silver nanoparticles using *Abelmoschus esculentus* (L.) pulp extract having anticancer (in vitro) and antimicrobial applications. **Arabian Journal of Chemistry**. 12(8): 2572-2584.
- Moody, B. (2013). Comparative inorganic chemistry 3rd edition. Elsevier, London, UK. 576 p.
- Mori, S. (1999). Iron acquisition by plants. **Current Opinion in Plant Biology**. 2(3): 250-253.
- Muhammad, I.D., and Rani, A. (2016). Recent advances in the synthesis and stabilization of nickel and nickel oxide nanoparticles: A green adeptness. **International Journal of Analytical Chemistry**. 2016: 1-14.
- Mukherji, S., Bharti, S., Shukla, G., and Mukherji, S. (2019). Synthesis and characterization of size- and shape-controlled silver nanoparticles. **Physical Sciences Reviews**. 4(1): 1-30.
- Muramoto, S., and Oki, Y. (1983). Removal of some heavy metals from polluted water by water hyacinth (*Eichhornia crassipes*). **Bulletin of Environmental Contamination and Toxicology**. 30(1): 170-177.
- Narayanan, K.B., and Sakthivel, N. (2010). Biological synthesis of metal nanoparticles by microbes. **Advances in Colloid and Interface Science**. 156(1): 1-13.
- Odkhuu, D., Taivansaikhan, P., Yun, W.S., and Hong, S.C. (2014). A first-principles study of magnetostrictions of Fe₃O₄ and CoFe₂O₄. **Journal of Applied Physics**. 115(17): 17A916-917A921.

- Ohlbaum, M., Wadgaonkar, S.L., van Bruggen, J.J.A., Nancharaiah, Y.V., and Lens, P.N.L. (2018). Phytoremediation of seleniferous soil leachate using the aquatic plants *Lemna minor* and *Egeria dens*. **Ecological Engineering**. 120: 321-328.
- Ojha, N.K., Zyryanov, G.V., Majee, A., Charushin, V.N., Chupakhin, O.N., and Santra, S. (2017). Copper nanoparticles as inexpensive and efficient catalyst: A valuable contribution in organic synthesis. **Coordination Chemistry Reviews**. 353: 1-57.
- Oliver, J. (2012). Formation of nanocrystalline phases in sol-gel masses in the Fe-WC (O) system and densification up to 1100 °C. **Procedia Materials Science**. 1(1): 95-103.
- Papageorgiou, M., Tselios, C., and Varotsis, C. (2019). Photosensitivity responses of *Sagittula stellata* probed by FTIR, fluorescence and raman microspectroscopy. **The Royal Society of Chemistry Advances**. 9(47): 27391-27397.
- Paul, W., and Sharma, C.P. (2010). 8 - Inorganic nanoparticles for targeted drug delivery. In: Sharma, C.P. (ed). *Biointegration of Medical Implant Materials*. Woodhead Publishing, Sawston, Cambridge, UK. pp. 204-235.
- Pelkonen, K.H., Heinonen-Tanski, H., and Hänninen, O.O. (2003). Accumulation of silver from drinking water into cerebellum and musculus soleus in mice. **Toxicology**. 186(1-2): 151-157.
- Pourrut, B., Shahid, M., Dumat, C., Winterton, P., and Pinelli, E. (2011). Lead uptake, toxicity, and detoxification in plants. **Reviews of Environmental Contamination and Toxicology**. 213: 113-136.

- Pratap, S.D., and Nath, S.O. (2011). Synthesis of micron-sized hexagonal and flower-like nanostructures of lead oxide (PbO₂) by anodic oxidation of lead. **Nano-Micro Letters**. 3(4): 223-227.
- Printz, B., Lutts, S., Hausman, J.-F., and Sergeant, K. (2016). Copper trafficking in plants and its implication on cell wall dynamics. **Frontiers in Plant Science**. 7(601): 1-16.
- Puig, S., Anders-Colas, N., Garica-Molina, A., and Penarrubia, L. (2007). Copper and iron homeostasis in Arabidopsis: Responses to metal deficiencies, interactions and biotechnological applications. **Plant, Cell & Environment**. 30(3): 271-290.
- Qiu, Y.-L., and Yu, J. (2003). *Azolla* – A model organism for plant genomic studies. **Genomics, Proteomics & Bioinformatics**. 1(1): 15-25.
- Rai, P.K. (2008). Technical note: Phytoremediation of Hg and Cd from industrial effluents using an aquatic free floating macrophyte *Azolla Pinnata*. **International Journal of Phytoremediation**. 10(5): 430-439.
- Rainbow, P.S. (2018). Trace metals in the environment and organisms: The British Isles as a case study. Cambridge University, London, UK. 756 p.
- Reddy, K., and DeBusk, W. (1984). Growth characteristics of aquatic macrophytes cultured in nutrient-enriched water: Water hyacinth, water lettuce, and pennywort. **Economic Botany**. 38(2): 229-239.
- Redwing, R. (2019). Materials in today's world. Trafalgar Square Publishing, Mishawaka, Indiana, USA. 96 p.
- Rezania, S., Taib, S.M., Din, M.M.F., Dahalan, F.A., and Kamyab, H. (2016). Comprehensive review on phytotechnology: Heavy metals removal by diverse

- aquatic plants species from wastewater. **Journal of Hazardous Materials**. 318: 587-599.
- Rieuwerts, J.S., Thornton, I., Farago, M.E., and Ashmore, M.R. (1998). Factors influencing metal bioavailability in soils: preliminary investigations for the development of a critical loads approach for metals. **Chemical Speciation & Bioavailability**. 10(2): 61-75.
- Roy, S., and Bysakh, S. (2011). Ultrafine PZT based ceramics synthesized by auto-ignition of metal-polymer gel: Enhanced sinterability and higher remnant polarization. **Materials Chemistry and Physics**. 126(3): 948-954.
- Saif, S., Tahir, A., and Chen, Y. (2016). Green synthesis of iron nanoparticles and their environmental applications and implications. **Nanomaterials**. 6(11): 209-216.
- Saleeb, N., Gooneratne, R., Cavanagh, J., Bunt, C., Hossain, A.K., Gaw, S., and Robinson, B. (2019). The mobility of silver nanoparticles and silver ions in the soil-plant system. **Journal of Environmental Quality**. 48(6): 1835-1841.
- Sanmuga, P.E., and Senthamil, S.P. (2017). Water hyacinth (*Eichhornia crassipes*): An efficient and economic adsorbent for textile effluent treatment – A review. **Arabian Journal of Chemistry**. 10: S3548–S3558.

- Santhosh, C., Nivetha, R., Kollu, P., Srivastava, V., Sillanpää, M., Grace, A.N., and Bhatnagar, A. (2017). Removal of cationic and anionic heavy metals from water by 1D and 2D-carbon structures decorated with magnetic nanoparticles. **Scientific reports**. 7(1): 14107-14107.
- Sarkar, A., and Jana, S. (1986). Heavy metal pollutant tolerance of *Azolla Pinnata*. **Water Air and Soil Pollution**. 27(1): 15-18.
- Schaper, A., Hou, H., Greiner, A., Schneider, R., and Phillipp, F. (2004). Copper nanoparticles encapsulated in multi-shell carbon cages. **Applied Physics A: Materials Science and Processing**. 78(1): 73-77.
- Schaumlöffel, D. (2012). Nickel species: Analysis and toxic effects. *Journal of Trace Elements in Medicine and Biology*. 26(1): 1-6.
- Shafi, N., Pandit, A.K., Kamili, A.N., and Mushtaq, B. (2015). Heavy metal accumulation by *Azolla pinnata* of Dal Lake ecosystem, India. **Journal of Environment Protection and Sustainable Development**. 1(1): 1-12.
- Shao, H., Zhang, X., Liu, S., Chen, F., Xu, J., and Feng, Y. (2011). Preparation of pure iron nanofibers via electrospinning. **Materials Letters**. 65(12): 1775-1777.
- Sharma, P., and Dubey, R.S. (2005). Lead toxicity in plants. **Brazilian Journal of Plant Physiology**. 17(1): 35-52.
- Shobha, N., Nanda, N., Giresha, A.S., Dharmappa, K.K., Nagabhushana, B.M., and Mylarappa, M. (2018). Synthesis and characterization of silver nanoparticles by solution combustion method and their biological studies. **Materials Today: Proceedings**. 5(10, Part 3): 22614-22620.

- Singh, A., Vyas, D., and Malaviya, P. (2016). Two-stage phyto-microremediation of tannery effluent by *Spirodela polyrrhiza* (L.) Schleid. and chromium resistant bacteria. **Bioresource Technology**. 216: 883-893.
- Singh, P. (2016). Biological synthesis of nanoparticles from plants and microorganisms. **Trends in Biotechnology**. 34(7): 588-599.
- Sivaraman, S.K., Elango, I., Kumar, S., and Santhanam, V. (2009). A green protocol for room temperature synthesis of silver nanoparticles in seconds. **Current Science**. 97(7): 1055-1059.
- Strüder, L. (2000). High-resolution imaging X-ray spectrometers: Nuclear instruments and methods in physics research. Elsevier, London, UK. 113 p.
- Suresh, S., Karthikeyan, S., and Jayamoorthy, K. (2016). FTIR and multivariate analysis to study the effect of bulk and nano copper oxide on peanut plant leaves. **Journal of Science: Advanced Materials and Devices**. 1(3): 343-350.
- Suresh, S., Karthikeyan, S., and Jayamoorthy, K. (2016). Spectral investigations to the effect of bulk and nano ZnO on peanut plant leaves. **Karbala International Journal of Modern Science**. 2(2): 69-77.
- Tadic, M., Milosevic, I., Kralj, S., Mitric, M., Makovec, D., Saboungi, M.-L., and Motte, L. (2017). Synthesis of metastable hard-magnetic Fe₂O₃ nanoparticles from silica-coated akaganeite nanorods. **Nanoscale**. 9(30): 10579-10584.
- Talebi, M., Tabatabaei, B.E.S., and Akbarzadeh, H. (2019). Hyperaccumulation of Cu, Zn, Ni, and Cd in *Azolla* species inducing expression of methallothionein and phytochelatin synthase genes. **Chemosphere**. 230: 488-497.

- Tamayo, L., Palza, H., Bejarano, J., and Zapata, P.A. (2019). Polymer composites with metal nanoparticles: Synthesis, properties, and applications. **Polymer Composites with Functionalized Nanoparticles**. 1: 249-286.
- Tamilvanan, A., Balamurugan, K., Ponappa, K., and Kumar, B.M. (2014). Copper nanoparticles: Synthetic strategies, properties and multifunctional application. **International Journal of Nanoscience**. 13(02): 1-22.
- Tang, Y., Chen, L., Wei, X., Yao, Q., and Li, T. (2013). Removal of lead ions from aqueous solution by the dried aquatic plant, *Lemna perpusilla* Torr. **Journal of Hazardous Materials**. 244-245: 603-612.
- Taylor, A.F., Rylott, E.L., Anderson, C.W.N., and Bruce, N.C. (2014). Investigating the toxicity, uptake, nanoparticle formation and genetic response of plants to gold. **Public Library of Science ONE**. 9(4): e93793-e93799.
- Tel-Or, E., and Forni, C. (2011). Phytoremediation of hazardous toxic metals and organics by photosynthetic aquatic systems. **Plant Biosystems**. 145(1): 224-235.
- Thakkar, K.N., Mhatre, S.S., and Parikh, R.Y. (2010). Biological synthesis of metallic nanoparticles. **Nanomedicine: Nanotechnology, Biology and Medicine**. 6(2): 257-262.
- Thakur, S., Singh, L., Wahid, Z.A., Siddiqui, M.F., Atnaw, S.M., and Din, M.F.M. (2016). Plant-driven removal of heavy metals from soil: Uptake, translocation, tolerance mechanism, challenges, and future perspectives. **Environmental Monitoring and Assessment**. 188(4): 1-11.

- Thomine, S., Wang, R., Ward, J.M., Crawford, N.M., and Schroeder, J.I. (2000). Cadmium and iron transport by members of a plant metal transporter family in *Arabidopsis* with homology to Nramp genes. **Proceedings of the National Academy of Sciences of the United States of America**. 97(9): 4991-4996.
- Tian, C.S., Qian, D., Wu, D., He, R.H., Wu, Y.Z., Tang, W.X., Yin, L.F., Shi, Y.S., Dong, G.S., Jin, X.F., Jiang, X.M., Liu, F.Q., Qian, H.J., Sun, K., Wang, L. M., Rossi, G., Qiu, Z.Q., and Shi, J. (2005). Body-centered-cubic nickel and its magnetic properties. **Physical Review Letters**. 94(13): 137210-137219.
- Titus, J.E., and Urban, R.A. (2009). Aquatic plants: **A general introduction**. **Encyclopedia of Inland Waters**. 1: 43-51.
- Tran, Q.H., and Le, A.-T. (2013). Silver nanoparticles: Synthesis, properties, toxicology, applications and perspectives. **Advances in Natural Sciences: Nanoscience and Nanotechnology**. 4(3): 1-20.
- Tripathi, D.K., Tripathi, A., Shweta, Singh, S., Singh, Y., Vishwakarma, K., Yadav, G., Sharma, S., Singh, V.K., Mishra, R.K., Upadhyay, R.G., Dubey, N.K., Lee, Y., and Chauhan, D.K. (2017). Uptake, accumulation and toxicity of silver nanoparticle in autotrophic plants, and heterotrophic microbes: A concentric review. **Frontiers in Microbiology**. 8(7): 1-16.
- Turhanen, P.A., Vepsäläinen, J.J., and Peräniemi, S. (2015). Advanced material and approach for metal ions removal from aqueous solutions. **Scientific reports**. 5: 8992-8992.

- Ushamani, M., and Renuka, M. (2017). Green synthesis, characterization and antibacterial property of silver nanoparticles using *Ocimum tenuiflorum*, *Azadirachta indica* and *Plectranthus amboinicus* leaf extracts. **International Journal of Scientific and Research Publications**. 7(10): 1-5.
- Verma, R., and Suthar, S. (2015). Lead and cadmium removal from water using duckweed – *Lemna gibba* L.: Impact of pH and initial metal load. **Alexandria Engineering Journal**. 54(4): 1297-1304.
- Volkman, M., Schliehe, C., and Bielewicz, T. (2019). Sculpting of lead sulfide nanoparticles by means of acetic acid and dichloroethane. **International Journal of Research in Physical Chemistry and Chemical Physics**. 229(1-2): 139-189.
- Wan, N.W.S., and Hanafiah, M.A. (2008). Removal of heavy metal ions from wastewater by chemically modified plant wastes as adsorbents: **A review**. **Bioresource Technology**. 99(10): 3935-3948.
- Wang, L., Hu, C., and Shao, L. (2017). The antimicrobial activity of nanoparticles: Present situation and prospects for the future. **International Journal of Nanomedicine**. 12: 1227-1249.
- Wang, Q., Lu, H., Chen, J., Jiang, Y., Williams, M.A., Wu, S., Li, J., Liu, J., Yang, G., and Yan, C. (2020). Interactions of soil metals with glomalin-related soil protein as soil pollution bioindicators in mangrove wetland ecosystems. **Science of the Total Environment**. 709: 1-41.
- Wang, W., Kerstetter, R.A., and Michael, T.P. (2011). Evolution of genome size in duckweeds (Lemnaceae). **Journal of Botany**. 2011: 1-9.

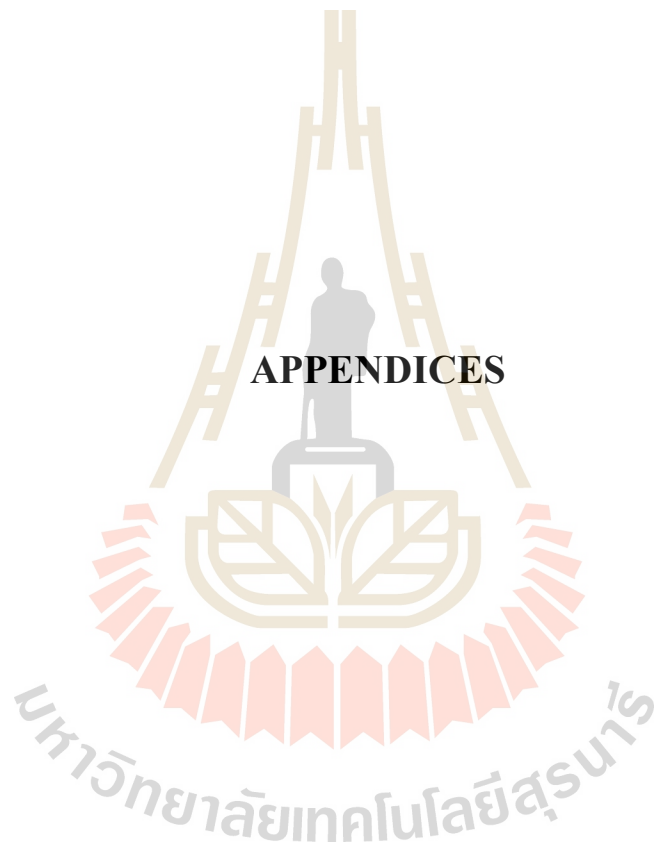
- Wang, X., Liu, X., and Xie, J. (2014). Mechanism of surface texture evolution in pure copper strips subjected to double rolling. **Progress in Natural Science: Materials International**. 24(1): 75-82.
- Wang, Y., and Xia, Y. (2004). Bottom-up and top-down approaches to the synthesis of monodispersed spherical colloids of low melting-point metals. **Nano Letters**. 4(10): 2047-2050.
- Wei, Z., Dong, L., and Tian, Z. (2009). Fourier transform infrared spectrometry study on early stage of cadmium stress in clover leaves. **Pakistan Journal of Botany**. 41(4): 1743-1750
- Xia, C., Hong, L., Yang, Y., Yanping, X., Xing, H., and Gang, D. (2019). Protein changes in response to lead stress of lead-tolerant and lead-sensitive industrial hemp using SWATH technology. **Genes**. 10(5): 1-16.
- Xia, Y., Xiong, Y., Lim, B., and Skrabalak, S.E. (2009). Shape-controlled synthesis of metal nanocrystals: Simple chemistry meets complex physics. **Angewandte Chemie International Edition**. 48(1): 60-103.
- Xu, G., Li, L., Shen, Z., Tao, Z., Zhang, Y., Tian, H., Wei, X., Shen, G., and Han, G. (2015). Magnetite Fe_3O_4 nanoparticles and hematite $\alpha\text{-Fe}_2\text{O}_3$ uniform oblique hexagonal microdisks, drum-like particles and spindles and their magnetic properties. **Journal of Alloys and Compounds**. 629: 36-42.
- Xu, Y., Lu, Y., Dai, X., and Dong, B. (2017). The influence of organic-binding metals on the biogas conversion of sewage sludge. **Water Research**. 126: 329-341.
- Yadav, H.K., and Raizaday, A. (2016). Chapter 12 - Inorganic nanobiomaterials for medical imaging. In: Grumezescu, A.M. (ed). *Nanobiomaterials in Medical Imaging*. William Andrew Publishing, London, UK. pp. 365-401.

- Yadav, L., Tripathi, R.M., Prasad, R., Pudake, R.N., and Mittal, J. (2017). Antibacterial activity of Cu nanoparticles against *Escherichia coli*, *Staphylococcus aureus* and *Pseudomonas aeruginosa*. **Nano Biomedicine and Engineering**. 9: 9-14.
- Yang, M.-H., Yuan, S.-S., Chung, T.-W., Jong, S.-B., Lu, C.-Y., Tsai, W.-C., Chen, W.-C., Lin, P.-C., Chiang, P.-W., and Tyan, Y.-C. (2014). Characterization of silk fibroin modified surface: A proteomic view of cellular response proteins induced by biomaterials. **BioMed Research International**. 2014: 1-13.
- Yew, Y.P., Shameli, K., Miyake, M., Ahmad Khairudin, N.B.B., Mohamad, S.E.B., Naiki, T., and Lee, K.X. (2018). Green biosynthesis of superparamagnetic magnetite Fe₃O₄ nanoparticles and biomedical applications in targeted anticancer drug delivery system: A review. **Arabian Journal of Chemistry**. 13(1): 2287-2308.
- Yonezawa, T. (2018). Application 78 - Preparation of metal nanoparticles and their application for materials. In: Naito, M., Yokoyama, T., Hosokawa, K., and Nogi, K. (ed). *Nanoparticle Technology Handbook (Third Edition)*. Elsevier Publishing, London, UK. pp. 829-837.
- Yousefi, R., Khorsand Zak, A., Jamali-Sheini, F., Huang, N.M., Basirun, W.J., and Sookhakian, M. (2014). Synthesis and characterization of single crystal PbO nanoparticles in a gelatin medium. **Ceramics International**. 40(8, Part A): 11699-11703.
- Yruela, I. (2009). Copper in plants: Acquisition, transport and interactions. **Functional Plant Biology**. 36(5): 409-430.

- Zambelli, B., Uversky, V.N., and Ciurli, S. (2016). Nickel impact on human health: An intrinsic disorder perspective. **Biochimica et Biophysica Acta (BBA) - Proteins and Proteomics**. 1864(12): 1714-1731.
- Zhang, T., Lu, Q., Su, C., Yang, Y., Hu, D., and Xu, Q. (2017). Mercury induced oxidative stress, DNA damage, and activation of antioxidative system and Hsp70 induction in duckweed (*Lemna minor*). **Ecotoxicology and Environmental Safety**. 143: 46-56.
- Zhang, Z., Sun, Y., Sun, C., Wang, N., and Zhang, Y. (2014). Adsorption of arsenite by six submerged plants from Lanshi lake, China. **Journal of Chemistry**. 2014: 1-7.
- Zhou, Y., Jin, C., Li, Y., and Shen, W. (2018). Dynamic behavior of metal nanoparticles for catalysis. **Nano Today**. 20: 101-120.



APPENDICES





APPENDIX A
CHEMICALS AND MEDIA

มหาวิทยาลัยเทคโนโลยีสุรนารี

1. General chemicals and materials

Copper nitrate	Merck, Darmstadt, Germany
Iron nitrate	Merck, Darmstadt, Germany
Nickel nitrate	Merck, Darmstadt, Germany
Lead nitrate	EMS, Hatfield, PA, USA
Silver nitrate	QRec, Auckland, New Zealand
Glutaraldehyde	Unilab, Auckland, New Zealand
Disodium hydrogen phosphate	Sigma Aldrich, Darmstadt, Germany
Dihydrogen phosphate	Sigma Aldrich, Darmstadt, Germany
Acetone	Unilab, Auckland, New Zealand

2. Spurr's resin media

Vinylcyclohexene Dioxide	EMS, Hatfield, PA, USA
Diglycidyl ether of polypropylene glycol	EMS, Hatfield, PA, USA
Nonenyl succinic anhydride	EMS, Hatfield, PA, USA
Dimethylaminoethanol	EMS, Hatfield, PA, USA



APPENDIX B
REAGENT PREPERATION

มหาวิทยาลัยเทคโนโลยีสุรนารี

1. Spurr's resin solution preparation

Components	Unit (g)		
	Firm	Hard	Soft
Vinylcyclohexene Dioxide (ERL)	4.10	4.10	4.10
Diglycidyl ether of polypropylene glycol (DER)	1.43	0.95	1.90
Nonenyl succinic anhydride (NSA)	5.90	5.90	5.90
Dimethylaminoethanol (DMAE)	0.10	0.10	0.10

The Spurr's resin embedding medium was recommended to **freshly prepare** as follows. Exact weights of ERL, DER, and NSA solutions were sequentially added into a disposable plastic beaker with continuous stirring. Different orders of adding chemicals caused solidification of the mixture. Then, DMAE solution was added and well mixed. This resin medium was ready to use, and the freshly prepared resin medium was recommended. If necessary, the resin medium could keep in a disposable syringe without air and sealed with parafilm to store in a freezer for few months.

2. Fixating and dehydrating agent

95% acetone solution, 100 mL

100% acetone	95	mL
Double deionization (DDI) water (autoclave)	5	mL

Freshly prepare and keep at 4 °C before using.

70% acetone solution, 100 mL

100% acetone	70	mL
--------------	----	----

DI water (autoclave)	30	mL
----------------------	----	----

Freshly prepare and keep at 4 °C before using.

50% acetone solution, 100 mL

100% acetone	50	mL
--------------	----	----

DDI water (autoclave)	50	mL
-----------------------	----	----

Freshly prepare and keep at 4 °C before using.

30% acetone solution, 100 mL

100% acetone	30	mL
--------------	----	----

DDI water (autoclave)	70	mL
-----------------------	----	----

Freshly prepare and keep at 4 °C before using.

1 M sodium phosphate buffer pH 7.0

Sodium dihydrogen phosphate (NaH_2PO_4)	31.20	g
---	-------	---

Disodium hydrogen phosphate (Na_2HPO_4)	28.39	g
---	-------	---

Adjust to pH 7.0 with NaH_2PO_4 or Na_2HPO_4 to a final volume of 1000 mL of

DDI water and autoclave

2.5% glutaldehyde solution, 100 mL

25% glutaldehyde solution	10	mL
---------------------------	----	----

Sodium phosphate buffer pH 7.0 (autoclave)	90	mL
--	----	----

10 mM Ethylenediaminetetraacetic acid; EDTA

100 mM EDTA	10	mL
-------------	----	----

DDI water (autoclave)	90	mL
-----------------------	----	----

Fresh prepare and keep at room temperature

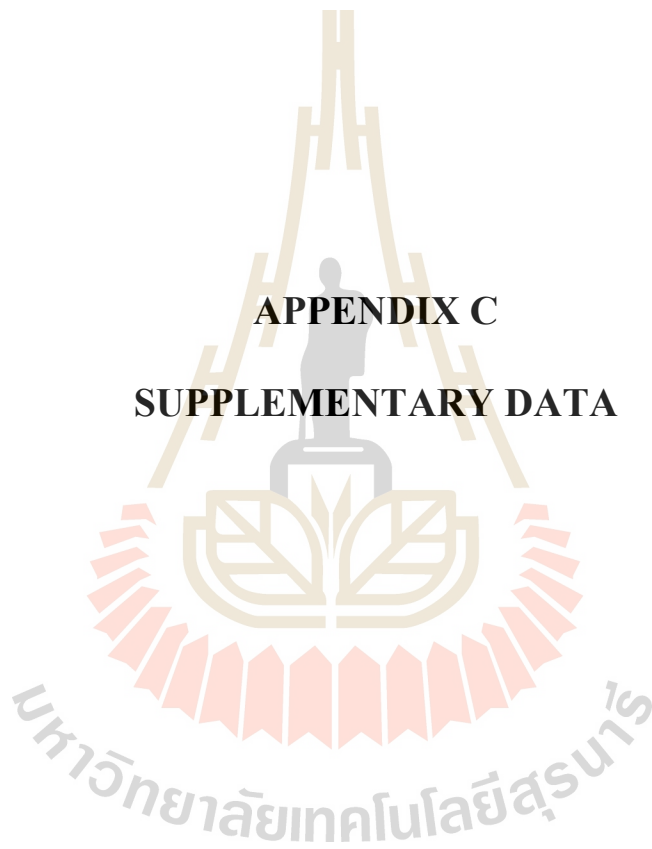
3. Infiltration and polymerization of embedding medium

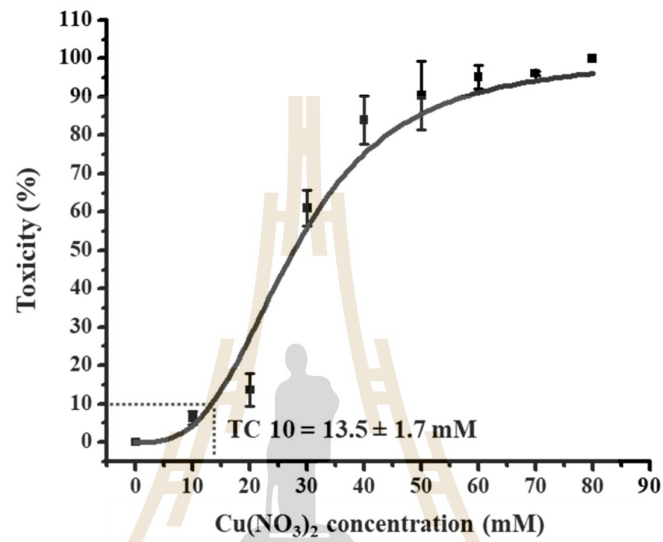
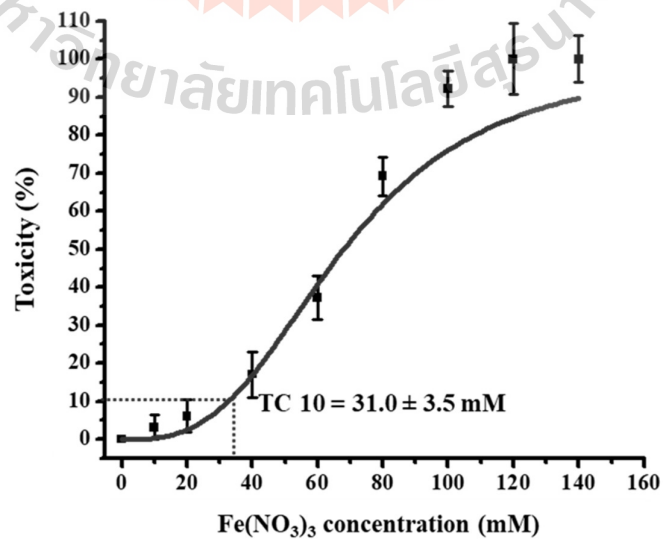
The plant samples were dehydrated in dilution series of 30% acetone (30 min), 50% acetone (30 min), 75% acetone (overnight), 95% acetone (30 min), and 100% acetone (30 min, twice), respectively. Then, the dehydrated plant samples were infiltrated with the mixture I (Spurr's resin embedding medium and acetone, 1:3 v/v) using a 1:2 w/v ratio in a circular rotary mixer (Neuation Technologies, Gujarat, India) at 10 rpm for 2–3 h. The mixture I was replaced with the mixture II (Spurr's resin embedding medium and acetone, 1:2 v/v) and further incubated overnight in a circular rotary mixer (10 rpm). Then, the mixture II was replaced with the mixture III (Spurr's resin embedding medium and acetone, 1:1 v/v) and further incubated for another 2–3 h. The mixture III was replaced with the Spurr's resin embedding medium and incubated for various periods depending on specimen sizes; small specimens (5–6 h) and large specimens (6–8 h or overnight). Then, the specimens were solidified at 50 °C for 12 h, followed by at 60 °C for 12–24 h.

4. Preparation of 0.1 M potassium phosphate buffer at 25 °C

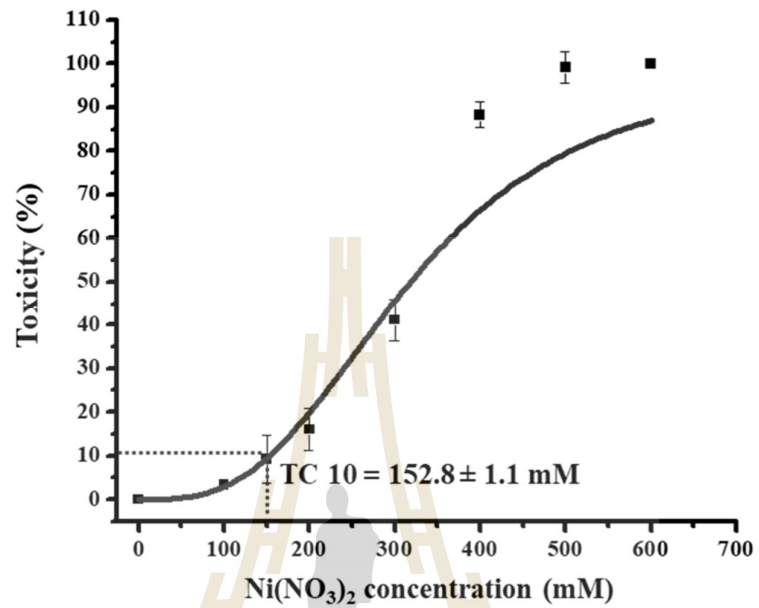
pH	Volume of 1 M K_2HPO_4 (mL)	Volume of 1 M KH_2PO_4 (mL)
6.2	19.2	80.0
6.4	27.8	72.2
6.6	38.1	61.9
6.8	49.7	50.3
7.0	61.5	38.5
7.2	71.7	28.3
7.4	80.2	19.8
7.6	86.6	13.4
7.8	90.8	9.2
8.0	94.0	6.0

APPENDIX C
SUPPLEMENTARY DATA

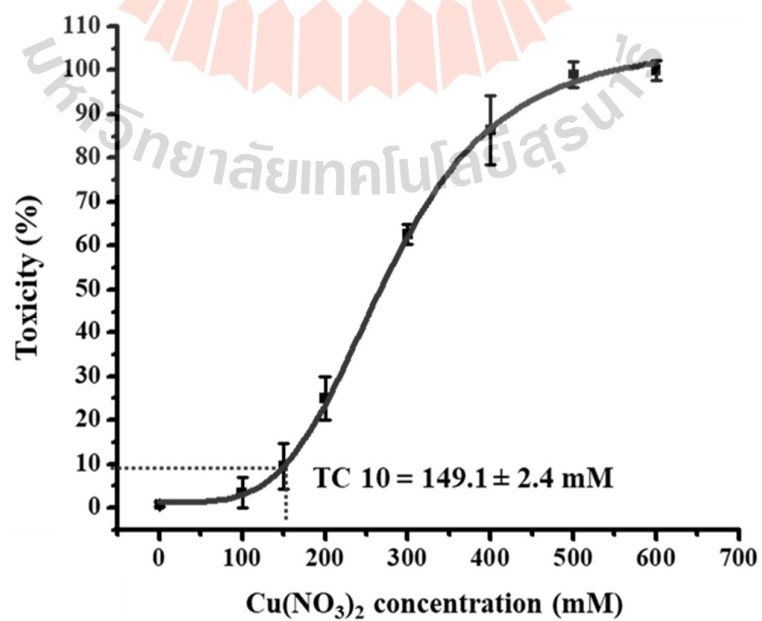


Data of the independently repeated experiments**1. The toxicity effects of five metal ions on *Azolla pinnata* R.Br.****1.1 The toxicity effects of $\text{Cu}(\text{NO}_3)_2$ on *Azolla pinnata* R.Br.****1.2 The toxicity effects of $\text{Fe}(\text{NO}_3)_3$ on *Azolla pinnata* R.Br.**

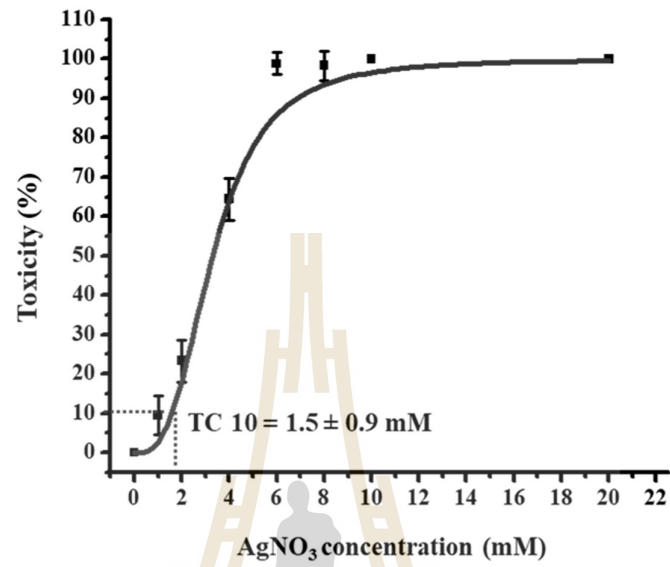
1.3 The toxicity effects of $\text{Ni}(\text{NO}_3)_2$ on *Azolla pinnata* R.Br.



1.4 The toxicity effects of $\text{Pb}(\text{NO}_3)_2$ on *Azolla pinnata* R.Br.

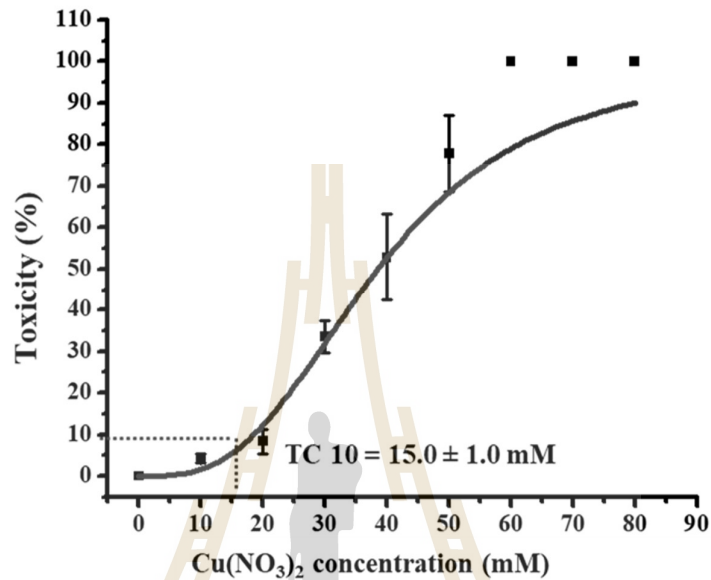


1.5 The toxicity effects of AgNO_3 on *Azolla pinnata* R.Br.

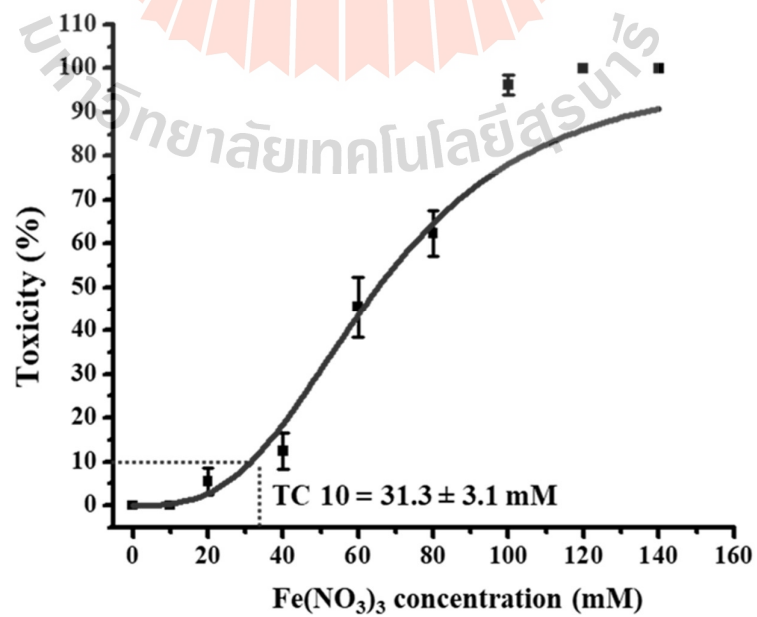


2. The toxicity effects of five metal ions on *Salvinia molesta* D.S. Mitch.

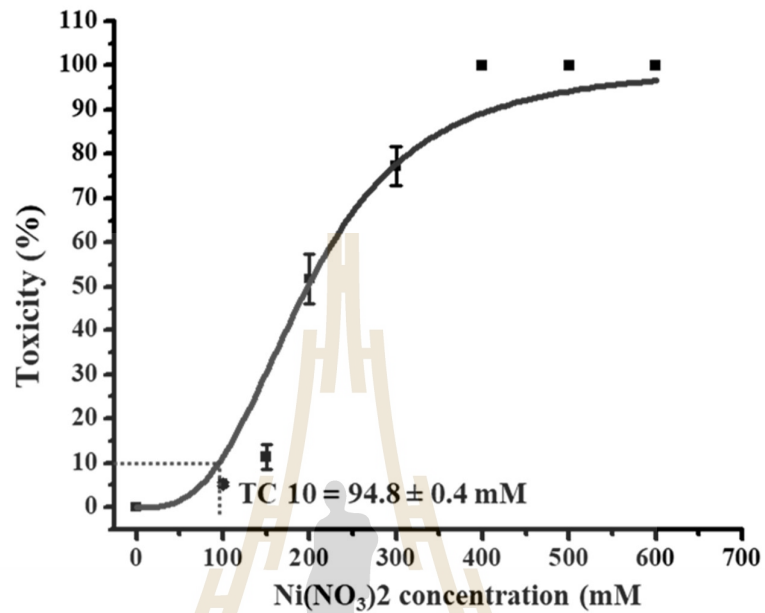
2.1 The toxicity effects of $\text{Cu}(\text{NO}_3)_2$ on *Salvinia molesta* D.S. Mitch.



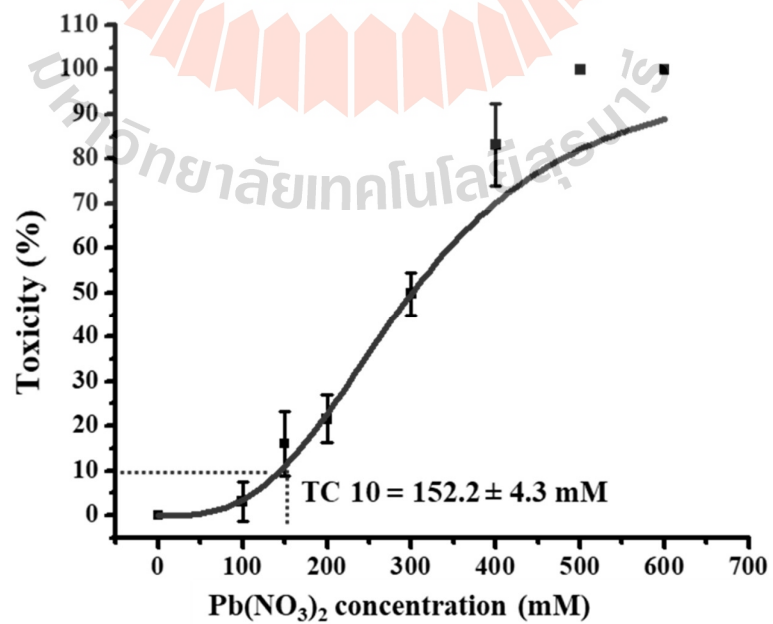
2.2 The toxicity effects of $\text{Fe}(\text{NO}_3)_3$ on *Salvinia molesta* D.S. Mitch.



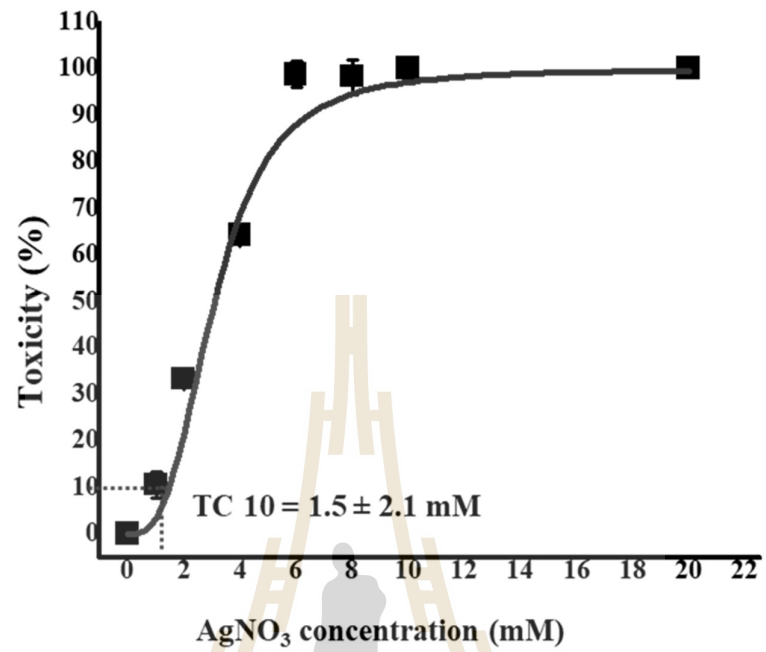
2.3 The toxicity effects of $\text{Ni}(\text{NO}_3)_2$ on *Salvinia molesta* D.S. Mitch.



2.4 The toxicity effects of $\text{Pb}(\text{NO}_3)_2$ on *Salvinia molesta* D.S. Mitch.

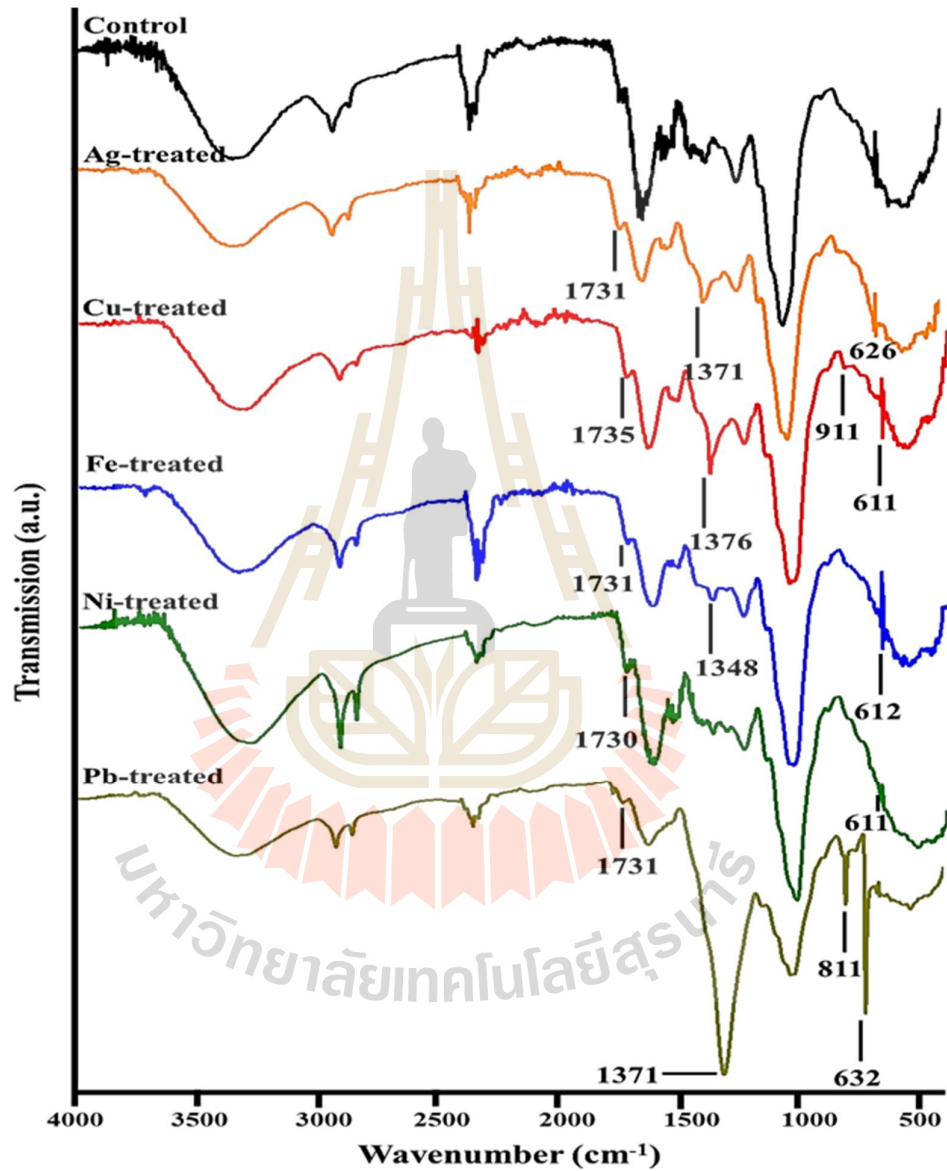


2.5 The toxicity effects of AgNO₃ on *Salvinia molesta* D.S. Mitch.



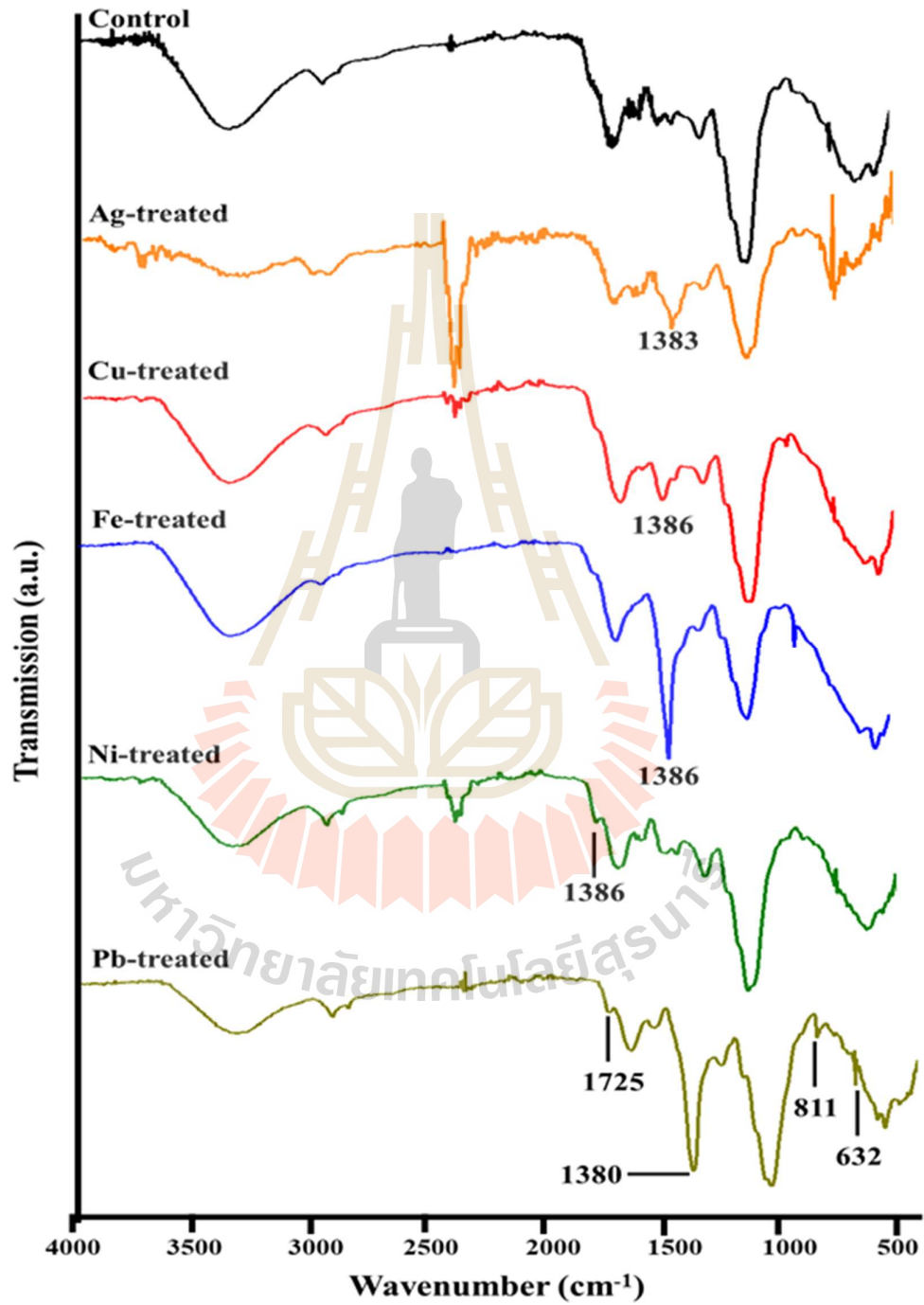
3. ATR-FTIR profiles in response to metal treatments of plants

3.1 ATR-FTIR profiles in response to AgNO_3 on *Azolla pinnata* R.Br.



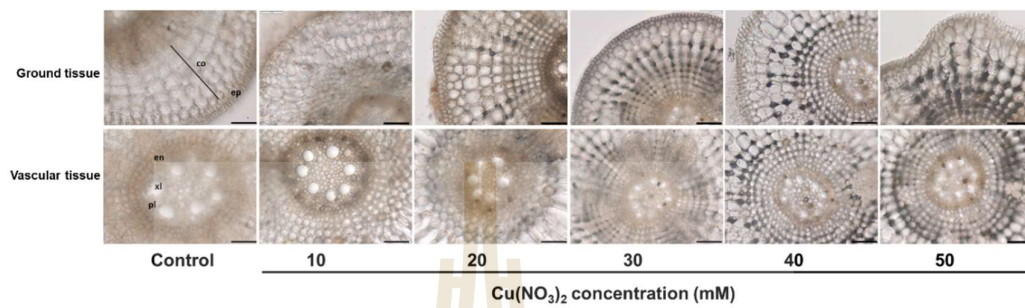
3.2 ATR-FTIR profiles in response to AgNO₃ on *Salvinia molesta* D.S.

Mitch.

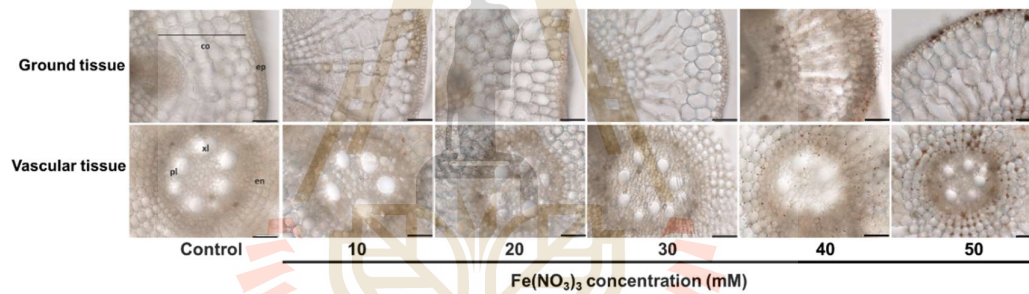


4. Cross-sections of ground and vascular tissues of water hyacinth roots exposed to five metal ions solutions observed under a light microscope

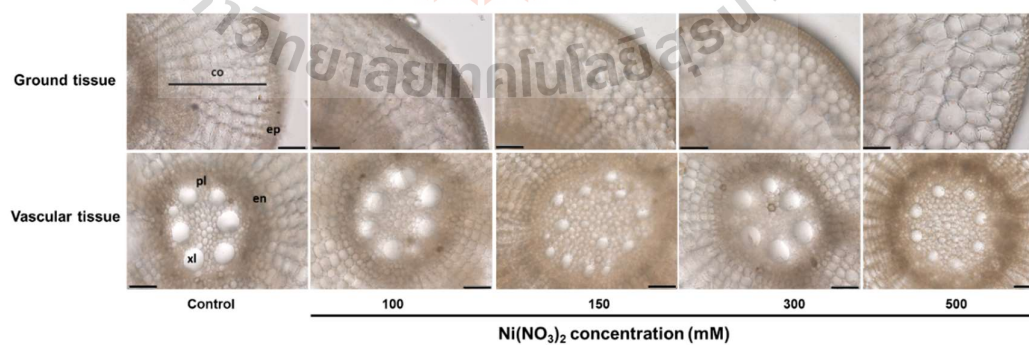
3.1 Cross-sections of water hyacinth roots exposed to $\text{Cu}(\text{NO}_3)_2$ solution



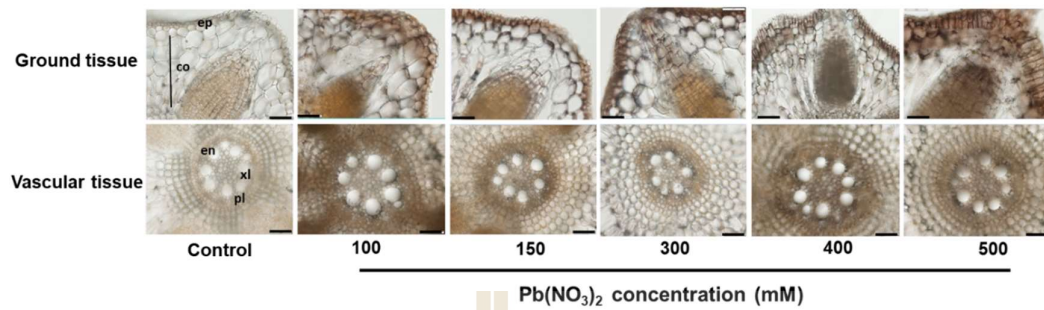
3.2 Cross-sections of water hyacinth roots exposed to $\text{Fe}(\text{NO}_3)_3$ solution



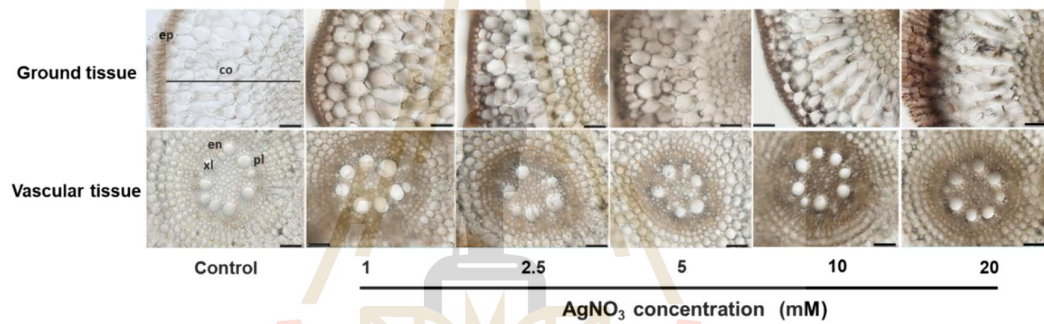
3.3 Cross-sections of water hyacinth roots exposed to $\text{Ni}(\text{NO}_3)_2$ solution



3.4 Cross-sections of water hyacinth roots exposed to $\text{Pb}(\text{NO}_3)_2$ solution



3.5 Cross-sections of water hyacinth roots exposed to AgNO_3 solution



CURRICULUM VITAE

Ms. Jiraporn Chumpol was born in Khon Kaen Province, Thailand. She received the Bachelor's degree in Chemistry from Mahasarakham University in 2010 and the Master's degree in Biochemistry from Khon Kaen University in 2013. She has pursued the Ph.D. degree in Environmental Biology at Suranaree University of Technology. Her research expertise is in the field of nano-biology and bio-innovated products. During her study, she has produced several publications in the international journals with ISI impact factor including:

1. 2020. **Chumpol J** and Siri S. Light-mediated green synthesis of DNA-capped silver nanoparticles and their antibacterial activity. *Journal of Nanoscience and Nanotechnology*. 20(3): 1678-1684 (IF: 1.354).
2. 2019. Chumpol J and Siri S. In vivo formation of spherical and rod lead nanoparticles in root cells of water velvet (*Azolla pinnata*). *Biotechnology and Applied Biochemistry*. Accepted Articles: 10 December 2019.
3. 2018. **Chumpol J** and Siri S. Simple green production of silver nanoparticles facilitated by bacterial genomic DNA and their antibacterial activity. *Artificial Cells, Nanomedicine, and Biotechnology*. 46(3): 619-625 (IF: 4.462).
4. 2016. **Chumpol J** and Siri S. Electrospun cellulose acetate membrane for size separating and antibacterial screening of crude polysaccharides. *IET Nanobiotechnology*. 10(4): 405-410 (IF 2015 = 1.5).